TOPICS IN CLASSICAL AND QUANTUM INTEGRABILITY

By

JASEN A. SCARAMAZZA

A dissertation submitted to the

School of Graduate Studies

Rutgers, The State University of New Jersey

In partial fulfillment of the requirements

For the degree of

Doctor of Philosophy

Graduate Program in Physics and Astronomy

Written under the direction of

Joel L. Lebowitz and Emil A. Yuzbashyan

And approved by

New Brunswick, New Jersey

May, 2019

ABSTRACT OF THE DISSERTATION

Topics in classical and quantum integrability

By JASEN A. SCARAMAZZA

Dissertation Director:

Joel L. Lebowitz and Emil A. Yuzbashyan

This Thesis is an amalgamation of research I conducted as a physics graduate student at Rutgers University. Each chapter stands independently of the others with its own introduction and set of references, though Chapters 4 and 5 treat the same subject and may be read in succession. The chapters are presented roughly in reverse chronological order, so that the first chapters are my most recent work.

The common threads of this research program are the statistical and dynamical properties of many body systems, both in and out of equilibrium. Save for Chapter 6, the works are strongly associated with physical models called integrable, whose Hamiltonians have a comparatively large number of conservation laws with respect to generic models. Using numerical and analytical techniques, we shall explore the effects of integrability on a diverse set of phenomena including far-from-equilibrium steady states in Chapter 2, heat conductivity in Chapter 3, and Hamiltonian level statistics in Chapters 4-5. We also characterize these phenomena for systems that are not quite integrable, but are in certain ways close to integrable.

The chapters in this Thesis are based on the following works:

J. A. Scaramazza, P. Smacchia, and E. A. Yuzbashyan, Consequences of integrability breaking in quench dynamics of pairing Hamiltonians, arXiv:1812.04410 (2018). Accepted by Phys. Rev. B Jan. 2019.

J. L. Lebowitz and J. A. Scaramazza, Ballistic Transport in the classical Toda chain with harmonic pinning, arXiv:1801.07153 (2018).

A. Dhar, A. Kundu, J. L. Lebowitz and J. A. Scaramazza, Transport properties of the classical Toda chain: effect of a pinning potential, arXiv:1812.11770 (2018). Submitted to J. Stat. Phys. Jan. 2019.

E. A. Yuzbashyan, B. S. Shastry and J. A. Scaramazza, Rotationally invariant ensembles of integrable matrices, Phys. Rev. E **93**, 052114 (2016).

J. A. Scaramazza, B. S. Shastry and E. A. Yuzbashyan, Integrable matrix theory: Level statistics, Phys. Rev. E **94**, 032106 (2016).

J. L. Lebowitz and J. A. Scaramazza, A note on Lee-Yang zeros in the negative half-plane, J. Phys.: Condens. Matter **28**, 414004 (2016).

Acknowledgments

Wendy, Jen, Grover, P.C., Jeff, Sam, Hong, Larry, Tom, Joel, Emil, and many others.

Dedication

To Josh, Trina, Jake and Jon

Table of Contents

Abstract ii

Acknowledgments iv

Dedication v

1. Introduction 1

- 1.1. Consequences of integrability breaking in quench dynamics of pairing Hamiltonians 2
- 1.2. Nonequilibrium transport in the Toda chain with harmonic pinning 3
- 1.3. Rotationally invariant ensembles of integrable matrices 3
- 1.4. Integrable matrix theory: Level statistics 4
- 1.5. A note on Lee-Yang zeros in the negative half-plane 5

2. Consequences of integrability breaking in quench dynamics of pairing Hamiltonians 6

- 1. Introduction 6
- 2. Models and pseudospin representation 10
- 3. Main results 15
- 4. Ground state and quench protocol 17
- 5. Simulations of nonequilibrium phases and stability analysis 20
  - 5.1. Phases I and II 22
  - 5.2. Stability analysis 27

5.3. Phase III 32

Universality of elliptic oscillations 32

Relaxation time 37

6. Phase III asymptotic solution 41

6.1. External driving 42

6.2. Phase III spin solution in the separable BCS model 44

6.3. Asymptotic self-consistency 46

6.4. Self-consistent solutions in the separable BCS model 47

7. Quasiperiodic Phase IV 49

8. Conclusion 50

A. Mean-field equations of motion 57

B. Integrable limit of spin-orbit quenches 60

C. Integrability breaking forbids asymptotic reduction 66

C.1. Existence of reduced solutions implies integrability and vice versa . . 66

C.2. Asymptotic $\Delta(t)$ does not match the 2-spin solution in nonintegrable cases 70

D. The link between Lax constructions and the stability analysis 73

D.1. Lax norms 73

D.2. Phase I-II transition 75

D.3. Phase II-III transition 76

D.4. Real parts of Lax roots at the transitions 78

s-wave, II-III 78

$p + ip$, II-III 80

3. Nonequilibrium transport in the Toda chain with harmonic pinning . . 92

1. Introduction 92

2. The model 93

3. Nondissipative behavior 95
3.1. Ballistic transport 95
3.2. Persistent heat currents in the periodic chain 98
3.3. Poincaré sections 100
A. Addendum 103

4. Rotationally invariant ensembles of integrable matrices 108
1. Introduction 108
2. Rotationally invariant construction of type-1 integrable matrix ensembles . 112
3. Probability density function of type-1 integrable ensemble 116
4. Parameter shifts 119
5. Higher types 121
5.1. Rotationally invariant construction 123
5.2. Probability distribution function for ensembles of type-$M > 1$ integrable matrices 127
6. Discussion 128
A. Degenerate E implies u-independent symmetry in type-1 matrices 131
B. Ansatz matrices at $x_0 = 0$ are type-1 134

5. Integrable matrix theory: Level statistics 144
1. Introduction 144
2. Level statistics of type-1 integrable matrices 149
2.1. Type-1 families, primary parametrization 149
2.2. Universality of Poisson statistics 151
2.3. Crossover in coupling parameter x 153
2.4. Correlations between matrix parameters 155
2.5. Basis matrices: how many conservation laws? 159

3. Statistics of integrable matrices of higher types 170
    3.1. Ansatz type-M families 170
    3.2. Correlations in ansatz parameters 173
    3.3. Basis matrices: ansatz higher types 174
4. Analytical results: perturbation theory 176
5. Ergodicity in integrable matrix ensembles 179
6. Conclusion 192
A. Unfolding spectra 195

6. A note on Lee-Yang Zeros in the negative half-plane 204
1. Introduction 204
2. General properties of L-Y zeros 205
3. Results for L-Y zeros in the negative half plane 207
4. The virial expansion 210
    4.1. Hard core lattice gases in 1D 212
    4.2. Square well interactions 215
A. Virial coefficients for the 2-row monomer-dimer problem 218

Chapter 1

Introduction

As is reflected in the wider world of many body theory, the various results found in these chapters range from abstract mathematical constructions to concrete statements about collective phenomena. On one end of this axis we develop the basis invariant construction of ensembles of random matrices modelling quantum integrable models introduced in Ch. 4, and the subsequent numerical study of the level statistics of these ensembles of Ch. 5. Slightly less esoteric is the discussion of the location of the zeros of grand canonical partition functions (Lee-Yang zeros) in Ch. 6, where we find connections between the distributions of these zeros and bounds on macroscopic statistical properties. In Ch. 2, we lead a detailled discussion into the far-from-equilibrium coherent phases of a large class of nonintegrable superconducting models undergoing a sudden change in the system Hamiltonian, i.e., a quantum quench. Important results here include an expanded taxonomy of steady states, a long time scale associated with integrability breaking, and a physically motivated description of the nonequilibrium phase transitions. Finally, Ch. 3 is a numerical study of the classic problem of heat conductivity in a one-dimensional classical system. We find that the Toda lattice, which is integrable, perturbed by an on-site harmonic pinning maintains a nearly ballistic conductivity for rather large system sizes before true diffusive scaling appears.

It will now be useful to introduce each of these works individually.

1.1 Consequences of integrability breaking in quench dynamics of pairing Hamiltonians

We study the collisionless dynamics of two classes of nonintegrable pairing models. One is a BCS model with separable energy-dependent interactions, the other – a 2D topological superconductor with spin-orbit coupling and a band-splitting external field. The long-time quantum quench dynamics at integrable points of these models are well understood. Namely, the squared magnitude of the time-dependent order parameter $\Delta(t)$ can either vanish (Phase I), reach a nonzero constant (Phase II), or periodically oscillate as an elliptic function (Phase III). We demonstrate that nonintegrable models too exhibit some or all of these nonequilibrium phases. Remarkably, elliptic periodic oscillations persist, even though both their amplitude and functional form change drastically with integrability breaking. Striking new phenomena accompany loss of integrability. First, an extremely long time scale emerges in the relaxation to Phase III, such that short-time numerical simulations risk erroneously classifying the asymptotic state. This time scale diverges near integrable points. Second, an entirely new Phase IV of quasiperiodic oscillations of $|\Delta|$ emerges in the quantum quench phase diagrams of nonintegrable pairing models. As integrability techniques do not apply for the models we study, we develop the concept of asymptotic self-consistency and a linear stability analysis of the asymptotic phases. With the help of these new tools, we determine the phase boundaries, characterize the asymptotic state, and clarify the physical meaning of the quantum quench phase diagrams of BCS superconductors. We also propose an explanation of these diagrams in terms of bifurcation theory.

Based on:

J. A. Scaramazza, P. Smacchia, and E. A. Yuzbashyan, Consequences of integrability breaking in quench dynamics of pairing Hamiltonians, arXiv:1812.04410 (2018). Accepted by Phys. Rev. B Jan. 2019.

1.2 Nonequilibrium transport in the Toda chain with harmonic pinning

We investigate, via numerical simulation, heat transport in the nonequilibrium stationary state (NESS) of the 1D classical Toda chain with an additional pinning potential, which destroys momentum conservation. The NESS is produced by coupling the system, via Langevin dynamics, to two reservoirs at different temperatures. To our surprise, we find that when the pinning is harmonic, the transport is seemingly ballistic. We also find that on a periodic ring with nonequilibrium initial conditions and no reservoirs, the energy current oscillates without decay. Lastly, Poincaré sections of the 3-body case indicate that for all tested initial conditions, the dynamics occur on a 3-dimensional manifold. These observations suggest that the N-body Toda chain with harmonic pinning may be integrable. Alternatively, and more likely, this would be an example of a nonintegrable system without momentum conservation for which the heat flux is ballistic.*

Based on:

J. L. Lebowitz and J. A. Scaramazza, Ballistic Transport in the classical Toda chain with harmonic pinning, arXiv:1801.07153 (2018).

A. Dhar, A. Kundu, J. L. Lebowitz and J. A. Scaramazza, Transport properties of the classical Toda chain: effect of a pinning potential, arXiv:1812.11770 (2018). Submitted to J. Stat. Phys. Jan. 2019.

*More recent work shows that the heat flux is indeed diffusive, but that this model's finite size effects are very strong. We shall refer to a recent paper by P. Di Cintio, S. Iubini, S. Lepri and R. Livi, as well as the expanded version of this work by A. Dhar, A. Kunda, J.L. Lebowitz and J.A. Scaramazza.

1.3 Rotationally invariant ensembles of integrable matrices

We construct ensembles of *random integrable matrices* with any prescribed number of nontrivial integrals and formulate *integrable matrix theory* (IMT) – a counterpart of random matrix theory (RMT) for quantum integrable models. A type-M family of integrable matrices consists of exactly $N-M$ independent commuting $N\times N$ matrices linear in a real parameter. We first develop a rotationally invariant parametrization of such matrices, previously only constructed in a preferred basis. For example, an arbitrary choice of a vector and two commuting Hermitian matrices defines a type-1 family and vice versa. Higher types similarly involve a random vector and two matrices. The basis-independent formulation allows us to derive the joint probability density for integrable matrices, similar to the construction of Gaussian ensembles in the RMT.

Based on:

E. A. Yuzbashyan, B. S. Shastry and J. A. Scaramazza, Rotationally invariant ensembles of integrable matrices, Phys. Rev. E **93**, 052114 (2016).

1.4 Integrable matrix theory: Level statistics

We study level statistics in ensembles of integrable $N\times N$ matrices linear in a real parameter x. The matrix $H(x)$ is considered integrable if it has a prescribed number $n>1$ of linearly independent commuting partners $H^i(x)$ (integrals of motion) $\left[H(x),H^i(x)\right]=0$, $\left[H^i(x),H^j(x)\right]=0$, for all x. In a recent work, we developed a basis-independent construction of $H(x)$ for any n from which we derived the probability density function, thereby determining how to choose a typical integrable matrix from the ensemble. Here, we find that typical integrable matrices have Poisson statistics in the $N\to\infty$ limit provided n scales at least as $\log N$; otherwise, they exhibit level repulsion. Exceptions to the Poisson case occur at isolated coupling values $x=x_0$ or when correlations are introduced between typically independent matrix parameters. However, level statistics cross over to Poisson at $\mathcal{O}(N^{-0.5})$ deviations from these exceptions, indicating that non-Poissonian statistics characterize only subsets of measure zero in the parameter space. Furthermore, we present strong numerical evidence that ensembles of integrable matrices are stationary and ergodic with respect to nearest neighbor level statistics.

Based on:

J. A. Scaramazza, B. S. Shastry and E. A. Yuzbashyan, Integrable matrix theory: Level statistics, Phys. Rev. E **94**, 032106 (2016).

1.5 A note on Lee-Yang zeros in the negative half-plane

We obtain lower bounds on the inverse compressibility of systems whose Lee-Yang zeros of the grand-canonical partition function lie in the left half of the complex fugacity plane. This includes in particular systems whose zeros lie on the negative real axis such as the monomer-dimer system on a lattice. We also study the virial expansion of the pressure in powers of the density for such systems. We find no direct connection between the positivity of the virial coefficients and the negativity of the L-Y zeros, and provide examples of either one or both properties holding. An explicit calculation of the partition function of the monomer-dimer system on 2 rows shows that there are at most a finite number of negative virial coefficients in this case.

Based on:

J. L. Lebowitz and J. A. Scaramazza, A note on Lee-Yang zeros in the negative half-plane, J. Phys.: Condens. Matter **28**, 414004 (2016).

Chapter 2

Consequences of integrability breaking in quench dynamics of pairing Hamiltonians

1 Introduction

The past fifteen years have borne witness to impressive advances in the ability to experimentally control many-body systems where dissipative and decoherence effects are strongly suppressed. Studies of cold atomic gases [1, 2, 3, 4, 5, 6, 7, 8, 9, 10], solid state pump-probe experiments [13, 11, 12, 14, 15] and quantum information processing [16, 17, 18, 19, 20, 21, 22, 23] can now explore coherent many-body dynamics for long time scales, paving the way for the characterization of new phenomena. In particular, cold atomic gases with tunable interactions [24, 25, 27, 26, 28, 29] are an instrumental experimental tool in the quest to understand previously inaccessible aspects of far from equilibrium many-body dynamics.

A major focus of recent theory and experiment has been the unitary time evolution of a system, initially in the ground state, subject to a sudden perturbation [30, 31, 32]. This experimental protocol, known as a quantum quench, can induce long-lived states with properties strikingly different from those of equilibrium states at similar energy scales. In this work, we focus on the quench dynamics of various superconducting models, which is a modern reformulation of the longstanding problem of nonequilibrium superconductivity in the collisionless regime [33, 34, 35, 36]. A canonical result is that the infinitesimal perturbation of a Bardeen-Cooper-Schrieffer (BCS) s-wave superconductor leads to power law oscillatory relaxation of the order parameter amplitude $|\Delta|$ to a constant value [35].

Decades later, it was discovered that larger deviations could give rise to different dynamical phases identified by the asymptotic behavior of the amplitude of the order parameter [37, 38, 39, 40, 41, 42, 43, 44]. Consider the dynamics of Δ after quenches of the coupling g in various superconducting models. When the final coupling g_f is small enough, Δ vanishes rapidly in time; this behavior characterizes what we call Phase I. For intermediate g_f, $|\Delta|$ exhibits oscillatory power law decay to a nonzero constant (Phase II). For larger g_f, $|\Delta|$ exhibits persistent periodic oscillations (Phase III) – a nonlinear manifestation of what is known in the literature as the Higgs or amplitude mode [45, 46, 47, 48, 49, 50, 51, 52].

The exact quantum quench phase diagrams of the s-wave superconductor were eventually constructed using a sophisticated analytical method that relies on the model's integrability [53]. It turns out that the integrable $p + ip$ topological superconductor exhibits the same three phases, and similar analytical tools lead to the construction of its phase diagrams [54]. Thus, there may appear to be some profound connection between integrability and these three dynamical phases, but nonintegrable models also have Phases I and II [45, 40, 55, 56, 57] and Phase III-like behavior is thought to persist in some nonintegrable models as well. On the other hand, the existence of Phase III in such models has not been convincingly established beyond the linear regime and aspects of quench dynamics unique to the nonintegrable case have not been explored.

Overall, the description of these nonequilibrium dynamical phases lacks a unifying mechanism applicable to finite quenches of nonintegrable pairing models. Here we present an in-depth study of the nonequilibrium phases of various nonintegrable superconducting models with and without spin-orbit coupling. A common feature of models we consider is that the order parameter takes the form of a single complex number. We establish that Phase III persists when integrability is broken [58] and give strong numerical evidence that the persistent oscillations are always elliptic, which generalizes the known behavior of integrable models [37, 53, 54].

Although the integrable and nonintegrable phenomenology are similar, we find that integrability breaking has profound consequences. Unique to nonintegrable models is an *extremely long relaxation time scale* τ which diverges as one approaches integrable points and is most prominent in quenches to Phase III. One must analyze dynamics beyond τ to truly observe Phase III, which has not been done in other studies. As illustrated in Fig. 2.1, for $t < \tau$, $|\Delta|$ may oscillate with several frequencies and a slowly evolving amplitude, both of which undermine naive analyses restricted to $t < \tau$. One may incorrectly conclude from the transient dynamics that the asymptotic nonequilibrium phase has several undamped frequencies, or that $|\Delta|$ is oscillating periodically while in fact the amplitude is still changing. Nonintegrable Phase III oscillations further require comparatively more elaborate elliptic functions to describe the oscillations.

To complicate the picture even further, certain quantum quenches of nonintegrable pairing models genuinely do not fit into any of the Phases I, II and III. Here the asymptotic $|\Delta|$ is truly *quasiperiodic*, leading us to conclude that there are regions of quasiperiodicity – *a new Phase IV* – in the quantum quench phase diagrams of these models.

Another consequence of integrability breaking arises in the analytical description of the three nonequilibrium phases. In the integrable case, there is a dynamical reduction in the number of degrees of freedom of the system [53, 54] such that Phases I, II and III correspond to an effective classical spin Hamiltonian with 0, 1 and 2 spins, respectively. Phase III in the general case, however, does not admit such a 2-spin representation. As a surrogate to this analytical method, we propose a stability analysis of Phases I and II that applies generally to finite quenches. The stability analysis is based on linearizing around the asymptotic solutions to the equations of motion in each of the phases. We can then nonperturbatively determine the phase I-II boundary as well as the phase II-III boundary in nonintegrable pairing models. Finally, we return to Phase III and argue that the self-consistency condition (gap equation) is responsible not only for the existence of persistent periodic oscillations of $|\Delta|$, but also for selecting elliptic functions amongst all possible periodic functions.

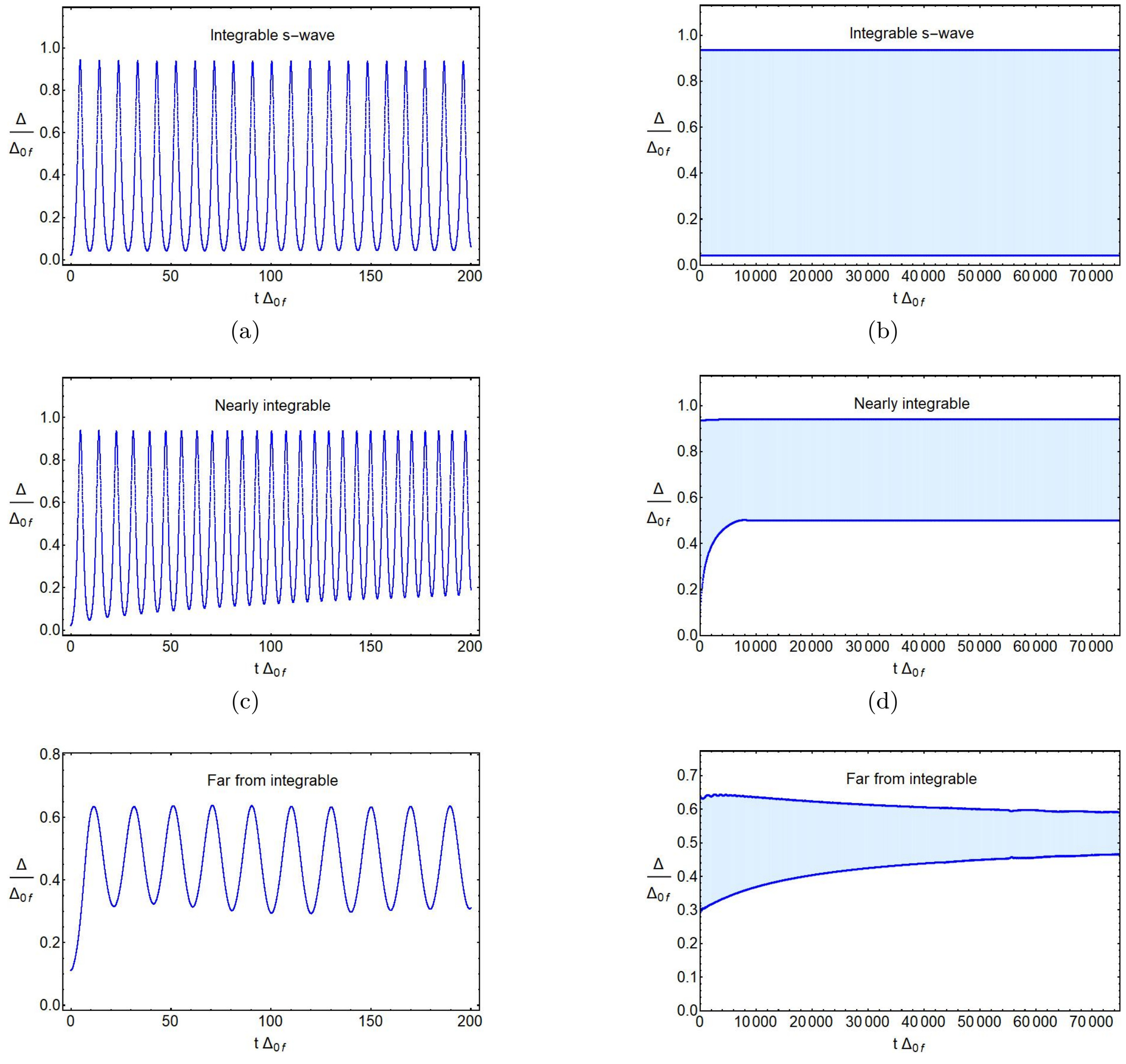

(a) (b) (c) (d) (e) (f)

Figure 2.1: Illustration of the large time scale τ that emerges in Phase III quenches $g_i \to g_f$ of nonintegrable pairing models. In all plots, the equilibrium gap corresponding to the initial coupling g_i is $\Delta_{0i} = 1.33 \times 10^{-3} W$, while that for the final coupling g_f is $\Delta_{0f} = 0.4W$, and we took $N = 2 \times 10^5$ equally spaced single-particle energy levels on the interval $[-W/2, W/2]$. The lines in the plots on the right are the local minima and maxima of the oscillations. In terms of the single-particle level spacing δ, the evolution in the right column goes out to $t_{\max} = 0.94\delta^{-1}$. In (a) and (b), we see that the persistent elliptic oscillations in the integrable s-wave case stabilize after a small number of oscillations. In (c) and (d), the amplitude of the oscillations takes roughly a thousand times longer to stop changing. In (e) and (f), integrability is strongly broken and it is not even clear whether the oscillations stabilize to a constant amplitude. The nonintegrable model used was the separable BCS model (2.9) with $f(\varepsilon)$ from Eq. (2.23). The nearly integrable version uses $\gamma = W$, while the far from integrable one has $\gamma = 1.33 \times 10^{-2} W$.

2 Models and pseudospin representation

In this paper, we consider quantum quenches in two types of nonintegrable pairing models

$$\begin{aligned}\hat{H}_f &= \sum_{j\lambda}\varepsilon_j \hat{c}^\dagger_{j\lambda}\hat{c}_{j\lambda} - \frac{1}{g}\hat{\Delta}^\dagger\hat{\Delta}, \quad \hat{\Delta}\equiv g\sum_j f_j \hat{c}_{j\downarrow}\hat{c}_{j\uparrow},\\ \hat{H}_{so} &= \sum_{\mathbf{k}ab}\Big[(\varepsilon_k\delta_{ab} - h\sigma^z_{ab}) + \alpha(k_y\sigma^x_{ab} - k_x\sigma^y_{ab})\Big]\hat{c}^\dagger_{\mathbf{k}a}\hat{c}_{\mathbf{k}b} -\\ &\quad -\frac{1}{g}\hat{\Delta}^\dagger\hat{\Delta}, \quad \hat{\Delta}\equiv g\sum_{\mathbf{k}}\hat{c}_{-\mathbf{k}\downarrow}\hat{c}_{\mathbf{k}\uparrow}.\end{aligned} \tag{2.1}$$

The Hamiltonian $\hat{H}_f$ is a separable BCS Hamiltonian where the ε_j are N single-particle energy levels, $\hat{c}^\dagger_{j\lambda}$ ($\hat{c}_{j\lambda}$) is a fermion creation (annihilation) operator for an electron with energy ε_j and spin index λ, $g > 0$ is the pairing interaction strength and $f_j \equiv f(\varepsilon_j)$ is a generic function of ε_j. The Hamiltonian $\hat{H}_{so}$ describes a 2D topological spin-orbit coupled superconductor with s-wave interactions [59, 60]. Here $\mathbf{k} = (k_x, k_y)$ is a two-dimensional momentum vector, σ^j are Pauli matrices, h is a Zeeman field and α is the Rashba spin-orbit coupling. We will take the density of states to be constant for both models, which is the case in 2D or at weak coupling, so that the single-particle energy levels are distributed uniformly on an interval of length W, called the bandwidth.

Apart from certain choices of $f(x)$, the separable BCS Hamiltonian $\hat{H}_f$ is a toy model for breaking integrability. The choice of $f^2(x) = C_1 + C_2 x$ produces a quantum integrable Hamiltonian [61, 62]; for example, $f(x) = 1$ and $f(x) = \sqrt{x}$ correspond to the s-wave [39] and $p + ip$ [63, 64] BCS models, respectively. A notable nonintegrable case is the $d + id$ model [65], where $f(x) = x$. The spin-orbit Hamiltonian $\hat{H}_{so}$, on the other hand, can be realized with cold Fermi gases [66, 67, 68, 69, 70, 71, 72, 73, 74, 75].

As both Hamiltonians in Eq. (2.1) have infinite range interactions, the mean-field approximation is expected to be exact in the thermodynamic ($N \to \infty$) limit. We therefore replace 2-body operators as follows $\hat{c}^\dagger\hat{c}^\dagger\hat{c}\hat{c} \approx \langle\hat{c}^\dagger\hat{c}^\dagger\rangle\hat{c}\hat{c} + \hat{c}^\dagger\hat{c}^\dagger\langle\hat{c}\hat{c}\rangle - \langle\hat{c}^\dagger\hat{c}^\dagger\rangle\langle\hat{c}\hat{c}\rangle$ in the equations of motion. We also diagonalize the noninteracting part of $\hat{H}_{so}$ through a unitary transformation $U_{\mathbf{k}}$ which is detailed in Appendix A. Up to additive constants, the effective mean-field Hamiltonians of Eq. (2.1) are

$$\begin{aligned}
\hat{H}_f &= \sum_{j\lambda=\uparrow\downarrow} \varepsilon_j \hat{c}^\dagger_{j\lambda}\hat{c}_{j\lambda} - \sum_j f_j \Big[\Delta^* \hat{c}_{j\downarrow}\hat{c}_{j\uparrow} + h.c.\Big],\\
\hat{H}_{so} &= \sum_{\mathbf{k}\lambda=\pm} \varepsilon_{k\lambda}\hat{a}^\dagger_{\mathbf{k}\lambda}\hat{a}_{\mathbf{k}\lambda} - \bigg(\frac{\Delta}{2}\sum_{\mathbf{k}\lambda} e^{-i\theta_{\mathbf{k}}}\Big[\lambda \sin\phi_k \hat{a}^\dagger_{\mathbf{k}\lambda}\hat{a}^\dagger_{-\mathbf{k}\lambda} + \\
&\quad + \cos\phi_k \hat{a}^\dagger_{-\mathbf{k}\lambda}\hat{a}^\dagger_{\mathbf{k}\bar{\lambda}}\Big] + h.c.\bigg)
\end{aligned} \tag{2.2}$$

The new parameters in $\hat{H}_{so}$ are

$$\begin{aligned}
&\cos\phi_k = \frac{h}{R_k}, \quad \sin\phi_k = \frac{\alpha k}{R_k},\\
&R_k = \sqrt{h^2 + \alpha^2 k^2},\\
&\varepsilon_{k\lambda} = \varepsilon_k - \lambda R_k, \quad \lambda = \pm, \quad \bar{\lambda} = -\lambda,\\
&\mathbf{k} = k_x + i\,k_y = k e^{i\,\theta_{\mathbf{k}}}.
\end{aligned} \tag{2.3}$$

Note that both $\alpha = 0$ and $h = 0$ correspond to integrable points of the spin-orbit model; in both cases, $\hat{H}_{so}$ becomes a Hamiltonian for two bands of independent s-wave BCS models. Most importantly, the mean-field order parameters $\Delta \equiv \Delta(t)$ are defined in terms of expectation values

$$\begin{aligned}
\Delta &= g\sum_j f_j \langle \hat{c}_{j\downarrow}\hat{c}_{j\uparrow}\rangle,\\
\Delta &= \frac{g}{2}\sum_{\mathbf{k}\lambda=\pm} e^{i\,\theta_{\mathbf{k}}}\Big[\lambda\sin\phi_k\langle \hat{a}_{-\mathbf{k}\lambda}\hat{a}_{\mathbf{k}\lambda}\rangle + \cos\phi_k \langle \hat{a}_{\mathbf{k}\lambda}\hat{a}_{-\mathbf{k}\bar{\lambda}}\rangle\Big],
\end{aligned} \tag{2.4}$$

for their respective models.

We will discuss the mean-field dynamics generated by Hamiltonians (2.2) in terms of Anderson pseudospins $\hat{\mathbf{s}}_j = (\hat{s}^x_j, \hat{s}^y_j, \hat{s}^z_j)$ which will allow for intuitive visualizations of the dynamics of different nonequilibrium phases. The transformation from fermions to pseudospins is given by

$$\hat{s}_j^- = \hat{s}_j^x - i\,\hat{s}_j^y = \hat{c}_{j\downarrow}\hat{c}_{j\uparrow}, \quad \hat{s}_j^z = \frac{1}{2}(\hat{c}_{j\uparrow}^\dagger\hat{c}_{j\uparrow} + \hat{c}_{j\downarrow}^\dagger\hat{c}_{j\downarrow} - 1). \tag{2.5}$$

In the spin-orbit case the pseudospin representation requires an additional set of auxiliary variables. For the sake of brevity, we relegate the derivations of the pseudospin equations of motion to Appendix A and simply state them here.

In the mean-field equations of motion that follow, $\mathbf{s} = \langle\hat{\mathbf{s}}\rangle$ are to be understood as classical variables satisfying the angular momentum Poisson brackets $\{s_j^a, s_k^b\} = -\delta_{jk}\epsilon_{abc}s_j^c$. In the separable BCS model, we have

$$\dot{\mathbf{s}}_j = \mathbf{b}_j \times \mathbf{s}_j, \quad \mathbf{b}_j = (-2f_j\Delta_x, -2f_j\Delta_y, 2\varepsilon_j), \tag{2.6}$$

where self-consistency requires

$$\Delta = g\sum_j f_j s_j^- = \Delta_x - i\Delta_y. \tag{2.7}$$

The spin-length $s_j = 1/2$ is conserved by Eqs. (2.6), which together with Eq. (2.7) are the equations of motion of the following classical spin Hamiltonian:

$$\begin{aligned} H_f &= \sum_j 2\varepsilon_j s_j^z - g\sum_{j,k} f_j f_k s_j^+ s_k^- \\ &= \sum_j 2\varepsilon_j s_j^z - |\Delta|^2/g. \end{aligned} \tag{2.8}$$

Note that without loss of generality, we can choose f_j to be real and nonnegative as we have done above. Indeed, let $f_j = |f_j|e^{-i\theta_j}$ be general complex numbers and

$$H_f = \sum_j 2\varepsilon_j s_j^z - g\sum_{j,k} f_j f_k^* s_j^+ s_k^-. \tag{2.9}$$

We redefine the spins by making local rotations around the z-axis, $s_j^- \to s_j^- e^{-i\theta_j}$. In terms of the new spins the Hamiltonian becomes

$$H_f = \sum_j 2\varepsilon_j s_j^z - g \sum_{j,k} |f_j||f_k| s_j^+ s_k^-, \tag{2.10}$$

and the order parameter is $\Delta = \sum_j |f_j| s_j^-$. This transformation does not affect spin (angular momentum) Poisson brackets and therefore the equations of motion retain their form. We thus arrive at the same problem only with $f_j \to |f_j|$.

We use capital letters $\mathbf{S}_{\mathbf{k}\lambda}$ to denote the classical pseudospins in the spin-orbit model and must introduce (see Appendix A) a set of auxiliary variables: the scalars $T_\mathbf{k}$ and vectors $\mathbf{L}_{\mathbf{k}\pm}$, where $\mathbf{L}_{\mathbf{k}+}$ and $\mathbf{L}_{\mathbf{k}-}$ differ only in sign of the z-component. The equations of motion are

$$\begin{aligned}
\dot{\mathbf{S}}_{\mathbf{k}\lambda} &= \mathbf{B}_{k\lambda} \times \mathbf{S}_{\mathbf{k}\lambda} + \mathbf{m}_k \times \mathbf{L}_{\mathbf{k}\lambda} - \mathbf{m}_k T_\mathbf{k}, \\
\dot{L}^x_{\mathbf{k}\lambda} &= -2\varepsilon_k L^y_{\mathbf{k}\lambda} + \frac{m_k^y}{2}\big[S^z_{\mathbf{k}+} + S^z_{\mathbf{k}-}\big] + B^x_{k\lambda} T_\mathbf{k}, \\
\dot{L}^y_{\mathbf{k}\lambda} &= 2\varepsilon_k L^x_{\mathbf{k}\lambda} - \frac{m_k^x}{2}\big[S^z_{\mathbf{k}+} + S^z_{\mathbf{k}-}\big] + B^y_{k\lambda} T_\mathbf{k}, \\
\dot{L}^z_{\mathbf{k}\lambda} &= -2R_k \lambda T_\mathbf{k} + \frac{m_k^x}{2}\big[S^y_{\mathbf{k}\lambda} - S^y_{\mathbf{k}\bar{\lambda}}\big] - \frac{m_k^y}{2}\big[S^x_{\mathbf{k}\lambda} - S^x_{\mathbf{k}\bar{\lambda}}\big], \\
\dot{T}_\mathbf{k} &= 2R_k L^z_{\mathbf{k}+} - B^x_{k+} L^x_{\mathbf{k}+} - B^y_{k+} L^y_{\mathbf{k}+} + \\
&\quad + \frac{1}{2}\mathbf{m}_k \cdot \big[\mathbf{S}_{\mathbf{k}+} + \mathbf{S}_{\mathbf{k}-}\big],
\end{aligned} \tag{2.11}$$

where the momentum dependent fields $\mathbf{B}_{k\lambda}$ and $\mathbf{m}_k$ are defined in terms of the order parameter Δ

$$\begin{aligned}
\Delta &= \frac{g}{2} \sum_{\mathbf{k}\lambda} \big[\sin\phi_k S^-_{\mathbf{k}\lambda} + \cos\phi_k L^-_{\mathbf{k}\lambda}\big] \\
&= \Delta_x - i\Delta_y, \\
\mathbf{B}_{k\lambda} &= (-2\sin\phi_k \Delta_x, -2\sin\phi_k \Delta_y, 2\varepsilon_{k\lambda}), \\
\mathbf{m}_k &= (-2\cos\phi_k \Delta_x, -2\cos\phi_k \Delta_y, 0).
\end{aligned} \tag{2.12}$$

The first of these equations is the self-consistency relationship for the spin-orbit model. The equation for $\dot{\mathbf{S}}_{\mathbf{k}\lambda}$ in Eq. (2.11) corrects an error in a previous paper [56], which is missing the last term. For each $\mathbf{k}$, there is a conserved quantity analogous to pseudospin length

$$N_{\mathbf{k}}^2 = 2T_{\mathbf{k}}^2 + \sum_{\lambda} \left[\mathbf{S}_{\mathbf{k}\lambda}^2 + \mathbf{L}_{\mathbf{k}\lambda}^2 \right] = \frac{1}{4}. \tag{2.13}$$

Similar to Eq. (2.8), the classical spin-orbit Hamiltonian in pseudospin notation has a simple and compact expression

$$H_{so} = \sum_{\mathbf{k}\lambda} 2\varepsilon_{k\lambda} S_{\mathbf{k}\lambda}^z - 2|\Delta|^2/g. \tag{2.14}$$

Because of the simple relationship connecting $\mathbf{L}_{\mathbf{k}+}$ to $\mathbf{L}_{\mathbf{k}-}$, each momentum vector $\mathbf{k}$ corresponds to ten dynamical variables $(\mathbf{S}_{\mathbf{k}+}, \mathbf{S}_{\mathbf{k}-}, \mathbf{L}_{\mathbf{k}+}, T_{\mathbf{k}})$ constrained by Eq. (2.13). Note that $T_{\mathbf{k}}$ and $L_{\mathbf{k}\lambda}^z$ do not appear in (2.14), but as discussed in Appendix A, they are necessary for the closure of the equations of motion. From now on we simplify notation to $\mathbf{L}_{\mathbf{k}} \equiv \mathbf{L}_{\mathbf{k}+}$ and define the 10-dimensional vector $\mathbf{\Gamma}_{\mathbf{k}} \equiv (\mathbf{S}_{\mathbf{k}+}, \mathbf{S}_{\mathbf{k}-}, \mathbf{L}_{\mathbf{k}}, T_{\mathbf{k}})$.

Finally, the conservation of the total number of fermions N_f in each model corresponds to the conservation of total z-component in the pseudospin language

$$N_f = \sum_j (2s_j^z + 1), \tag{2.15}$$

for the separable BCS model and

$$N_f = \sum_{\mathbf{k}\lambda} \left(S_{\mathbf{k}\lambda}^z + \frac{1}{2} \right), \tag{2.16}$$

for the spin-orbit model.

3 Main results

The main purpose of this work is to compare the nonequilibrium phases of quenches from the ground state of nonintegrable pairing Hamiltonians, such as those in Eq. (2.1), to those of the integrable s-wave [53] and p-wave [54] models. Some qualitative aspects of the primary phases are independent of integrability insofar as the squared modulus of the order parameter Δ may exhibit any of three distinct asymptotic behaviors in the continuum limit: it can relax to zero (Phase I), relax to a nonzero constant value (Phase II), or display persistent periodic elliptic oscillations (Phase III).

We first show the existence of these three phases in Sects. 5.1-5.3 through direct numerical simulation of the dynamics. In Sect. 5.2 we present a stability analysis of the phases of the separable BCS models which leads to conditions for nonequilibrium phase transitions. The stability analysis applied to integrable cases reduces to the known results that relied on exact solvability [54, 53]. Our analysis provides a physical explanation for the transitions in terms of the frequencies of linearized perturbations $\delta\Delta(t)$ of the asymptotic Δ. The transition from Phase I to Phase II occurs through an exponential instability characterized by a pair of conjugate imaginary frequencies in the linearization spectrum, while that of Phase II to III occurs either when small harmonic oscillations fail to dephase or when an exponential instability occurs.

The appearance of some or all of Phases I-III in nonintegrable models suggests an underlying universality to quench dynamics, but we show that the story is less straightforward. One the one hand, these phases are understood in the integrable cases [53, 54]. There is a dynamical reduction of the number of effective degrees of freedom, so that at large times the dynamics are governed by a Hamiltonian of the same form, but which has just a few collective degrees of freedom. The three phases correspond to 0, 1 or 2 effective spins for each phase, respectively. On the other hand, the nonintegrable dynamics admit no known analogous reduction because the 2-spin solutions to the equations of motion do not reproduce the observed asymptotic behavior of Δ in Phase III. If such a reducing "flow" in time of the Hamiltonian occurs in the nonintegrable case, then the form of the Hamiltonian itself must change. For specifics on this latter point, see Appendix C.

Importantly, nonintegrable pairing models also display dynamics markedly different from those in the main three phases. We illustrate this behavior with two examples in Sect. 7 – one for the spin-orbit Hamiltonian and one for a particle-hole symmetric separable BCS Hamiltonian – where the magnitude of the order parameter oscillates quasiperiodically. We interpret this observation as an indication of a new quasiperiodic phase (Phase IV) unique to quantum quench phase diagrams of these models.

More subtle details of the dynamics in the main three phases change drastically once integrability is broken. We show in Sect. 5.3 that nonintegrable models take an extremely long time to relax to Phase III. This time scale is absent in the integrable case, yet it diverges when one approaches the integrable limit. One must take this time scale into account when studying Phase III on the basis of numerical simulation alone. For example, in the weak coupling regime, the nonintegrable $d + id$ model may appear to quickly enter Phase III [76] while in fact the minima of $|\Delta|$ oscillations have not converged to a fixed value. The further into the weak coupling regime one explores, the longer the relaxation time. Quenches outside of weak coupling have faster dynamics, but exhibit behavior that markedly contrasts with Phase III, and above a certain energy threshold the asymptotic state collapses rapidly to Phase II. This long relaxation time is typical in the nonintegrable case.

Despite these consequences of breaking integrability, our mixed strategy of simulation and stability analysis applies to the two rather different classes of nonintegrable pairing models found in Eq. (2.1). The separable BCS permits a standard Anderson pseudospin representation and is a single band model, while the spin-orbit model requires an expanded pseudospin representation, has multiple bands and a topological quantum phase transition.

Yet both models have a single complex order parameter, which we believe is the essential characteristic that leads to the three phases.

The self-consistency relationship (2.7) for the order parameter is central to both our stability analysis of Phases I and II in Sect. 5.2 and our investigations of Phase III in Sect. 6. In the former case, the frequencies of harmonic perturbations of a given nonequilibrium phase are constrained by the self-consistency requirement. As for Phase III, we show in Sect. 6 that there is always a periodic solution to the spin equations of motion when $\Delta(t)$ is periodic, and that the general spin solution precesses around the periodic one. We then argue through numerical examples that further imposing the self-consistency requirement on $\Delta(t)$ selects elliptic functions amongst all possible periodic $\Delta(t)$.

4 Ground state and quench protocol

In a quantum quench, we prepare the system in the ground state with an initial order parameter $\Delta = \Delta_0 e^{-2i\mu t}$, which corresponds to system parameters such as the interaction strength g, the equilibrium chemical potential μ, the magnetic field h and the spin-orbit strength α. The amplitude Δ_0 is constant in the ground state. At time $t = 0$, we suddenly change one of these parameters, which throws the system out of equilibrium. In the separable BCS model we will consider quenches $g_i \to g_f$, but we will label the initial and final states by the coordinates $\Delta_{0i} \equiv \Delta_0(g_i)$ and $\Delta_{0f} \equiv \Delta_0(g_f)$. In the spin-orbit model, we will consider quenches of the magnetic field $h_i \to h_f$. The fermion number N_f is fixed across the quench in both cases, which implies that the equilibrium chemical potential μ changes with h.

For a given Δ_0 and μ, we express the ground state configuration of the separable BCS model in a frame that rotates around the z-axis with frequency 2μ. We then orient each $\mathbf{s}_j$

against the magnetic field $\mathbf{b}_j$, the z-component of which is shifted by 2μ,

$$\begin{aligned} s_{j0}^- = \frac{f_j \Delta_0}{2E_j}, \quad s_{j0}^z = -\frac{\varepsilon_j - \mu}{2E_j}, \\ E_j(\Delta) \equiv \sqrt{(\varepsilon_j - \mu)^2 + f^2(\varepsilon_j)|\Delta|^2}. \end{aligned} \tag{2.17}$$

The relationship between Δ_0, g, N_f and μ obtains from the application of the definition of Δ in (2.7) to (2.15) and the configuration in (2.17),

$$\frac{1}{g} = \sum_j \frac{f_j^2}{2E_j}, \quad N_f = \sum_j \left(1 - \frac{\varepsilon_j - \mu}{E_j}\right) \tag{2.18}$$

We will assert without loss of generality that Δ_{0i} is real in both models, which can always be achieved by a time-independent rotation in the xy-plane in pseudospin space.

Unless otherwise stated, we will simplify the analysis of the separable BCS model by restricting ourselves to cases where the order parameter Δ remains real for all time, i.e., $\Delta_y(t) = 0$. To achieve this, we will consider the particle-hole symmetric case where the energies ε_j are symmetrically distributed around the chemical potential μ, which is set to zero without loss of generality. We will also only consider even functions $f(x) = f(-x)$. Under these conditions, any initial spin configuration that satisfies the symmetry conditions $s^z(\varepsilon_j) = -s^z(-\varepsilon_j)$, $s^+(\varepsilon_j) = s^-(-\varepsilon_j)$, as does the ground state (2.17), will do so for all time. This fact can be verified with the equations of motion (2.6) by considering time derivatives of quantities such as $s^z(\varepsilon_j) + s^z(-\varepsilon_j)$, which vanish under the aforementioned assumptions. We will not use particle-hole symmetry in the $d + id$ model, where $f(x) = x$ and ε_j will be distributed on a positive interval. Further, Eqs. (2.6) and (2.7) are invariant under the time-reversal transformation

$$\begin{aligned} s_j^z(t) \to s_j^z(-t), \quad s_j^\pm(t) \to s_j^\mp(-t), \\ \Delta(t) \to \Delta^*(-t). \end{aligned} \tag{2.19}$$

Since the initial conditions (2.17) at $t = 0$ also have this property, it holds at all times.

The ground state of the spin-orbit model is less obvious [56]

$$\begin{aligned} S^x_{\mathbf{k}\lambda 0} &= \frac{\Delta_0 \sin\phi_k}{D_k}\left[\Delta_0^2 + \xi^2_{k\bar{\lambda}} + E_{k+}E_{k-}\right], \\ S^z_{\mathbf{k}\lambda 0} &= -\frac{1}{D_k}\Bigg[\xi_{k\lambda}(E_{k+}E_{k-} + \xi^2_{k\bar{\lambda}} + \Delta_0^2 \sin^2\phi_k) + \\ &\quad + \Delta_0^2 \cos^2\phi_k \xi_{k\bar{\lambda}}\Bigg], \\ L^x_{\mathbf{k}0} &= \frac{\Delta_0 \cos\phi_k}{D_k}\left[\Delta_0^2 + \xi_{k+}\xi_{k-} + E_{k+}E_{k-}\right], \\ L^z_{\mathbf{k}0} &= \frac{1}{D_k}\left[2R_k\Delta_0^2 \cos\phi_k \sin\phi_k\right], \\ \xi_{k(\lambda)} &\equiv \varepsilon_{k(\lambda)} - \mu, \\ E_{k\lambda}(\Delta) &\equiv \left[\xi_k^2 + \Delta^2 + R_k^2 - 2R_k\lambda\sqrt{\xi_k^2 + \cos^2\phi_k\Delta^2}\right]^{1/2}, \\ D_k &\equiv 2E_{k+}E_{k-}(E_{k+} + E_{k-}), \end{aligned} \tag{2.20}$$

while $S^y_{\mathbf{k}\lambda 0} = L^y_{\mathbf{k}0} = T_{\mathbf{k}0} = 0$. The corresponding self-consistent equation relating Δ_0 to g is

$$\frac{2}{g} = \sum_{\mathbf{k}\lambda} \frac{E_{k+}E_{k-} + \Delta_0^2 + \sin^2\phi_k\xi^2_{\mathbf{k}\lambda} + \cos^2\phi_k\xi_{\mathbf{k}\lambda}\xi_{\mathbf{k}\bar{\lambda}}}{2E_{k+}E_{k-}(E_{k+} + E_{k-})}. \tag{2.21}$$

The quantities $2E_j(\Delta)$ and $2E_{\mathbf{k}\lambda}(\Delta)$ in (2.17) and (2.20) are the excitation energies obtained by diagonalization of the quadratic mean-field Hamiltonians in Eqs. (2.2) at a given Δ.

For given values of g, N_f, α and h, one can simultaneously solve Eq. (2.16) and Eq. (2.21) using the ground state configurations to obtain the corresponding equilibrium chemical potential μ and ground state gap Δ_0. As the ground state is rotationally symmetric in $\mathbf{k}$, and the equations of motion preserve this symmetry, in our numerics we always replace sums over momenta with sums over energies with a flat density of states $\sum_{\mathbf{k}} \to \sum_{\varepsilon}$. The level spacing δ is related to the number of spins N and the bandwidth W through

$$\delta = \frac{W}{N-1}. \tag{2.22}$$

Formally, in 2D this means $N - 1 = \frac{W}{2\pi} A$, where A is the physical area of the system. Fig. 2.2 shows an example of the relationship between different parameters for the spin-orbit model.

5 Simulations of nonequilibrium phases and stability analysis

Now we numerically simulate the equations of motion (2.6) and (2.11) and plot the behavior of $\Delta(t)$ for each of the three phases in Sects. 5.1 and 5.3. In Sect. 5.3, we also characterize the long time scale of nonintegrable models in Phase III. In Sect. 5.2, we introduce a stability analysis for Phases I and II that gives the conditions under which a nonequilibrium phase transition occurs.

We will consider several integrability-breaking functions for $f(\varepsilon)$, which appears in the separable BCS equations of motion Eq. (2.6). All $f(\varepsilon)$ considered here will be even functions, and as we discuss in Sect. 5.2, the particular form of $f(\varepsilon)$ affects which phases occur. With this in mind, we consider the "Lorentzian" coupling [45]

$$f_{\mathrm{lor}}(\varepsilon, \gamma) = \frac{\gamma}{\sqrt{\gamma^2 + \varepsilon^2}}, \tag{2.23}$$

the "sine" coupling,

$$f_{\sin}(\varepsilon, \gamma) = 1 + \sin^2(\varepsilon/\gamma), \tag{2.24}$$

and the "cube root" coupling,

$$f_{\mathrm{cub}}(\varepsilon, \gamma) = \frac{(\gamma^3 + |\varepsilon|^3)^{1/3}}{\gamma}. \tag{2.25}$$

The parameter γ is fixed for any particular Hamiltonian, and it characterizes how strongly integrability is broken. For $\gamma \gtrsim W$, we have $f(\varepsilon, \gamma) \sim 1$ in all three cases, which we consider to be "nearly integrable". For $\gamma \ll W$, integrability is strongly broken.

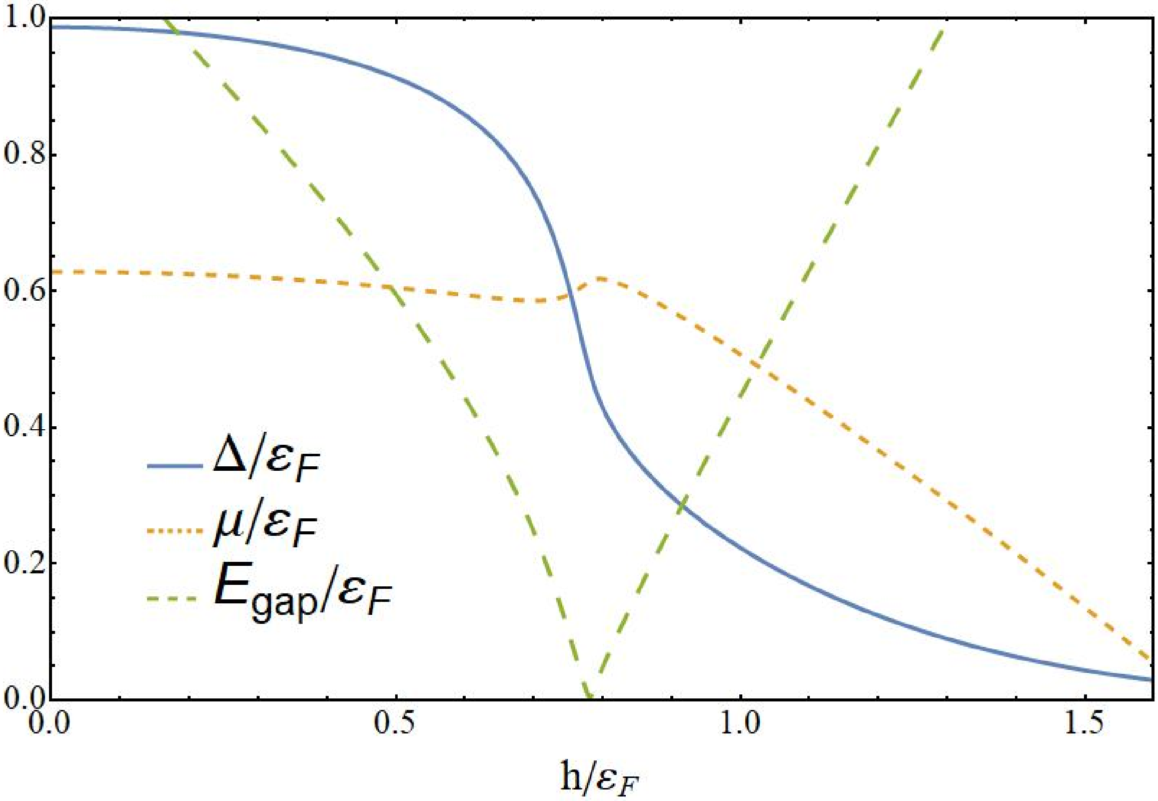

Figure 2.2: Ground state order parameter Δ_0, chemical potential μ and $E_{\text{gap}} = E_{k=0,+} = (\sqrt{\Delta_0^2 + \mu^2} - h)^2$ as functions of the external field h in the spin-orbit model. One simultaneously solves the fermion number equation (2.16) and the self-consistency relationship Eq. (2.21) with the ground state configuration (2.20). The vanishing of E_{gap} corresponds to a topological quantum phase transition. The number of fermions is $N_f = 0.65N$, where N is the number of spins. We express energies in units of the bandwidth W, including the spin-orbit coupling $\alpha^2 = 0.1W$, the level spacing $\delta = W/(N-1)$, and the BCS coupling $g = 0.9\delta$. The Fermi energy in these units is $\varepsilon_F = \frac{W}{2N}N_f = 0.325W$. These spin-orbit model parameters remain the same for the remainder of this work, up to adjusting the value of N. We do not consider a similar plot for the separable BCS model because in the particle-hole symmetric case considered, the fermion number $N_f = N$ and thus $\mu = 0$.

We control for finite size effects in our simulations by increasing N until $\Delta(t)$ in the time window of interest no longer changes when N is doubled. In practice, we find that finite size effects become significant at times $t > t_{\mathrm{fs}}$, where

$$t_{\mathrm{fs}} \approx \frac{1}{\delta} = \frac{N-1}{W}, \tag{2.26}$$

is the inverse single-particle level spacing, see also Ref. [53]. To observe the asymptotic dynamics, N has to be sufficiently large, so that the relaxation time $\tau < t_{\mathrm{fs}}$.

5.1 Phases I and II

Figs. 2.3-2.5 contain examples of Phase I and Phase II quenches in both the separable BCS and spin-orbit models. To heuristically understand the emergence of these two phases, one can insert the prescribed behavior of Δ into the equations of motion (2.6) and (2.11). This examination of the asymptotic solutions to the equations of motion in each phase will be important for the stability analyses of Sect. 5.2.

The following applies to the separable BCS models in the particle-hole symmetric limit, but the analysis is analogous when this symmetry is broken and in the spin-orbit case. In Phase I, we set Δ to zero

$$\begin{aligned} \dot{s}_j^z &= 0, \\ \dot{s}_j^x &= -2\varepsilon_j s_j^y, \\ \dot{s}_j^y &= 2\varepsilon_j s_j^x. \end{aligned} \tag{2.27}$$

The most general solution that conserves both $s_j^2 = 1/4$ and the time-reversal symmetry

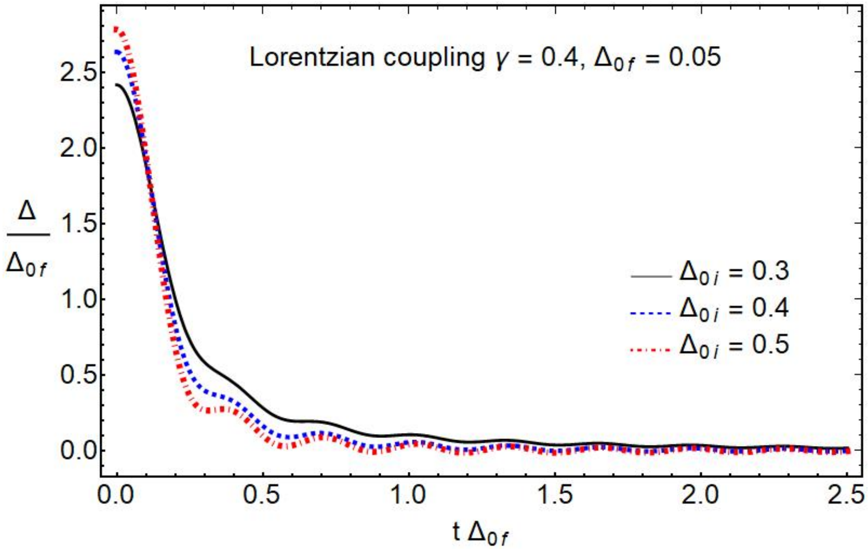

(a)

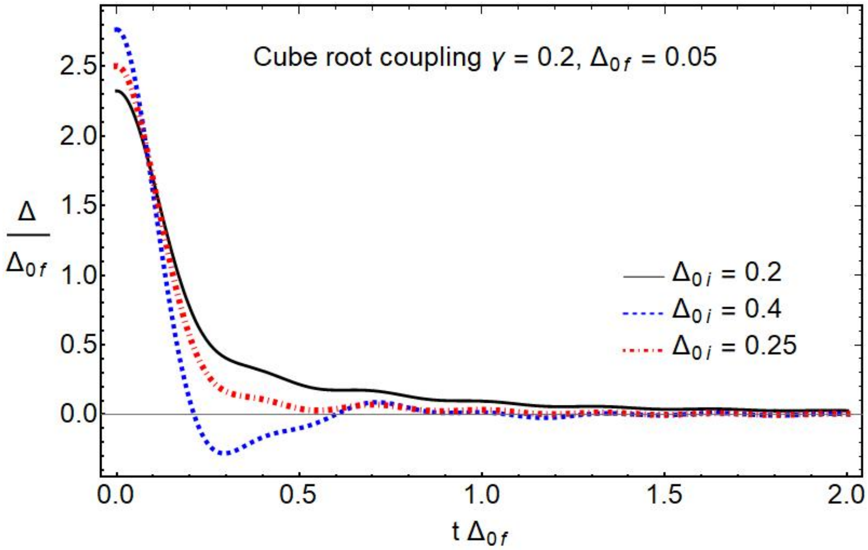

(b)

Figure 2.3: Examples of Phase I quenches for separable BCS models. The equilibrium gaps Δ_{0i}, Δ_{0f} and integrability breaking parameter γ are given in units of the bandwidth W, and there are $N = 5 \times 10^4$ (a) and $N = 2 \times 10^5$ (b) spins. The initial rapid decay of Δ is shown, but out of caution one must simulate to longer times (still smaller than the inverse level spacing) in order to verify that the phase is indeed stable.

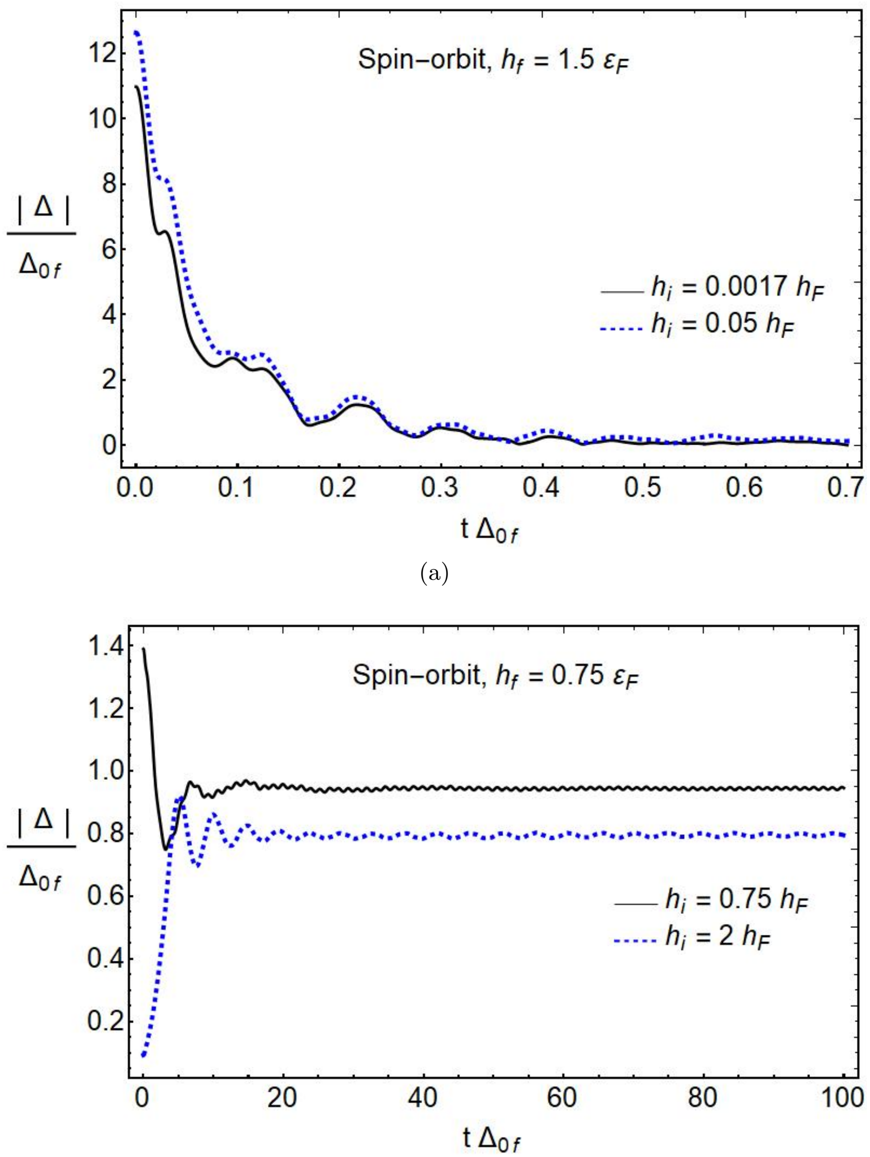

(a)

(b)

Figure 2.4: Quenches in the spin-orbit model that lead to (a) Phase I and (b) Phase II. Here the number of single-particle energies is $N = 10^4$, and all other parameters are the same as given in the caption of Fig. 2.2.

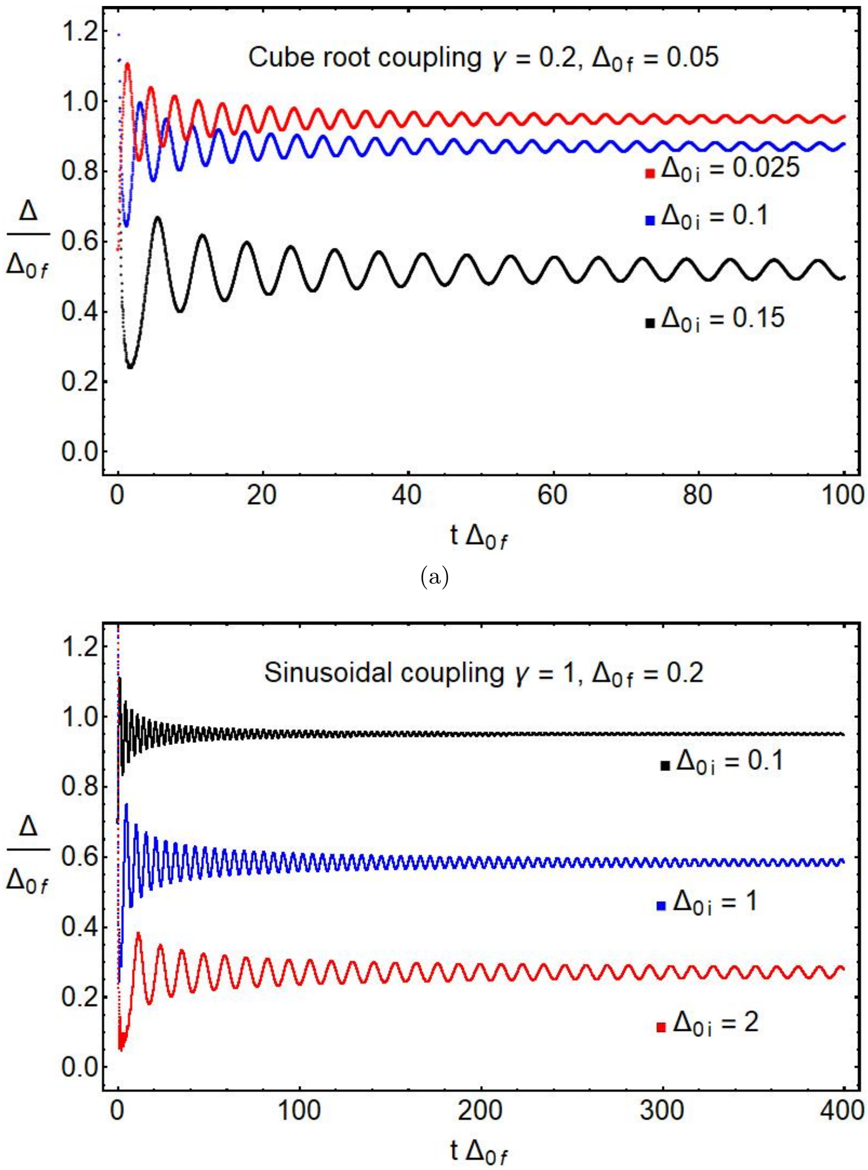

(a)

(b)

Figure 2.5: Examples of Phase II quenches for separable BCS models. In (a) $N = 2 \times 10^5$ spins, and the quench from $\Delta_{0i} = 0.15W$ is close to the Phase I-II boundary. In (b), $N = 5 \times 10^4$. The oscillatory power law decay to a constant value takes a rather long time, and we have verified out to $t\delta = 2$ in (a) and $t\delta = 0.5$ in (b) that the amplitude of the oscillations is indeed decreasing to zero with power-law decay. In both plots, Δ_0 and γ are expressed in units of the bandwidth.

(2.19) is

$$\begin{aligned} s_j^z &= z_j, \\ s_j^x &= x_j \cos(2\varepsilon_j t), \\ s_j^y &= x_j \sin(2\varepsilon_j t), \\ z_j^2 &= 1/4 - x_j^2. \end{aligned} \tag{2.28}$$

where z_j is the Phase I steady state spin-profile. In order for (2.28) to make sense as a solution to the actual equations of motion, Eq. (2.7) must hold, i.e., we must have that $\Delta = g_f \sum_j f_j s_j^-$ equals zero, which is called the self-consistency condition. Strictly speaking, the solution (2.28) violates the self-consistency condition

$$\Delta = g_f \sum_j f_j x_j \cos(2\varepsilon_j t) \neq 0, \tag{2.29}$$

but as the number of single-particle energies N goes to infinity, i.e., in the continuum limit when the sum in Eq. (2.29) turns into an integral, Δ from Eq. (2.29) vanishes through dephasing for $1 \ll t \ll 1/\delta = (N-1)/W$. This description is invalid for $t \sim N/W$. In this sense, we refer to the solution (2.28) as asymptotically self-consistent, which is a concept we will often use in the remainder of this paper.

Let us now replace Δ with $\Delta_\infty \neq 0$ in Eq. (2.6) to examine the asymptotic solutions corresponding to Phase II

$$\begin{aligned} \dot{s}_j^z &= -2 f_j s_j^y \Delta_\infty, \\ \dot{s}_j^x &= -2\varepsilon_j s_j^y, \\ \dot{s}_j^y &= 2\varepsilon_j s_j^x + 2 f_j s_j^z \Delta_\infty. \end{aligned} \tag{2.30}$$

The solution which preserves spin length and the time-reversal symmetry is then

$$\begin{aligned} s_j^z &= Z_j + \zeta_j \cos(b_j t), \\ s_j^x &= -\frac{f_j \Delta_\infty}{\varepsilon_j} Z_j + \frac{\varepsilon_j}{f_j \Delta_\infty} \zeta_j \cos(b_j t), \\ s_j^y &= \frac{b_j}{2 f_j \Delta_\infty} \zeta_j \sin(b_j t), \end{aligned} \tag{2.31}$$

where Z_j is the Phase II steady state spin profile, which, along with Δ_∞, determines the other constants

$$\begin{aligned} b_j &= 2\sqrt{\varepsilon_j^2 + f_j^2 \Delta_\infty^2}, \\ \zeta_j^2 &= \frac{f_j^2 \Delta_\infty^2}{b_j^2} - \frac{f_j^2 \Delta_\infty^2}{\varepsilon_j^2} Z_j^2. \end{aligned} \tag{2.32}$$

The solution (2.31) must be asymptotically self-consistent, i.e., for $N \to \infty$, $\lim_{t\to\infty} \Delta = \Delta_\infty$, which implies

$$1 = -g_f \sum_j \frac{f_j^2 Z_j}{\varepsilon_j}, \tag{2.33}$$

which is the nonequilibrium analogue of the ground state self-consistency requirement (2.18).

5.2 Stability analysis

Now we consider the stability of Phases I and II for the separable BCS model by linearizing the equations of motion (2.27) and (2.30) about the asymptotic states given in (2.28) and (2.31), respectively. The main result is Eq. (2.42), which is the equation for frequencies of linearized perturbations to the asymptotic $\Delta(t)$ of either Phase I or Phase II. For Phase I, the appearance of a complex conjugate pair of imaginary frequencies signals an exponential instability. For Phase II, a solution ω_0 to Eq. (2.42) may enter the band gap, or a complex conjugate pair of frequencies may appear. The former case, which occurs in the integrable

s-wave and $p + ip$ models, signifies a transition to Phase III because the linearized gap $\delta\Delta(t)$ oscillates persistently, i.e., it does not dephase. In Appendix D, we show that the nonequilibrium phase transitions predicted by this stability analysis both match and give a physical interpretation to the results obtained in integrable models [53, 54] using tools inextricably linked to exact solvability.

Although the final result (2.42) applies generally, we limit the discussion to the particle-hole symmetric case to simplify the presentation. Let $\mathbf{s}_j = \mathbf{s}_{j0} + \delta\mathbf{s}_j$, where $\mathbf{s}_{j0}$ is the Phase I asymptotic solution from Eq. (2.28). Neglecting second and higher order terms, the linearized equations for the spin components are

$$\begin{aligned} \delta\dot{s}_j^z &= -2f_j s_{j0}^y \delta\Delta \\ \delta\dot{s}_j^x &= -2\varepsilon_j \delta s_j^y, \\ \delta\dot{s}_j^y &= 2\varepsilon_j \delta s_j^x + 2f_j z_j \delta\Delta, \\ \delta\Delta &\equiv g_f \sum_j f_j \delta s_j^x. \end{aligned} \tag{2.34}$$

Expanding $\mathbf{s}_j(t)$ in Fourier components

$$\begin{aligned} \delta\mathbf{s}_j(t) &= \sum_\omega \delta\widetilde{\mathbf{s}}_j(\omega) e^{-i\omega t}, \\ \delta\Delta &= \sum_\omega \delta\widetilde{\Delta}(\omega) e^{-i\omega t}, \end{aligned} \tag{2.35}$$

and using the Fourier space version of the self-consistency relation in Eq. (2.34), we find the following equation for the allowable frequencies ω

$$1 = 4g_f \sum_j \frac{f_j^2 \varepsilon_j z_j}{\omega^2 - 4\varepsilon_j^2}. \tag{2.36}$$

The following discussion uses particle-hole symmetry along with the empirical fact that for quenches from the ground state, $z_j\varepsilon_j < 0$ in Phase I. Upon inspecting Eq. (2.36), one determines that there are $N/2$ unique ω_j^2, of which all but one lie between consecutive $4\varepsilon_j^2$.

The remaining ω_0^2 is less than the smallest $4\varepsilon_j^2$, and can therefore be negative. A negative ω_0^2 corresponds to a pair of conjugate imaginary frequencies, and therefore an exponential instability in $\delta\mathbf{s}_j$. We thus determine the Phase I boundary in $(\Delta_{0i}, \Delta_{0f})$ space to be those values for which ω_0^2 passes through zero.

The stability analysis for Phase II follows a similar logic. Consider the linearized equations of motion

$$\begin{aligned}
\delta\dot{s}_j^z &= -2f_j s_{j0}^y \delta\Delta - 2f_j \Delta_\infty \delta s_j^y, \\
\delta\dot{s}_j^x &= -2\varepsilon_j \delta s_j^y, \\
\delta\dot{s}_j^y &= 2\varepsilon_j \delta s_j^x + 2f_j s_{j0}^z \delta\Delta + 2f_j \Delta_\infty \delta s_j^z,
\end{aligned} \tag{2.37}$$

where now $\mathbf{s}_{j0}$ is the Phase II asymptotic solution from Eq. (2.31). Again changing to the Fourier basis, we solve for $\delta\widetilde{s}_j^x(\omega)$ and apply the self-consistency condition for $\delta\widetilde{\Delta}(\omega)$, which reads

$$\begin{aligned}
&\delta\widetilde{\Delta}(\omega)\left(1 - 4g_f \sum_j \frac{\varepsilon_j f_j^2 Z_j}{\omega^2 - b_j^2}\right) = \\
&= \frac{2g_f}{\omega} \sum_j \varepsilon_j f_j^2 \zeta_j \left(\frac{\delta\widetilde{\Delta}(\omega + b_j)}{\omega + b_j} + \frac{\delta\widetilde{\Delta}(\omega - b_j)}{\omega - b_j}\right).
\end{aligned} \tag{2.38}$$

Although in principle Eq. (2.38) can be solved numerically with Z_j and Δ_∞ as input, such an approach is needlessly complex and obscures the mechanism by which Phase II gives way to Phase III. The difficulty presented by Eq. (2.38) stems from the fact that we required exact self-consistency. It turns out that relaxing this requirement to asymptotic self-consistency, defined in Sect. 5.1, suffices to understand the Phase II-III transition.

We return to Eq. (2.37) and solve it in the time domain under the assumption $\delta\Delta(t) = \delta_+ e^{-i\omega_0 t} + \delta_- e^{i\omega_0 t}$. We neglect higher order harmonics because the Phase III oscillations near the II-III boundary are small. Under this ansatz, $\delta s_j^x(t)$ has six frequencies: $\pm\omega_0$ and $\pm\omega_0 \pm b_j$. If ω_0 is a real frequency isolated from the continuum of b_j defined in Eq. (2.32), then the constant Δ_∞ of Phase II is "unstable" in the sense that oscillatory perturbations do not dephase. The self-consistent equation for this harmonic $\delta\Delta(t)$ is

$$\begin{aligned} 1 = 4g_f \sum_j \frac{f_j^2 \varepsilon_j Z_j}{\omega_0^2 - b_j^2} + \\ + \frac{2g_f}{\omega_0} \sum_j \left(\frac{e^{ib_j t} f_j^2 \varepsilon_j \zeta_j}{\omega_0 - b_j} + [b_j \to -b_j] \right). \end{aligned} \tag{2.39}$$

This relation cannot hold for arbitrary t, but it will in the continuum limit if we require $\omega_0^2 < b_{\min}^2$ and $t \to \infty$, which allows the harmonic ansatz to be asymptotically self-consistent due to dephasing. Thus the equation for ω_0, the frequency of a harmonic perturbation to Δ_∞ in Phase II, is

$$1 = 4g_f \sum_j \frac{f_j^2 \varepsilon_j Z_j}{\omega_0^2 - b_j^2}. \tag{2.40}$$

Eq. (2.40) generalizes the small quench linearization method developed in Ref. [45], which we recover by replacing Z_j of Eq. (2.40) with the z-component spin profile of the g_i ground state. For the Lorentzian coupling, ω_0 lies in the band gap for infinitesimal quenches, so that linearized Phase III oscillations do not decay [45].

In order to understand whether the finite quench dynamics admit such an isolated ω_0, consider the implications of (2.40) combined with (2.33) for the Δ_∞ of Phase II. We find

$$\begin{aligned} \frac{\omega_0^2}{4\Delta_\infty^2} &= \frac{I_1(\omega_0^2)}{I_2(\omega_0^2)}, \\ I_1(\omega_0^2) &\equiv g_f \sum_j \frac{f_j^4 Z_j}{\varepsilon_j(\omega_0^2 - b_j^2)}, \\ I_2(\omega_0^2) &\equiv g_f \sum_j \frac{f_j^2 Z_j}{\varepsilon_j(\omega_0^2 - b_j^2)}. \end{aligned} \tag{2.41}$$

It helps to analyze (2.41) under the simplifying assumption that $Z_j/\varepsilon_j < 0$, which holds exactly for the integrable s-wave model, and is therefore applicable in the weak-coupling regime ($\Delta_{0i}, \Delta_{0f} \ll W$) of the general separable case [53]. With this restriction, Eq. (2.40) implies ω_0^2 is real, while Eq. (2.41) requires $\omega_0^2 > 0$, i.e., the allowed frequencies ω_0 are purely real. We now examine the effect of the function f_j in determining whether solutions ω_0^2 to Eq. (2.41) are isolated from the b_j^2 continuum.

If $f_j < f(0)$ for all j and $b^2_{\text{min}} = 4\Delta_\infty^2$, then Eq. (2.41) has a solution $0 < \omega_0^2 < b^2_{\text{min}}$, and oscillations of $\delta\Delta(t)$ do not dephase. In this scenario, Phase III is the asymptotic state due the presence of persistent periodic oscillations about the Phase II solution. If $f_j < f(0)$ for all j and $b^2_{\text{min}} < 4\Delta_\infty^2$, then the relationship between ω_0^2 and b^2_{min} is not immediately obvious from Eq. (2.41). The Lorentzian coupling, where $f_j = \gamma(\gamma^2 + \varepsilon_j^2)^{-1/2}$, allows for both possibilities: If $\Delta_\infty \leqslant \gamma$, then $b^2_{\text{min}} = 4\Delta_\infty^2$ and Phase II is not the asymptotic state. If $\Delta_\infty > \gamma$, then $b^2_{\text{min}} = 4\gamma(2\Delta_\infty - \gamma)$, and we cannot characterize solutions to Eq. (2.41) without detailed knowledge of Z_j and Δ_∞.

If $f_j \geqslant f(0)$ for all j, then $b^2_{\text{min}} = 4\Delta_\infty^2$ and we find that solutions ω_0^2 to Eq. (2.41) are not isolated from the b_j^2 continuum. In this case, the harmonic ansatz for $\delta\Delta(t)$ is not asymptotically self-consistent, and there are no persistent small oscillations about Phase II. The integrable s-wave model is defined by $f_j = f(0) = 1$, in which case $\omega_0^2 = 4\Delta_\infty^2$ is the only solution to Eq. (2.41), which is not isolated. On the other hand, Phase III exists in the s-wave case [53]. Therefore, $f_j \geqslant f(0)$ does not imply that such models will always reach Phase II. Indeed, the relaxation to Phase II is always accompanied by nonperturbative oscillations which persist in the case of Phase III.

Thus, even under the simplifying assumptions of particle-hole symmetry and $Z_j/\varepsilon_j < 0$, the stability analysis of Phase II reveals a variety of possible behaviors in the separable BCS models. The nature of $f(\varepsilon)$ near $\varepsilon = 0$ (the Fermi surface) is especially crucial to determining whether oscillations fully dephase to Phase II – a statement which extends to the non-particle-hole symmetric case in the weak coupling regime.

Upon relaxing the restriction $Z_j/\varepsilon_j < 0$, isolated solutions to Eq. (2.41) can have nonzero imaginary part, thereby allowing for the possibility of exponential instabilities to Phase II solutions (see Fig. 2.10). In the non-particle-hole symmetric case, $\Delta(t) = \Delta_\infty e^{-2i\mu_\infty t}$ in Phase II, and the equation for the frequencies of harmonic $\delta\Delta(t)$ can be expressed in the form

$$\begin{aligned} S_2^2(\omega_0) &= \big(S_1(\omega_0)-1\big)^2 + \big(S_1(\omega_0)-1\big)S_3(\omega_0),\\ S_1(\omega_0) &\equiv 4g_f\sum_j \frac{\widetilde{\varepsilon}_j f_j^2 Z_j}{\omega_0^2-\widetilde{b}_j^2},\\ S_2(\omega_0) &\equiv 2g_f\omega_0\sum_j \frac{f_j^2 Z_j}{\omega_0^2-\widetilde{b}_j^2},\\ S_3(\omega_0) &\equiv 4g_f\Delta_\infty^2\sum_j \frac{f_j^4 Z_j}{\widetilde{\varepsilon}_j(\omega_0^2-\widetilde{b}_j^2)}, \end{aligned} \tag{2.42}$$

where

$$\widetilde{\varepsilon}_j \equiv \varepsilon_j - \mu_\infty, \quad \widetilde{b}_j \equiv 2\sqrt{\widetilde{\varepsilon}_j^2 + f_j^2\Delta_\infty^2}. \tag{2.43}$$

The self-consistency equation for $\Delta(t)$ in Phase II has the same form as Eq. (2.33), with the substitution $\varepsilon_j \to \widetilde{\varepsilon}_j$. In the particle-hole symmetric limit, $S_2(\omega_0) = 0$ and the correct solution to Eq. (2.42) solves Eq. (2.40). In the limit $\Delta_\infty \to 0$, (2.42) is also the stability equation for Phase I. In Appendix D, we show that the Phase I-II and Phase II-III transitions given by (2.42) are identical to those obtained using exact solvability in the integrable s-wave and $p+ip$ models.

5.3 Phase III

Universality of elliptic oscillations

The asymptotic Phase III solution is significantly more complicated than its Phase I and Phase II counterparts (2.28) and (2.31). We derive this solution in Sect. 6. Presently we provide evidence that the asymptotic behavior of $\Delta(t)$ can always be described by Jacobi elliptic functions. Consider first the particle-hole symmetric limit, for which we find

$$\dot{\Delta}^2(t) = P_4[\Delta(t)], \quad \text{as } t \to \infty, \tag{2.44}$$

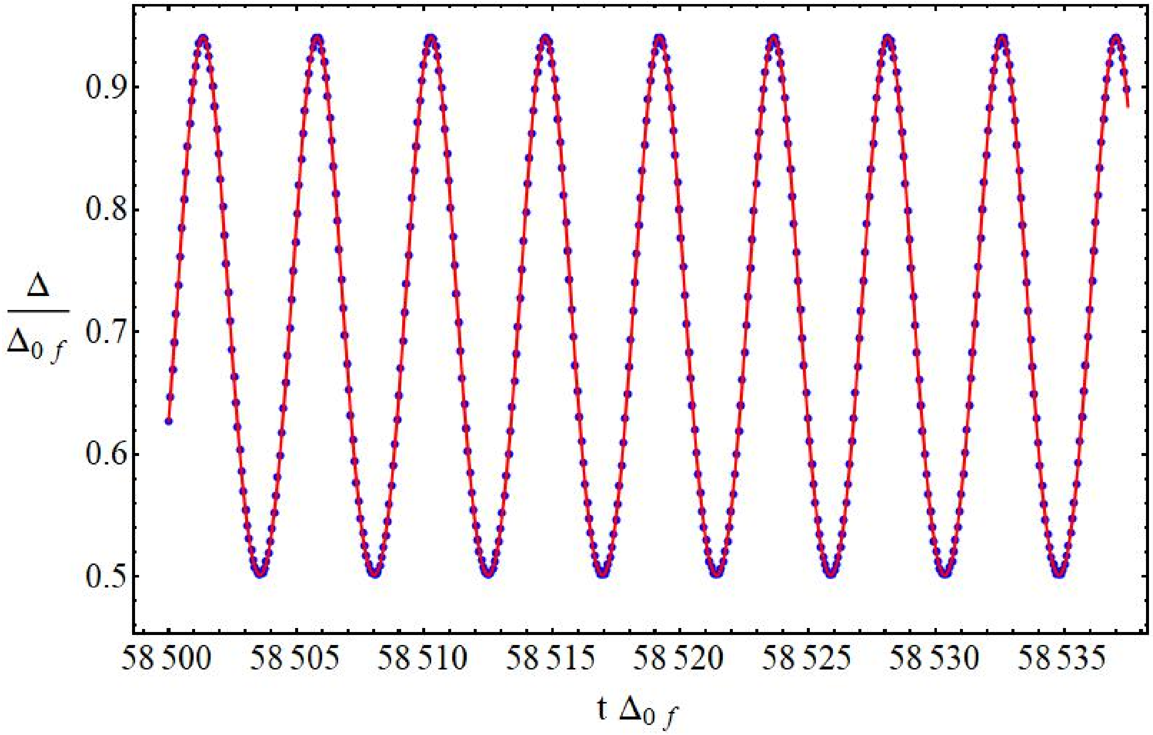

Figure 2.6: The quench in the Lorentzian separable BCS model (blue dots) from Fig. 2.1 (c) and (d) $[\gamma = W]$ and the corresponding elliptic function fit (solid red) from Eq. (2.46) with $a \approx 0.868205$, $\Delta_+ \approx 0.941415$, $\Delta_- \approx 0.501511$, $\widetilde{\Delta}_+ = \widetilde{\Delta}_-^* \approx 0.915740 + 0.002407i$ and $t_0 = 2.801929$. To obtain these parameters, we fit $\dot{\Delta}$ to Eq. (2.44) and then shift by the appropriate t_0. If a fifth order polynomial is used instead of $P_4[\Delta(t)]$, the coefficient of the Δ^5 term is -6.08×10^{-5}, providing further evidence that this asymptotic $\Delta(t)$ is indeed an elliptic function. Although only a short time frame is shown, this fit works well for the entire time interval from $t\Delta_{0f} = 10^4$, which is the time scale after which the oscillation amplitude stabilizes, to the times shown. In this fitting procedure, Δ is given in units of $\Delta_{0f} = 0.4W$ and time is measured in units of Δ_{0f}^{-1} as pictured. In terms of the level spacing $\delta = 5 \times 10^{-6} W$, the time domain pictured is $0.73125 < t\delta < 0.731688$.

where $P_4[\Delta(t)]$ is a generic fourth-order polynomial in $\Delta(t)$. Now parametrize $P_4[\Delta(t)]$ as

$$\begin{aligned} P_4[\Delta(t)] = -a^2(\Delta(t) - \Delta_+)(\Delta(t) - \Delta_-)\times \\ \times(\Delta(t) + \widetilde{\Delta}_+)(\Delta(t) + \widetilde{\Delta}_-), \end{aligned} \tag{2.45}$$

where the real coefficients $\Delta_\pm$ are the maximum and minimum values of $\Delta(t)$, while $\widetilde{\Delta}_\pm$ are either complex conjugate or independent real numbers. This parametrization leads to the following solution for $\Delta(t)$

$$\begin{aligned} \Delta(t) &= \frac{\widetilde{\Delta}_+(\Delta_+ + \widetilde{\Delta}_-)\mathrm{dn}^2[ab(t-t_0), m] - \widetilde{\Delta}_-(\Delta_+ + \widetilde{\Delta}_+)}{\Delta_+ + \widetilde{\Delta}_+ - (\Delta_+ + \widetilde{\Delta}_-)\mathrm{dn}^2[ab(t-t_0), m]}, \\ m &\equiv \frac{(\Delta_+ - \Delta_-)(\widetilde{\Delta}_+ - \widetilde{\Delta}_-)}{(\Delta_+ + \widetilde{\Delta}_-)(\Delta_- + \widetilde{\Delta}_+)}, \\ b &\equiv \frac{1}{2}\sqrt{(\Delta_+ + \widetilde{\Delta}_-)(\Delta_- + \widetilde{\Delta}_+)}, \end{aligned} \tag{2.46}$$

where $\mathrm{dn}[t, m]$ is the Jacobi-dn function. When particle-hole symmetry does not hold, then one replaces $\Delta(t)$ with $|\Delta(t)|^2$ in Eqs. (2.44)-(2.46). In Figs. 2.6 and 2.7 we show that Phase III oscillations in separable BCS models satisfy Eq. (2.44) and Eq. (2.46), while Fig. 2.8 shows the same for the spin-orbit model.

As a general rule of thumb, most spin-orbit quenches that superficially appear to relax to Phase III really have not. Fig. 2.8 is the result of a thorough search of the parameter space in order to find a true Phase III quench within a computationally achievable time. On the one hand, the final field h_f has to be large enough so as to nonperturbatively break integrability, for small perturbations lead to long relaxation times. On the other hand, the fields cannot be so large as to suppress the equilibrium gap Δ_0 scale, which is the scale of the oscillation frequency. The value of α must also break integrability nonperturbatively, but a larger α also requires a larger number of spins to reach the thermodynamic limit. Finally, it turns out that a smaller Fermi energy relative to the bandwidth promotes a faster relaxation time. We discuss this Phase III relaxation time further in Sect. 5.3 in the context of the separable BCS models.

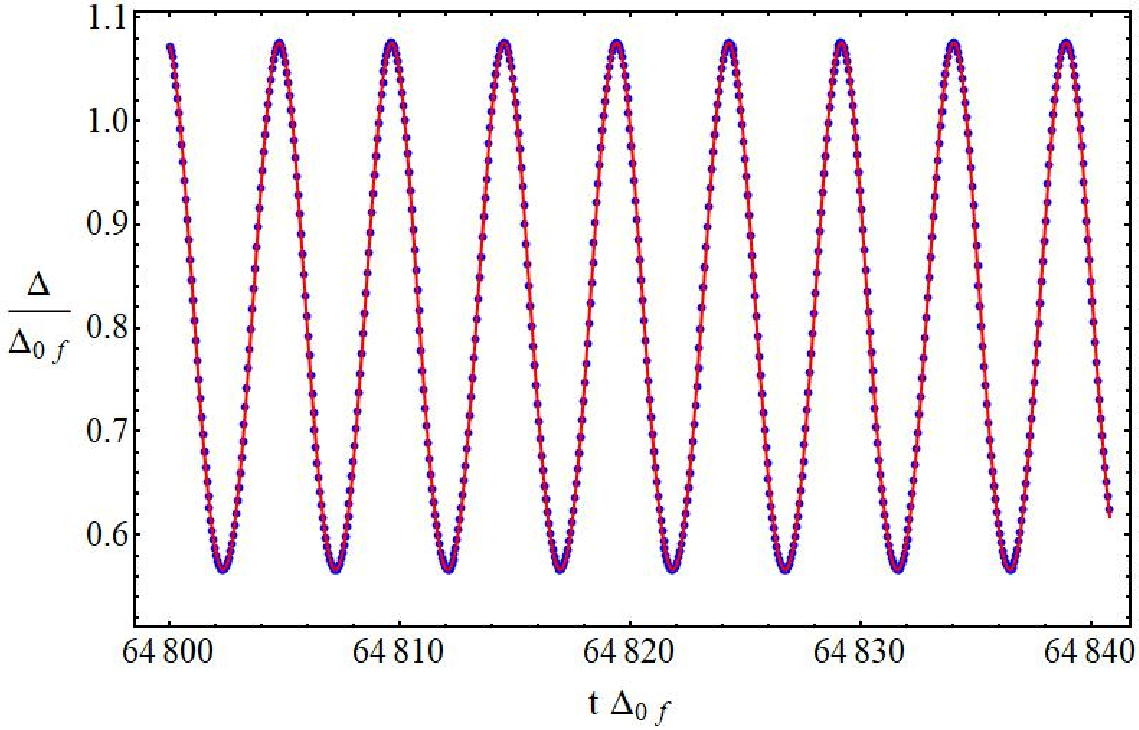

Figure 2.7: A Phase III quench in a $f(\varepsilon) = \exp[-|\varepsilon|/\gamma]$ separable BCS model (blue dots), where $\gamma = 0.5W$, $N = 2 \times 10^5$, $\Delta_{0i} = 0.04W$, $\Delta_{0f} = 0.8W$. The corresponding elliptic function fit (solid red) from Eq. (2.46) has $a \approx 0.821896$, $\Delta_+ \approx 1.075648$, $\Delta_- \approx 0.566069$, $\widetilde{\Delta}_+ = \widetilde{\Delta}_-^* \approx 0.010686 + 1.327633i$ and $t_0 = 2.131916$. To obtain these parameters, we fit $\dot{\Delta}$ to Eq. (2.44) and then shift by the appropriate t_0. If a fifth order polynomial is used instead of $P_4[\Delta]$, the coefficient of the Δ^5 term is 4.22×10^{-9}. In this fitting procedure, Δ is given in units of Δ_{0f} and time is measured in units of Δ_{0f}^{-1} as pictured. In terms of the level spacing δ, the time domain pictured is $0.405 < t\delta < 0.40525$.

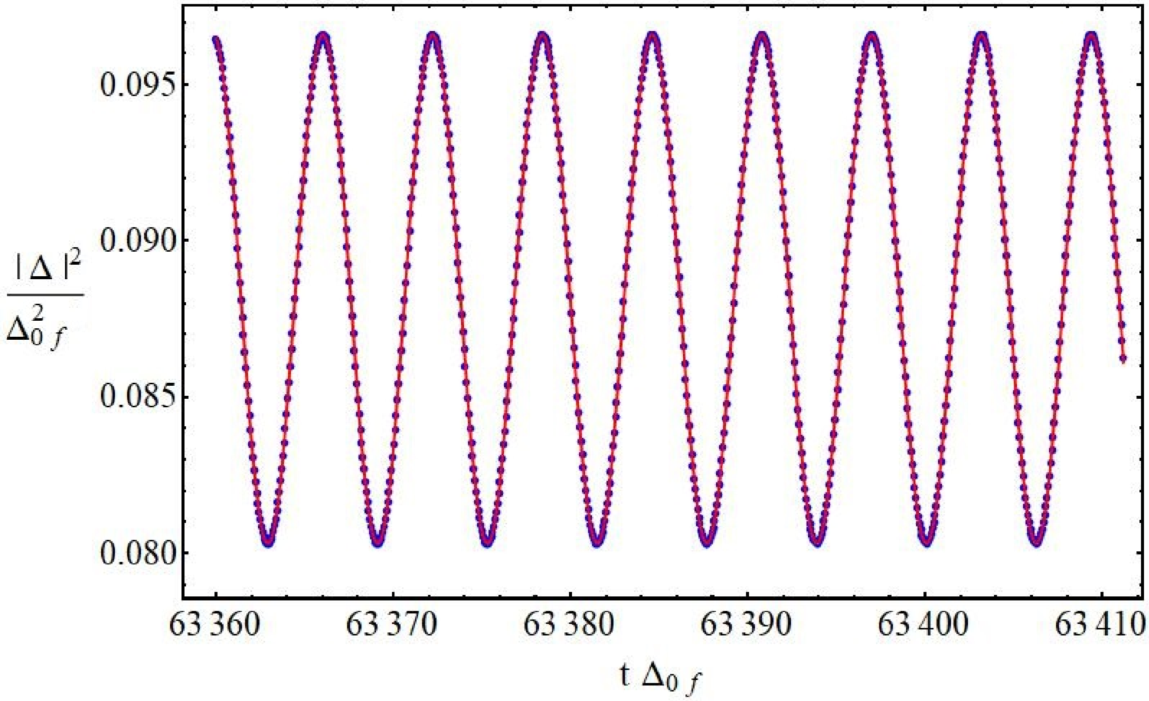

Figure 2.8: A Phase III quench in the spin-orbit model (blue dots), where in units of the bandwidth W: $\varepsilon_F = 0.1$, $\alpha^2 = 0.9$, $gN = 2.315999$, $h_i = 1.998980$, $h_f = 0.801020$. These parameters uniquely determine the initial and final equilibrium gaps and chemical potentials through the use of Eq. (2.16) and Eq. (2.21). The energies ε_j are uniformly distributed in the interval $[0, W]$, and the number of pseudospins is $N = 8 \times 10^4$. As particle-hole symmetry does not hold, we fit $\Omega \equiv |\Delta|^2$ to the elliptic function definition in Eq. (2.46). The fit is $a \approx 0.776633$, $\Delta_+ \approx 0.096608$, $\Delta_- \approx 0.080316$, $\widetilde{\Delta}_+ = \widetilde{\Delta}_-^* \approx 0.873604 + 0.883872i$ and $t_0 = 3.033272$. The fit (solid red) is good for all $t > \tau$, where τ is the relaxation time defined in Sect. 5.3. Here $\tau\Delta_{0f} \approx 3050$. In the fitting procedure, Δ is given in units of Δ_{0f} and time is measured in units of Δ_{0f}^{-1} as pictured. In terms of the level spacing δ, the time domain pictured is $1.472 < t\delta < 1.473$, shortly after which finite size effects take over.

For the integrable s-wave case it can be shown analytically [53] that $\widetilde{\Delta}_\pm = \Delta_\pm$ and $a = 1$, which greatly simplifies $P_4[\Delta(t)]$ and $\Delta(t) \to \Delta_+ \mathrm{dn}[\Delta_+(t - t_0), 1 - \frac{\Delta_-^2}{\Delta_+^2}]$. The mechanism behind the emergence of the three phases in the s-wave Hamiltonian is a dynamical reduction in the number of degrees of freedom. The Phase III asymptotic solution for $\Delta(t)$ is identical with that of a 2-spin s-wave Hamiltonian, while Phases II and I correspond to 1-spin and 0-spin solutions, respectively. In Phase III, this technique does not work for the separable BCS models. In Appendix C, we show that the 2-spin solution for these nonintegrable models is identical to that of the integrable case, up to a rescaling of time, while the general asymptotic solution that we observe is Eq. (2.46). Thus, if a reduction mechanism exists in the nonintegrable cases, the form of the m-spin Hamiltonian must also change.

Relaxation time

In Sect. 5.2 we saw that there are examples of nonintegrable separable BCS models where the constant Δ_∞ of Phase II is unstable to harmonic perturbations, and in Sect. 5.3 we gave evidence that the Phase III oscillations of these models are elliptic functions. This behavior is typical of integrable models as well, although the form of the elliptic functions changes once integrability is broken. A more important difference, however, is that a long relaxation time scale τ emerges before the system truly reaches Phase III.

Fig. 2.9 gives an example of the long relaxation time in the $d + id$ model, which is the separable BCS model with $f(\varepsilon) = \varepsilon$. The initial dynamics at weak coupling seem to indicate [76] that $|\Delta(t)|$ oscillates with a single frequency reminiscent of Phase III. Upon closer inspection, however, the amplitude of the oscillations slowly changes with no indication of stabilizing. In Fig. 2.10, quenches at higher energies provide further evidence that the long-time asymptotic state is difficult to determine based on the short-time dynamics.

Let us now explore the dependence of the relaxation time τ on Δ_{0i}, Δ_{0f} and γ in the Lorentzian separable BCS model defined in Eq. (2.23). We define τ as the minimum time after which the minimum of $|\Delta(t)|$ oscillations stays within $\eta = 10^{-4}$ of its asymptotic value.

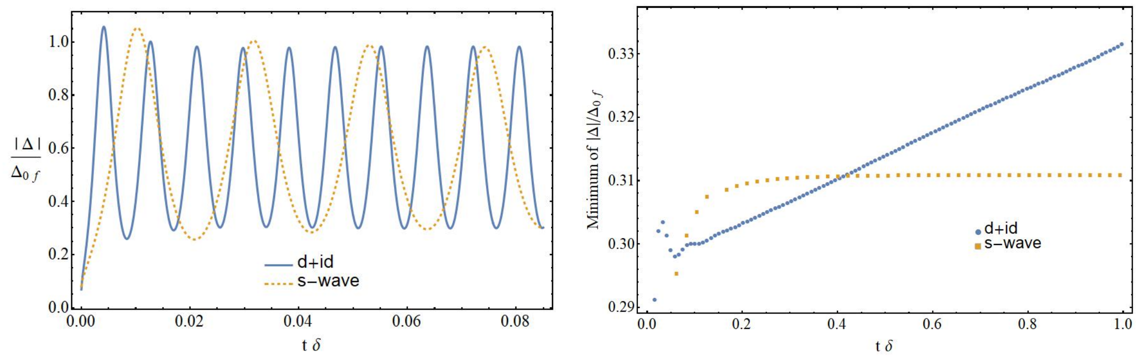

(a) (b)

Figure 2.9: Example of a deceitful quench in the $f(\varepsilon) = \varepsilon$ $(d + id)$ separable BCS model, which at short times seems to enter Phase III on a similar time scale as the corresponding integrable s-wave quench with the same parameters. Part (b) shows that minimum of the $d + id$ $|\Delta(t)|$ is actually evolving over the entire time scale considered, and it is not clear what the asymptotic phase is. For both models, we used 4×10^4 single-particle energies ε_j uniformly distributed on the interval $[0, W]$, $\Delta_{0f} = 0.00625W$, $\Delta_{0i} = 0.05\Delta_{0f}$, $\varepsilon_F = 0.25W$ [77]. In Fig. 2.10, we explore similar quenches in the $d + id$ model at larger energy scales, where the dynamics are faster.

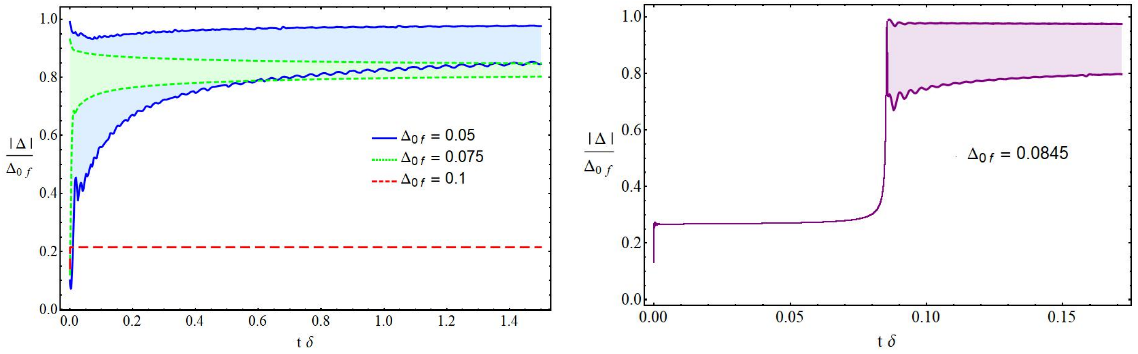

(a) (b)

Figure 2.10: Study of the long time dynamics of $d + id$ model quenches, continued from Fig. 2.9. We keep the same parameters and the same ratio $\Delta_{0i}/\Delta_{0f} = 0.05$ while varying Δ_{0f}. Pictured are the maxima and minima of oscillations of $|\Delta|$. Part (a) shows that below a certain critical $\Delta_{0f} \sim 0.0845W$, the amplitude of $|\Delta|$ oscillations evolves over an extremely long time scale. When $\Delta_{0f} = 0.05W$, there are also multiple incommensurate frequencies, and it is unclear whether the asymptotic state is Phase II, III, or something else entirely. When $\Delta_{0f} = 0.075W$, the decay in amplitude of $|\Delta|$ resembles typical decays to Phase II seen in other models (see Fig. 2.5). At $\Delta_{0f} = 0.1W$, the system rapidly enters Phase II at a smaller Δ_∞ than would be inferred from the other two cases, indicating that we have crossed a transition point. Part (b) shows a quench at this transition point, where the Phase II state seen for $\Delta_{0f} = 0.1W$ exhibits an exponential instability and moves to an oscillatory state with unknown asymptotic behavior. The integrable s-wave BCS model, $f(\varepsilon) = 1$, is deep in Phase III for all these values of Δ_{0f} and Δ_{0i}.

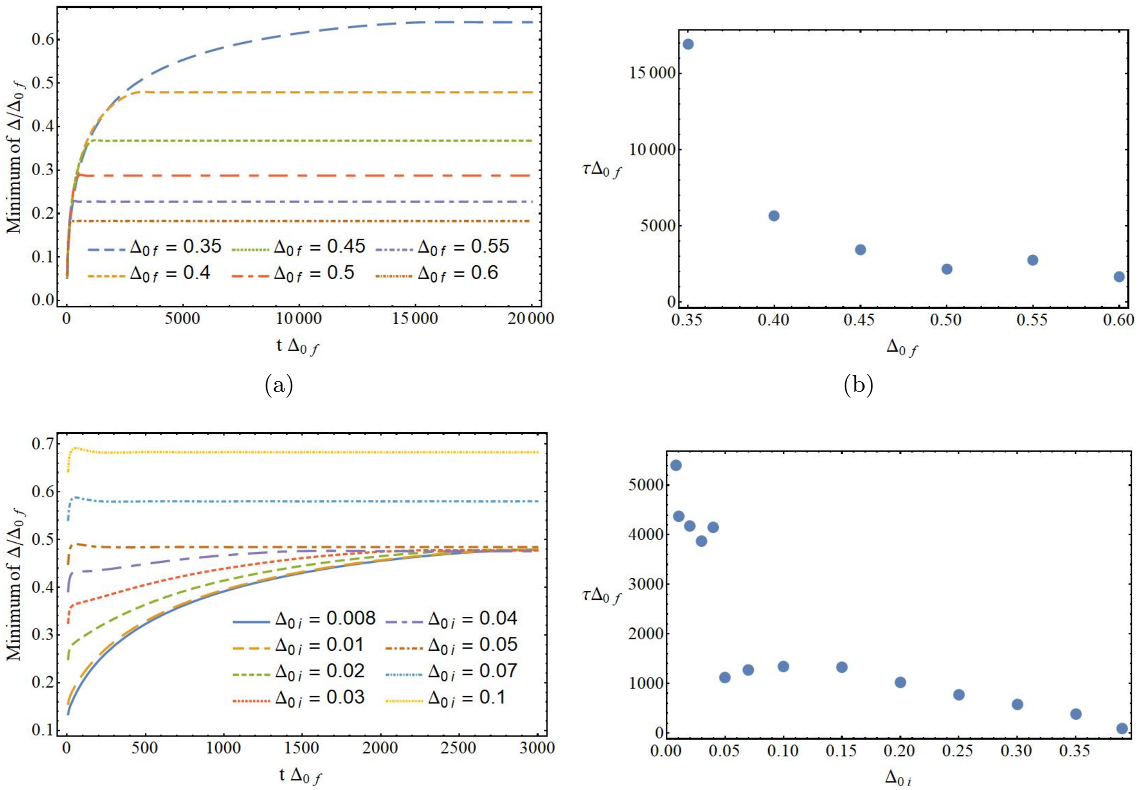

(a) (b)

(c) (d)

Figure 2.11: Nonintegrable pairing models exhibit an extremely long relaxation time τ when the asymptotic state is Phase III, which is most prominent in the evolution of the minima of the oscillations of $\Delta(t)$. Pictured is a study of τ as a function of Δ_{0f}, at fixed $\Delta_{0i} = 10^{-3}W$ (a,b), and τ as a function of Δ_{0i} at fixed $\Delta_{0f} = 0.4W$ (c,d) in the Lorentzian model at $\gamma = 0.8W$ in the particle-hole symmetric case. The time τ is not monotonic in either case, but it is generally a decreasing function of the initial and final coupling strengths g_i and g_f. In all plots, Δ_{0i} and Δ_{0f} are given in units of the bandwidth W. In (a,b) $2.4 \times 10^4 > N > 1.2 \times 10^4$ and in (c,d) $N = 8400$.

This definition of τ and the precise value of η are somewhat arbitrary, but empirically we find that the minima of $|\Delta(t)|$ take longer to relax to the stationary value than the maxima. Typically, the minimum will increase for a time until it begins to oscillate with decreasing amplitude about a final value. Most importantly, this definition of τ delineates clearly the difference between integrable and nonintegrable behavior. Fig. 2.11 shows the dependence of τ on the values of Δ_{0i} and Δ_{0f}, with one or the other fixed. Generally speaking, we find that quenches at lower energy scales increase τ.

More interesting is the dependence of τ on γ, the integrability-breaking parameter, at

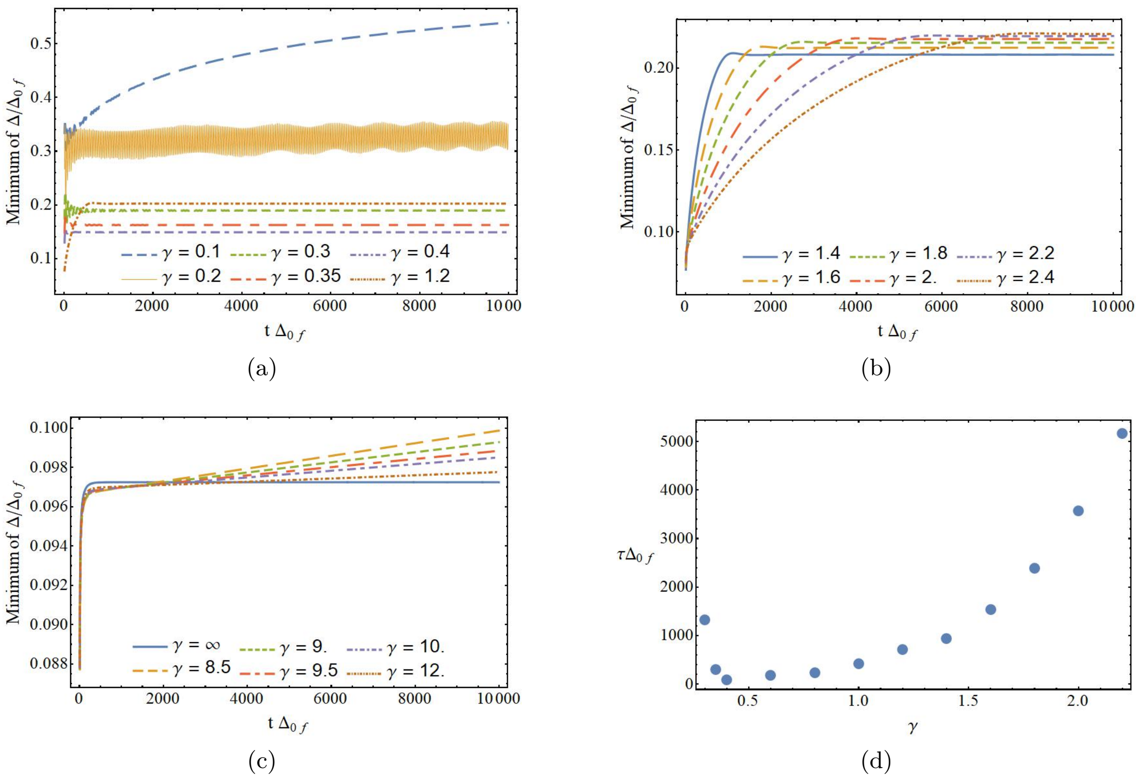

(a) (b) (c) (d)

Figure 2.12: Study of the relaxation time τ, see Fig. 2.11, in the Lorentzian model as a function of the integrability breaking parameter γ at fixed $\Delta_{0i} = .005W$ and $\Delta_{0f} = 0.6W$, where $\gamma = \infty$ is the integrable s-wave model. For these quench parameters, both the Lorentzian and s-wave models enter Phase III. Parts (a)-(c) show how the minimum of $\Delta(t)$ slowly evolves and reaches an asymptote, while part (d) gives τ near $\gamma = 0.4W$, where the minimum satisfies $\tau_{\min}\Delta_{0f} \approx 89$. This minimum is still greater than the relaxation time of the s-wave case, where $\tau\Delta_{0f} \approx 65$. The relaxation time increases sharply away from $\gamma = 0.4W$, especially in the direction of decreasing gamma, where $\tau\Delta_{0f} \approx 64500$ at $\gamma = 0.11W$. In all plots, γ is given in units of the bandwidth W and $N = 5500$.

fixed $(\Delta_{0i}, \Delta_{0f})$. First, let us examine quenches that lead to Phase III in both the Lorentzian and integrable s-wave models. Fig. 2.12 shows that τ has single minimum for $\gamma \sim 0.4W$ and increases away from this point both as $\gamma \to 0$ and as $\gamma \to \infty$. In all cases, the relaxation time of quenches in the integrable s-wave model, which is the $\gamma \to \infty$ limit of our separable BCS Hamiltonians, is far smaller. We believe that the increase of τ as $\gamma \to \infty$ is indicative of nonperturbative behavior of the dynamics in the vicinity of the integrable limit, see Sect. 8.

The behavior of $f(\varepsilon)$ as $\gamma \to 0$ is model dependent; in the case of the Lorentzian model, the stability analysis of Sect. 5.2 indicates that Phase II is unstable to harmonic

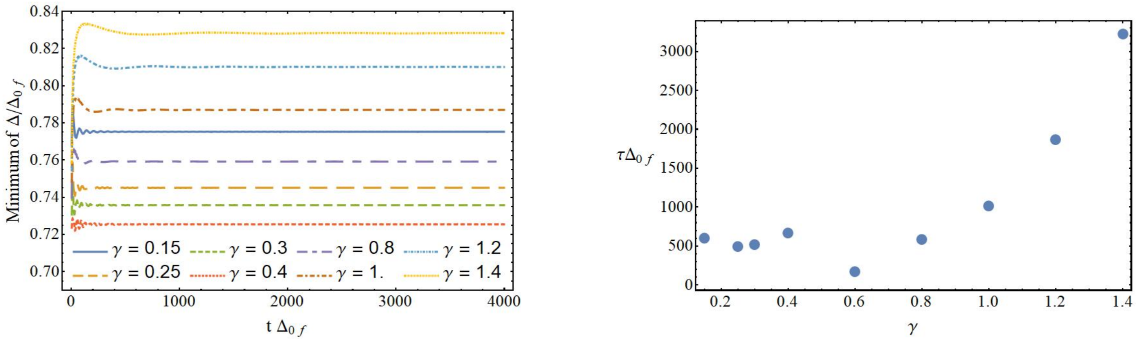

(a) (b)

Figure 2.13: Study of the relaxation time τ in the Lorentzian model as a function of the integrability breaking parameter γ at fixed $\Delta_{0i} = 0.2W$ and $\Delta_{0f} = 0.6W$. For these quench parameters, the s-wave model enters Phase II, while the Lorentzian enters Phase III. Part (a) shows how the minimum of $\Delta(t)$ slowly evolves and reaches an asymptote, while part (b) gives τ_{min} near $\gamma = 0.6W$, where $\tau_{\text{min}}\Delta_{0f} \approx 175$. The relaxation time increases away from $\gamma = 0.6W$ in both directions. In all plots, γ is given in units of the bandwidth W and $N = 2800$.

perturbations if $\gamma > \Delta_\infty$; otherwise, Phase II could be stable. We observe in Fig. 2.12 large oscillations in the evolution of the minimum of $\Delta(t)$ at $\gamma = 0.2W$, behavior which occurs in the range $0.13W \lesssim \gamma \lesssim 0.26W$ For $\gamma \lesssim 0.13W$, the minima oscillations disappear and τ begins to dramatically increase. Despite this qualitative change in the evolution of $|\Delta(t)|$, down to at least $\gamma = 0.11W$ we still find that the system eventually enters Phase III with a reduced amplitude of oscillation.

Fig. 2.13 is similar to Fig. 2.12, except we now choose Δ_{0i} and Δ_{0f} such that the (integrable) s-wave model enters Phase II. The behavior of τ with respect to γ is qualitatively similar, except there is no regime where the minimum of $\Delta(t)$ undergoes large oscillations.

The spin-orbit model also has a very long relaxation time to Phase III. In order to observe this asymptotic state, as is shown in Fig. 2.8, one must carefully choose model and quench parameters, otherwise τ is simply too large for our present numerical study.

6 Phase III asymptotic solution

We now explore the structure of the Phase III asymptotic state. First, we treat $\Delta(t)$ as a periodic external driving and show that there is always a periodic solution for the classical pseudospins (and auxiliary functions in the spin-orbit model), and then we provide evidence that the class of periodic $\Delta(t)$ that are also self-consistent are elliptic functions.

6.1 External driving

In the separable BCS model, the mean-field dynamics can be described alternatively by a Gaussian wave function with complex Bogoliubov amplitudes $u_j(t)$ and $v_j(t)$

$$|\psi\rangle = \prod_j [u_j^*(t) + v_j^*(t)\hat{c}_{j\uparrow}^\dagger \hat{c}_{j\downarrow}^\dagger]|0\rangle, \tag{2.47}$$

where normalization requires $|v_j|^2 + |u_j|^2 = 1$. The equations of motion for $u(t)$ and $v(t)$ follow from the time-dependent Schrödinger equation $i\frac{\partial}{\partial t}|\psi\rangle = \hat{H}|\psi\rangle$ applied to (2.47) with the mean-field Hamiltonian from (2.2),

$$i\frac{d}{dt}\begin{pmatrix} u_j(t) \\ v_j(t) \end{pmatrix} = \begin{pmatrix} \varepsilon_j & f_j\Delta \\ f_j\Delta^* & -\varepsilon_j \end{pmatrix}\begin{pmatrix} u_j(t) \\ v_j(t) \end{pmatrix}, \tag{2.48}$$

where we shifted the Hamiltonian by a constant $\hat{H} = \hat{H}_f - \sum_j \varepsilon_j$ in order to make it traceless. The mapping to the classical pseudospins is

$$s_j^- = u_j v_j^*, \quad s_j^z = \frac{|v_j|^2 - |u_j|^2}{2}. \tag{2.49}$$

We shall discuss the nature of the asymptotic Phase III $\Delta(t)$ in terms of $v(t)$ and $u(t)$. To do so, consider first Eq. (2.48) with a periodic $\Delta(t) = \Delta(t+T)$ that is not necessarily self-consistent, which decouples each pair of (u_j, v_j) from all the others. The abstract form of Eq. (2.48) is

$$i\frac{d}{dt}\begin{pmatrix} \mathbf{u} \\ \mathbf{v} \end{pmatrix} = \mathbf{h}(t)\begin{pmatrix} \mathbf{u} \\ \mathbf{v} \end{pmatrix} \tag{2.50}$$

with

$$\mathbf{h}(t) = \begin{pmatrix} \mathbb{A} & \mathbb{B}(t) \\ \mathbb{B}^\dagger(t) & -\mathbb{A} \end{pmatrix}, \tag{2.51}$$

where $\mathbf{u}$ and $\mathbf{v}$ are m-dimensional vectors, $\mathbb{A}$ is a constant real symmetric $m \times m$ matrix, $\mathbb{B}(t)$ is a complex $m \times m$ matrix periodic in t with period T, and we dropped the index j for simplicity. The forthcoming discussion is valid for all systems of this form, see also Ref. [53]. For example, the spin-orbit dynamics admit such a representation with $m = 4$, while $m = 1$ in the separable BCS model.

As $\mathbf{h}(t)$ is periodic by assumption, the Floquet theorem applies. There are thus $2m$ independent solutions $\boldsymbol{\psi}_i(t)$ to Eq. (2.50) of the form

$$\boldsymbol{\psi}_i(t) = e^{\delta_i t} \begin{pmatrix} \mathbf{U}_i(t) \\ \mathbf{V}_i(t) \end{pmatrix}, \quad i = 1 \ldots 2m, \tag{2.52}$$

where the $\mathbf{U}_i(t)$ and $\mathbf{V}_i(t)$ are periodic with the same period as $\mathbf{h}(t)$ and the δ_i are complex numbers known as Floquet exponents. The solutions $\boldsymbol{\psi}_i(t)$ therefore have the property

$$\boldsymbol{\psi}_i(t + T) = \rho_i \boldsymbol{\psi}_i(t), \quad \rho_i \equiv e^{\delta_i T}, \tag{2.53}$$

where the ρ_i are known as Floquet multipliers. Because $\mathbf{h}(t)$ is Hermitian, Eq. (2.50) conserves the norm of the solutions $\boldsymbol{\psi}_i(t)$, which implies $|\rho_i| = 1$ and $\delta_i = i\nu_i$ for ν_i real. Furthermore, the particular form of $\mathbf{h}(t)$ implies that if $\boldsymbol{\psi} = (\mathbf{u}, \mathbf{v})^T$ is a solution then so is $\widetilde{\boldsymbol{\psi}} = (\mathbf{v}^*, -\mathbf{u}^*)^T$. This pairing of solutions implies that if δ_i is a Floquet exponent, then so is $-\delta_i$. In Sect. 6.2, we will use this latter fact to prove that there is always a periodic spin solution to Eq. (2.6) for a given periodic $\Delta(t)$.

Before continuing, we note that the Phase III asymptotic $\Delta(t)$ is only periodic in the particle-hole limit of the separable BCS model. In the general case, $\Delta(t) = F(t)e^{-2i\mu_\infty t}$, where $F(t)$ is periodic. Nonetheless, we can still reduce this problem, where $\mathbf{h}(t)$ is not periodic, to the periodic case by absorbing the phase $2\mu_\infty t$ in the following manner:

$$\begin{aligned}\mathbf{v}' &= \mathbf{v}\, e^{-i\mu_\infty t},\\ \mathbf{u}' &= \mathbf{u}\, e^{i\mu_\infty t},\\ \mathbb{A}' &= \mathbb{A} - \mu_\infty \mathbb{1},\end{aligned} \tag{2.54}$$

so that the time evolution of $(\mathbf{u}', \mathbf{v}')^T$ is described by Eq. (2.50) with periodic $\mathbf{h}(t)$ of the form given in Eq. (2.51) where $\mathbb{A}$ is replaced by $\mathbb{A}'$. In terms of the pseudospin representation of the dynamics, this transformation amounts to an overall time-dependent rotation about the z-axis with frequency $2\mu_\infty$.

6.2 Phase III spin solution in the separable BCS model

Now we draw our attention to the behavior of the spin solutions to the separable BCS model for the periodic external $\Delta(t)$ considered in the previous section. The dimension of the matrix $\mathbf{h}(t)$ is now $2m = 2$ and there are two independent solutions to the Floquet problem

$$\boldsymbol{\psi}_{1j}(t) = e^{i\nu_j t}\begin{pmatrix} U_j(t) \\ V_j(t)\end{pmatrix}, \quad \boldsymbol{\psi}_{2j}(t) = e^{-i\nu_j t}\begin{pmatrix} V_j^*(t) \\ -U_j^*(t)\end{pmatrix},$$

where $U_j(t)$ and $V_j(t)$ are periodic and we restored the index j. Using $\boldsymbol{\psi}_{1j}(t)$ and Eq. (2.49), we can construct a periodic spin solution $\boldsymbol{\sigma}_j(t)$ [i.e., a periodic solution of Eq. (2.6) for the given external $\Delta(t)$ that does not necessarily satisfy Eq. (2.7)],

$$\begin{aligned}\sigma_j^-(t) &= U_j(t)V_j^*(t),\\ \sigma_j^z(t) &= \frac{|V_j(t)|^2 - |U_j(t)|^2}{2}.\end{aligned} \tag{2.55}$$

We will now show that the most general spin solution $\mathbf{s}_j(t)$ precesses about the periodic solution $\boldsymbol{\sigma}_j(t)$ with a variable angular velocity. First we write the general solution $\boldsymbol{\Psi}_j(t)$ as a linear combination of $\boldsymbol{\psi}_{1j}(t)$ and $\boldsymbol{\psi}_{2j}(t)$

$$\boldsymbol{\Psi}_j(t) = \cos\frac{\theta_j}{2}\boldsymbol{\psi}_{1j}(t) + \sin\frac{\theta_j}{2}\boldsymbol{\psi}_{2j}(t). \tag{2.56}$$

Although the coefficients of linear combination are in principle complex, we can drop the constant overall phase of $\boldsymbol{\Psi}_j(t)$ as well as absorb $\frac{1}{2}\times$the remaining constant relative phase into the definitions of $U_j(t)$ and $V_j(t)$. Once again using (2.49), we now write $\boldsymbol{\Psi}_j(t)$ in terms of spin variables. It is helpful to first parametrize $U_j(t)$ and $V_j(t)$ as

$$\begin{aligned} U_j(t) &= |U_j(t)|e^{\frac{i}{2}[\alpha_j(t)-2\nu_j t-\beta_j(t)]}, \\ V_j(t) &= |V_j(t)|e^{\frac{i}{2}[\alpha_j(t)-2\nu_j t+\beta_j(t)]}, \end{aligned} \tag{2.57}$$

whence

$$\begin{aligned} s_j^- &= \cos\theta_j\,\sigma_j^- + \sin\theta_j\frac{\sigma_j^-}{|\sigma_j^-|}\left(\sigma_j^z\cos\alpha_j - \frac{i}{2}\sin\alpha_j\right), \\ s_j^z &= \cos\theta_j\,\sigma_j^z - \sin\theta_j\,|\sigma_j^-|\cos\alpha_j. \end{aligned} \tag{2.58}$$

Note that θ_j is the only time-independent quantity in Eq. (2.58). A geometric interpretation of the motion of the general solution $\mathbf{s}_j(t)$ with respect to the periodic solution $\boldsymbol{\sigma}_j(t)$ becomes clear once we use Eq. (2.58) to express $\mathbf{s}_j(t)$ in the body coordinate system of $\boldsymbol{\sigma}_j(t)$. Let $\hat{\mathbf{z}}'_j = \hat{\boldsymbol{\sigma}}_j$, while $\hat{\mathbf{x}}'_j$ lies along the line defined by the intersection of the plane spanned by $\{\hat{\mathbf{z}}'_j, \hat{\mathbf{z}}_j\}$ and that perpendicular to $\hat{\mathbf{z}}'_j$. Finally, $\hat{\mathbf{y}}'_j$ satisfies $\hat{\mathbf{y}}'_j\cdot\hat{\mathbf{x}}'_j = \hat{\mathbf{y}}'_j\cdot\hat{\mathbf{z}}'_j = 0$ and $\hat{\mathbf{x}}'_j\times\hat{\mathbf{y}}'_j = \hat{\mathbf{z}}'_j$. These definitions lead to

$$\begin{aligned} \hat{\mathbf{x}}'_j &= \frac{2}{|\sigma_j^-|}\left(\sigma_j^z\sigma_j^x\hat{\mathbf{x}}_j + \sigma_j^z\sigma_j^y\hat{\mathbf{y}}_j - |\sigma_j^-|^2\hat{\mathbf{z}}_j\right), \\ \hat{\mathbf{y}}'_j &= -\frac{\sigma_j^y}{|\sigma_j^-|}\hat{\mathbf{x}}_j + \frac{\sigma_j^x}{|\sigma_j^-|}\hat{\mathbf{y}}_j. \end{aligned} \tag{2.59}$$

The general spin solution $\mathbf{s}_j(t)$ in this new coordinate system is then

$$\begin{aligned} \mathbf{s}_j(t) &= \cos\theta_j \boldsymbol{\sigma}_j(t) + \sin\theta_j \boldsymbol{\sigma}_{j\perp}(t), \\ \boldsymbol{\sigma}_{j\perp}(t) &\equiv \frac{\cos\alpha_j(t)}{2}\hat{\mathbf{x}}'_j + \frac{\sin\alpha_j(t)}{2}\hat{\mathbf{y}}'_j, \end{aligned} \tag{2.60}$$

where $\boldsymbol{\sigma}_j \cdot \boldsymbol{\sigma}_{j\perp} = 0$ and $\boldsymbol{\sigma}_{j\perp}$ is not periodic. We see from Eq. (2.60) that $\mathbf{s}_j(t)$ makes a constant angle θ_j with the periodic solution and rotates about it with a variable angular frequency $\dot{\alpha}_j(t)$. From Eq. (2.57) and the periodicity of $U_j(t)$ and $V_j(t)$, we conclude that $\alpha_j(t) - 2\nu_j t$ is also periodic with the same period as the external $\Delta(t)$ driving the system.

6.3 Asymptotic self-consistency

Thus far, we have considered $\Delta(t)$ to be an external periodic driving that is not necessarily self-consistent. We showed for any such external driving, there is a corresponding periodic spin solution $\boldsymbol{\sigma}_j(t)$ with the same period as $\Delta(t)$. Furthermore, we derived in Eq. (2.60) that the general spin solution $\mathbf{s}_j(t)$ precesses in a simple manner about $\boldsymbol{\sigma}_j(t)$. In the true quench dynamics, however, $\Delta(t)$ must be self-consistent, and we now show that this requirement implies that there always exists a set of constants θ_j, such that the following integral equation holds for the asymptotic periodic $\Delta(t)$:

$$\Delta(t) = g_f \sum_j f_j \sigma_j^-[\Delta(t)] \cos\theta_j, \tag{2.61}$$

The notation $\boldsymbol{\sigma}_j = \boldsymbol{\sigma}_j[\Delta]$ emphasizes that the periodic spin solution is some complicated nonlocal function of $\Delta(t)$. An analogous expression to Eq. (2.61) exists for the spin-orbit model.

Eq. (2.61) is simply asymptotic self-consistency, as introduced in Sect. 5, applied to the Floquet problem studied in Sects. 6.1 and 6.2. To see this, suppose that we observe some Phase III asymptotic periodic $\Delta(t)$ after a quench from the ground state of the separable

BCS model, as discussed in Sect. 5.3. This $\Delta(t)$ is self-consistent by definition, i.e.,

$$\Delta(t) = g_f \sum_j f_j s_j^-(t), \tag{2.62}$$

which we write in terms of the underlying periodic spin solution $\boldsymbol{\sigma}_j$ by using Eq. (2.58)

$$\begin{aligned} \Delta &= g_f \sum_j f_j \Big(\sigma_j^-[\Delta] \cos\theta_j + \sigma_{j\perp}^-[\Delta] \sin\theta_j \Big), \\ \sigma_{j\perp} &\equiv \frac{\sigma_j^-}{|\sigma_j^-|} \Big(\sigma_j^z \cos\alpha_j - \frac{i}{2} \sin\alpha_j \Big), \\ \alpha_j(t) &= A_j(t) + 2\nu_j t, \quad A_j(t+T) = A_j(t), \end{aligned} \tag{2.63}$$

where ν_j is the imaginary part of the Floquet exponent as introduced in Eq. (2.52). As in our analysis of self-consistency in Phases I and II, Eq. (2.63) cannot hold exactly, this time because the sum over $\sigma_{j\perp}^-[\Delta]$ is the only non-periodic term. Nonetheless, under the reasonable assumption that $\nu_{j+1} - \nu_j \sim \delta$, where δ is the level spacing, the sum over $\sigma_{j\perp}^-[\Delta]$ dephases in $N \to \infty$ limit as $t \to \infty$ (the $N \to \infty$ limit comes first), leading to Eq. (2.61).

6.4 Self-consistent solutions in the separable BCS model

We have seen that an asymptotically self-consistent periodic $\Delta(t)$ satisfies the functional equation (2.61) in the separable BCS model. We now will give evidence that solutions to Eq. (2.61) are elliptic functions. In order to generate such solutions, fix a period T and write $\Delta(t)$ as a Fourier series

$$\Delta(t) = \sum_{n=-\infty}^{\infty} c_n e^{2\pi i n \frac{t}{T}}, \tag{2.64}$$

which we truncate to some $n_{\max}$, such that $c_n = 0$ if $|n| > n_{\max}$. In the particle-hole symmetric limit, $\Delta(t)$ is a real quantity that satisfies $\Delta(t) = \Delta(-t)$ [see Eq. (2.19)], so that c_n is real and equals c_{-n}.

For a fixed set of coefficients c_n, we determine $\sigma_j^x[\Delta(t)]$ by solving the equations of motion (2.6) from $t = 0$ to $t = T$ with $\Delta(t)$ given by (2.64). If the choice of c_n produces a self-consistent $\Delta(t)$, then it will be equal to the quantity $\Delta_{\text{comp}}(t)$ defined as

$$\Delta_{\text{comp}}(t) = g_f \sum_j f_j \sigma_j^x[\Delta(t)] \cos\theta_j, \tag{2.65}$$

for some set of θ_j. For most choices of c_n, however, Eq. (2.65) will not hold. As both $\Delta(t)$ and $\Delta_{\text{comp}}(t)$ are periodic functions of time with the same period, we define a distance $r(\{c_n\})$ as

$$r^2(\{c_n\}) = \int_0^T \Big(\Delta_{\text{comp}}(t) - \Delta(t)\Big)^2 dt. \tag{2.66}$$

A given $\Delta(t)$ is asymptotically self-consistent if and only if $r(\{c_n\}) = 0$.

We now explore the results of this procedure for the Lorentzian coupling of the separable BCS model for various values of the integrability breaking parameter γ. It turns out that this procedure works when we fix $\cos\theta_j = 1$, i.e., we find exactly (and not just asymptotically) self-consistent solutions. In order to find such solutions, we start from the known values of the Fourier coefficients of the s-wave ($\gamma = \infty$) solution, which are close to the Fourier coefficients of the $\gamma \gg 1$ solutions. We then progressively lower γ while finding Fourier coefficients that minimize $r(\{c_n\})$. Typically we obtain values of $r \sim 10^{-12} - 10^{-11}$ before declaring the solution self-consistent.

Fig. 2.14 gives of examples of such solutions at fixed Δ_{0f} and period T. Notably, there is a minimum $\gamma = \gamma_{\text{min}}$ below which the amplitude of oscillation vanishes. As γ is increased from this minimum, the amplitude of oscillations increases to a maximum and then decreases to a nonzero limiting value as $\gamma \to \infty$. Fig. 2.14 also shows the fast convergence of γ_{min} as a function of N for two examples of this procedure.

In Sect. 5.3, we argued through example quenches that the $\Delta(t)$ of Phase III are always elliptic functions, i.e., they satisfy Eq. (2.44). We show in Fig. 2.15 that the exactly self-consistent $\Delta(t)$ from Fig. 2.14 also satisfy Eq. (2.44) to a high degree of accuracy. The

Floquet analysis of the equations of motion from Sect. 6.1 applies to any periodic $\Delta(t)$. From Fig. 2.15, we conclude that the self-consistency requirement (2.61) is essential to selecting elliptic functions amongst all possible periodic functions.

7 Quasiperiodic Phase IV

Quenches that do not conform to Phases I-III are another intriguing consequence of integrability breaking. We present two such examples in Figs. 2.16 and 2.17. Figs. 2.16a and 2.17a show a particle-hole symmetric quench of the separable BCS Hamiltonian with sine coupling from Eq. (2.24). Figs. 2.16b and 2.17b depict a quench of the Zeeman field in the spin-orbit model (2.14). The quasiperiodic behavior of $\Delta(t)$ in Fig. 2.16a sets in very early on, as corroborated by Fig. 2.17a, and persists with no appreciable changes at least until the times shown in the figure. Similarly, Fig. 2.16b is representative of the long-time spin-orbit $|\Delta(t)|^2$ as evidenced by Fig. 2.17b. Based on our preliminary analysis of the Fourier spectrum of $|\Delta(t)|^2$ for this quench and of the maximal Lyapunov exponent with the method of local divergence rates [78], we believe that it too is quasiperiodic. However, a more careful study is needed to unambigously distinguish between quasiperiodicity and chaos in this case. Such a study is beyond the scope of the present paper, where we mainly focus on the properties of Phases I-III.

Note that the simulation times in Figs. 2.16 and 2.17 are enormous compared to the characteristic time of a single oscillation and even to typical Phase III relaxation times $\tau\Delta_{0f} \sim 10^3$ we observed in Sect. 5.3, cf. Fig. 2.12 and the caption to Fig. 2.8. Thus, both of these examples do not belong to Phases I, II, or III. We therefore conclude that there are regions of quasiperiodicity in the quantum quench phase diagrams of nonintegrable pairing models, which we call Phase IV.

8 Conclusion

The far-from-equilibrium steady states reached by nonintegrable pairing models after a quantum quench admit a similar taxonomy as do the integrable cases. We have shown that some or all of Phases I-III may occur in the separable BCS models and spin-orbit model defined in Eq. (2.1). The persistent periodic oscillations characterizing Phase III are always elliptic functions, regardless of whether the model is integrable. Moreover, we have developed a stability analysis of the three phases, summarized in Eq. (2.42), which generalizes known results in the integrable cases and elucidates the mechanism of nonequilibrium phase transitions using the language of linear analysis.

Despite these striking similarities, consequences accompany integrability breaking. As argued in Sect. 5.2, some nonintegrable models may not exhibit all three phases. At the same time, an entirely new quasiperiodic Phase IV emerges in certain models. Another key byproduct of integrability breaking is the emergence of a new, extremely long relaxation time scale τ when the asymptotic state either is or appears to be Phase III. For $t < \tau$, Δ can oscillate with more than one fundamental frequency and a slowly varying amplitude. This time scale is a generic feature of nonintegrable models, and its existence renders short-time analyses inadequate for determining the long-time dynamics. Moreover, τ diverges as we approach integrable points (e.g., as $\gamma^{-1} \to 0$ in the separable pairing models of Sect. 5), and it is often too large for the practical determination of the true asymptotic state.

While the squared modulus of $\Delta(t)$ [and $\Delta(t)$ itself in the particle-hole symmetric case] is always an elliptic function in Phase III, its parametrization is more complicated in nonintegrable models. As a result, the reduction mechanism discussed in Appendix C, which explains how Phase III manifests itself in the integrable models, does not apply to nonintegrable models. Nonetheless, we demonstrated in Sect. 6 that the common structure of the nonintegrable models implies the existence of a periodic solution to the classical pseudospin equations of motion if $\Delta(t)$ is taken to be a generic periodic external driving. Using numerical examples, we argued that further requiring $\Delta(t)$ to be self-consistent selects elliptic functions amongst all possible periodic functions.

It is instructive to discuss the BCS quench dynamics in terms of bifurcation theory [79, 80, 81]. For example, consider the particle-hole symmetric separable BCS models with real Δ. For fixed initial conditions (2.17) and any function $\Delta(t)$ with fixed $\Delta(0)$, the equations of motion (2.6) have a unique solution $\mathbf{s}_j[\Delta(t)] \equiv \mathbf{s}[\varepsilon_j, \Delta(t)]$. Eq. (2.7) then provides a closed nonlinear integral equation for $\Delta(t)$ [cf. Eq. (2.61)],

$$\Delta(t) = g_f \int d\varepsilon\, s_x[\varepsilon, \Delta(t)]. \tag{2.67}$$

Phase I is a fixed point, $\Delta = 0$, of this equation [82], while Phase II corresponds to two fixed points Δ_∞ and $e^{i\pi}\Delta_\infty = -\Delta_\infty$. In Phase III we end up on one of two limit cycles related to each other by a rotation by π around the z-axis [change of sign of $\Delta(t)$]. The Phase I to II and II to III transitions correspond to supercritical pitchfork and Hopf bifurcations, respectively, in this language [83]. The same results apply to the spin-orbit model (2.14). We also note that this quantum quench phase diagram is surprisingly similar to the nonequilibrium phase diagram of two atomic condensates coupled to a heavily damped cavity mode [84, 85]. The mean-field dynamics of the latter system are described by the driven-dissipative variant of the Bloch equations (2.6) for two classical spins representing individual condensates. Moreover, there are islands of quasiperiodicity in the phase diagram of the two coupled condensates, where the dynamics are very similar to that shown in Figs. 2.16 and 2.17.

Bifurcation theory also offers a plausible explanation for the divergence of the relaxation time τ near integrable points. Consider Phase III for an integrable pairing Hamiltonian, such as the particle-hole symmetric s-wave BCS model. Suppose the corresponding limit cycle loses stability as soon as integrability is broken and another limit cycle emerges as an attractor. An example of such behavior is the transcritical bifurcation [79, 80, 81]. Because the instability is weak for weak integrability breaking and because the evolution starts near the unstable limit cycle, the system takes a very long time τ to reach the attractor. The weaker the integrability breaking, the closer we are to the bifurcation and the longer the time τ.

An interesting open problem is to explore the newly discovered quasiperiodic Phase IV. In particular, one needs to investigate the possibility that asymptotic oscillations of $|\Delta(t)|$ for certain quenches may be chaotic, rather than quasiperiodic, i.e., the potential existence of a chaotic phase in addition to the quasiperiodic one. Let us also mention that quasiperiodic $|\Delta(t)|$ also occurs in integrable models, but only when the initial (pre-quench) state is a highly excited state instead of the ground state [86].

In this paper, we employed reduced BCS Hamiltonians (2.1) to model pairing dynamics. This description is valid only at times $t \ll \Gamma^{-1}$, where Γ is the highest among the rates of processes such Hamiltonians neglect. These processes include pair-breaking collisions [35, 36, 37, 53], three-body losses in ultracold gases [87], thermal fluctuations [88], etc. Thus, to reach the asymptotic state before these effects influence the dynamics, we need $\Gamma^{-1} \gg \tau$. In Phases II and III, this requirement is much more stringent than $\Gamma^{-1} \gg T_\Delta$ typically quoted in the literature on collisionless pairing dynamics. Here T_Δ is the characteristic period of $\Delta(t)$ oscillations (T_Δ is of the order of the inverse equilibrium gap Δ_{0f} in our separable BCS models). Another limitation is the parametric instability of Phase III with respect to spontaneous eruptions of spatial inhomogeneities [89, 90, 91, 92]. To avoid this instability, the system size has to be smaller than the superconducting coherence length.

Acknowledgements: We thank M. Dzero, A. J. Millis and A. Patra for helpful discussions. This work was supported by the National Science Foundation Grant DMR-1609829. J.A.S. was supported by a Rutgers University Louis Bevier Dissertation Completion Fellowship.

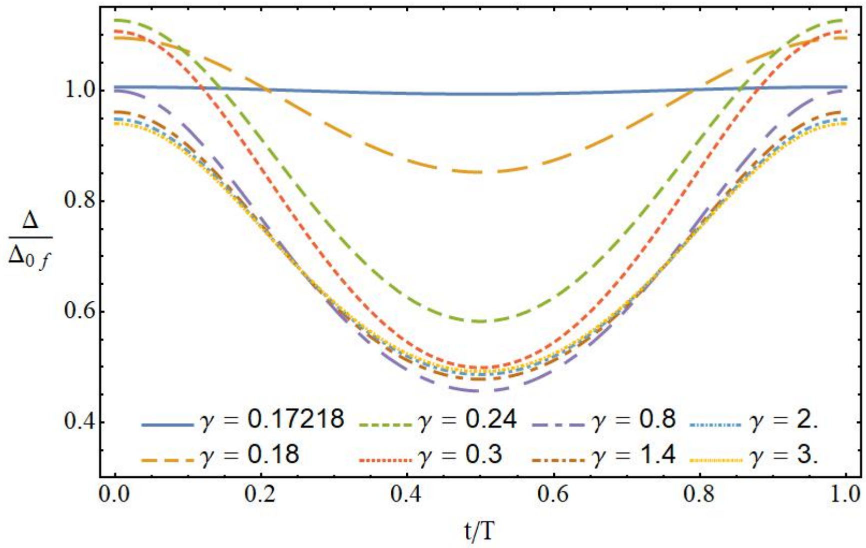

(a)

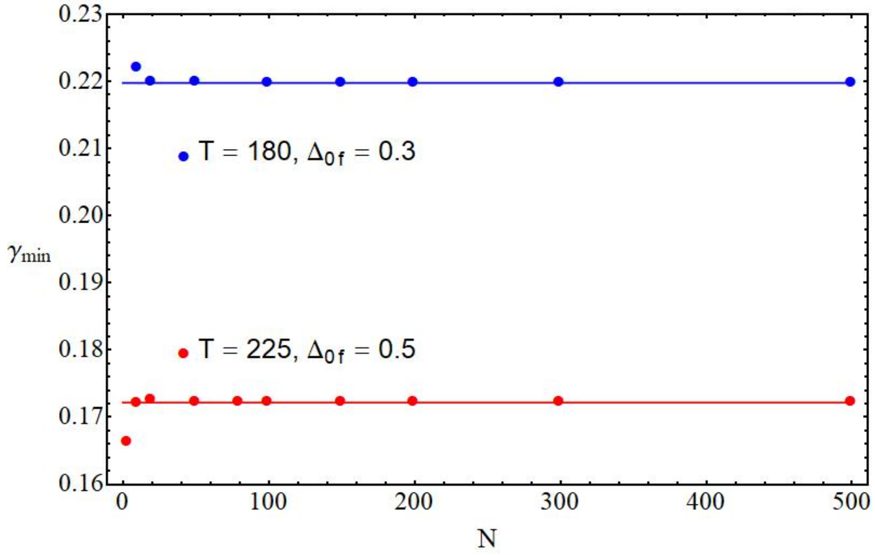

(b)

Figure 2.14: (a) Examples of exactly self-consistent, periodic $\Delta(t)$'s for the Lorentzian separable BCS equations of motion for different values of γ at fixed $\Delta_{0f} = 0.5W$, period $T = 225/W$, and $N = 500$. For these fixed parameters, below $\gamma_{\min} \sim 0.172W$ the only exactly self-consistent, periodic $\Delta(t)$ is a constant in time equal to the equilibrium value. (b) Convergence of $\gamma_{\min}$ as a function N. In both plots, Δ_{0f} and γ are given in units of W and T in units of W^{-1}.

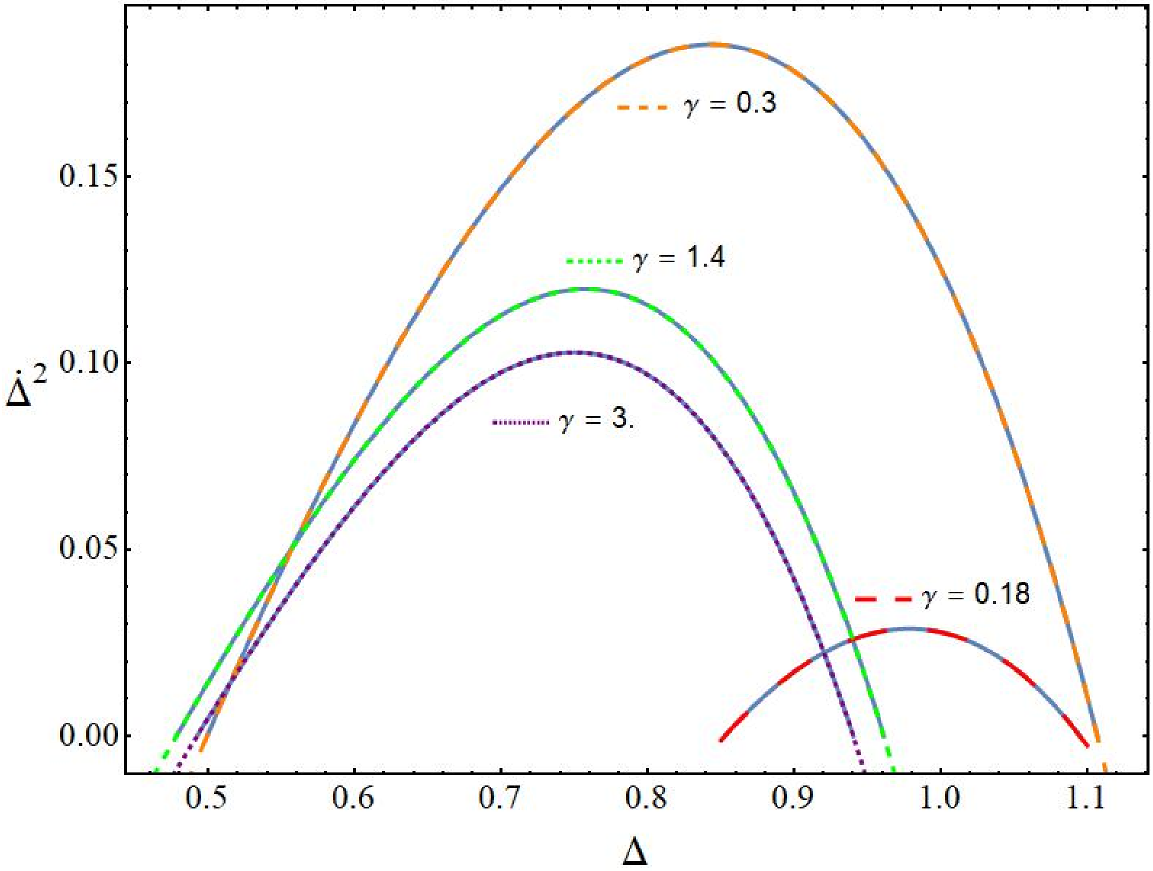

Figure 2.15: Evidence that the self-consistent periodic $\Delta(t)$ from Fig. 2.14 are elliptic functions. Squared time derivatives $\dot{\Delta}(t)$ as a function of $\Delta(t)$ are given by solid blue lines. These lines overlap strongly with the dashed lines, which are the fits to the defining differential equation for elliptic functions Eq. (2.44). If a Δ^5 coefficient is included in the fits, it is several orders of magnitude smaller than those for the 4th order fit shown here, providing strong evidence that $\dot{\Delta}^2(t)$ is indeed a 4th order polynomial in $\Delta(t)$. In this plot, γ is given in units of W and Δ in units of Δ_{0f}

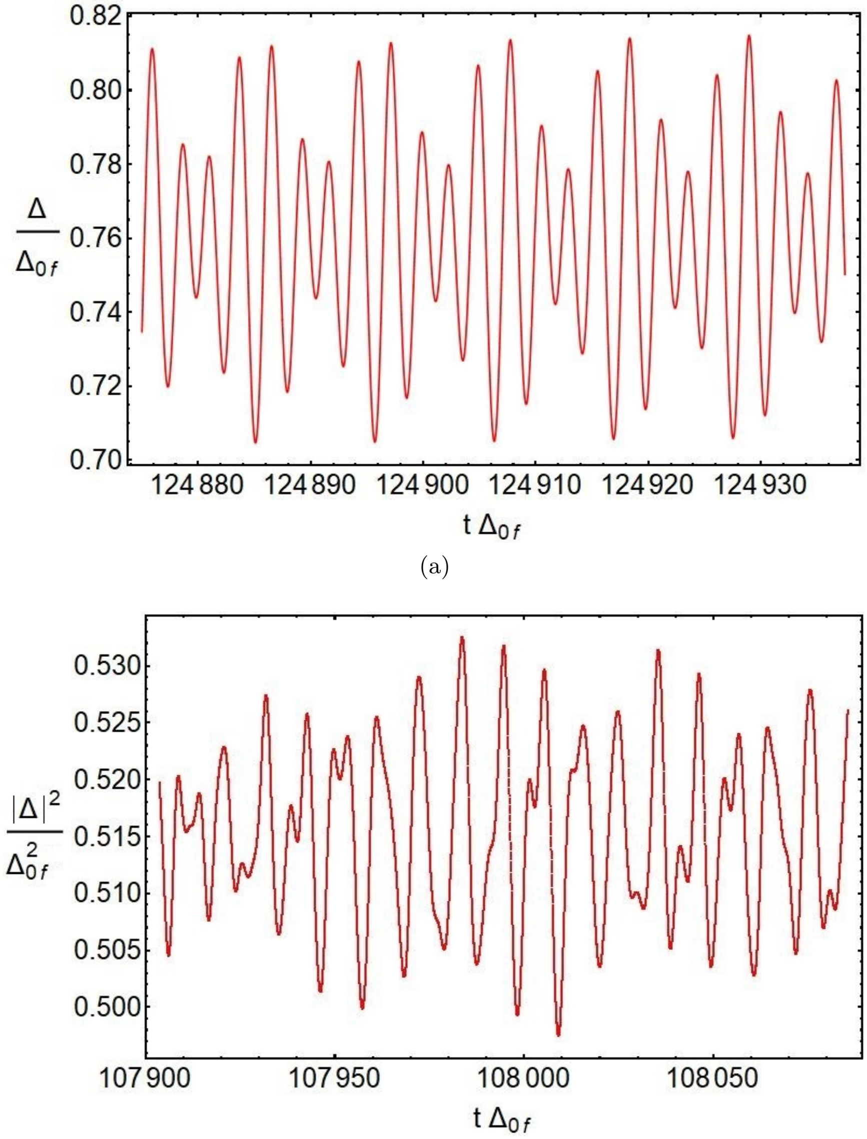

Figure 2.16: Quenches of nonintegrable separable BCS and spin-orbit models that do not conform to Phases I, II or III. This quasiperiodic dynamics of the order parameter emerge early and persist for the entire time of the simulation, see also Fig. 2.17. Plot (a) is the particle-hole symmetric separable BCS model with sine coupling from Eq. (2.24) and $N = 4 \times 10^5$ spins. In units of the bandwidth, the integrability breaking parameter is $\gamma = 0.075$, while $\Delta_{0i} = 0.05$ and $\Delta_{0f} = 0.5$. Part (b) is the spin-orbit model with $N = 2 \times 10^5$ spins. In units of the bandwidth: $\varepsilon_F = 0.4$, $\alpha^2 = 0.4$, $gN = 2$, $h_i = 2$, and $h_f = 0.514256$.

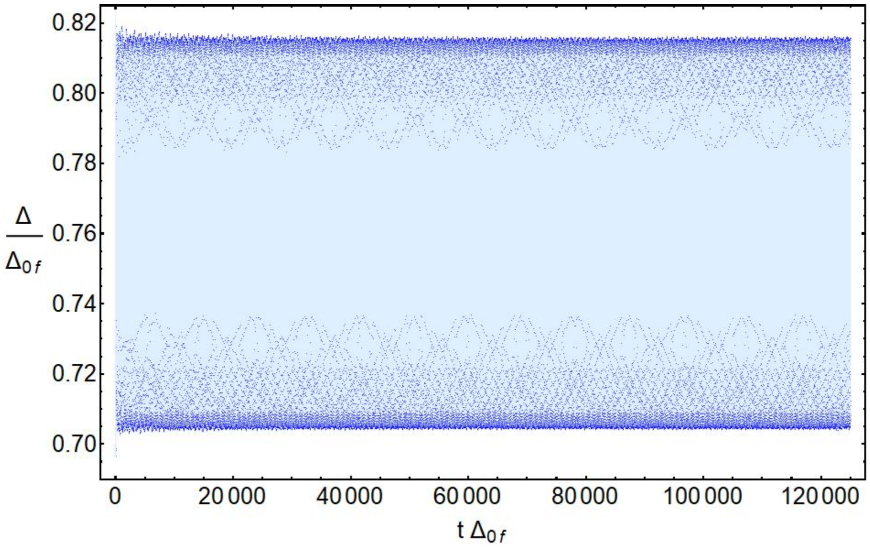

(a)

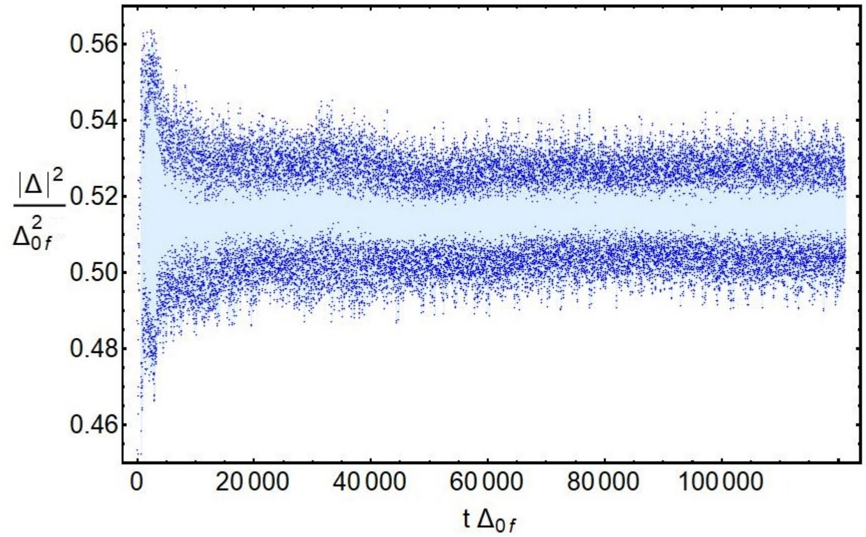

(b)

Figure 2.17: Darker blue points are local minima and maxima of the oscillations for the quenches from Fig. 2.16 for the entire time of the simulations. These plots suggest that there are regions of quasiperiodicity (Phase IV) in the quantum quench phase diagrams of nonintegrable pairing models. Part (a) is the same quench as in Fig. 2.16a, part (b) corresponds to Fig. 2.16b. In terms of the inverse level spacing, the time evolution goes out to $t_{\max} = 0.625\delta^{-1}$ in plot (a) and to $t_{\max} = \delta^{-1}$ in plot (b).

Appendix A

Mean-field equations of motion

The pseudospin equations of motion for the separable BCS model (2.6) obtain simply from the Heisenberg equations of motion $\frac{d}{dt}\hat{A} = i\,[\hat{H}, \hat{A}]$ applied to the mean-field $\hat{H}_f$ in Eq. (2.2) and the pseudospin operators $\hat{\mathbf{s}}$ defined in Eq. (2.5). The classical spin variables $\mathbf{s}$ are the expectation values of the pseudospin operators $\mathbf{s} = \langle \hat{\mathbf{s}} \rangle$, and the time-dependent order parameter Δ is determined self-consistently according to Eq. (2.7).

The generalized pseudospin representation of $\hat{H}_{so}$ from Eq. (2.1) requires more work [56]. First, we diagonalize the kinetic part of $\hat{H}_{so}$ through the following unitary transformation to new fermionic operators $\hat{a}_{\mathbf{k}\pm}$

$$\begin{aligned} &U_{\mathbf{k}} \begin{pmatrix} \hat{c}_{\mathbf{k}\uparrow} \\ \hat{c}_{\mathbf{k}\downarrow} \end{pmatrix} = \begin{pmatrix} \hat{a}_{\mathbf{k}+} \\ \hat{a}_{\mathbf{k}-} \end{pmatrix} \\ &U_{\mathbf{k}} = \begin{pmatrix} \cos\frac{\phi_k}{2} & -i\,e^{-i\theta_{\mathbf{k}}}\sin\frac{\phi_k}{2} \\ \sin\frac{\phi_k}{2} & i\,e^{-i\theta_{\mathbf{k}}}\cos\frac{\phi_k}{2} \end{pmatrix}, \end{aligned} \tag{A.1}$$

where $\mathbf{k} = ke^{i\theta_{\mathbf{k}}}$ and ϕ_k is defined in terms of the model parameters in Eq. (2.3). One can check that the new elementary excitation energies are $\varepsilon_{\mathbf{k}\pm} \equiv \varepsilon_{\mathbf{k}} \mp R_{\mathbf{k}}$. Eq. (A.1) implies

$$\begin{aligned} \hat{c}_{-\mathbf{k}\downarrow}\hat{c}_{\mathbf{k}\uparrow} = & \frac{-i\,e^{i\theta_{\mathbf{k}}}}{2}\Big(\sin\phi_{\mathbf{k}}(\hat{a}_{-\mathbf{k}+}\hat{a}_{\mathbf{k}+} - \hat{a}_{-\mathbf{k}-}\hat{a}_{\mathbf{k}-}) + \\ & + \cos\phi_{\mathbf{k}}(\hat{a}_{\mathbf{k}-}\hat{a}_{-\mathbf{k}+} + \hat{a}_{\mathbf{k}+}\hat{a}_{-\mathbf{k}-}) + \\ & + \hat{a}_{\mathbf{k}+}\hat{a}_{-\mathbf{k}-} + \hat{a}_{-\mathbf{k}+}\hat{a}_{\mathbf{k}-}\Big). \end{aligned} \tag{A.2}$$

Upon summing over $\mathbf{k}$, the last two terms in parentheses cancel with momenta of opposite sign. Therefore, the interaction term of (2.1) in this new basis becomes

$$
\begin{aligned}
g\sum_{\mathbf{k}\mathbf{k}'}\hat{c}^{\dagger}_{\mathbf{k}\uparrow}\hat{c}^{\dagger}_{-\mathbf{k}\downarrow}\hat{c}_{-\mathbf{k}'\downarrow}\hat{c}_{\mathbf{k}'\uparrow} &= \frac{1}{g}\hat{\Delta}^{\dagger}\hat{\Delta}, \\
\hat{\Delta} &\equiv \frac{g}{2}\sum_{\mathbf{k}\lambda} e^{i\theta_{\mathbf{k}}}\Big(\lambda\sin\phi_{\mathbf{k}}\hat{a}_{-\mathbf{k}\lambda}\hat{a}_{\mathbf{k}\lambda} + \cos\phi_{\mathbf{k}}\hat{a}_{\mathbf{k}\lambda}\hat{a}_{-\mathbf{k}\bar{\lambda}}\Big),
\end{aligned}
\tag{A.3}
$$

and upon taking the mean-field approximation $\hat{c}^{\dagger}\hat{c}^{\dagger}\hat{c}\hat{c} \approx \langle\hat{c}^{\dagger}\hat{c}^{\dagger}\rangle\hat{c}\hat{c} + \hat{c}^{\dagger}\hat{c}^{\dagger}\langle\hat{c}\hat{c}\rangle - \langle\hat{c}^{\dagger}\hat{c}^{\dagger}\rangle\langle\hat{c}\hat{c}\rangle$, the interaction term becomes

$$
\begin{aligned}
\hat{\Delta}^{\dagger}\hat{\Delta} &\approx \Delta^{*}\hat{\Delta} + \Delta\hat{\Delta}^{\dagger} - \Delta^{*}\Delta, \\
\Delta &\equiv \langle\hat{\Delta}\rangle.
\end{aligned}
\tag{A.4}
$$

Neglecting the constant term $\Delta^{*}\Delta/g$, we arrive at the mean-field spin-orbit Hamiltonian $\hat{H}_{so}$ in the $\hat{a}$ basis found in (2.2). Similar to the separable BCS model, we now search for a set of quadratic fermionic operators whose equations of motion are closed. Define the following operators

$$
\begin{aligned}
\hat{S}^{z}_{\mathbf{k}\lambda} &= \frac{1}{2}\big(\hat{a}^{\dagger}_{\mathbf{k}\lambda}\hat{a}_{\mathbf{k}\lambda} + \hat{a}^{\dagger}_{-\mathbf{k}\lambda}\hat{a}_{-\mathbf{k}\lambda} - 1\big), \\
\hat{S}^{-}_{\mathbf{k}\lambda} &= \lambda\eta_{\mathbf{k}}\hat{a}_{-\mathbf{k}\lambda}\hat{a}_{\mathbf{k}\lambda}, \\
\hat{L}^{z}_{\mathbf{k}\lambda} &= -\frac{\lambda}{4}\big(\hat{a}^{\dagger}_{\mathbf{k}+}\hat{a}_{\mathbf{k}-} + \hat{a}^{\dagger}_{-\mathbf{k}+}\hat{a}_{-\mathbf{k}-} + \\
&\qquad + \hat{a}^{\dagger}_{\mathbf{k}-}\hat{a}_{\mathbf{k}+} + \hat{a}^{\dagger}_{-\mathbf{k}-}\hat{a}_{-\mathbf{k}+}\big), \\
\hat{L}^{-}_{\mathbf{k}\lambda} &= \frac{\eta_{\mathbf{k}}}{2}\big(\hat{a}_{\mathbf{k}+}\hat{a}_{-\mathbf{k}-} + \hat{a}_{\mathbf{k}-}\hat{a}_{-\mathbf{k}+}\big), \\
\hat{T}_{\mathbf{k}} &= \frac{i}{4}\big(-\hat{a}^{\dagger}_{\mathbf{k}+}\hat{a}_{\mathbf{k}-} - \hat{a}^{\dagger}_{-\mathbf{k}+}\hat{a}_{-\mathbf{k}-} + \\
&\qquad + \hat{a}^{\dagger}_{\mathbf{k}-}\hat{a}_{\mathbf{k}+} + \hat{a}^{\dagger}_{-\mathbf{k}-}\hat{a}_{-\mathbf{k}+}\big),
\end{aligned}
\tag{A.5}
$$

where $\eta_{\mathbf{k}} = e^{i\,\theta_{\mathbf{k}}} = -\eta_{-\mathbf{k}}$ and, as usual, $\hat{S}^{-} = \hat{S}^{x} - i\,\hat{S}^{y}$ and $\hat{L}^{-} = \hat{L}^{x} - i\,\hat{L}^{y}$.

One can check that $\hat{\mathbf{S}}_{\mathbf{k}\lambda}$, $\hat{\mathbf{L}}_{\mathbf{k}\lambda}$ and $\hat{T}_{\mathbf{k}}$ are Hermitian operators. There is reflection symmetry in $\mathbf{k}$-space: $\hat{A}_{-\mathbf{k}\lambda} = \hat{A}_{\mathbf{k}\lambda}$ for all operators $\hat{A}_{\mathbf{k}\lambda}$ in (A.5), as well as the following band symmetry for $\hat{\mathbf{L}}_{\mathbf{k}\lambda}$: $\hat{L}^{-}_{\mathbf{k}+} = \hat{L}^{-}_{\mathbf{k}-}$ and $\hat{L}^{z}_{\mathbf{k}+} = -\hat{L}^{z}_{\mathbf{k}-}$.

We apply the Heisenberg equations of motion to (A.5) and $\hat{H}_{so}$ from (2.2) and then take expectation values to arrive at the generalized pseudospin equations of motion (2.11). The time-dependent order parameter $\Delta = \langle\hat{\Delta}\rangle$ as a function of the new variables can be found in Eq. (2.12). The factor $\eta_{\mathbf{k}}$ does not appear in Eq. (2.11), implying that the dynamics preserve any radial symmetry found in the initial state. As all initial states considered in this work are radially symmetric, one can opt to label the generalized pseudospin variables by their single-particle energies rather than their momentum vector.

Appendix B

Integrable limit of spin-orbit quenches

The authors of Ref. [55] created a full nonequilibrium phase diagram of the spin-orbit model for quenches of the magnetic field $h_i \to h_f$ as a function of h_i and h_f. However, this phase diagram needs to be revised by running simulations to much longer times $t > \tau$, which, in particular, may modify the Phase II-III boundary [93]. The phase diagram of Ref. [55] is also missing the quasiperiodic Phase IV discovered in the present work.

In Ref. [56], an attempt was made to analyze interaction and external field quenches to the integrable limit $h_f = 0$, but mistakes led to an incorrect phase diagram for the interaction quenches. Here we correct those mistakes and generate a correct phase diagram.

When the external field h is set to zero, H_{so} from (2.14) becomes equivalent to the integrable s-wave model with a dispersion relation $\varepsilon_{\mathbf{k}\lambda} = \frac{k^2}{2} - \lambda\alpha k$. This becomes clear in the equations of motion (2.11) with $\cos\phi_k = 0$ and $\sin\phi_k = 1$, where the spin degrees of freedom $\mathbf{S}_{\mathbf{k}\lambda}$ decouple from the others and Δ depends only on $\mathbf{S}_{\mathbf{k}\lambda}$. In what follows, the initial state of the system will be the ground state for some $h_i \geqslant 0$ given by (2.20), and the Hamiltonian for $t \geqslant 0$ is

$$\begin{aligned} H &= \sum_{\mathbf{k}\lambda} 2\varepsilon_{k\lambda} S^z_{\mathbf{k}\lambda} - 2|\Delta|^2/g_f, \\ \Delta &= \frac{g_f}{2}\sum_{\mathbf{k}\lambda} S^-_{\mathbf{k}\lambda}, \quad \varepsilon_{\mathbf{k}\lambda} = \frac{k^2}{2} - \lambda\alpha k. \end{aligned} \tag{B.1}$$

We use the integrability of H to construct the exact phase diagram using a technique imported from Refs. [53] which we now summarize briefly. The analysis centers around a quantity $\mathbf{L}(u)$ called the Lax vector (not to be confused with the variables $\mathbf{L}_{\mathbf{k}\lambda}$)

$$\mathbf{L}(u) = -\frac{2}{g_f}\hat{\mathbf{z}} + \sum_{\mathbf{k}\lambda} \frac{\mathbf{S}_{\mathbf{k}\lambda}}{u - \varepsilon_{k\lambda}}. \tag{B.2}$$

The integrability of H follows from the fact that $L^2(u)$ is conserved by the time evolution for arbitrary u, which implies conservation of the $2N$ roots of $L^2(u)$, which we call u_j. As demonstrated in Ref. [53], each of the asymptotic nonequilibrium phases corresponds a unique number of isolated complex pairs of u_j in the continuum limit. Phase I corresponds to zero isolated u_j, Phase II corresponds to one pair, and Phase III corresponds to two pairs. As the u_j are constants of the motion, we can evaluate $L^2(u)$ at $t = 0$ to determine the number of isolated pairs of u_j and thus generate the phase diagram for a given h_i.

Let us first start with the case when $h_i = 0$ and we quench the interaction $g_i \to g_f$. In this case the ground state self-consistency relationship is

$$\frac{2}{g_{i,f}} = \sum_{\mathbf{k}\lambda} \frac{1}{2E_{\mathbf{k}\lambda}}, \quad E_{\mathbf{k}\lambda} = \sqrt{(\varepsilon_{\mathbf{k}\lambda} - \mu_{i,f})^2 + \Delta_{0i,f}^2}. \tag{B.3}$$

Using Eq. (B.3) along with the initial state given by Eq. (2.17), we find that the initial Lax vector has the form

$$\begin{aligned} \mathbf{L}(u) &= \left(\Delta_{0i} L_x(u),\, 0,\, (\mu_i - u)L_x(u) - \widetilde{\beta}\right), \\ L_x(u) &= \sum_{\mathbf{k}\lambda} \frac{1}{2(u - \varepsilon_{\mathbf{k}\lambda})E_{\mathbf{k}\lambda}}, \quad \widetilde{\beta} \equiv \frac{2}{g_f} - \frac{2}{g_i}. \end{aligned} \tag{B.4}$$

If $g_f = g_i$, i.e., the zero quench, then $\widetilde{\beta} = 0$ and the only complex pair of roots is $u_\pm = \pm i\,\Delta_{0i} + \mu$. This is the degenerate Phase II case, where $\Delta(t) = \Delta_{0i}$ identically. When $g_f \neq g_i$, $L^2(u) = 0$ implies

$$\sum_{\mathbf{k}\lambda} \frac{1}{(u - \varepsilon_{\mathbf{k}\lambda})\sqrt{(\varepsilon_{\mathbf{k}\lambda} - \mu_i)^2 + \Delta_{0i}^2}} = -\frac{2\widetilde{\beta}}{u - \mu_i \pm i\,\Delta_{0i}}. \tag{B.5}$$

We now construct the phase diagram shown in Fig. B.1 for the $h_i = h_f = 0$, $g_i \rightarrow g_f$ quenches in the spin-orbit model. As we will not utilize particle-hole symmetry, the chemical potential μ must be calculated from the fermion number Eq. (2.16), which in the present case reads

$$N_f = \sum_{\mathbf{k}\lambda} \bigg(-\frac{\varepsilon_{\mathbf{k}\lambda} - \mu}{2\sqrt{(\varepsilon_{\mathbf{k}\lambda} - \mu)^2 + \Delta_{0i}^2}} + \frac{1}{2} \bigg). \tag{B.6}$$

In the continuum limit, we have the following translation from sums over $\mathbf{k}\lambda$ to integrals over the continuum for arbitrary functions $F(\varepsilon_{\mathbf{k}\lambda})$

$$\begin{aligned} \sum_{\mathbf{k}\lambda} F(\varepsilon_{\mathbf{k}\lambda}) &= \frac{N}{W} \int_{-\varepsilon_b}^{W_-} F(x)\nu_\alpha(x)dx, \\ \nu_\alpha(x) &= \begin{cases} \frac{2}{\sqrt{1+x/\varepsilon_b}}, & -\varepsilon_b \leqslant x \leqslant 0 \\ 2, & 0 \leqslant x \leqslant W_+ \\ 1 - \frac{1}{\sqrt{1+x/\varepsilon_b}}, & W_+ \leqslant x \leqslant W_- \end{cases}, \\ \varepsilon_b \equiv \alpha^2/2,& \quad W_\lambda \equiv W - 2\lambda\sqrt{\varepsilon_b W}. \end{aligned} \tag{B.7}$$

Thus, the spin-orbit coupling α at $h = 0$ has the simple effect of introducing a peculiar density of states $\nu_\alpha(x)$ to the s-wave problem. Let $\widetilde{B} = \lim_{N\to\infty} \widetilde{\beta}/N$ and $n = \lim_{N\to\infty} N_f/N$, the latter of which is fixed for the entire phase diagram. For a given pair $(\Delta_{0f}, \Delta_{0i})$, we first solve for (μ_f, μ_i) and then for $\widetilde{B}$ through the following integral equations:

$$\begin{aligned} 2n &= \int_X \bigg(1 - \frac{x - \mu_{i,f}}{\sqrt{(x-\mu_{i,f})^2 + \Delta_{0i,f}^2}}\bigg), \\ 2\widetilde{B} &= \int_X \bigg(\frac{1}{\sqrt{(x-\mu_f)^2 + \Delta_{0f}^2}} - \frac{1}{\sqrt{(x-\mu_i)^2 + \Delta_{0i}^2}}\bigg), \\ \int_X (\cdot) &\equiv \frac{1}{W}\int_{-\varepsilon_b}^{W_-} (\cdot)\nu(x)dx. \end{aligned} \tag{B.8}$$

We then use $\widetilde{B}$ and μ_i as input for the following integral equation:

$$\int_X \frac{1}{(u-x)\sqrt{(x-\mu_i)^2+\Delta_{0i}^2}} = -\frac{2\widetilde{B}}{u-\mu_i \pm i\,\Delta_{0i}}, \tag{B.9}$$

which we solve for u. The number of complex pairs of roots to Eq. (B.9) determines which nonequilibrium phase the system enters.

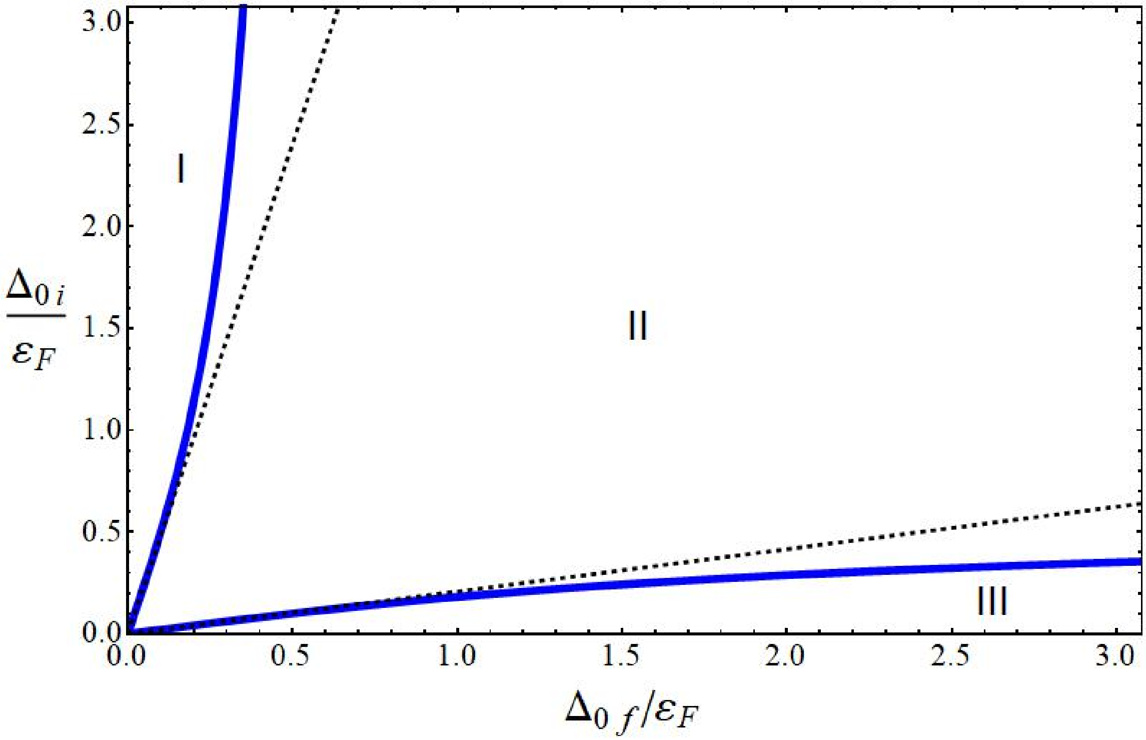

Figure B.1: Phase diagram for interaction quenches $g_i \to g_f$ in the integrable limit $h_f = h_i = 0$ of the spin-orbit model. Apart from the varying coupling constant g, the model parameters are the same as found in Fig. 2.2. The black dotted lines $\Delta_{0i} = e^{\pm\pi/2}\Delta_{0f}$ indicate the weak coupling limit ($\Delta \ll W$) phase boundaries [53]. The thick blue lines mark the true phase boundaries, which are characterized by the appearance of a new pair of complex roots of Eq. (B.9) when passing from Phase I to Phase II or Phase II to Phase III.

Quenches from $h_i \neq 0$ to $h_f = 0$ still undergo integrable dynamics, except now the initial state is no longer the s-wave ground state. We consider the behavior of the zeros of $L^2(u)$ with respect to h_i in the continuum limit with the spin-orbit parameters given in Fig. 2.2. The Lax vector is still as defined in Eq. (B.2), but we now enter the spin-orbit ground state (2.20) into the equation $L^2(u_j) = 0$, which implies $L^x(u_j) = \pm i\,L^z(u_j)$. The spin components of the $h_i \neq 0$ ground state are functions of the form $F_\lambda(\varepsilon_{\mathbf{k}})$ instead of $F(\varepsilon_{\mathbf{k}\lambda})$; we therefore do not use (B.7) for the continuum limit, but rather

$$\sum_{\mathbf{k}\lambda} F_\lambda(\varepsilon_{\mathbf{k}}) = \frac{N}{W}\int_0^W \Big(F_+(x) + F_-(x)\Big)dx. \tag{B.10}$$

The result of the root calculation is given in Fig. B.2, where we plot the absolute value of the imaginary part of each root pair. For small h_i, there is only one pair of complex roots, i.e., the asymptotic phase is Phase II. At a certain critical h_i, a second pair of complex roots appears, and the system enters Phase III. For larger h_i, the two pairs of roots merge into one and the system reenters Phase II. Phase I does not occur in $h_f = 0$ quenches for the parameters we used.

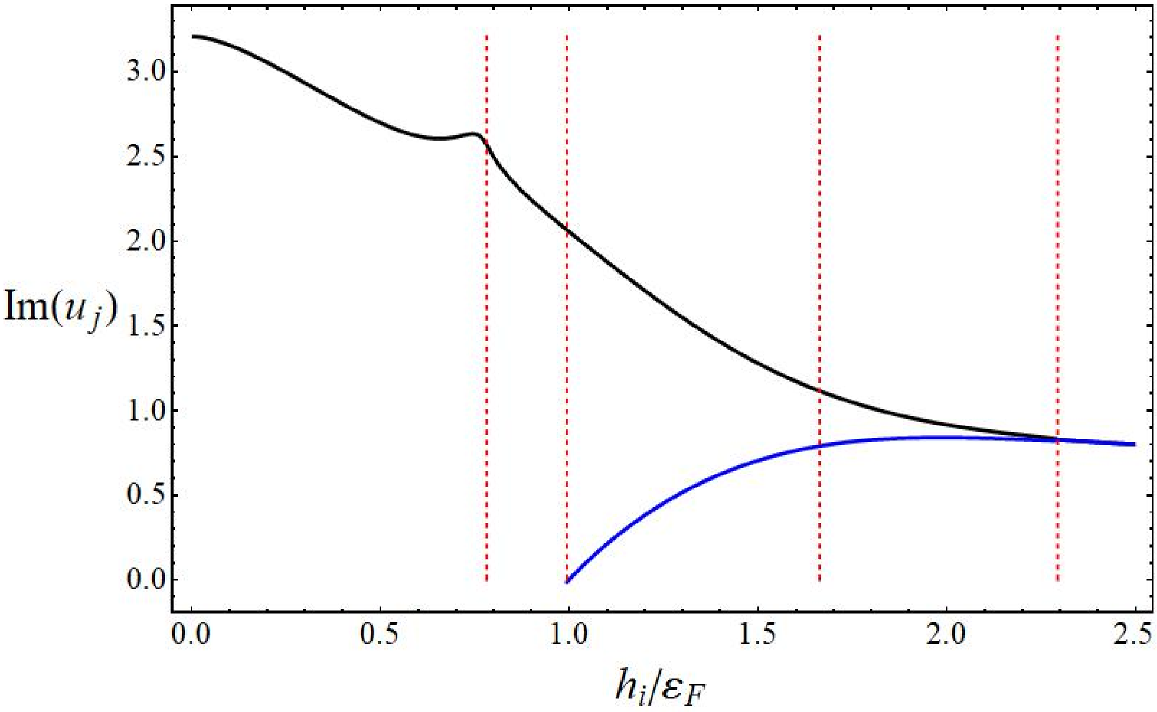

Figure B.2: Behavior of the roots of $L^2(u)$ for quenches from the ground state of $h_i \neq 0$ to $h_f = 0$ in the continuum limit with spin-orbit parameters as given in Fig. 2.2. Each solid line is the absolute value of the imaginary part of a pair of complex conjugate roots. Regions of h_i with one such line indicate that the asymptotic state is Phase II, while the region where there are two separate lines indicate Phase III. The vertical dashed lines indicate various critical values of h_i where the system undergoes a phase transition or crossover. From left to right, $h_1 = 0.7813\varepsilon_F$ is the topological transition of the ground state, $h_2 = 0.9938\varepsilon_F$ is a Phase II-III transition, $h_3 = 1.6625\varepsilon_F$ is the BCS-BEC crossover, and $h_4 = 2.2938\varepsilon_F$ is a Phase III-II transition which also appears to correspond to $\Delta_{0i} = 0$ being the only self-consistent initial equilibrium gap. These critical values of h_i depend in general on the various spin-orbit model parameters.

Appendix C

Integrability breaking forbids asymptotic reduction

An important property of the quench dynamics of integrable s and $(p+ip)$-wave Hamiltonians is the dynamical reduction in the number of degrees of freedom at $t \to +\infty$ in the thermodynamic limit [53, 54]. In particular, Phase III in these models corresponds to the motion of two collective classical spins $\mathbf{S}_1$ and $\mathbf{S}_2$ governed by a Hamiltonian of the same form. The asymptotic order parameter $\Delta(t)$ in Phase III coincides with that of the 2-spin problem. Further, there are special *reduced solutions* of equations of motion with the same $\Delta(t)$ that are of the form

$$\mathbf{s}_j = \alpha_j \mathbf{S}_1 + \beta_j \mathbf{S}_2 + \eta_j \hat{\mathbf{z}}, \tag{C.1}$$

where α_j, β_j and η_j are time-independent and $\hat{\mathbf{z}}$ is a unit vector along the z-axis. These observations lead to an analytical expression for $\Delta(t)$ and, moreover, help to construct the full asymptotic spin configuration in Phase III. We note also that, as we will see below, for the s-wave BCS model in the particle-hole symmetric case, (C.1) is equivalent to the ansatz of Ref. [37].

We will now show that the above reduction mechanism relies on integrability and breaks down for nonintegrable separable BCS models. We will prove two independent statements: (i) reduced solutions exist only when $f^2(x) = C_1 + C_2 x$, i.e. only when the Hamiltonian is integrable [61, 62] and (ii) $\Delta(t)$ for a 2-spin separable BCS Hamiltonian with an arbitrary choice of new $\varepsilon_{1,2}$, $f_{1,2}$ and g does not match the asymptotic $\Delta(t)$ we obtained in Sect. 5.3.

C.1 Existence of reduced solutions implies integrability and vice versa

We will follow the same steps as in the derivation of the 2-spin solutions in Ref. [53] and show that it only works for special choices of $f(x)$. First, we treat the general non-particle-hole symmetric case.

Let

$$\Delta = \Omega e^{-i\Phi}. \tag{C.2}$$

The 2-spin (reduced) Hamiltonian is

$$\begin{aligned} H_{\text{red}} &= \sum_{j=1}^{2} 2\widetilde{\varepsilon}_j S_j^z - \widetilde{g}\sum_{j,k} \widetilde{f}_j \widetilde{f}_k S_j^- S_k^+ = \\ &= \sum_{j=1}^{2} 2\widetilde{\varepsilon}_j S_j^z - \frac{|\Delta|^2}{\widetilde{g}}, \end{aligned} \tag{C.3}$$

where $\Delta = \widetilde{g}(\widetilde{f}_1 S_1^- + \widetilde{f}_2 S_2^-)$. We take both $\widetilde{f}_k$ to be nonzero, because otherwise the two spins simply decouple and rotate uniformly around the z-axis.

Energy and $S_1^z + S_2^z$ are conserved. Since there are two conservation laws and two degrees of freedom, H_{red} is integrable. For more than two spins, integrability persists only for special choices of $\widetilde{f}_k$. This fact alone already distinguishes the 2-spin problem from that of a generic N-spin separable BCS Hamiltonian.

Conservation of energy and $S_1^z + S_2^z$ read

$$\begin{aligned} 2\widetilde{\varepsilon}_1 S_1^z + 2\widetilde{\varepsilon}_2 S_2^z &= \widetilde{E} + \frac{\Omega^2}{\widetilde{g}}, \\ S_1^z + S_2^z &= \text{const}, \end{aligned} \tag{C.4}$$

We need $\widetilde{\varepsilon}_1 \neq \widetilde{\varepsilon}_2$ or $|\Delta|$ will be constant. We use Eq. (C.4) to express S_k^z in terms of Ω^2,

$$S_k^z = \widetilde{a}_k \Omega^2 + \widetilde{b}_k, \quad k = 1, 2; \tag{C.5}$$

where $\widetilde{a}_k$ and $\widetilde{b}_k$ are time-independent and $\widetilde{a}_1 = -\widetilde{a}_2 \neq 0$. Furthermore, Eq. (C.1) implies a similar expression for s_j^z in terms of the order parameter amplitude,

$$s_j^z = a_j \Omega^2 + b_j. \tag{C.6}$$

Conservation of the energy

$$E = \sum_j 2\varepsilon_j s_j^z - \frac{|\Delta|^2}{g}, \tag{C.7}$$

and of $J_z = \sum_j s_j^z$ require

$$\sum_j a_j = 0, \quad \sum_j 2\varepsilon_j a_j = \frac{1}{g}. \tag{C.8}$$

We write the Bloch equations for the separable BCS Hamiltonian as

$$\dot{s}_j^z = -i f_j (s_j^- \Delta^* - s_j^+ \Delta), \tag{C.9}$$

$$\dot{s}_j^- = -2i f_j s_j^z \Delta - 2i\varepsilon_j s_j^-. \tag{C.10}$$

Since the equations of motion and Eqs. (C.5) and (C.6) for the reduced solution and the 2-spin problem have the same form, we can treat both of them simultaneously.

Substituting Eq. (C.6) into Eq. (C.9), we find

$$s_j^- e^{i\Phi} - s_j^+ e^{-i\Phi} = 2i \frac{a_j}{f_j} \dot{\Omega}. \tag{C.11}$$

Next, we multiply Eq. (C.10) by $e^{i\Phi}$ and add the resulting equation to its complex conjugate,

$$\frac{d}{dt}\left(s_j^- e^{i\Phi} + s_j^+ e^{-i\Phi}\right) = \frac{4a_j\varepsilon_j}{f_j}\dot{\Omega} - 2\frac{a_j}{f_j}\dot{\Phi}\dot{\Omega}, \tag{C.12}$$

where we made use of Eq. (C.11). Integrating and adding the resulting equation and Eq. (C.11), we obtain

$$s_j^- e^{i\Phi} = \frac{2a_j\varepsilon_j}{f_j}\Omega - \frac{a_j}{f_j}A + i\frac{a_j}{f_j}\dot{\Omega} + \frac{a_j c_j}{f_j}, \tag{C.13}$$

where $\frac{a_j c_j}{f_j}$ is the integration constant and $A = \int dt \dot{\Phi}\dot{\Omega}$. The self-consistency condition $\Delta = g\sum_j f_j s_j^-$, combined with Eq. (C.8), implies $\sum_j a_j c_j = 0$.

The analogous expressions for the 2-spin problem are

$$S_k^- e^{i\Phi} = \frac{2\widetilde{a}_k\widetilde{\varepsilon}_k}{\widetilde{f}_k}\Omega - \frac{\widetilde{a}_k}{\widetilde{f}_k}A + i\frac{\widetilde{a}_k}{\widetilde{f}_k}\dot{\Omega} + \frac{\widetilde{a}_k\widetilde{c}_k}{\widetilde{f}_k}, \tag{C.14}$$

and $\widetilde{a}_1\widetilde{c}_1 + \widetilde{a}_2\widetilde{c}_2 = \widetilde{a}_1(\widetilde{c}_1 - \widetilde{c}_2) = 0$. Therefore, $\widetilde{c}_1 = \widetilde{c}_2$ and the last term in Eq. (C.14) can be absorbed into A, which is defined up to a constant anyway, i.e.,

$$S_k^- e^{i\Phi} = \frac{2\widetilde{a}_k\widetilde{\varepsilon}_k}{\widetilde{f}_k}\Omega - \frac{\widetilde{a}_k}{\widetilde{f}_k}A + i\frac{\widetilde{a}_k}{\widetilde{f}_k}\dot{\Omega}. \tag{C.15}$$

Since s_j^- is related to S_1^- and S_2^- via Eq. (C.1), this also eliminates the last term in Eq. (C.13), i.e.,

$$s_j^- e^{i\Phi} = \frac{2a_j\varepsilon_j}{f_j}\Omega - \frac{a_j}{f_j}A + i\frac{a_j}{f_j}\dot{\Omega}. \tag{C.16}$$

Combining the conservation of the spin norm, $s_j^2 = (s_j^z)^2 + |s_j^-|^2$, with Eqs. (C.6) and (C.16), we derive the following differential equation for Ω:

$$(a_j\Omega^2 + b_j)^2 + \frac{(2a_j\varepsilon_j\Omega - a_jA)^2 + a_j^2\dot{\Omega}^2}{f_j^2} = s_j^2, \tag{C.17}$$

or, equivalently,

$$\begin{split}\dot{\Omega}^2 + f_j^2\Omega^4 + \Omega^2\left(2\frac{f_jb_j}{a_j} + 4\varepsilon_j^2\right) - 4\varepsilon_jA\Omega \\ + A^2 + \frac{f_j^2(b_j^2 - s_j^2)}{a_j^2} = 0.\end{split} \tag{C.18}$$

This equation implies, among other things, that A is a function of Ω. Indeed, consider a set of numbers x_j, such that $\sum_j x_j = 0$. Multiplying Eq. (C.18) by x_j and summing over j, we find

$$A\Omega = \lambda\Omega^4 + 2\mu\Omega^2 + \kappa, \tag{C.19}$$

where λ, μ and κ are real constants. Substituting this back into Eq. (C.18), we obtain

$$\frac{\dot{w}^2}{4} + \lambda^2 w^4 + (f_j^2 - 4\lambda\xi_j)w^3 + \left(\frac{2f_j b_j}{a_j} + 2\lambda\kappa + 4\xi_j^2\right) w^2 + \left(\frac{f_j^2(b_j^2 - s_j^2)}{a_j^2} - 4\kappa\xi_j\right) w + \kappa^2 = 0, \tag{C.20}$$

where $w = \Omega^2$ and $\xi_j = \varepsilon_j - \mu$. These equations are consistent only when the coefficients of powers of w are j-independent. In particular, we must have $f_j^2 = 4\lambda\xi_j + \text{const.}$, i.e.,

$$f_j^2 = C_1 + C_2\varepsilon_j, \tag{C.21}$$

where C_1 and C_2 are real constants. This is the most general form of f_j for which the separable BCS Hamiltonian (2.8) is known to be integrable [61, 62]. In particular, C_2=0 corresponds to the s-wave and $C_1 = 0$ to the $(p + ip)$-wave models. Conversely, when Eq. (C.21) holds and the separable Hamiltonian is therefore integrable, the j-independence of coefficients at w^2 and w determines a_j and b_j, and Eq. (C.20) means that $w = |\Delta|^2$ is a certain elliptic function of time.

C.2 Asymptotic $\Delta(t)$ does not match the 2-spin solution in nonintegrable cases

In Sect. 5.3 we numerically determined $\Delta(t)$ in two nonintegrable separable BCS Hamiltonians, see Eq. (2.46). Here we show that $\Delta(t)$ for the most general separable 2-spin Hamiltonian (C.3) cannot match Eq. (2.46).

Since $\Delta(t)$ in Eq. (2.46) is real, we take Δ in the 2-spin problem to be real as well, though we do not a priori assume particle-hole symmetry in the 2-spin problem. All we need is to specialize the derivation of the previous subsection to the case of real Δ. Then, the Bloch equations become

$$\begin{aligned}\dot{S}_j^z &= -2\widetilde{f}_j S_j^y \Delta,\\ \dot{S}_j^x &= -2\widetilde{\varepsilon}_j S_j^y,\\ \dot{S}_j^y &= 2\widetilde{\varepsilon}_j S_j^x + 2\widetilde{f}_j S_j^z \Delta.\end{aligned} \tag{C.22}$$

Substituting Eq. (C.5) into the first two equations of motion, we obtain

$$S_k^y = -\frac{\widetilde{a}_k}{\widetilde{f}_k}\dot{\Delta}, \tag{C.23}$$

and

$$S_k^x = \frac{2\widetilde{\varepsilon}_k \widetilde{a}_k}{\widetilde{f}_k}\Delta + \frac{\widetilde{a}_k \widetilde{c}_k}{\widetilde{f}_k}, \tag{C.24}$$

where $\frac{\widetilde{a}_k \widetilde{c}_k}{\widetilde{f}_k}$ is the integration constant. As before, the self-consistency condition $\widetilde{g}(\widetilde{f}_1 S_1^- + \widetilde{f}_2 S_2^-) = \Delta$ together with $\widetilde{a}_1 = -\widetilde{a}_2$ imply $\widetilde{c}_1 = \widetilde{c}_2 \equiv \widetilde{c}$, and the conservation of spin length $(S_k^x)^2 + (S_k^y)^2 + (S_k^z)^2 = S_k^2$ yields

$$\dot{\Delta}^2 + (2\widetilde{\varepsilon}_k \Delta + \widetilde{c})^2 + \left(\widetilde{f}_k \Delta^2 + \frac{\widetilde{b}_k \widetilde{f}_k}{\widetilde{a}_k}\right)^2 = \frac{S_k^2 \widetilde{f}_k^2}{\widetilde{a}_k^2}. \tag{C.25}$$

Equating the coefficients at different powers of Δ for $k = 1$ and 2, we find $\widetilde{c}(\widetilde{\varepsilon}_1 - \widetilde{\varepsilon}_2) = 0 \Rightarrow \widetilde{c} = 0$,

$$\widetilde{f}_1 = \widetilde{f}_2 \equiv \widetilde{f}, \tag{C.26}$$

and two more relationships that constrain $\widetilde{a}_k$ and $\widetilde{b}_k$. The constraint (C.26) is a consequence of the requirement that Δ be real. Now Eq. (C.25) is of the form

$$\dot{\Delta}^2 = -\widetilde{f}^2(\Delta^2 - \Delta_+^2)(\Delta^2 - \Delta_-^2). \tag{C.27}$$

This is the same as the equation for the asymptotic $\Delta(t)$ for the integrable s-wave BCS Hamiltonian in the particle-hole symmetric case up to rescaling $\Delta_{\text{new}} = \widetilde{f}\Delta$. This is not surprising because $\widetilde{f}_1 = \widetilde{f}_2 = \widetilde{f}$ and the factor of $\widetilde{f}^2$ in Eq. (C.3) can be absorbed into the coupling constant, $\widetilde{g}_{\text{new}} = \widetilde{f}^2\widetilde{g}$ resulting in an integrable s-wave BCS Hamiltonian for two spins with $\Delta_{\text{new}} = \widetilde{g}_{\text{new}}(S_1^- + S_2^-) = \widetilde{f}\Delta$. The solution of Eq. (C.27) is $\Delta(t) = \Delta_+ \text{dn}[\widetilde{f}\Delta_+(t-t_0), 1-\frac{\Delta_+^2}{\Delta_-^2}]$. As we saw in Sect. 5.3, in the nonintegrable case we find instead a more general differential equation Eq. (2.44) with the solution given by Eq. (2.46).

Appendix D

The link between Lax constructions and the stability analysis

As mentioned above, the separable BCS model is integrable when $f_j^2 = C_1\varepsilon_j + C_2$. Two important cases are the s-wave model where $f_j = 1$ and the $p + ip$ model where $f_j = \sqrt{\varepsilon_j}$. In past work [53, 54], integrability has been exploited to determine the nonequilibrium asymptotic phases through the use of Lax constructions. These techniques are useful for constructing phase diagrams, but the physical interpretation of the phase transitions is obscured by the use of exact solvability. We demonstrate here that the stability equation Eq. (2.42), which applies to the nonintegrable cases as well, both predicts the same transition points and clarifies the physical meaning of the Lax construction.

In the following, we will assume the quantities Z_j, Δ_∞ and μ_∞ are given. They are functions of the quench parameters Δ_{0i}, Δ_{0f}, the particle number N_f, and the Fermi energy ε_F.

D.1 Lax norms

In the s-wave model, the Lax vector is [53]

$$\mathbf{L}_s(u) = -\frac{\hat{\mathbf{z}}}{g_f} + \sum_j \frac{\mathbf{s}_j}{u - \varepsilon_j}, \tag{D.1}$$

while in the $p + ip$ model its components are [54]

$$\begin{aligned} L_p^+(u) &= \sum_j \frac{\sqrt{\varepsilon_j} s_j^+}{u - \varepsilon_j}, \\ L_p^-(u) &= \sum_j \frac{\sqrt{\varepsilon_j} s_j^-}{u - \varepsilon_j}, \\ L_p^z(u) &= \sum_j \frac{\varepsilon_j s_j^-}{u - \varepsilon_j} - \frac{1}{g_f}, \end{aligned} \tag{D.2}$$

where u is a complex (spectral) parameter.

We focus on the norms of these quantities, defined as $L^2(u) = L_x^2(u) + L_y^2(u) + L_y^2(u)$ in the s-wave case and $L_2(u) = uL^+(u)L^-(u) + [L^z(u)]^2$ for $p + ip$. Integrability follows from the fact that the $L^2(u)$ and $L_2(u)$ are conserved by the time evolution for arbitrary u, which implies conservation of their roots u_j. As demonstrated in Refs. [53] and [54] and discussed in Appendix B, each of the asymptotic nonequilibrium phases corresponds a unique number of isolated complex pairs of u_j in the continuum limit. Phase I corresponds to zero isolated u_j, Phase II corresponds to one pair, and Phase III corresponds to two pairs.

The main result of this Appendix is that the roots of the Lax norm u and the frequencies ω of $\delta\Delta(t)$ are related by $u - u_r = \pm\frac{1}{2}\sqrt{\omega^2 - b_{\min}^2}$, where u_r is the real part of the root (cf. Refs. [42, 53]), and $b_{\min}$ is the band edge in the frequency spectrum ($b_{\min} = 0$ in Phase I). Thus, the new pair of complex conjugate Lax roots appears at the same time that ω emerges into the band gap (i.e., $\omega^2 < b_{\min}^2$ in Phase II and $\omega^2 < 0$ in Phase I). Here and below in this Appendix, we use the same notation u for the roots and for generic values of the spectral parameter.

One may plug into the Lax norms the asymptotic spin solution (2.31) for Phase II, but we shall use solutions that do not impose particle-hole symmetry. Letting $\widetilde{\varepsilon}_j = \varepsilon_j - \mu_\infty$, and noting that sums over the time-dependent terms dephase in the $t \to \infty$ limit, we find

$$\begin{aligned} L^2(u) &= \left(-\frac{1}{g_f} + \sigma_1\right)^2 + \Delta_\infty^2 \sigma_2^2, \\ \sigma_1 &\equiv \sum_j \frac{Z_j}{u - \varepsilon_j}, \quad \sigma_2 \equiv \sum_j \frac{Z_j}{\widetilde{\varepsilon}_j (u - \varepsilon_j)}, \\ L_2(u) &= \left(-\frac{1}{g_f} + p_1\right)^2 + u \Delta_\infty^2 p_2^2 \\ p_1 &\equiv \sum_j \frac{\varepsilon_j Z_j}{u - \varepsilon_j}, \quad p_2 \equiv \sum_j \frac{\varepsilon_j Z_j}{\widetilde{\varepsilon}_j (u - \varepsilon_j)}. \end{aligned} \tag{D.3}$$

Eq. (D.3) reduces to the Phase I Lax norms when $\Delta_\infty = 0$ and by convention $Z_j \to z_j$. In Phase II, Eq. (D.3) is supplemented by the self-consistency relationship

$$1 = -g_f \sum_j \frac{f_j^2 Z_j}{\widetilde{\varepsilon}_j}. \tag{D.4}$$

D.2 Phase I-II transition

In the s-wave case, and in Phase I, we compare the stability equation Eq. (2.42) to the vanishing of the Lax norm $L^2(u) = 0$. After some algebra, Eqs. (2.42) and $L^2(u) = 0$ become

$$\frac{1}{g_f} = \sum_j \frac{z_j}{\pm\frac{1}{2}\omega_0 + \mu_\infty - \varepsilon_j}, \tag{D.5a}$$

$$\frac{1}{g_f} = \sum_j \frac{z_j}{u - \varepsilon_j}, \tag{D.5b}$$

respectively. We argued in Sect. 5.2 that the Phase I-II transition occurs when a purely imaginary pair of complex conjugate ω_0 emerges as solutions to Eq. (D.5a), implying an exponential instability to Phase I. The Lax construction stipulates that the same transition occurs when an isolated pair of complex conjugate u solve Eq. (D.5b). In order for these two methods to match, we must make the identification $u - \mu_\infty = \pm\frac{1}{2}\omega_0$, i.e., the real part of the emergent Lax norm pair of roots must be μ_∞. We prove this is the case in Sect. D.4.

The corresponding equations for Phase I in the $p+ip$ model are

$$\frac{1}{g_f} = \sum_j \frac{\varepsilon_j z_j}{\pm\frac{1}{2}\omega_0 + \mu_\infty - \varepsilon_j}, \tag{D.6a}$$

$$\frac{1}{g_f} = \sum_j \frac{\varepsilon_j z_j}{u - \varepsilon_j}, \tag{D.6b}$$

and the same identification reconciles the two approaches.

D.3 Phase II-III transition

In Phase II, one applies the self-consistency relationship (D.4) to the Lax norms (D.3). In the s-wave case, $L^2(u) = 0$ becomes

$$0 = \big[(u-\mu_\infty)^2 + \Delta_\infty^2\big]\left(\sum_j \frac{Z_j}{\widetilde{\varepsilon}_j(u-\varepsilon_j)}\right)^2, \tag{D.7}$$

and we see the single pair of isolated conjugate roots are $u_\pm = \mu_\infty \pm i\Delta_\infty$. The equation for the second pair of isolated roots that would signal a transition to Phase III is therefore

$$0 = \sum_j \frac{Z_j}{\widetilde{\varepsilon}_j(u-\varepsilon_j)}. \tag{D.8}$$

After applying Eq. (D.4) to the quantities $S_j(\omega_0)$ in the stability equation (2.42), we find for the s-wave model

$$S_1(\omega) - 1 = \left(\frac{\omega^2}{4\Delta_\infty^2} - 1\right) S_3(\omega). \tag{D.9}$$

This simplifies Eq. (2.42) to

$$0 = \sum_j \frac{Z_j}{\widetilde{\varepsilon}_j(\pm y + \mu_\infty - \varepsilon_j)}, \quad y = \frac{1}{2}\sqrt{\omega^2 - 4\Delta_\infty^2}. \tag{D.10}$$

Matching (D.10) to (D.8), we make the correspondence $u - \mu_\infty = \pm\frac{1}{2}\sqrt{\omega_0^2 - 4\Delta_\infty^2}$. As we discussed in Sect. 5.2, an ω_0 emerging out of the continuum and into the band gap signals the transition to Phase III. The band edge in the s-wave model is precisely $2\Delta_\infty$. We show in Sect. D.4 that the new pair of conjugate Lax roots has real part μ_∞. Therefore, the two approaches predict the same phase transition.

In the $p + ip$ case, $L_2(u) = 0$ couples with (D.4) to give

$$0 = \left[u\Delta_\infty^2 + (u - \mu_\infty)^2\right]\left(\sum_j \frac{\varepsilon_j Z_j}{\widetilde{\varepsilon}_j(u - \varepsilon_j)}\right)^2. \tag{D.11}$$

The single pair of isolated roots of Phase II is then

$$u_\pm = u_c \pm i\Delta_\infty\sqrt{\mu_\infty - \frac{\Delta_\infty^2}{4}}; \quad u_c \equiv \mu_\infty - \frac{\Delta_\infty^2}{2}, \tag{D.12}$$

and the emergent pair of conjugate roots solves

$$0 = \sum_j \frac{\varepsilon_j Z_j}{\widetilde{\varepsilon}_j(u - \varepsilon_j)}. \tag{D.13}$$

To show that the stability analysis reproduces Eq. (D.13), we will need two relations. The first holds in general by applying the self-consistency relation (D.4) to the sums in (2.42)

$$\begin{aligned} S_1(\omega) - 1 &= \omega^2 S_4(\omega) - S_3(\omega), \\ S_4(\omega) &\equiv g_f \sum_j \frac{f_j^2 Z_j}{\widetilde{\varepsilon}_j(\omega^2 - \widetilde{b}_j^2)}, \end{aligned} \tag{D.14}$$

while the second is specific to the $p + ip$ model

$$S_2(\omega) = -2\omega\mu_\infty S_4(\omega) + \frac{\omega}{2\Delta_\infty^2} S_3(\omega). \tag{D.15}$$

We substitute Eqs. (D.14)-(D.15) into Eq. (2.42), which becomes a quadratic function of

S_3 and S_4. The solution is

$$0 = \sum_j \frac{Z_j}{\widetilde{\varepsilon}_j(\pm y + u_c - \varepsilon_j)}, \quad y = \frac{1}{2}\sqrt{\omega^2 - B_1^2}, \tag{D.16}$$

where $B_1 = \sqrt{4\mu_\infty \Delta_\infty^2 - \Delta_\infty^4}$ is the band edge when $u_c \geqslant 0$. In this parameter range, we identity $u - u_c = \pm\frac{1}{2}\sqrt{\omega^2 - B_1^2}$. We show in Sect. D.4 that the real part of the emergent Lax roots is u_c, and therefore the stability analysis and Lax constructions give the same Phase II-III transition. When $u_c < 0$, the band edge is no longer B_1, and we believe there to be no Phase II-III transition in that case.

D.4 Real parts of Lax roots at the transitions

The equivalence between the Lax construction and the stability analysis relies on the fact that the real parts of the emerging Lax roots are equal to μ_∞ at the Phase I-II transition in both integrable models, μ_∞ at the Phase II-III transition in the s-wave model, and $\mu_\infty - \frac{\Delta_\infty^2}{2}$ at the Phase II-III transition in the $p + ip$ model. In other words, the emergent second pair of isolated roots has the same real part as the first pair of isolated roots.

The Phase I-II transition real parts can be understood by a continuity argument. In the s-wave model, Eq. (D.7) implies that the single pair of roots can be written as $u_\pm = \mu_\infty \pm i\Delta_\infty$. As we approach the I-II boundary, Δ_∞ decreases continuously to zero, which implies the real part of both roots at the boundary is μ_∞. In the $p + ip$ case, a similar argument follows from Eq. (D.12).

s-wave, II-III

We use results from the spin reduction mechanism, discussed in Appendix C, of the s-wave model to obtain the real parts of the Lax roots at the Phase II-III transition. This discussion quotes several results directly from Sect. II B 3 of Ref. [53]. The isolated roots in Phase III of $L^2(u)$ are given by the roots of the 2-spin spectral polynomial [53] $Q_4(u)$

$$Q_4(u) = \left[(u-\mu)^2 - \rho\right]^2 - \kappa(u-\mu) - \chi. \tag{D.17}$$

We determine the real parameters μ, ρ, κ and χ at the transition, which will then give the roots of $Q_4(u)$. To do so, we use the differential equation and solution for the 2-spin Δ, which is identical to that of the Phase III asymptotic Δ of the many-body problem, which we write as $\Delta = |\Delta|e^{-i\Phi}$. Let $w = |\Delta|^2 = \Lambda^2 + h_1$, where h_1 is a constant. The differential equation for w is

$$0 = \dot{w}^2 + 4w^3 + 16\rho w^2 + 16\chi w + 4\kappa^2, \tag{D.18}$$

while the equation for the phase Φ is

$$\dot{\Phi} = 2\mu - \frac{\kappa}{\Lambda^2 + h_1}. \tag{D.19}$$

Upon rewriting (D.18) as an equation for Λ, we find

$$\dot{\Lambda}^2 = -(\Lambda_+^2 - \Lambda^2)(\Lambda_-^2 - \Lambda^2), \tag{D.20}$$

where the constants $\Lambda_\pm$ are the maximum and minimum of the Λ oscillations which are functions of the constants ρ, χ and κ. The solution of interest to Eq. (D.20) is

$$\Lambda = \Lambda_+ \mathrm{dn}\left[\Lambda_+(t-t_0), 1 - \frac{\Lambda_-^2}{\Lambda_+^2}\right]. \tag{D.21}$$

Near the II-III transition, the oscillations of Λ are small and it sufficient to keep only the first harmonic of Eq. (D.21)

$$\begin{aligned} &\Lambda \approx \Lambda_0 + \delta \cos\big[\omega_0(t-t_0)\big], \\ &\delta \ll \Lambda_0, \quad \omega_0 \approx 2\Lambda_0. \end{aligned} \tag{D.22}$$

As we approach the II-III transition, $\Delta \to \Delta_\infty e^{-2i\mu_\infty t}$. Because $|\Delta|^2 = \Lambda^2 + h_1$ has the same frequency as Λ^2, and the frequency of small oscillations of $|\Delta|^2$ at the II-III transition is $2\Delta_\infty$, we conclude $\Lambda_0 = \Delta_\infty$ and $h_1 = 0$. Using Eq. (D.19), we also find $\kappa = 0$ and $\mu = \mu_\infty$.

It remains to determine the constants ρ and χ, which we do by plugging (D.22) into (D.18) and considering the $\mathcal{O}(\delta^0)$ and $\mathcal{O}(\delta)$ terms separately. The result is $\rho = -\frac{\Delta_\infty^2}{2}$ and $\chi = \frac{\Delta_\infty^4}{4}$. The roots of the spectral polynomial $Q_4(u)$ from Eq. (D.17) at the Phase II-III transition therefore solve

$$0 = \left[(u-\mu_\infty)^2 + \frac{\Delta_\infty^2}{2}\right]^2 - \frac{\Delta_\infty^4}{4}. \tag{D.23}$$

One solution to (D.23) is $u_\pm = \mu_\infty \pm i\Delta_\infty$, which is the single isolated pair characteristic of Phase II. The other solution is a double root at $u = \mu_\infty$, i.e., the new pair of roots that emerges in Phase III has real part μ_∞.

$p + ip$, II-III

In order to prove that the Lax construction and stability analysis predict the same $p + ip$ Phase II-III transition, we needed to assume that the real part of the emerging second pair of roots equals that of the first pair of roots $u_\pm$ from (D.12). Using results from Ref. [54], we now show that this is indeed the case.

For brevity, our derivation will use the conventions of Ref. [54], where the definitions of some quantities differ by numerical factors. One redefines $\varepsilon \to 2\varepsilon$, $2G \to g$, $\sqrt{2}\Delta \to \Delta$

and $u \to 2u$ in order to translate quantities from Ref. [54] to those in this work. While some details of the derivation depend on such conventions, the conclusion does not. We also assume $u_c \equiv \mathrm{Re}[u_\pm] \geqslant 0$, which is the parameter regime where we show the equivalence of the Lax construction and stability analysis for the $p + ip$ model.

Eq. (4.3) of Ref. [54] gives the isolated pair of roots in Phase II to be $u_\pm = u_c \pm 2iE_{\mathsf{min}}$, where E_{min} is the minimum of the asymptotic dispersion relation [see text below Eq. (5.29) in Ref. [54]]. According to Eq. (4.39) in Ref. [54] the frequency of small oscillations in Phase III close to the Phase II-III boundary is

$$\Omega_c = \sqrt{(u_{\mathfrak{r}} - u_c)^2 + 4E_{\mathsf{min}}^2}, \tag{D.24}$$

where $u_{\mathfrak{r}}$ is the real part of the pair of roots absent in Phase II. The frequency Ω_c should match the frequency of dephasing oscillations in Phase II close to the boundary. The text below Eq. (3.53) in Ref. [54] says that the latter frequency is

$$\Omega = 2E_{\mathsf{min}}. \tag{D.25}$$

Setting $\Omega_c = \Omega$, implies that on the Phase II-III boundary

$$u_{\mathfrak{r}} = u_c. \tag{D.26}$$

Bibliography

[1] T. Kinoshita, T. Wenger, and D. S. Weiss, A quantum Newton's cradle, Nature **440**, 900 (2006).

[2] H. Lignier, C. Sias, D. Ciampini, Y. Singh, A. Zenesini, O. Morsch, and E. Arimondo, Dynamical Control of Matter-Wave Tunneling in Periodic Potentials, Phys. Rev. Lett. **99**, 220403 (2007).

[3] S. Hofferberth, I. Lesanovsky, B. Fischer, T. Schumm, and J. Schmiedmayer, Non-equilibrium coherence dynamics in one-dimensional Bose gases, Nature **449** 324 (2007).

[4] C. N. Weiler, T. W. Neely, D. R. Scherer, A. S. Bradley, M. J. Davis, and B. P. Anderson, Spontaneous vortices in the formation of Bose-Einstein condensates, Nature **455**, 948 (2008).

[5] A. Widera, S. Trotzky, P. Cheinet, S. Fölling, F. Gerbier, I. Bloch, V. Gritsev, M. D. Lukin, and E. Demler, Quantum Spin Dynamics of Mode-Squeezed Luttinger Liquids in Two-Component Atomic Gases, Phys. Rev. Lett. **100**, 140401 (2008).

[6] M. Gring, M. Kuhnert, T. Langen, T. Kitagawa, B. Rauer, M. Schreitl, I. Mazets, D. Adu Smith, E. Demler, and J. Schmiedmayer, Relaxation and Prethermalization in an Isolated Quantum System, Science **337**, 1318 (2012).

[7] T. Langen, S. Erne, R. Geiger, B. Rauer, T. Schweigler, M. Kuhnert, W. Rohringer, I. E. Mazets, T. Gasenzer, and J. Schmiedmayer, Experimental observation of a generalized Gibbs ensemble, Science **348**, 207 (2015).

[8] Y. Tang, W. Kao, K.-Y. Li, S. Seo, K. Mallayya, M. Rigol, S. Gopalakrishnan, and

B. L. Lev, Thermalization near Integrability in a Dipolar Quantum Newton's Cradle, Phys. Rev. X **8**, 021030 (2018).

[9] M. A. Norcia, R. J. Lewis-Swan, J. R. K. Cline, B. Zhu, A. M. Rey, J. K. Thompson, Cavity-mediated collective spin-exchange interactions in a strontium superradiant laser, Science **361**, 259 (2018).

[10] S. Smale, P. He, B. A. Olsen, K. G. Jackson, H. Sharum, S. Trotzky, J. Marino, A. M. Rey, J. H. Thywissen, Observation of a Dynamical Phase Transition in the Collective Heisenberg Model, arXiv:1806.11044 (2018).

[11] T. Kampfrath, K. Tanaka, K. A. Nelson, Resonant and nonresonant control over matter and light by intense terahetz transients, Nat. Phot. **7**, 680 (2013).

[12] C. Giannetti, M. Capone, D. Fausti, M. Fabrizio, F. Parmigiani and D. Mihailovic, Ultrafast optical spectroscopy of strongly correlated materials and high-temperature superconductors: a non-equilibrium approach, Adv. Phys. **65**, 58 (2016).

[13] D. Fausti, R. I. Tobey, N. Dean, S. Kaiser, A. Dienst, M. C. Hoffmann, S. Pyon, T. Takayama, H. Takagi and A. Cavalieri, Light-induced superconductivity in a stripe-ordered cuprate, Science **331**, 189 (2011).

[14] R. Matsunaga, Y. I. Hamada, K. Makise, Y. Uzawa, H. Terai, Z. Wang and R. Shimano, Higgs amplitude mode in the BCS superconductors $\mathrm{Nb}_{1-x}\mathrm{Ti}_x\mathrm{N}$ induced by terahertz pulse excitation, Phys. Rev. Lett. **111**, 057002 (2013).

[15] R. Matsunaga, N. Tsuji, H. Fujita, A. Sugioka, K. Makise, Y. Uzawa, H. Terai, Z. Wang, H. Aoki and R. Shimano, Light-induced collective pseudospin precession resonating with Higgs mode in a superconductor, Science **345**, 1145 (2014).

[16] H. Ribeiro, J. R. Petta, and G. Burkard, Interplay of charge and spin coherence in Landau-Zener-Stückelberg-Majorana interferometry, Phys. Rev. B **87**, 235318 (2013).

[17] P. Richerme, Z.-X. Gong, A. Lee, C. Senko, J. Smith, M. Foss-Feig, S. Michalakis, A. V. Gorshkov and C. Monroe, Non-local propagation of correlations in quantum systems with long-range interactions, Nature **511**, 198 (2014).

[18] L. Wang, C. Zhou, T. Tu, H.-W. Jiang, G.-P. Guo, and G.-C. Guo, Quantum simulation of the Kibble-Zurek mechanism using a semiconductor electron charge qubit, Phys. Rev. A **89**, 022337 (2014).

[19] R. Barends, L. Lamata, J. Kelly, L. García-Álvarez, A.G. Fowler, A. Megrant, E. Jeffrey, T. C. White, D. Sank, J.Y. Mutus *et. al.*, Digital quantum simulation of fermionic models with a superconducting circuit, Nature Comm. **6**, 7654 (2015).

[20] J. M. Nichol, S. P. Harvey, M. D. Shulman, A. Pal, V. Umansky, E. I. Rashba, B. I. Halperin, and Amir Yacoby, Quenching of dynamic nuclear polarization by spin-orbit coupling in GaAs quantum dots, Nature Comm. **6**, 7682 (2015).

[21] C. Song, K. Xu, W. Liu, C. Yang, S.-B. Zheng, H. Deng, Q. Xie, K. Huang, Q. Guo, L. Zhang *et. al.*, 10-Qubit Entanglement and Parallel Logic Operations with a Superconducting Circuit, Phys. Rev. Lett. **119**, 180511 (2017).

[22] H. Bernien, S. Schwartz, A. Keesling, H. Levine, A. Omran, H. Pichler, S. Choi, A. S. Zibrov, M. Endres, M. Greiner, V. Vuletić and M. D. Lukin, Probing many-body dynamics on a 51-atom quantum simulator, Nature **551**, 579 (2017).

[23] J. Zhang, G. Pagano, P. W. Hess, A. Kyprianidis, P. Becker, H. Kaplan, A. V. Gorshkov, Z.-X. Gong and C. Monroe, Observation of a many-body dynamical phase transition with a 53-qubit quantum simulator, Nature **551**, 601 (2017).

[24] A. Regal, M. Greiner, and D. S. Jin, Observation of Resonance Condensation of Fermionic Atom Pairs, Phys. Rev. Lett. **92**, 040403 (2004).

[25] M. W. Zwierlein, C. A. Stan, C. H. Schunck, S. M. F. Raupach, A. J. Kerman, and

W. Ketterle, Condensation of Pairs of Fermionic Atoms near a Feshbach Resonance, Phys. Rev. Lett. **92**, 120403 (2004).

[26] M. W. Zwierlein, J. R. Abo-Shaeer, A. Schirotyek, C. H. Schunck and W. Ketterle, Vortices and superfluidity in a strongly interacting Fermi gas, Nature **435**, 1047 (2005).

[27] I. Bloch, J. Dalibard and W. Zwerger, Many-body physics with ultracold gases, Rev. Mod. Phys. **80**, 885 (2008).

[28] S. Giorgini, L. P. Pitaevskii and S. Stringari, Theory of ultracold atomic Fermi gases, Rev. Mod. Phys. **80**, 1215 (2008).

[29] I. Bloch, J. Dalibard and S. Nascimbène, Quantum simulations with ultracold quantum gases, Nature Phys. **8**, 267 (2012).

[30] A. Polkovnikov, K. Sengupta, A. Silva and M. Vengalattore, *Colloquium*: Nonequilibrium dynamics of closed interacting quantum systems. Rev. Mod. Phys. **83**, 863 (2011).

[31] J. Eisert, M. Friesdorf, C. Gogolin, Quantum many-body systems out of equilibrium, Nature Phys. 11, 124 (2015).

[32] R. Vasseur and J. E. Moore, Nonequilibrium quantum dynamics and transport: from integrability to many-body localization, J. Stat. Mech. 064010 (2016).

[33] P. W. Anderson, Random-Phase Approximation in the Theory of Superconductivity, Phys. Rev. **112**, 1900 (1958).

[34] V. P. Galaiko, Kinetic Equations for Relaxation Processes in Superconductors, Sov. Phys. JETP **34**, 203 (1972).

[35] A. F. Volkov and S. M. Kogan, Collisionless relaxation of the energy gap in superconductors, Sov. Phys. JETP 38, 1018 (1974).

[36] Yu. M. Galperin, V. I. Kozub, and B. Z. Spivak, Stability of the nonequilibrium states of a superconductor with a finite difference between the populations of the electron and hole-like spectral branches, Sov. Phys. JETP **54**, 1126 (1981).

[37] R. A. Barankov, L. S. Levitov, and B. Z. Spivak, Collective Rabi Oscillations and Solitons in a Time-Dependent BCS Pairing Problem, Phys. Rev. Lett. **93**, 160401 (2004).

[38] M. Amin, E. Bezuglyi, A. Kijko, and A. Omelyanchouk, Wigner distribution function formalism for superconductors and collisionless dynamics of the superconducting order parameter, Low Temp. Phys. **30**, 661 (2004).

[39] E. A. Yuzbashyan, B. L. Altshuler, V. B. Kuznetsov, and V. Z. Enolskii, Solution for the dynamics of the BCS and central spin problems, J. Phys. A **38**, 7831 (2005).

[40] M. H. Szymanska, B. D. Simons, and K. Burnett, Dynamics of the BCS-BEC Crossover in a Degenerate Fermi Gas, Phys. Rev. Lett. **94**, 170402 (2005).

[41] E. A. Yuzbashyan, B. L. Altshuler, V. B. Kuznetsov, and V. Z. Enolskii, Nonequilibrium Cooper pairing in the nonadiabatic regime, Phys. Rev. B **72**, 220503(R) (2005).

[42] E. A. Yuzbashyan, O. Tsyplyatyev and B. Altshuler, Relaxation and persistent oscillations of the order parameter in fermionic condensates, Phys. Rev. Lett **96**, 097005 (2006).

[43] R. A. Barankov and L. S. Levitov, Synchronization in the BCS pairing dynamics as a critical phenomenon, Phys. Rev. Lett. **96**, 230403 (2006).

[44] E. A. Yuzbashyan and M. Dzero, Dynamical vanishing of the order parameter in a fermionic condensate, Phys. Rev. Lett. **96**, 230404 (2006).

[45] R. A. Barankov and L. S. Levitov, Excitation of the dissipationless Higgs mode in a fermionic condensate, arXiv:0704.1292 (2007).

[46] D. Pekker and C. M. Varma, Amplitude/Higgs modes in condensed matter physics, Ann. Rev. Cond. Mat. Phys. **6**, 269 (2015).

[47] A. Pashkin and A. Leitenstorfer, Particle physics in a superconductor, Science **345**, 1121 (2014).

[48] Y. Barlas and C. M. Varma, Amplitude or Higgs modes in *d*-wave superconductors, Phys. Rev. B. **87**, 054503 (2013).

[49] B. Nosarzewski, B. Moritz, J. K. Freericks, A. F. Kempter and T. P. Devereaux, Amplitude mode oscillations in pump-probe photoemission spectra from a *d*-wave superconductor, Phys. Rev. B **96**, 184518 (2017).

[50] S. Hannibal, P. Kettmann, M. D. Croitoru, A. Vagov, V. M. Axt and T. Kuhn, Quench dynamics of an ultracold Fermi gas in the BCS regime: Spectral properties and confinement-induced breakdown of the Higgs mode, Phys. Rev. A **91**, 043630 (2015).

[51] H. Krull, N. Bittner, G. S. Uhrig, D. Manske and A. P. Schnyder, Coupling of Higgs and Leggett modes in non-equilibrium superconductors, Nat. Comm. **7**, (2016).

[52] A. Moor, A. F. Volkov and K. B. Efetov, Amplitude Higgs mode and admittance in superconductors with a moving condensate, Phys. Rev. Lett. **118**, 047001 (2017).

[53] E. A. Yuzbashyan, M. Dzero, V. Gurarie and M. S. Foster, Quantum quench phase diagrams of an *s*-wave BCS-BEC condensate, Phys. Rev. A **91**, 033628 (2015).

[54] M. S. Foster, M. Dzero, V. Gurarie and E. A. Yuzbashyan, Quantum quench in a $p+ip$ superfluid: Winding numbers and topological states far from equilibrium, Phys. Rev. B **88**, 104511 (2013).

[55] Y. Dong, L. Dong, M. Gong and H. Pu, Dynamical phases in quenched spin-orbit-coupled degenerate Fermi gas, Nat. Comm. **6**, 6103 (2015).

[56] M. Dzero, A. A. Kirmani and E. A. Yuzbashyan, Nonadiabatic dynamics of superfluid spin-orbit-coupled degenerate Fermi gas, Phys. Rev. A **92**, 053626 (2015).

[57] F. Peronaci, M. Schiró and M. Capone, Transient dynamics of *d*-wave superconductors after a sudden quench, Phys. Rev. Lett. **115**, 257001 (2015).

[58] Not all three phases are necessarily present in a given model, e.g., there are models where Phase II [45] or Phase III [57] are absent, see also the discussion in Sect. 5.2

[59] M. Sato, Y. Takahashi, and S. Fujimoto, Non-Abelian topological order in s-wave superfluids of ultracold fermionic atoms, Phys. Rev. Lett. 103, 020401 (2009).

[60] M. Sato, Y. Takahashi, and S. Fujimoto, Non-Abelian topological orders and Majorana fermions in spin-singlet superconductors, Phys. Rev. B 82, 134521 (2010).

[61] R. W. Richardson, New Class of Solvable and Integrable Many-Body Models, arXiv:cond-mat/0203512 (2002).

[62] G. Ortiz, R. Somma, J. Dukelsky, and S. Rombouts, Exactly-solvable models derived from a generalized Gaudin algebra, Nucl. Phys. B **707**, 421 (2005).

[63] C. Dunning, M. Ibanez, J. Links, G. Sierra, and S.-Y. Zhao, Exact solution of the $p+ip$ pairing Hamiltonian and a hierarchy of integrable models, J. Stat. Mech. P08025 (2010).

[64] M. A. Rombouts, J. Dukelsky, and G. Ortiz, Quantum phase diagram of the integrable $p_x + ip_y$ fermionic superfluid, Phys. Rev. B **82**, 224510 (2010).

[65] I. Marquette and J. Links, Integrability of an extended $d+id$-wave pairing Hamiltonian, Nucl. Phys. B **866**, 378 (2013).

[66] V. Makhalov, K. Martiyanov and A. Turlapov, Observation of two-dimensional Fermi gas of atoms, Phys. Rev. Lett **105**, 030404 (2010).

[67] B. Fröhlich, M. Feld, E. Vogt, M. Koschorreck, W. Zwerger and M. Köhl, Radio-frequency spectroscopy of a strongly interacting two-dimensional Fermi gas, Phys. Rev. Lett. **106**, 105301 (2011).

[68] P. Dyke, E. D. Kuhnle, S. Whitlock, H. Hu, M. Mark, S. Hoinka, M. Lingham, P. Hannaford and C. J. Vale, Crossover from 2D to 3D in a weakly interacting Fermi gas, Phys. Rev. Lett. **106**, 105304 (2011).

[69] P. Wang, Z. Q. Yu, Z. Fu, J. Miao, L. Huang, S. Chai, H. Zhai and J. Zhang, Spin-orbit coupled degenerate Fermi gases, Phys. Rev. Lett. **109**, 095301 (2012).

[70] L. W. Cheuk, A. T. Sommer, Z. Hadzibabic, T. Yefsah, W. S. Bakr and M. W. Zwierlein, Spin-injection spectroscopy of a spin-orbit coupled Fermi gas, Phys. Rev. Lett. **109**, 095302 (2012).

[71] R. A. Williams, M. C. Beeler, L. J. LeBlanc, K. Jiménez-García and I. B. Spielman, Raman-induced interactions in a single-component Fermi gas near an *s*-wave Feshbach resonance, Phys. Rev. Lett **111**, 095301 (2013).

[72] Z. Fu, L. Huang, Z. Meng, P. Wang, L. Zhang, S. Zhang, H. Zhai, P. Zhang and J. Zhang, Production of Feshbach molecules induced by spin-orbit coupling in Fermi gases, Nature Phys. **10**, 110 (2014).

[73] V. Makhalov, K. Martiyanov and A. Turlapov, Ground-state pressure of quasi-2D Fermi and Bose gases, Phys. Rev. Lett. **112**, 045301 (2014).

[74] L. Huang, Z. Meng, P. Wang, P. Peng, S. L. Zhang, L. Chen, D. Li, Q. Zhou and J. Zhang, Experimental realization of two-dimensional synthetic spin-orbit coupling in ultracold Fermi gases, Nature Phys. **12**, 540 (2016).

[75] H. Zhai, Degenerate quantum gases with spin-orbit coupling: a review, Rep. Prog. Phys. **78**, 026001 (2015).

[76] A. A. Kirmani and M. Dzero, Short-time order parameter dynamics in $d + id$-wave fermionic superfluids, arXiv:1804.11257 (2018).

[77] One can choose the parameters differently in the two models, e.g., choose a different ε_F in the s-wave model, so that the first few oscillations almost coincide [76]. However, such fine-tuning seems unwarranted and, in any case, the longer-time dynamics will disagree.

[78] H. Kantz, A robust method to estimate the maximal Lyapunov exponent of a time series, Phys. Lett. A **185**, 77 (1994).

[79] J. D. Crawford, Introduction to bifurcation theory, Rev. Mod. Phys. **63**, 991 (1991).

[80] Y. A. Kuznetsov, *Elements of Applied Bifurcation Theory, Second Edition* (Springer-Verlag, 1998).

[81] R. C. Hilborn, *Chaos and Nonlinear Dynamics, An Introduction for Scientists and Engineers, Second Edition* (Oxford University Press, 2001).

[82] In equilibrium, i.e., when $g_f = g_i$, Eq. (2.67) is simply the BCS gap equation with two fixed points $\Delta = 0$ and $\Delta = \pm\Delta_{0i}$ corresponding to the normal and the BCS ground states, respectively.

[83] In the absence of particle-hole symmetry, Phase II is a simple limit cycle $\Delta_\infty e^{-2i\mu_\infty t}$ (circle in the plane of complex Δ). Phase III is a 2D (two fundamental frequencies) torus (annulus in the plane of complex Δ). Phase I-II and II-III transitions are then analogous to supercritical Hopf and Neimark-Sacker (torus) bifurcations.

[84] A. Patra, B. L. Altshuler and E. A. Yuzbashyan, Driven-Dissipative Dynamics of Atomic Ensembles in a Resonant Cavity: Nonequilibrium Phase Diagram and Periodically Modulated Superradiance, arXiv:1811.01515 (2018).

[85] A. Patra, B. L. Altshuler and E. A. Yuzbashyan, Chaotic Synchronization between Atomic Clocks, arXiv:1811.02148 (2018).

[86] E. A. Yuzbashyan, Normal and anomalous solitons in the theory of dynamical Cooper pairing, Phys. Rev. B 78, 184507 (2008).

[87] M. S. Foster, V. Gurarie, M. Dzero and E. A. Yuzbashyan, Quench-induced Floquet topological p-wave superfluids, Phys. Rev. Lett. **113**, 076403 (2014).

[88] E. A. Yuzbashyan and O. Tsyplyatyev, Dynamics of emergent Cooper pairing at finite temperatures, Phys. Rev. B **79**, 132504 (2009).

[89] M. Dzero, E. A. Yuzbashyan and B. L. Altshuler, Cooper pair turbulence in atomic Fermi gases, Eur. Phys. Lett. **85** 20004 (2009).

[90] M. S. Foster, E. A. Yuzbashyan and B. L. Altshuler, Quantum quench in 1D: Coherent inhomogeneity amplification and 'supersolitons', Phys. Rev. Lett. **105**, 135701 (2010).

[91] G.-W. Chern and K. Barros, Nonequilibrium dynamics of superconductivity in the attractive Hubbard model, arXiv:1803.04118 (2018).

[92] M. Dzero, E. A. Yuzbashyan, B. L. Altshuler, Comment on "Nonequilibrium dynamics of superconductivity in the attractive Hubbard model", arXiv:1806.03474 (2018).

[93] Note that Ref. [55] has a different convention of naming Phases I and III. The only example of Phase III $|\Delta(t)|$ dynamics shown in Ref. [55] is for the integrable case $h_f = 0$, when the long relaxation time τ is absent.

Chapter 3

Nonequilibrium transport in the Toda chain with harmonic pinning

1 Introduction

The transport of thermal energy in Hamiltonian systems is a problem of great theoretical and practical interest [1, 2]. In its simplest form, one considers heat flow in the nonequilibrium stationary state (NESS) of a system in contact with two thermal reservoirs at different temperatures. Very little is known rigorously about this problem except in the case of harmonic crystals [3] or hard rods in 1D [4]. These models are special cases of the larger class of integrable models, whose extensive numbers of conserved quantities are expected in general to lead to ballistic heat transport [5, 6, 7, 8]. This means that if a system of length N (and cross-section A) is put in contact with heat reservoirs at temperatures T_L and T_R, $T_L > T_R$, at its left and right ends, then the heat flow in the stationary state J would be (except for boundary effects) independent of N. This is what is observed for the Toda lattice and it stands in contrast to the case where we have dissipative transport satisfying Fourier's law, where J would be proportional to N^{-1}.

In the absence of exact results, one has to rely on heuristics and simulations. A large number of these have focused on 1D systems. These have led to the following commonly accepted truths (CAT): Integrable systems such as the Toda chain [10, 9, 5], the Calogero-Moser system, the harmonic chain, and hard rods have ballistic transport, i.e., $J \sim N^0$. Nonlinear non-integrable systems such as Fermi-Pasta-Ulam (FPU) chains [11] or the diatomic Toda chain [12] have $J \sim N^{-\alpha}$ with $\alpha < 1$, for the momentum conserving case: the actual value of α depends on the system. When a nonintegrable system does not conserve momentum due to pinning by a one body potential, the transport is diffusive, also called "normal", with $\alpha = 1$.

We find, via numerical simulations, that the Toda chain with harmonic pinning seemingly has ballistic transport of heat. Because this system is generally believed to be nonintegrable, either the prevailing wisdom about 1D transport needs modification or this system is in fact integrable. In either case, the result is rather surprising and requires further investigation. We note that the Poincaré sections of the 3-body case indicate that the dynamics take place on a 3-dimensional manifold for all tested initial conditions, indicating that there are 3 conserved quantities in this case (the first two being the Hamiltonian itself and a quantity corresponding to the harmonic motion of the center of mass). The surprising transport properties that we observe are similar to another recent study of different aspects of energy transport of the harmonically pinned Toda chain [13], which we briefly discuss at the end of this work. We also note that when the pinning is done by a quartic potential, then the heat transport is clearly not ballistic, although we cannot give clear evidence that $\alpha = 1$. We suspect the transport is indeed diffusive, as quartic pinning is sufficient to induce diffusive scaling in the harmonic chain [14].

2 The model

Consider a 1-dimensional chain of $N + 2$ labeled particles, i.e., located on the lattice $L = \{0, 1, ..., N, N + 1\}$, with the following classical Hamiltonian H

$$H = \sum_{i=0}^{N+1} \left[\frac{p_i^2}{2} + \frac{\nu^2}{z} q_i^z + V(r_i) \right], \quad r_i \equiv q_{i+1} - q_i, \quad z \text{ even.} \tag{2.1}$$

Here $\{q_i\}$ are the displacements of the particles, $\{p_i\}$ are their momenta, ν is the strength of the one-body pinning potential and $V_i \equiv V(r_i)$ is the interaction potential. For periodic boundary conditions $V_{N+1} = V(q_0 - q_{N+1})$ while for fixed boundary conditions $V_{N+1} = 0$

and $q_0 = q_{N+1} = p_0 = p_{N+1} = 0$. When $\nu = 0$ and

$$V_i = \frac{a}{b}\exp[-br_i], \quad a, b > 0, \tag{2.2}$$

the system is the Toda chain [15], which is a well-known integrable model for both periodic and fixed boundary conditions [16, 17]. Unless otherwise specified, V_i will refer to the Toda interaction for the remainder of this work.

In this note, we numerically investigate the heat transport properties of the fixed boundary Toda chain with the addition of an on-site harmonic potential, i.e., $\nu \neq 0$ and $z = 2$. In general, such a modification is expected to break the integrability of the $\nu = 0$ system when the number of particles is greater than 2. Indeed, the only obvious conserved quantities when $\nu \neq 0$ are H itself and the center of mass term h_c

$$h_c = \frac{1}{2}\left(\sum_{i=0}^{N+1} p_i\right)^2 + \frac{\nu^2}{2}\left(\sum_{i=0}^{N+1} q_i\right)^2. \tag{2.3}$$

We couple particles 1 and N of the chain to Langevin baths with a coupling constant μ, which act as thermal reservoirs at temperatures T_L and T_R and induce a nonequilibrium steady state (NESS). The infinitesimal generator of motion $\mathcal{L}$ is therefore

$$\begin{aligned}
\mathcal{L}(\cdot) &= \mu B_{1,T_L}(\cdot) + \mu B_{N,T_R}(\cdot) + \mathcal{A}(\cdot), \\
A(\cdot) &= \sum_{j=1}^{N}(p_{j+1} - p_j)\partial_{r_j} + \\
&\quad + \sum_{j=1}^{N}(V_j' - V_{j-1}' - \nu^2 q_j^{z-1})\partial_{p_j}, \\
B_{j,T_{L/R}}(\cdot) &= -p_j\,\partial_{p_j} + T\,\partial_{p_j}^2, \\
&\quad j = 1,\, N; \quad \mu = \text{ bath coupling,}
\end{aligned} \tag{2.4}$$

where $V_j' \equiv \frac{dV(r_j)}{dr_j}$. For systems like Eq. (2.4), the integrability of the bulk dynamics plays a central role in determining the transport properties [5], although in the quantum mechanical case this statement requires qualification [18]. The central quantity of interest is the average heat current J, which in the NESS is given by

$$J = \langle J_j \rangle = -\left\langle \frac{1}{2}(p_j + p_{j+1})V_j' \right\rangle, \quad j \in [2, N-1], \tag{2.5}$$

where $\langle\cdot\rangle$ refers to the NESS average, which in simulations is computed by first allowing the system sufficient time to relax to the NESS before time averaging. Also of interest is the NESS temperature profile T_j

$$T_j = \langle p_j^2 \rangle, \quad j \in [1, N]. \tag{2.6}$$

In the following, we will give evidence that when $z = 2$, $J \sim N^0$ and that T_j is independent of j in the bulk, with a jump in T_j at the reservoirs. These two properties are only expected to hold when the bulk dynamics are integrable. Indeed, because these bulk dynamics are expected to be nonintegrable and break translational invariance, one would expect $J \sim N^{-1}$ and T_j to be a continous curve interpolating between T_L and T_R. We then show that when the pinning is anharmonic, e.g., $z = 4$, then the system satisfies the ordinary expectations. Spurred by the unexpected harmonic pinning result, we then give further evidence of nondissipative behavior in this model. We caution that these numerical results are restricted to small systems ($N \leqslant 400$) and that further investigation is needed to determine the precise transport properties of this model.

3 Nondissipative behavior

3.1 Ballistic transport

Consider the dynamics Eq. (2.4) for the Toda interaction Eq. (2.2) and $z = 2$ (harmonic pinning). We integrate Eq. (2.4) using a velocity Verlet algorithm adapted to include the Langevin reservoirs [19]. In Fig. 3.1, we show the steady state temperature profiles for

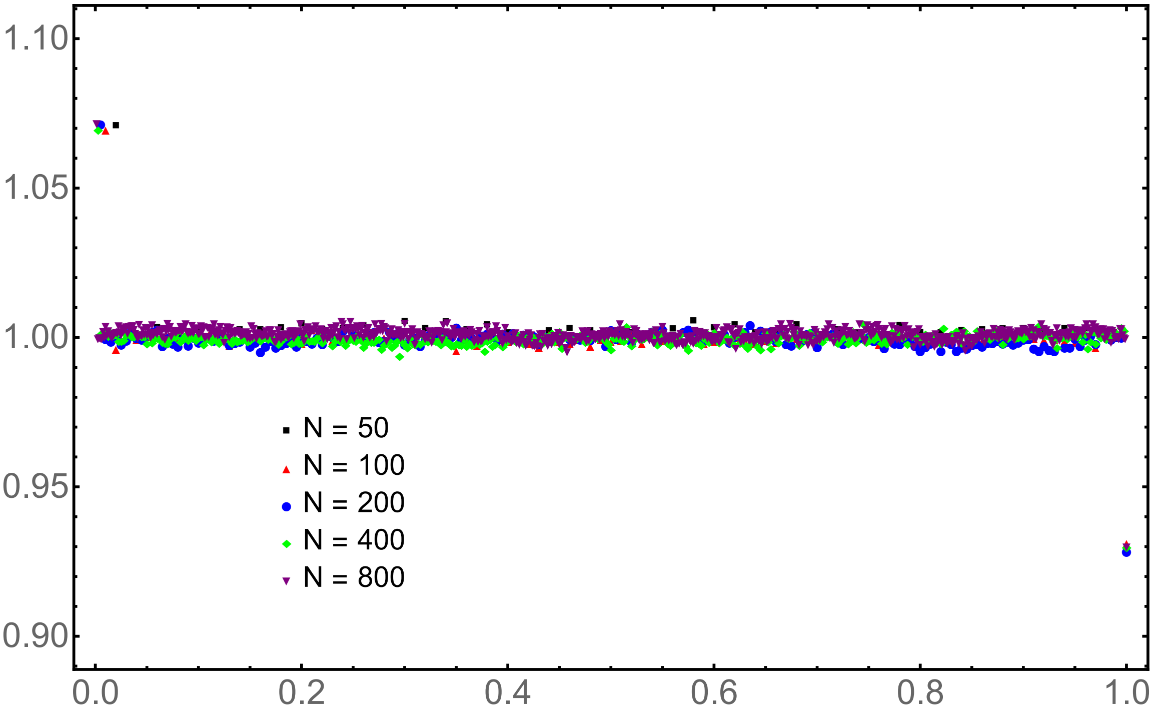

Figure 3.1: Temperature profiles ($T_L = 1.1$, $T_R = 0.9$) for the Toda chain with harmonic pinning ($a = b = \mu = \nu = 1$, $z = 2$). The j-th particle occupies position $x_j = j/N$. The ratios of the bulk currents are $J_{100}/J_{50} = 0.975$, $J_{200}/J_{100} = 1.001$, $J_{400}/J_{200} = 0.995$, and $J_{800}/J_{400} = 0.991$. We use the bulk current because its variance is reduced by averaging over the chain.

several N as well as the corresponding steady state heat current profiles given by Eq. (2.5). If we denote J_{Bulk} by the average of Eq. (2.5) over the entire bulk of the chain and $J_{L(R)}$ as the steady-state averages of the energy flux from the left (right) Langevin baths, we have

$$\begin{aligned} J_{\text{Bulk}} &= \frac{1}{N-2}\sum_{j=2}^{N-1}\langle J_j\rangle, \\ J_L &= \mu(T_L - \langle p_1^2\rangle), \\ J_R &= \mu(\langle p_N^2\rangle - T_R). \end{aligned} \tag{3.1}$$

We find numerically that the three currents from Eq. (3.1) agree quite closely.

The flat temperature profile and non-scaling current illustrated in Fig. 3.1 is expected for the $\nu = 0$ (integrable) case, but it is entirely surprising for $\nu \neq 0$. Upon varying ν we found that J is a decreasing function of ν, as expected for pinned chains [20]. We show a marked

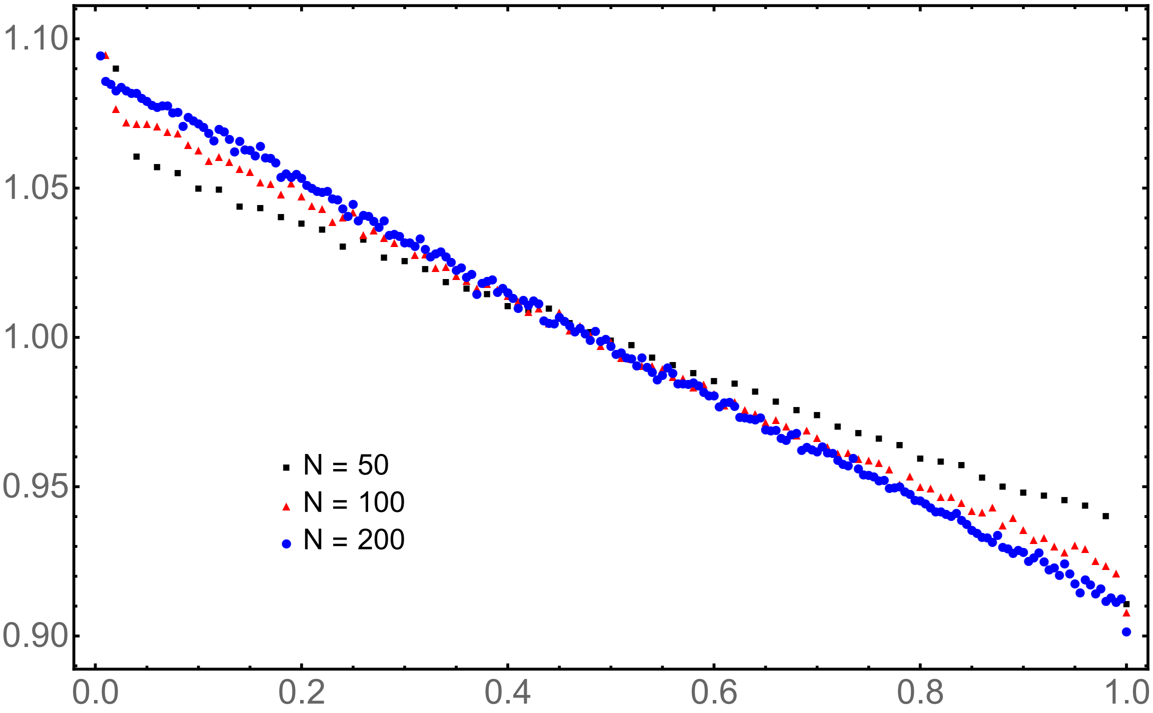

Figure 3.2: Temperature profiles and currents for the Toda chain with quartic pinning ($z = 4$), with all parameters the same as in Fig. 3.1. Note that with increasing N the profile approaches a smooth curve between $T_L = 1.1$ and $T_R = 0.9$. The ratios of the bulk currents are $J_{100}/J_{50} = 0.597$, $J_{200}/J_{100} = 0.564$, which hints that the system is starting to demonstrate diffusive scaling for relatively small N.

change in behavior in Fig. 3.2 for the Toda chain with quartic pinning ($z = 4$). There, as N increases, the temperature profiles approach a smooth curve interpolating between T_L and T_R, and the current J roughly halves when N is doubled.

It may be possible to analytically determine whether or not the heat conductivity of the harmonically pinned Toda chain is infinite using the methods developed in [21]. One can exploit the known underlying integrability of the unpinned Toda chain in order to obtain bounds on the conductivity when additional dynamics, such as pinning, are included. An infinite heat conductivity would mean that the current scales as $N^{-\alpha}$ for some $\alpha \geqslant 0$ that is strictly less than 1, where $\alpha = 0$ is the ballistic case.

3.2 Persistent heat currents in the periodic chain

Consider now the dynamics of the system with Hamiltonian 2.1, $z = 2$, and interaction 2.2 with periodic boundary conditions and no external driving. Given the observed ballistic heat transport in the corresponding driven system, one expects any initial heat current to propagate without dissipation in the periodic system. In Fig. 3.3, we observe such behavior in a 200 particle system for times long enough for the current to propagate many times around the chain. Similar nondissipative behavior in the harmonically pinned Toda chain with open boundary was numerically observed in [22]. In that context, the Toda potential Eq. (2.2) arises as an effective interaction between well-separated solitons of certain solutions of the Gross-Pitaevskii PDE, which models solitons in Bose-Einstein condensates [23, 24]. When the Toda chain was placed in a harmonic trap (which is mathematically identical to pinning each particle in the chain), a Toda soliton was observed to oscillate persistently like the spheres of a Newton's cradle. In diffusive systems, any initial current decays to thermal noise as exemplified in Fig. 3.3 when the Toda chain is subject to quartic pinning (z = 4).

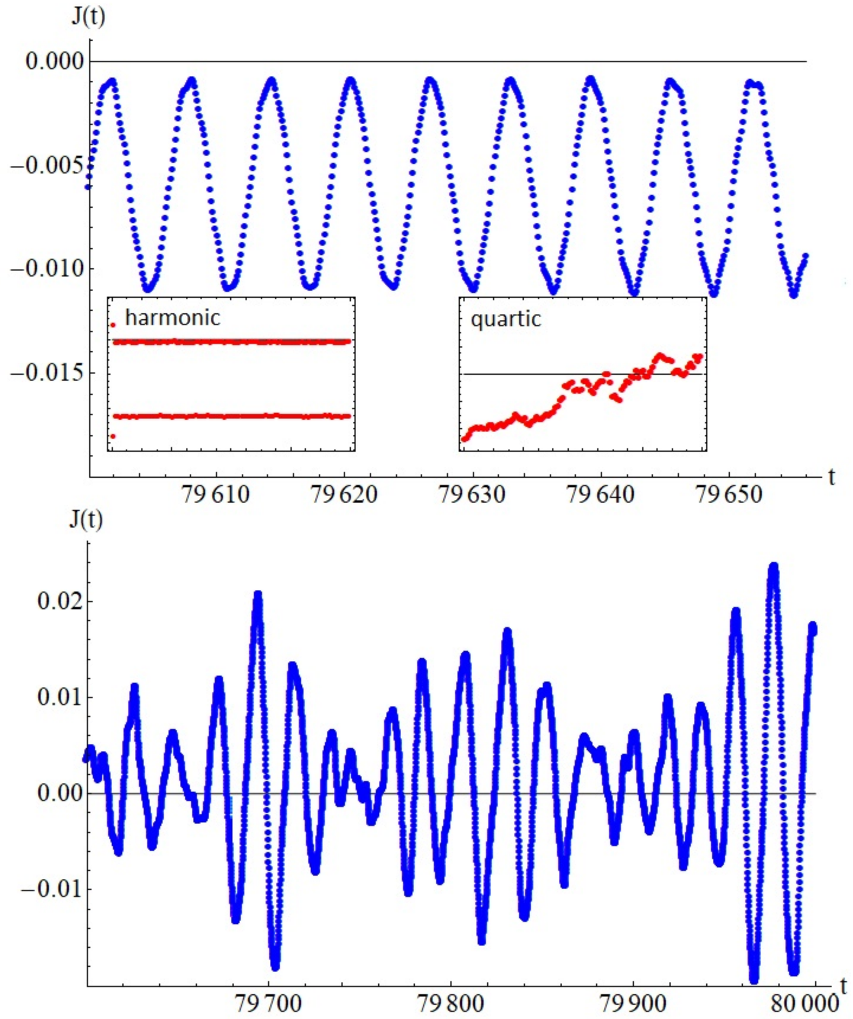

Figure 3.3: Initial and long time behavior of the persistent total current in the Toda chain from Eq. (2.1) and Eq. (2.2) ($a = b = 1$) with harmonic pinning (top, $z = 2$, $\nu = 1$) and quartic pinning (bottom $z = 4$, $\nu = 1$) and periodic boundary conditions, $N = 198$. The dominant frequency of the long time current in the harmonic case is very close to the value of the pinning frequency. The dynamics were integrated with a timestep of $dt = 10^{-4}$, and initial condition $q_0(0) = -1$, $p_1(0) = 1$, $q_2(0) = 1$, with all other initial coordinates and momenta zero. The same dynamics with $dt = 10^{-3}$ are nearly identical. Inserts: locally averaged maxima and minima of the current for the harmonic (left) and quartic (right) pinning cases for times $t \in [0, 8 \times 10^4]$. Note the decay of the current in the quartic pinning case.

3.3 Poincaré sections

The observations of Sec. 3.1 and Sec. 3.2 for $z = 2$ sharply contradict the CAT about the behavior for nonintegrable chains that break momentum conservation. On the other hand, it is possible that the Toda chain with harmonic pinning is in fact integrable. Indeed, the Calogero-Moser Hamiltonian remains integrable when harmonic pinning is added [25]. While it is highly unlikely that such a simple generalization of a well-known integrable model would have escaped notice for decades, we present dynamical evidence that a higher conservation law exists for 3 particle Toda chains with harmonic pinning. To do so, we construct Poincaré sections of the open chain dynamics, where the end particles are free to move. Each time the particle labeled "0" returns to its initial position, we record the momenta of all three particles. If the system were nonintegrable, the dynamics of the 3-body case would take place of a 4-dimensional manifold, for there are 6 degrees of freedom corresponding to the positions and momenta, and the conserved Hamiltonian and the conserved term h_c from Eq. (2.3) reduce this number to 6 - 2 = 4. By recording sections when $q_0 = q_0(0)$ and $p_j = p$ for either $j = 0$, 1 or 2, we therefore expect to obtain a 4 - 2 = 2 dimensional cross section of the dynamics. For all initial conditions we tested, however, such cross sections are 1-dimensional curves, indicating the presence of an additional conserved quantity. We illustrate this point in Fig. 3.4. If there exists a third conserved quantity that Poisson commutes with h_c, the 3-body case is integrable.

We emphasize that the mere existence of initial conditions that constrain the dynamics to lower dimensional manifolds is generic to nonintegrable models. If, however, *all* initial conditions lead to such constrained dynamics, as is the case for Liouville integrability, then it is quite likely that more conserved quantities exist. We tested several random initial conditions for the 3-body case.

After an initial draft of this work, we became aware of a recent work [13] in which the equipartition properties of an isolated Toda chain with harmonic pinning were studied. The authors initially excited the low frequency harmonic modes and found that for intermediate

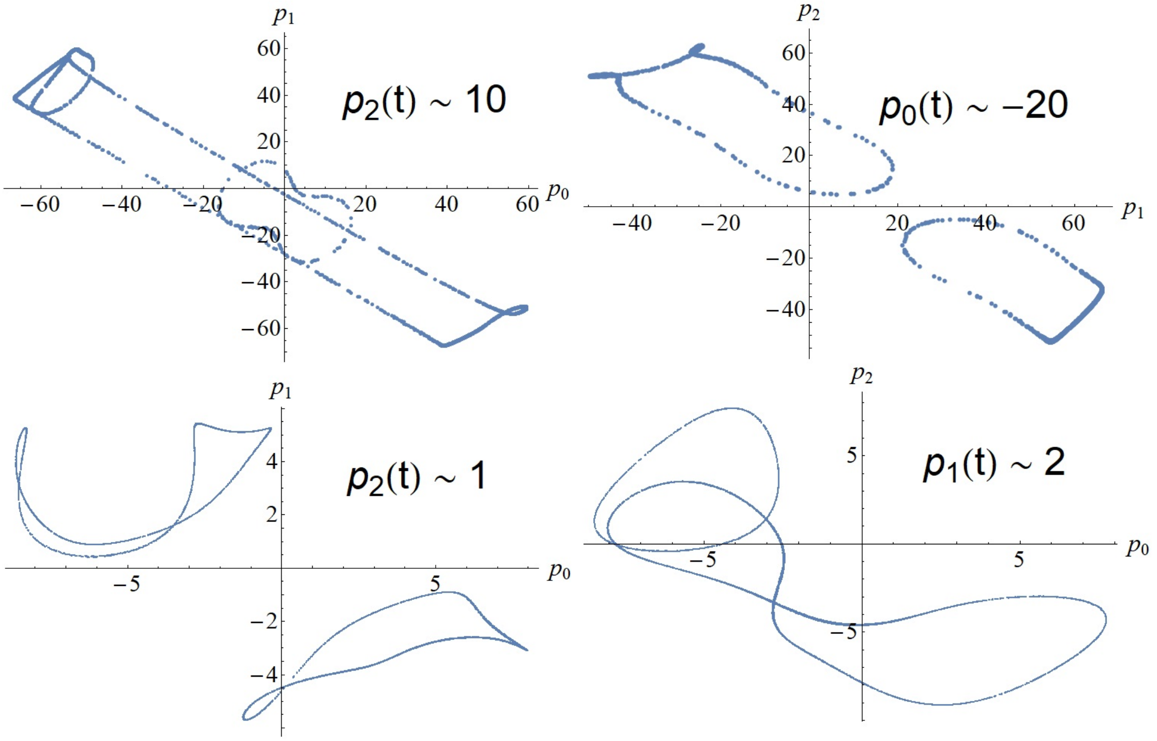

Figure 3.4: Poincaré sections for the 3-body open Toda chain ($a = b = 1$) with harmonic pinning ($z = 2$, $\nu = 1$). The four images correspond to two different runs (top, bottom) where the momenta p_j were recorded each time $q_0(t) \sim q_0(0)$ (within a tolerance of $\delta = 0.001$). Within each cross section is indicated which momentum is kept fixed and the corresponding value. The tolerance of the fixed momentum is adjusted to allow enough points to make the shape of the curves clear.

times the energy distribution across all modes evolves very little, which also happens for the integrable Toda chain. For very long times in the pinned chain, however, they find that higher modes become excited. This observation is taken as evidence that the pinned chain is not integrable, and that equipartition occurs only after extraordinarily long time scales. If this were the case, it would account for the very small amount of dissipation we observe with increasing N in Fig. 3.1, and the transport would not be ballistic. On the other hand, the distribution of harmonic modes necessarily changes for any anharmonic chain, integrable or not. Moreover, the authors of [13] note that despite the excitation of higher harmonic modes, nothing close to equipartition over any time scale is observed in the pinned chain.

If the harmonically pinned Toda chain is not integrable, recent developments in quantum integrability may offer insight into possible mechanisms for our observations. In Bethe ansatz solvable quantum models placed in external traps that break integrability, the untrapped integrability is responsible for a type of effective macroscopic integrability described by generalized hydrodynamics [27]. For continuous quasiparticle distributions, generalized hydrodynamics admits an infinity of conserved quantities for any external potential. Our observations for the classical pinned Toda chain may have their origins in a similar mechanism.

Acknowledgements: We are indebted to Abhishek Dhar and Aritra Kundu for providing independent verification of the flat temperature profile. We also thank Cédric Bernardin, Stefano Olla, Herbert Spohn, Ovidiu Costin, Rodica Costin and Panayotis Kevrekidis for very useful comments. JAS thanks Mitchell Dorrell for his generous computer programming guidance. The work of JLL was supported by AFOSR grant FA9550-16-1-0037. JAS was supported by a Rutgers University Bevier Fellowship.

Appendix A

Addendum

The original results of this work have been presented here, but in recent months the open-ended questions regarding the quadratically-pinned Toda chain have been partially answered [28, 29]. Ref. [28] found that the transport is indeed diffusive and the N-body chain nonintegrable due to a positive Lyapunov exponent, although the finite size effects are unusually strong and some solitonic-like excitations propagate well in the presence of the harmonic potential. In Ref. [29], Abhishek Dhar and Aritra Kundu improved upon our simulations presented here, and similarly found diffusive transport and a positive Lyapunov exponent. It turns out that the diffusive behavior is much easier to see at high temperatures, leading Ref. [29] to the conclusion that the seemingly-ballistic behavior is due to the quadratically pinned Toda chain behaving like a pinned harmonic chain for small oscillations. Fig. A.1 shows an emergent slope for high temperature nonequilibrium simulations.

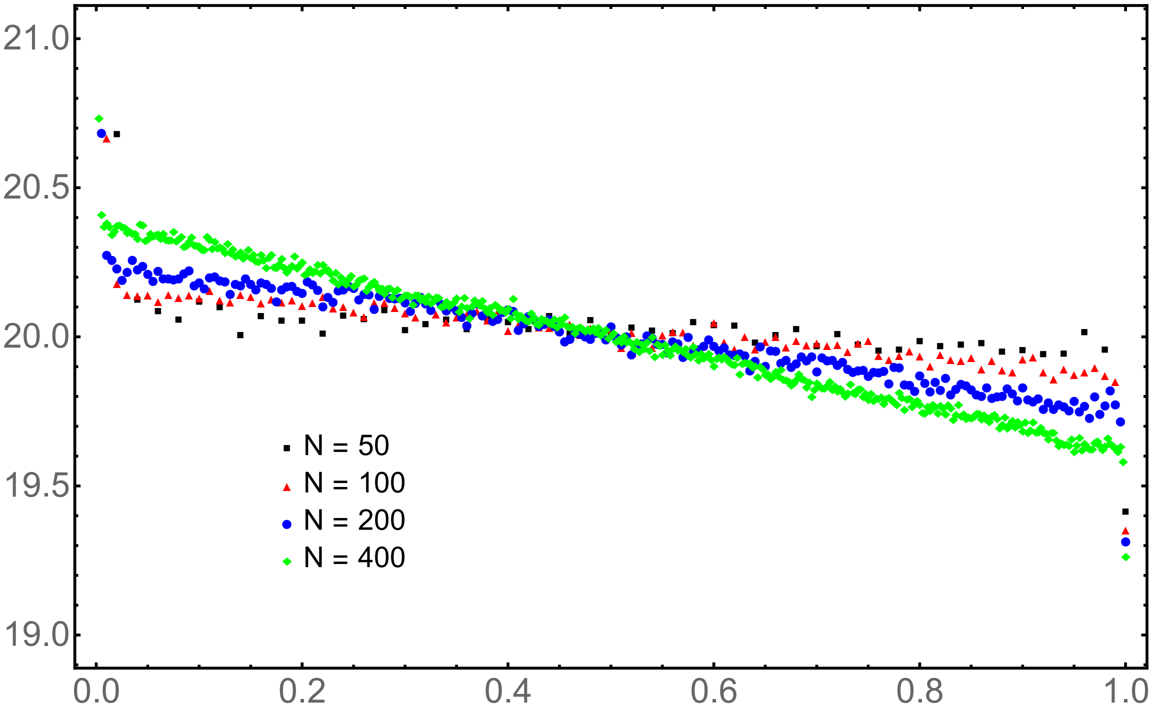

Figure A.1: Temperature profiles ($T_L = 21$, $T_R = 19$) for the Toda chain with harmonic pinning ($a = b = \mu = 1$, $\nu = 2$, $z = 2$). The j-th particle occupies position $x_j = j/N$. The ratios of the bulk currents are $J_{100}/J_{50} = 0.915$, $J_{200}/J_{100} = 0.862$, $J_{400}/J_{200} = 0.812$. The emergence of a nonzero slope and clear dissipation of the current with system size demonstrates that the transport is not ballistic.

Bibliography

[1] S. Lepri, ed. Thermal transport in low dimensions. Springer International Publishing, 2016.

[2] F. Bonetto, J. L. Lebowitz and L. Rey-Bellet, Fourier's law: a challenge for theorists, arXiv:math-ph/0002052.

[3] Z. Rieder, J. L. Lebowitz and E. Lieb, Properties of a harmonic crystal in a stationary nonequilibrium state, J. Math. Phys. **8**, 1073 (1967).

[4] H. Spohn. Large Scale Dynamics of Interacting Particles. Springer-Verlag, Berlin Heidelberg, 1991.

[5] X. Zotos, Ballistic transport in classical and quantum integrable systems, J. Low Temp. Phys. **126**, 1185 (2002).

[6] P. Mazur, Non-ergodicity of phase functions in certain systems, Physica **43**, 533 (1969).

[7] M. Suzuki, Ergodicity, constants of motion, and bounds for susceptibilities, Physica **51**, 277 (1971).

[8] A. Kundu and A. Dhar, Equilibrium dynamical correlations in the Toda chain and other integrable models, Phys. Rev. E **94**, 062130 (2016).

[9] M. Toda, Solitons and heat conduction, Phys. Scr. **20**, 424 (1979).

[10] B. S. Shastry and A. P. Young, Dynamics of energy transport in a Toda ring, Phys. Rev. B **82**, 104306 (2010).

[11] Focus Issue: The 'Fermi-Pasta-Ulam' problem - the first 50 years, Chaos **15** (2005).

[12] T. Hatano, Heat conduction in the diatomic Toda lattice revisited, Phys. Rev. E **59**, R1 (1999).

[13] Z. Zhang, C. Tang, J. Kang and P. Tong, Dynamical energy equipartition of the Toda model with additional on-site potentials, Chin. Phys. B **26**, 100505 (2017).

[14] K. Aoki, J. Lukkarinen and H. Spohn, Energy transport in weakly anharmonic chains, J. Stat. Phys. **124**, 1105 (2006).

[15] M. Toda, Waves in Nonlinear lattice, Supp. Prog. Theor. Phys. **45**, 174 (1970).

[16] M. Hénon, Integrals of the Toda lattice, Phys. Rev. B **9**, 1921 (1974).

[17] H. Flaschka, The Toda lattice II: existence of integrals, Phys. Rev. B **9**, 1924 (1974).

[18] J. Wu and M. Berciu, Heat transport in quantum spin chains: Relevance of integrability, Phys. Rev. B **83**, 214416 (2011).

[19] M. P. Allen and D. J. Tildesley. Computer Simulation of Liquids. Oxford University Press, New York, 1991.

[20] D. Roy and A. Dhar, Heat transport in ordered harmonic lattices, J. Stat. Phys. **131**, 535 (2008).

[21] C. Bernardin and S. Olla, Transport properties of a chain of anharmonic oscillators with random flip of velocities, J. Stat. Phys. **145**, 1224 (2011).

[22] M. Ma, R. Navarro, and R. Carretero-González, Solitons riding on solitons and the quantum Newton's cradle, Phys. Rev. E **93**, 022202, (2016).

[23] A. Weller, J. P. Ronzheimer, C. Gross, J. Esteve, M. K. Oberthaler, D. J. Frantzeskakis, G. Theocharis, and P. G. Kevrekidis, Experimental Observation of Oscillating and Interacting Wave Dark Solitons, Phys. Rev. Lett. **101**, 130401 (2008).

[24] M. P. Coles, D. E. Pelinovsky, and P. G. Kevrekidis, Excited states in the large density limit: a variational approach, Nonlinearity **23**, 1753 (2010).

[25] E. Corrigan and R. Sasaki, Quantum versus classical integrability in Calogero-Moser systems, J. Phys. A: Math. Gen. **35**, 7017 (2002).

[26] A. Dhar, private communication.

[27] J. S. Caux, B. Doyon, J. Dubail, R. Konik and T. Yoshimura, Hydrodynamics of the interacting Bose gas in the Quantum Newton Cradle setup, arXiv:1711.00873 (2017).

[28] P. Di Cintio, S. Iubini, S. Lepri and R. Livi, Transport in perturbed classical integrable systems: The pinned Toda chain, Chaos, Solitons & Fractals **117**, 249 (2018).

[29] A. Dhar, A. Kundu, J. L. Lebowitz and J. A. Scaramazza, Transport properties of the classical Toda chain: effect of a pinning potential, arXiv:1812.11770 (2018).

Chapter 4

Rotationally invariant ensembles of integrable matrices

1 Introduction

It is well established that random matrix theory (RMT) describes the universal features of energy spectra of various quantum systems [1, 2, 3, 4, 5, 6]. RMT does not, however, capture the typical behavior observed in exactly solvable many-body models, such as e.g. Poisson level statistics [7, 8, 9, 10, 11, 12, 13]. Though there exist matrix ensembles (e.g. band matrices [14, 15], or an invariant ensemble related to the thermodynamics of non-interacting fermions [16]) that display this kind of behavior, it is desirable to have a formulation that is both (i) basis-independent and (ii) stems from a well-defined notion of quantum integrability. The purpose of the present work is an explicit construction of ensembles that have both these properties, thereby bridging the gap and providing the missing ensemble – integrable matrix theory (IMT) – for the analysis of quantum integrability.

We recently proposed a simple notion of an integrable matrix (quantum integrability) that leads to an explicit construction of various classes of parameter-dependent commuting matrices [17, 18, 19, 20, 21]. In this approach, we consider $N\times N$ Hermitian matrices $H(u) = T + uV$ linear in a real parameter u. We call $H(u)$ integrable if it has at least one nontrivial (other than a linear combination of itself and the identity matrix) commuting partner of the form $\bar{H}(u) = \bar{T} + u\bar{V}$, i.e. $[H(u), \bar{H}(u)] = 0$ for all u. To appreciate the motivation behind this definition, consider exactly solvable many-body models such as the 1D Hubbard [22, 23, 24], XXZ spin chain [25, 26, 27, 28] or Gaudin magnets [29] in the presence of an external magnetic field [30, 31, 32]. Suppose we specialize to a particular number of sites and fix all quantum numbers corresponding to parameter-independent symmetries (e.g. number of spin up and down electrons, total momentum etc. in the case of the Hubbard model). Such blocks are integrable matrices under our definition. Indeed, they are linear in a real parameter (Hubbard U, anisotropy, the magnetic field) and all have at least one nontrivial integral of motion linear in the parameter. The Gaudin model has as many linear integrals as spins [30], while the Hubbard and XXZ models in general have at least one such nontrivial linear integral in addition to more with polynomial parametric dependence [33, 34, 35, 36].

Remarkably, it turns out that merely requiring the existence of commuting partners with fixed parameter-dependence leads to a range of profound consequences. First, it implies a categorization of integrable matrices according to the number of their integrals of motion. We say that $H(u)$ belongs to a type-M *integrable family* if there are exactly $n = N - M$ linearly independent $N \times N$ Hermitian matrices [37] $H^i(u) = T^i + uV^i$ that commute with $H(u)$ and among themselves at all u and have no common u-independent symmetry [38], i.e. no $\Omega \neq c\mathbb{1}$ such that $[\Omega, H^i(u)] = 0$ for all i and u. A type-M family is therefore an n-dimensional vector space, where $H^i(u)$ provide a basis, the general member of the family being $H(u) = \sum_i d_i H^i(u)$, where d_i are real numbers. The maximum possible value of n is $n = N - 1$ (type-1 or maximally commuting Hamiltonians), while a generic $H(u)$ (e.g. with randomly generated T and V) defines a trivial integrable family where $n = 1$.

Let us briefly recount further consequences of the commutation requirement and related developments. Integrable 3×3 matrices first appear in Ref. [17]. Shastry constructed a class of $N \times N$ commuting matrices [18] in 2005, which are type-1 in the above classification. Owusu et. al. [19] subsequently developed a transparent parametrization of type-1, an exact solution for their energy spectra, proposed the above notion of an integrable matrix, and proved that energy levels of any type-1 matrix cross at least once as functions of u. Later work parametrized [20] all type-2, 3 and a subclass of type-M for any $M > 3$. Let us also note the Yang-Baxter formulation [21] and eigenstate localization properties [39] for

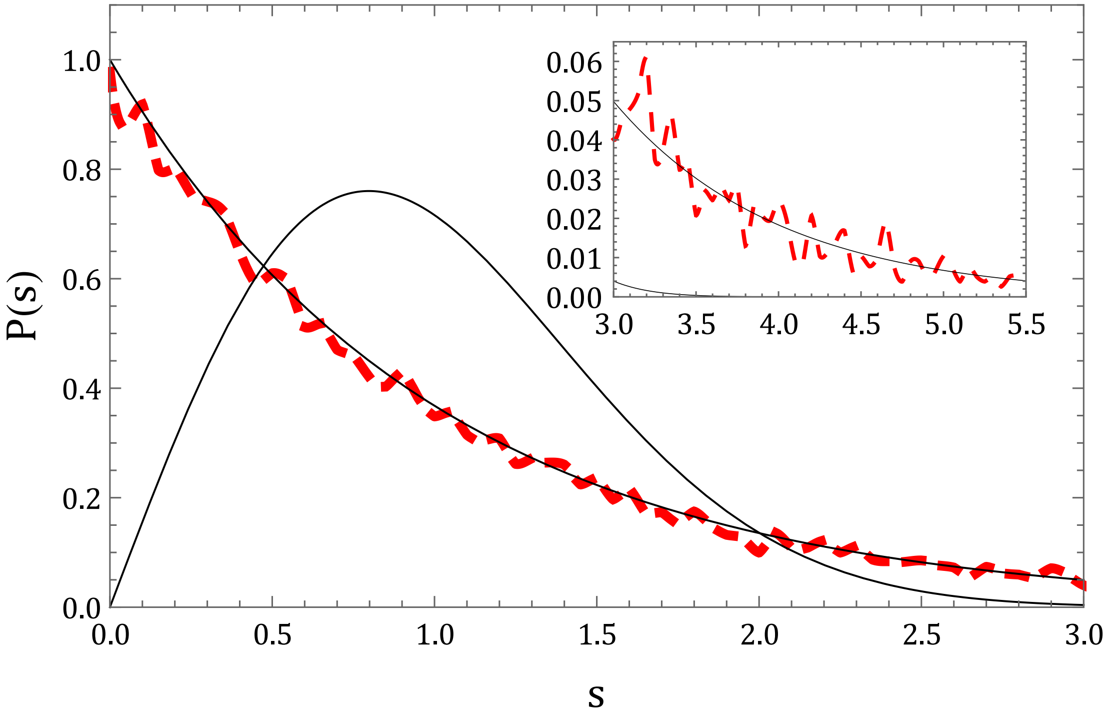

Figure 1.1: The normalized level spacing distribution $P(s)$ of a single 20000×20000 real symmetric integrable matrix $H(u) = T + uV$ at $u = 1$. This matrix, whose construction is detailed in Sect. 5, has exactly 297 nontrivial commuting partners (conservation laws) linear in the parameter u and is therefore type-19703 by our classification. The solid curves are a Poisson distribution $P(s) = e^{-s}$ and the Wigner surmise for real symmetric random matrices $P(s) = \frac{\pi}{2} s\, e^{-\frac{\pi}{4}s^2}$. Poisson level statistics, as shown here, are typical for the invariant integrable matrices described in this work. Inset: Tails of the same curves.

type-1.

However, existing parametrizations are tied to a particular basis, which prevents an unbiased choice of an integrable matrix and obscures the origin of the parameters. Recall that the invariance of the probability distribution with respect to a change of basis is a key requirement in RMT [2]. Similarly, a rotationally invariant formulation is necessary for a proper construction of integrable matrix *ensembles*. Here we first derive such a formulation and then obtain an appropriate probability distribution of *random integrable* matrices with a given number of integrals of motion. In a follow-up work [40] we will study level statistics of these ensembles as well as spectral statistics of individual integrable matrices, see Fig. 1.1 for an example.

More specifically, consider type-1 matrices in the parametrization of Ref. [19]. Up to an arbitrary shift by the identity matrix, a general real symmetric type-1 matrix $H(u) = T + uV$ reads

$$H(u) = \frac{1}{2}\sum_{k\neq j}\frac{d_k - d_j}{\varepsilon_k - \varepsilon_j}(\gamma_k\gamma_j p_{kj} - \gamma_j^2 p_k - \gamma_k^2 p_j) + u\sum_{k=1}^{N} d_k p_k, \tag{1.1}$$

where $d_k, \varepsilon_k, \gamma_k$ are $3N$ arbitrary real numbers, $p_{kj} = |k\rangle\langle j| + |j\rangle\langle k|$, $p_k = |k\rangle\langle k|$, and $|k\rangle$ are the normalized eigenstates of V (shared by all V^i). This expression immediately yields kj-th matrix element of $H(u)$ in the basis where V is diagonal. Parameters ε_k and γ_k specify the commuting family, while d_k pick a particular matrix within the family. Note that $H(u) = \sum_k d_k H^k(u)$, i.e. $H^k(u) = \frac{\partial}{\partial d_k}H(u)$ where $[H^j(u), H^k(u)] = 0$, $\forall j, k$. The question is, what is the natural choice of $d_k, \varepsilon_k, \gamma_k$? More precisely, what is the probability distribution function of these parameters? For example, we can take ε_k to be uncorrelated random numbers or eigenvalues of a random matrix from the Gaussian unitary, orthogonal or symplectic ensembles (GUE, GOE, or GSE). Moreover, it turns out that certain choices drastically affect the level statistics, e.g. those where d_k and ε_k are correlated [21, 40].

We will see below that each type-1 family is uniquely specified by a choice of a Hermitian matrix E and a vector $|\gamma\rangle$, ε_k and γ_k in Eq. (1.1) being the eigenvalues of E and components of $|\gamma\rangle$, respectively. On the same grounds as in RMT, an appropriate choice is therefore to take E from the GUE (GOE for real symmetric, GSE for Hermitian quaternion-real matrices [2]) and $|\gamma\rangle$ to be an appropriate random vector. Note that this choice follows from either rotational invariance of the distribution function combined with statistical independence of the matrix elements or, alternatively, from maximizing the entropy of the distribution [2]. Finally, d_k are the eigenvalues of V and we will show that they are distributed as GUE (GOE, GSE) eigenvalues uncorrelated with ε_k. Our construction of integrable matrix ensembles for higher types ($M > 1$) is restricted to the real symmetric case, is more complex and involves the deformation of an auxiliary type-1 family. However, it ultimately amounts to the same choice of $|\gamma\rangle$ and two matrices from the GOE.

2 Rotationally invariant construction of type-1 integrable matrix ensembles

We start with certain preliminary considerations valid for all types. The defining commutation requirement, $[H^i(u), H^j(u)] = 0$ for all u, reduces to three u-independent relations

$$[V^i, V^j] = 0, \quad [T^i, V^j] = [T^j, V^i], \quad [T^i, T^j] = 0. \tag{2.1}$$

The second of these relations is equivalent to

$$T^i = W^i + [V^i, S], \quad [V^i, W^i] = 0, \tag{2.2}$$

where S is an antihermitian matrix characteristic of the commuting (integrable) family. Note that S is independent of the element in the family, i.e. for any $H(u) = T + uV$ in the family, T and V are related through

$$T = W_V + [V, S], \quad [V, W_V] = 0, \tag{2.3}$$

with the same S.

Now we specialize to type-1. Since all T^i commute, they share the same eigenstates $|\alpha_k\rangle$ and therefore

$$T^i = \sum_{k=1}^{N} t_k^i |\alpha_k\rangle\langle\alpha_k|. \tag{2.4}$$

By definition of type-1, there are $N - 1$ linearly independent T^i. Together with $\mathbb{1} = \sum_k |\alpha_k\rangle\langle\alpha_k|$, we have N independent linear equations for N unknown projectors $|\alpha_k\rangle\langle\alpha_k|$ with a unique solution in terms of T^i for each $|\alpha_k\rangle\langle\alpha_k|$. Let $|\alpha_1\rangle \equiv |\gamma\rangle$ for notational convenience. Thus,

$$|\gamma\rangle\langle\gamma| = a_0\mathbb{1} + \sum_i a_i T^i, \tag{2.5}$$

where a_i are real numbers (real scalars in the quaternion case).

Consider an element of the commuting family $\Lambda(u) = a_0\mathbb{1} + \sum_i a_i H^i(u)$. By construction

$$\Lambda(u) = |\gamma\rangle\langle\gamma| + uE, \tag{2.6}$$

where E is an $N \times N$ Hermitian matrix with either complex, real, or quaternion real entries. Moreover, E is nondegenerate, for any degeneracies [41] in E imply a u-independent symmetry Ω (see Appendix A) contrary to the above definition of an integrable family. Every type-1 integrable family thus contains such a $\Lambda(u)$ given by Eq. (2.6) with a rank one T-part [42]. We will now show that the converse is also true. In other words, *any* $\Lambda(u)$ (i.e. an arbitrary choice of a vector $|\gamma\rangle$ and a nondegenerate Hermitian matrix E) uniquely specifies a type-1 family.

We begin with an arbitrary $\Lambda(u) = |\gamma\rangle\langle\gamma| + uE$ from which we will construct a type-1 integrable family of matrices $\{H^i(u)\}_\Lambda$. We require that $\Lambda(u)$, henceforth known as the “reduced Hamiltonian”, be an element of this putative family. Then Eq. (2.2) gives

$$|\gamma\rangle\langle\gamma| = W_E + [E, S], \quad [E, W_E] = 0. \tag{2.7}$$

Eq. (2.7) uniquely determines the matrix elements of S as a function of E and $|\gamma\rangle$. We then consider $H(u) = T + uV$ and impose $[\Lambda(u), H(u)] = 0$, $\forall u$, which implies (see Eq. (2.1) and Eq. (2.2))

$$\begin{aligned} &[V, E] = 0. \\ &T = W + [V, S], \quad [V, W] = 0, \\ &[T, |\gamma\rangle\langle\gamma|] = 0. \end{aligned} \tag{2.8}$$

The third equation implies $|\gamma\rangle$ is an eigenstate of T. Via a non-essential shift of T by a multiple of the identity we set the corresponding eigenvalue to zero, i.e. $T\,|\gamma\rangle = 0$. We will see that the choice of V in Eq. (2.8) uniquely specifies T, and therefore determines $H(u)$.

As E is nondegenerate, $\Lambda(u)$ has no permanent degeneracies (eigenvalues degenerate at all u) and therefore any $H^i(u)$ and $H^j(u)$ so constructed will satisfy $[H^i(u), H^j(u)] = 0$, $\forall u$.

We have thus constructed a type-1 integrable family $\{H^i(u)\}_\Lambda$ from an arbitrary reduced Hamiltonian $\Lambda(u) = |\gamma\rangle\langle\gamma| + uE$. But from the considerations at the beginning of this section, we know that *all* type-1 families contain a reduced matrix $\Lambda(u)$. It follows that our basis-independent construction, i.e. Eqs. (2.7-2.8), produces all type-1 matrices.

It is not immediately obvious from Eqs. (2.7-2.8) that a simple parametrization of matrix elements follows. It is therefore helpful to select a preferred basis and write them in components to demonstrate the feasibility of the construction. In the shared diagonal basis of the matrices E and V, Eq. (2.7) implies

$$S_{ij} = \frac{\gamma_i \gamma_j^*}{\varepsilon_i - \varepsilon_j}, \tag{2.9}$$

where $E = \mathrm{diag}(\varepsilon_1, \varepsilon_2, \ldots, \varepsilon_N)$ and γ_i are the components of $|\gamma\rangle$. The components γ_j are either complex, real, or quaternion real, corresponding to the three possibilites for the Hermitian matrix E. Therefore γ_j^* denotes complex conjugation in the first two cases and quaternion conjugation in the third case. Let $V = \mathrm{diag}(d_1, d_2, \ldots, d_N)$, then Eq. (2.8) gives

$$\begin{aligned} T_{ij} = H_{ij}(u) &= \gamma_i \gamma_j^* \frac{d_i - d_j}{\varepsilon_i - \varepsilon_j}, \quad i \neq j, \\ T_{ii} + uV_{ii} = H_{ii}(u) &= u\, d_i - \sum_{j \neq i} |\gamma_j|^2 \frac{d_i - d_j}{\varepsilon_i - \varepsilon_j}. \end{aligned} \tag{2.10}$$

Now consider the eigenvalue equation $\Lambda(u)|\varphi\rangle = u\lambda|\varphi\rangle$ for the reduced Hamiltonian,

$$|\gamma\rangle\langle\gamma|\varphi\rangle + uE|\varphi\rangle = u\lambda|\varphi\rangle, \tag{2.11}$$

where we introduced a factor of u for convenience. In components this yields

$$\varphi_k = \frac{\gamma_k}{u(\lambda - \varepsilon_k)} \langle \gamma | \varphi \rangle. \tag{2.12}$$

The "self-consistency" condition $\sum_k \gamma_k^* \varphi_k = \langle \gamma | \varphi \rangle$ then implies an equation for λ

$$u = \sum_{j=1}^{N} \frac{|\gamma_j|^2}{\lambda - \varepsilon_j}, \tag{2.13}$$

This equation has N real roots λ_i for $i = 1, \ldots, N$ that play a special role in the exact solution (and the analysis of level crossings) of type-1 Hamiltonians [19]. In particular, the eigenvalues η_i of $H(u)$ from Eq. (2.10) are

$$\eta_i = \sum_{j=1}^{N} \frac{|\gamma_j|^2 d_j}{\lambda_i - \varepsilon_j} = \langle \gamma | \, V \, | i \rangle, \tag{2.14}$$

and the corresponding unnormalized eigenstates $|i\rangle$ according to Eq. (2.12) read

$$|i\rangle_k \equiv \varphi_k^{(i)} = \frac{\gamma_k}{\lambda_i - \varepsilon_k}, \tag{2.15}$$

Note that these are the components of $|i\rangle \equiv |\varphi^{(i)}\rangle$ in the eigenbasis of V and that $u\lambda_i$ are the eigenvalues of the reduced Hamiltonian.

Finally, using Eqs. (2.7-2.8), one can show that if a family of commuting matrices $H^j(u)$ is Hermitian (real-symmetric, Hermitian quaternion-real) for all u, the corresponding matrices E and V^j are also Hermitian (real-symmetric, Hermitian quaternion-real) and the vector $|\gamma\rangle$ is complex (real, quaternion real) and vice versa. We will show next in Sect. 3 that these three choices correspond to selecting these objects from the GUE, GOE or GSE, respectively. Recall that, physically speaking, GUE matrices break time reversal invariance. GOE and GSE matrices are invariant under time reversal, while GSE matrices futhermore break rotational invariance and represent systems with half-integer spin [1, 2].

3 Probability density function of type-1 integrable ensemble

In Sect. 2, we found that any Hermitian type-1 integrable matrix is specified by the choice of a vector $|\gamma\rangle$ and two Hermitian matrices E and V satisfying $[E, V] = 0$. Consider the set of all type-1 $N \times N$ matrices as a random ensemble $\mathcal{H}_N^1(u)$ with a probability density function (PDF) $P(\gamma, E, V)$ on the parameters $|\gamma\rangle, E$ and V. The probability of obtaining a matrix $H(u) \in \mathcal{H}_N^1(u)$ characterized by parameters in the region between (γ, E, V) and $(\gamma + d\gamma, E + dE, V + dV)$ is $P(\gamma, E, V)\, d\gamma\, dE\, dV$, where

$$\begin{aligned} d\gamma &= \prod_{i=1}^{N} d\,\mathrm{Re}(\gamma_i)\, d\,\mathrm{Im}(\gamma_i), \\ dV &= \prod_{j<i} d\,\mathrm{Re}(V_{ij})\, d\,\mathrm{Im}(V_{ij}) \prod_{k} d\,V_{kk}. \end{aligned} \tag{3.1}$$

Here we derive a basis-independent $P(\gamma, E, V)$ in a manner similar to the construction of the PDF of the Gaussian RMT ensembles [2]. As indicated in Eq. (3.1), we will restrict our notation to complex Hermitian matrices. Matrices and vectors with quaternion entries have four real numbers associated to each off-diagonal matrix element and to each vector component. We find that the eigenvalues of E and V (the ε_i and d_i in Eq. (2.10)) come from independent GUE, GOE or GSE eigenvalue distributions $\Omega(a)$

$$\Omega(a) \propto \prod_{i<j} |a_i - a_j|^{\beta} e^{-\sum_k a_k^2}, \tag{3.2}$$

where $\beta = 2$, 1 and 4 for the GUE, GOE, and GSE, respectively. The eigenvalue sets are independent essentially because eigenvalues of a random matrix are independent of the eigenvectors, and the $[E, V] = 0$ requirement only constrains eigenvectors. The final expression for $P(\gamma, E, V)$ is Eq. (3.10), while the corresponding PDF for the parameters from Eq. (2.10), denoted $P(\gamma, \varepsilon, d)$, is Eq. (3.11).

There are two approaches to this derivation, both of which give the same result. First, one can maximize the entropy functional [2, 45],

$$S[P] = -\langle \ln(P) \rangle = -\int_X P(\gamma, E, V) \ln(P(\gamma, E, V)) d\gamma \, dE \, dV, \tag{3.3}$$

subject to constrained averages, where the set X includes all parameter values such that $|\gamma|^2 = 1$ and $[E, V] = 0$. The constrained averages in this case are $\langle 1 \rangle = 1$, $\langle \mathrm{Tr}\, E^2 \rangle = \langle \mathrm{Tr}\, V^2 \rangle = \alpha$, $\alpha \in \mathbb{R}^+$. Alternatively, one may postulate that $(|\gamma\rangle, E, V)$ are independent objects, each with its own PDF given by known results from RMT [2, 3] before projecting the product of these PDFs into the constrained space $[E, V] = 0$. We use the latter strategy in what follows.

As $|\gamma\rangle$ is independent of E and V, we have

$$P(\gamma, E, V) = P(\gamma) \, P(E, V). \tag{3.4}$$

The function $P(\gamma)$ is well known in RMT [3]

$$P(\gamma) \propto \delta \left(1 - |\gamma|^2\right), \tag{3.5}$$

which is the only invariant $P(\gamma)$ that preserves the norm $|\gamma| = 1$.

We now determine $P(E, V)$, which is the crux of the whole derivation. Consider the PDF $P_0(A, B)$ of two independent $N \times N$ random matrices A and B from the GUE or GOE

$$\begin{gathered} P_0(A, B) dA \, dB = P_0(A) P_0(B) dA \, dB, \\ P_0(A) \propto e^{-\mathrm{Tr}\, A^2}. \end{gathered} \tag{3.6}$$

To project $P_0(A, B)$ from Eq. (3.6) into the constrained space $[A, B] = 0$, it is convenient to make a change of variables from the matrix elements A_{ij} (respectively B_{ij}) to the eigenvalues a_i (b_i) and functions f of eigenvectors q_i^a (q_i^b). It is well known that the Jacobian

$J(A_{ij}; a_i, f(q_i^a))$ of this transformation factorizes [2]

$$P_0(A,B)\,dA\,dB = \Omega(a)\Omega(b)\,da\,db\,df(q^a)\,df(q^b),$$

$$\begin{aligned} \Omega(a) &\propto \prod_{j<i} |a_i - a_j|^\beta e^{-\operatorname{Tr} A^2}, \\ da &= \prod_i da_i, \quad df(q^a) = \prod_i df(q_i^a). \end{aligned} \tag{3.7}$$

We will not specify the precise form of the function $f(q^a)$. Also, by making the change of variables $\{A_{ij}\} \to \{a_i, q_i^a\}$, we have implicitly selected a particular gauge of eigenvectors of A (i.e. the eigenvectors have fixed phases).

If A and B are nondegenerate, $[A,B] = 0$ is equivalent to $q_i^a = q_i^b$, $\forall i$. If A or B have degeneracies, there are many ways for the commutator to vanish, but Eq. (3.7) shows $P_0(A,B)$ itself vanishes for any degeneracies. Therefore, the probability $P_{\text{comm}}^{A,B}$ that two given matrices A and B commute is

$$P_{\text{comm}}^{A,B} = \prod_j \delta\left(f(q_j^a) - f(q_j^b)\right) + (\text{degen. terms})\,. \tag{3.8}$$

It follows that the measure $P(E,V)\,dE\,dV$ for commuting matrices E and V is

$$\begin{aligned} P(E,V)\,dE\,dV \propto \Omega(\varepsilon)\Omega(v) \prod_j \delta(q_j^\varepsilon - q_j^v) \times \\ d\varepsilon\,dv\,dq^\varepsilon\,df(q^v), \end{aligned} \tag{3.9}$$

where ε_i (v_i) are eigenvalues of E (V). Thus

$$\begin{aligned} P(\gamma,E,V)d\gamma\,dE\,dV \propto \delta\left(1 - |\gamma|^2\right)\Omega(\varepsilon)\Omega(v) \times \\ \prod_j \delta(q_j^\varepsilon - q_j^v)\,d\gamma\,d\varepsilon\,dv\,dq^\varepsilon\,df(q^v). \end{aligned} \tag{3.10}$$

Now we integrate out the eigenvectors in order to obtain the joint PDF $P(\gamma, \varepsilon, d)$ for the parameters appearing in Eq. (2.10)

$$\begin{aligned} P(\gamma, \varepsilon, d) \propto \delta\left(1 - |\gamma|^2\right) \times& \\ \prod_{i<j} |\varepsilon_i - \varepsilon_j|^\beta |d_i - d_j|^\beta e^{-\sum_k \varepsilon_k^2} e^{-\sum_k d_k^2},& \end{aligned} \tag{3.11}$$

where we substituted $v_i \to d_i$ in order to be consistent with the notation in previous papers. Eq. (3.11) is particularly significant because it allows one to study the level statistics of the ensemble of $N \times N$ type-1 integrable matrices $\mathcal{H}_N^1$, which according to numerical simulations generally turn out to be Poisson [40].

4 Parameter shifts

Here we consider two parameter shifts that leave the commuting family invariant. The second is useful in the rotationally invariant construction of type-M integrable matrices for $M > 1$ in Sect. 5. First, we can shift the parameter $u \to u - u_0 \equiv \tilde{u}$ for some fixed u_0 and rewrite $H(u) = T + uV$ as

$$\begin{aligned} H(u) &= \widetilde{H}(\tilde{u}) \\ &= T(u_0) + \tilde{u}\, V, \end{aligned} \tag{4.1}$$

where $T(u_0) = T + u_0 V$. The relation between the new T-part and V must have the same form as Eq. (2.2), i.e.

$$T(u_0) = W(u_0) + [V, S(u_0)], \quad [V, W(u_0)] = 0. \tag{4.2}$$

In the present case $S(u_0) = S$, $W(u_0) = W + u_0 V$. For type-1 matrices in particular Eq. (2.7) only changes by a simple $W_E \to W_E + u_0 E$.

We can also redefine the parameter as $x = 1/u$ and (via multiplication by x) transfer the parameter dependence from V to T and then shift the new parameter $x \to x - x_0 \equiv \widetilde{x}$

$$\begin{aligned} H(x) &= xT + V \\ &= \widetilde{H}(\widetilde{x}) \\ &= \widetilde{x}T + H(x_0), \end{aligned} \tag{4.3}$$

where $H(x_0) = x_0 T + V$ becomes the new V-part. This transformation is more interesting, and has consequences for our construction of type $M > 1$ matrices.

Note that there is an asymmetry in transformation properties under shifts in u and x introduced by our choice to express T through V in Eq. (2.2) rather than the other way around. We have

$$\begin{aligned} T = W(x_0) + [H(x_0), S(x_0)], \\ [H(x_0), W(x_0)] = 0. \end{aligned} \tag{4.4}$$

The x_0-dependencies of $W(x_0)$ and $S(x_0)$ are nontrivial. We see that the matrix T, and by extension the whole commuting family, is characterized by a continuum of antihermitian matrices $S(x_0)$, corresponding to the shift freedom in x_0. In particular $S(0) = S$, the unshifted antihermitian matrix.

Specializing to type-1, we understand $S(x_0)$ better by examining the shifted reduced Hamiltonian

$$\begin{aligned} \Lambda(x) &= x\,|\gamma\rangle\langle\gamma| + E \\ &= \widetilde{\Lambda}(\widetilde{x}) \\ &= \widetilde{x}\,|\gamma\rangle\langle\gamma| + \Lambda(x_0), \end{aligned} \tag{4.5}$$

from which Eq. (4.4) becomes

$$|\gamma\rangle\langle\gamma| = W_\Lambda(x_0) + [\Lambda(x_0), S(x_0)], \qquad [\Lambda(x_0), W_\Lambda(x_0)] = 0. \tag{4.6}$$

As in Eq. (2.7), Eq. (4.6) is the defining equation for $S(x_0)$, whose matrix elements obtain most conveniently from the eigenbasis of $\Lambda(x_0)$.

The matrix $\Lambda(x_0) = x_0\,|\gamma\rangle\langle\gamma| + E$ takes the role of E in Eq. (2.7). In particular,

$$S_{ij}(x_0) = \frac{\alpha_i \alpha_j^*}{\lambda_i - \lambda_j}, \tag{4.7}$$

where λ_i are the eigenvalues of $\Lambda(x_0)$ given by Eq. (2.13) with $u \to 1/x_0$, and α_i are the components of $|\gamma\rangle$ in the eigenbasis of $\Lambda(x_0)$.

5 Higher types

Integrable matrices $H(u) = T + uV$ of type $M \geqslant 1$ have exactly $n = N - M$ nontrivial linearly independent commuting partners for all u. The restriction on n for higher types tends to complicate their parametrizations – most notably the matrix V is no longer arbitrary. Previous work [20] developed a parametrization (in the eigenbasis of V) called the "ansatz type-M" construction, valid for all $M \geqslant 1$. This construction is complete for $M = 1, 2$ in the sense that one can fit any such integrable matrix into the ansatz construction. Numerical work and parameter counting suggest that it is similarly complete for $M = 3$, but produces only a subset of measure zero among all type $M > 3$ matrices. Finally, the type-1 construction of Sect. 2 maps into the ansatz type-1 construction and vice versa. The parametrization of Ref. [20] reads

$$\begin{aligned} H_{ij}(u) &= T_{ij} = \gamma_i\gamma_j \frac{d_i - d_j}{\varepsilon_i - \varepsilon_j}\frac{\Gamma_i + \Gamma_j}{2}, \quad i \neq j, \\ H_{ii}(u) &= uV_{ii} + T_{ii} \\ &= u\, d_i - \sum_{j\neq i} \gamma_j^2 \frac{d_i - d_j}{\varepsilon_i - \varepsilon_j}\frac{\Gamma_i + \Gamma_j}{2}\frac{\Gamma_j + 1}{\Gamma_i + 1}, \end{aligned} \tag{5.1}$$

where the γ_i and ε_i are free real parameters, and the *constrained* d_i and Γ_i obey the following equations with free parameters g_i, P_i and x_0

$$\begin{aligned} d_i &= \frac{1}{x_0}\sum_{j=1}^{N-M} \frac{g_j}{\langle j|j\rangle}\frac{1}{\lambda_j - \varepsilon_i}, \\ \Gamma_i^2 &= 1 + \frac{1}{x_0}\sum_{j=N-M+1}^{N} \frac{P_j}{\langle j|j\rangle}\frac{1}{\lambda_j - \varepsilon_i}, \end{aligned} \tag{5.2}$$

where λ_i and $\langle i|i\rangle$ are related to ε_i and γ_i through

$$\begin{aligned} \frac{1}{x_0} &= \sum_{j=1}^{N} \frac{\gamma_j^2}{\lambda_i - \varepsilon_j}, \\ \langle i|i\rangle &= \sum_{j=1}^{N} \frac{\gamma_j^2}{(\lambda_i - \varepsilon_j)^2}. \end{aligned} \tag{5.3}$$

Note that λ_i and $|i\rangle$ are the eigenvalues and eigenstates, respectively, of a certain *auxiliary* type-1 family, see Eqs. (2.13) and (2.15).

The signs of Γ_i are arbitrary [46] and each set of sign choices corresponds to a different commuting family. The choice of x_0, ε_i (equivalently λ_i), γ_i, and P_i [47] defines the commuting family while varying g_i produces different matrices within a given family. Ref. [20] proves that these equations indeed produce type-M integrable matrices and also determines the eigenvalues of $H(u)$.

5.1 Rotationally invariant construction

Here we present a rotationally invariant formulation of the real symmetric ansatz construction of an $N \times N$ Hamiltonian $H(u)$. We emphasize that unlike the type-1 case we do not have a clear constructive way of motivating the final expressions other than the fact that they reproduce the above basis-specific expressions.

We start with Eq. (5.1). Consider three mutually commuting real symmetric matrices V, E and Γ. In their shared eigenbasis

$$\begin{aligned} V &= \mathrm{diag}(d_1, d_2, \ldots, d_N), \\ E &= \mathrm{diag}(\varepsilon_1, \varepsilon_2, \ldots, \varepsilon_N), \\ \Gamma &= \mathrm{diag}(\Gamma_1, \Gamma_2, \ldots, \Gamma_N), \\ |\gamma\rangle &= (\gamma_1, \gamma_2, \ldots, \gamma_N). \end{aligned} \tag{5.4}$$

Further, define an antisymmetric matrix S_M through

$$\begin{aligned} W_E + [E, S_M] &= \frac{\Gamma\,|\gamma\rangle\langle\gamma| + |\gamma\rangle\langle\gamma|\,\Gamma}{2}, \\ [E, W_E] &= 0. \end{aligned} \tag{5.5}$$

The matrix T obeys

$$T = W_V + [V, S_M], \quad [V, W_V] = 0, \tag{5.6}$$

which is Eq. (2.3) with $S \to S_M$. We then require that $(\Gamma + \mathbb{1})\,|\gamma\rangle$ be an eigenstate of T

$$T(\Gamma + \mathbb{1})\,|\gamma\rangle = 0, \tag{5.7}$$

where we set the corresponding eigenvalue to zero via a shift of T by a multiple of the identity. This equation replaces the type-1 equation $T\,|\gamma\rangle = t\,|\gamma\rangle$. Basis-independent Eqs. (5.5-5.7) are equivalent to Eq. (5.1).

The next step is to express the constraints (5.2) in a basis-independent form. To this end we introduce an auxiliary type-1 family with the reduced Hamiltonian

$$\Lambda = x_0\,|\gamma\rangle\langle\gamma| + E, \tag{5.8}$$

where we have elected to transfer the parameter dependence to the T-part as discussed in Sect. 4. We consider this family at a fixed value of the parameter $x = x_0$, so we suppress the dependence on x_0 in the reduced Hamiltonian, $\Lambda(x_0) \to \Lambda$, as well as in other members of the auxiliary type-1 family.

By construction d_i are the eigenvalues of V and $\Gamma_i^2 - 1$ are the eigenvalues of a matrix $\Gamma^2 - \mathbb{1}$ simultaneously diagonal with V. Multiplying both sides of Eq. (5.2) by γ_i and using Eqs. (2.13) and (2.15), we see that Eq. (5.2) is equivalent to the following basis-independent equations

$$\begin{aligned} V\,|\gamma\rangle &= \frac{1}{x_0}\sum_{j=1}^{N-M} \frac{g_j}{\langle j|j\rangle}\,|j\rangle\,, \\ (\Gamma^2 - \mathbb{1})\,|\gamma\rangle &= \frac{1}{x_0}\sum_{j=N-M+1}^{N} \frac{P_j}{\langle j|j\rangle}\,|j\rangle\,. \end{aligned} \tag{5.9}$$

It remains to trace parameters g_i and P_i to an object with known transformation properties under a change of basis. By construction, the matrices V and $\Gamma^2 - \mathbb{1}$ are simultaneously diagonal with V-parts of the auxiliary type-1 family. We can therefore complement them to the corresponding members of this family as follows

$$H_1 = x_0 T_V + V, \quad H_2 = x_0 T_\Gamma + \Gamma^2 - \mathbb{1}, \tag{5.10}$$

where T_V and T_Γ are given by Eq. (2.8). In particular, $T_V\,|\gamma\rangle = T_\Gamma\,|\gamma\rangle = 0$, so that Eq. (5.9) implies

$$\begin{aligned} H_1 \left|\gamma\right\rangle &= \frac{1}{x_0} \sum_{j=1}^{N-M} \frac{g_j}{\langle j|j\rangle} \left|j\right\rangle, \\ H_2 \left|\gamma\right\rangle &= \frac{1}{x_0} \sum_{j=N-M+1}^{N} \frac{P_j}{\langle j|j\rangle} \left|j\right\rangle. \end{aligned} \tag{5.11}$$

Further, since $|j\rangle$ are eigenvectors of $H_{1,2}$, upon multiplying each side of Eq. (5.11) by $|i\rangle\langle i|$ we find

$$\begin{aligned} &H_1 \left|i\right\rangle = g_i \left|i\right\rangle, \quad H_2 \left|i\right\rangle = 0, \quad 1 \leqslant i \leqslant N-M, \\ &H_1 \left|i\right\rangle = 0, \quad H_2 \left|i\right\rangle = P_i \left|i\right\rangle, \quad N-M < i \leqslant N, \end{aligned} \tag{5.12}$$

where we used $\langle\gamma|j\rangle = x_0^{-1}$, which follows from Eqs. (2.13) and (2.15). Finally, Eq. (5.12) implies

$$H_1 H_2 = 0. \tag{5.13}$$

Define $G \equiv H_1 + H_2$ to be a real symmetric matrix with N unconstrained eigenvalues $(g_1, g_2, \ldots, g_{N-M}, P_{N-M+1}, \ldots, P_N)$. In order to guarantee that $H(u)$ be real symmetric, however, the numbers P_j and therefore the matrix G must be properly scaled so that the right hand side of the second relation in Eq. (5.2) is nonnegative [47].

We have therefore derived a basis-independent formulation of Eqs. (5.1-5.3) in terms of unconstrained (apart from the aforementioned scaling of G to ensure real Γ) quantities $(G, E, \left|\gamma\right\rangle, x_0)$. One works backwards from Eq. (5.13) to Eq. (5.5) to derive (Λ, V, Γ, T) in order to construct ansatz type-M matrices $H(u) = T + uV$. In fact, since Eq. (5.8) and Eq. (5.10) imply $[G, \Lambda] = 0$, we find it more natural to select $(\Lambda, G, \left|\gamma\right\rangle, x_0)$ and from them derive (E, V, Γ, T). We have no definitive argument, however, that favors one procedure over the other.

Let us now briefly recount the construction. Any real symmetric matrix G allows us to define two matrices H_1 and H_2 that satisfy Eq. (5.13)

$$\begin{aligned} G &= H_1 + H_2, \\ H_1 H_2 &= 0, \end{aligned} \tag{5.14}$$

where the type $M = \text{rank}(H_2)$, the number of non-zero eigenvalues of H_2. Let Λ be a real symmetric matrix satisfying $[G, \Lambda] = 0$. We derive E from Λ using Eq. (5.8), which generates an auxiliary type-1 integrable family of which Λ is the reduced Hamiltonian. Specifically, we obtain the type-1 antisymmetric matrix S through Eq. (2.7). The common eigenvectors $|i\rangle$ of Λ, H_1 and H_2 are given by Eq. (2.15) in the eigenbasis of E.

The next step is to obtain V and Γ^2 through Eq. (5.10). To do this we need matrices T_V and T_Γ, for which it is helpful to use the second parameter shift discussed in Sect. 4. We define the x_0-dependent type-1 antisymmetric matrix $S(x_0)$ through Eq. (4.6). Then T_V and T_Γ are obtained from

$$\begin{aligned} &T_V = W_1(x_0) + [H_1, S(x_0)], \quad [H_1, W_1(x_0)] = 0, \\ &T_\Gamma = W_2(x_0) + [H_2, S(x_0)], \quad [H_2, W_2(x_0)] = 0, \\ &T_{V,\Gamma} |\gamma\rangle = 0, \end{aligned} \tag{5.15}$$

which when combined with Eq. (5.10) determines V and Γ^2. The final step is to determine ansatz T through Eqs. (5.5-5.7). The choice of x_0, $|\gamma\rangle$, Λ and H_2 defines the ansatz type-M commuting family, while the choice of H_1 specifies a matrix within the family.

Setting $x_0 = 0$ seemingly simplifies the construction, because then we have $V = H_1$ and $\Gamma^2 - 1 = H_2$ and we bypass the auxiliary type-1 step in the derivation. Despite this simplication, $x_0 = 0$ actually produces *type-1* integrable matrices $H(u) = T + uV$ with M-fold degenerate V, which we prove in Appendix B. In this sense, ansatz type-M matrices $H(u) = T + uV$, for which V is generally non-degenerate, are deformations of degenerate type-1 families with deformation parameter x_0.

5.2 Probability distribution function for ensembles of type-$M > 1$ integrable matrices

Despite being significantly more complex than type-1 matrices, ansatz type-M matrices are similarly generated by the choice of two commuting random matrices G and Λ and a random vector $|\gamma\rangle$. Therefore, the derivation for the probability density function from Sect. 3, restricted to the GOE, also applies to ansatz matrices. Let c_i, $1 \leqslant i \leqslant N$ be the N eigenvalues of G and λ_i those of Λ. Using Eq. (3.11)

$$\begin{aligned} P_a(\gamma, c, \lambda) &\propto \delta\left(1-|\gamma|^2\right) \times \\ &\prod_{i<j} |c_i - c_j||\lambda_i - \lambda_j| e^{-\sum_k c_k^2} e^{-\sum_k \lambda_k^2} \\ &= \delta\left(1-|\gamma|^2\right) P(c) P(\lambda), \end{aligned} \tag{5.16}$$

where $(c_1, \ldots, c_N) = (g_1, \ldots, g_{N-M}, P_{N-M+1}, \ldots, P_N)$ in order to connect Eq. (5.16) to parameters appearing in Eqs. (5.1-5.3). As noted earlier, one may adopt the alternative viewpoint of selecting the matrix pair (G, E) instead of (G, Λ), where there is no commutation restriction on G and E. The PDF from this standpoint is then

$$\begin{aligned} P_b(\gamma, c, \varepsilon) &\propto \delta\left(1-|\gamma|^2\right) \times \\ &\prod_{i<j} |c_i - c_j||\varepsilon_i - \varepsilon_j| e^{-\sum_k c_k^2} e^{-\sum_k \varepsilon_k^2} \\ &= \delta\left(1-|\gamma|^2\right) P(c) P(\varepsilon), \end{aligned} \tag{5.17}$$

where ε_i are the eigenvalues of E. To be clear, Eq. (5.17) and Eq. (5.16) are two different PDFs for ansatz matrix parameters. To see this, we use Eq. (5.16) to write down the corresponding $P_a(\gamma, c, \varepsilon)$.

$$P_a(\gamma, c, \varepsilon) = \delta\left(1-|\gamma|^2\right) P(c) P(\lambda(\varepsilon, \gamma)) \left|\det \frac{\partial \lambda(\varepsilon, \gamma)}{\partial \varepsilon}\right|. \tag{5.18}$$

There is no *a priori* reason to expect the additional dependence on $|\gamma\rangle$ to cancel out in Eq. (5.18), much less for the resulting PDF to be equal to Eq. (5.17). It is interesting to note that Ref. [44] shows that if ε_i are GOE or GUE distributed, then λ_i will have the same characteristic level repulsion, though this fact alone is insufficient to prove $P_a(\gamma, c, \varepsilon) = P_b(\gamma, c, \varepsilon)$. We have no objective argument that prefers one distribution to the other, although we view $P_a(\gamma, c, \lambda)$ as the more natural choice due to its closer relationship to the type-1 case.

Lastly, we stress that in order for ansatz matrices $H(u)$ to be real symmetric, the parameters Γ_i in Eq. (5.1) must be real [47]. This requirement in turn places the restriction on a given G that the corresponding P_i must be scaled. Therefore, PDFs Eq. (5.16) and Eq. (5.17) are strictly speaking only correct for complex symmetric $H(u)$ and must be modified for real symmetric $H(u)$. For example, one can write $P_a^R(\gamma, c, \lambda) = P_a(\gamma, c, \lambda)\mathcal{I}(\gamma, c, \lambda)$ where $\mathcal{I}(\gamma, c, \lambda)$ is a binary indicator function for the condition $\Gamma_i \in \mathbb{R}$.

6 Discussion

We derived two basis-independent constructions of integrable matrices $H(u) = T + uV$ that were previously parametrized in a preferred basis – that of V. All type-1 matrices are constructed from Eqs. (2.7-2.8), while ansatz type-$M \geqslant 1$ are given by Eqs. (5.5-5.9) along with Eqs. (5.10-5.13). The primary significance in obtaining these basis-independent constructions is that one may now speak of and study random ensembles of integrable matrices in the same way that one studies ensembles of ordinary random matrices in random matrix theory (RMT), for which unitary invariance is a theoretical cornerstone [2].

The two invariant constructions involve choosing a vector $|\gamma\rangle$ and two matrices: E and V such that $[E, V] = 0$ for type-1, and Λ and G such that $[\Lambda, G] = 0$ for ansatz type-M. We showed that the eigenvalues of E and V come from independent GUE, GOE or GSE eigenvalue distributions. The eigenvalues of Λ and G, on the other hand come from independent GOE distributions. This result is significant because Ref. [40] shows that correlations between these matrix pairs induce level repulsion in integrable matrices, which generally have Poisson statistics.

It follows from the complete type-1 construction presented in Sect. 2 that if E, V and $|\gamma\rangle$ are selected from the GUE, GOE or GSE, then the corresponding integrable family of matrices $H^j(u)$ has the same time-reversal properties that define these three ensembles (the "3-fold way" [1, 2]) for all u, and vice-versa. It is possible (though not yet proved) that a similar statement is true for the natural mathematical and physical generalization of these ensembles, initiated by Altland and Zirnbauer [48], that includes charge conjugation (particle-hole) symmetry considerations as well. This "10-fold way" is useful in particular for classifying topological insulators and superconductors [49].

Given the known success of RMT in describing generic (e.g. chaotic) quantum Hamiltonians, one can now also study quantum integrability through the lens of an integrable ensemble theory – integrable matrix theory (IMT). More specifically, until now quantum integrability was mainly studied through specific models satisfying some loose criteria of integrability, whereas there now exists a new tool based on broad and rigorous definitions to study entire classes of quantum integrable models at once. One immediate use of IMT is the study of level statistics in integrable systems, a work soon to be released [40] by the authors. Another recent development is the proof that the generalized Gibbs ensemble (GGE) [45, 50, 51] is the correct density matrix for the long-time averages of observables evolving with type-1 Hamiltonians [52]. An interesting question is how well the GGE works for type $M > 1$ matrices under different scalings of M with N. Other possibilities include the characterization of localization [39] and the reversibility of unitary dynamics [53, 54, 55, 56] generated by matrices in IMT.

There are two further open problems raised in this work that we have not solved. One is the origin and motivation for the ansatz type-M construction found in Sect. 5, which as it stands is verifiably correct but rather ad-hoc in appearance. There ought to be an intuitive motivation for the construction as is the case for the clear and concise type-1 approach found in Sect. 2. Another open problem is the complete invariant construction of all type $M > 3$ matrices, of which only a subset is covered by the ansatz. The reduced Hamiltonian approach to the type-1 solution has an analogous generalization for type-M which could conceivably cover all such matrices, but the details involve working out the general constraints arising from the restricted linear independence of matrices in type-M families, which are nontrivial.

Acknowledgments: This work was supported in part by the David and Lucille Packard Foundation. The work at UCSC was supported by the U.S. Department of Energy (DOE), Office of Science, Basic Energy Sciences (BES) under Award # FG02-06ER46319.

Appendix A

Degenerate E implies u-independent symmetry in type-1 matrices

In Sect. 2 we constructed $N \times N$ type-1 families starting from a vector $|\gamma\rangle$ and a matrix E. The proof that this construction is exhaustive hinges on E being nondegenerate. We show here that a degenerate E implies a common u-independent symmetry prohibited by our definition of an integrable family [38, 41].

Suppose E has a two-fold degeneracy and consider Eq. (2.7) in the eigenbasis of E, so that $E = \text{diag}(\varepsilon, \varepsilon, \varepsilon_3, \ldots, \varepsilon_N)$. We furthermore pick the degenerate subspace of E that diagonalizes W_E. The off-diagonal components of Eq. (2.7) read

$$\gamma_i \gamma_j^* = (\varepsilon_i - \varepsilon_j) S_{ij}, \quad i \neq j. \tag{A.1}$$

This in particular implies that $\gamma_1 \gamma_2^* = 0$ and S_{12} is arbitrary. Without a loss of generality we let $\gamma_1 = 0$.

Now we turn our attention to $H(u) = T + uV$, where in this basis $V = \text{diag}(d_1, \ldots, d_N)$. Note that by definition of type-1 linear independence, for any integrable family there exists an $H(u)$ such that the matrix V is nondegenerate (this is the typical case, but it suffices that there exist one such matrix). Looking again at off-diagonal components, through Eq. (2.8) we find

$$H_{ij} = T_{ij} = (d_i - d_j) S_{ij}, \quad i \neq j. \tag{A.2}$$

At this point, we can *almost* see that $H(u)$ is block-diagonal, since any $S_{1j} = 0$ for $j \neq 2$.

In fact, we can visualize $H(u)$ through the following helpful schematic

$$H(u) = \begin{pmatrix} \times & \times & 0 & 0 & \dots & 0 \\ \times & \times & \times & \times & \dots & \times \\ 0 & \times & \times & \times & \dots & \times \\ 0 & \times & \times & \times & \dots & \times \\ \dots & & & \dots & & \dots \\ 0 & \times & \times & \times & \dots & \times \end{pmatrix},$$

where × represents possibly non-zero matrix elements. To show that $H(u)$ is indeed block-diagonal, we consider the eigenvalue equation

$$T\,|\gamma\rangle = t\,|\gamma\rangle, \tag{A.3}$$

which is true by construction of $\Lambda(u)$. Since $\gamma_1 = 0$, the first component of Eq. (A.3) combined with Eq. (A.2) implies

$$\sum_{j\neq 1}(d_1 - d_j)S_{1j}\gamma_j = 0, \tag{A.4}$$

and $S_{1j} = 0$ for $j \neq 2$ reduces this to

$$(d_1 - d_2)S_{12}\gamma_2 = 0. \tag{A.5}$$

As V is nondegenerate, Eq. (A.5) requires either $S_{12} = 0$ or $\gamma_2 = 0$. In the first case, $H(u)$

is of the form

$$H(u) = \begin{pmatrix} \times & 0 & 0 & 0 & \dots & 0 \\ 0 & \times & \times & \times & \dots & \times \\ 0 & \times & \times & \times & \dots & \times \\ 0 & \times & \times & \times & \dots & \times \\ \dots & & & \dots & & \dots \\ 0 & \times & \times & \times & \dots & \times \end{pmatrix},$$

while in the second case $S_{2j} = 0$, $j \neq 1$, from Eq. (A.1) and

$$H(u) = \begin{pmatrix} \times & \times & 0 & 0 & \dots & 0 \\ \times & \times & 0 & 0 & \dots & 0 \\ 0 & 0 & \times & \times & \dots & \times \\ 0 & 0 & \times & \times & \dots & \times \\ \dots & & & \dots & & \dots \\ 0 & 0 & \times & \times & \dots & \times \end{pmatrix}.$$

Either way, each member of the family $H(u)$ reduces to two such blocks indicating a u-independent symmetry. For example, Ω made of two similar blocks that are different multiples of identity commutes with $H(u)$.

Appendix B

Ansatz matrices at $x_0 = 0$ are type-1

Here we prove that ansatz type-M matrices $H(u) = T + uV$ become type-1 at $x_0 = 0$, which is most clearly seen in the eigenbasis of V. We first review the construction of ansatz matrices $H(u)$ at $x_0 = 0$. We then construct a particular type-1 family of matrices $\bar{H}(u)$ through Eqs. (2.7-2.8) and show that $[H(u), \bar{H}(u)] = 0$, $\forall u$.

We first consider ansatz type-M matrices $H(u) = T + uV$. At $x_0 = 0$, Eq. (5.10) implies that $V = H_1$ and $\Gamma^2 - \mathbb{1} = H_2$, so that [46]

$$\begin{aligned} V &= \mathrm{diag}(d_1, d_2, \ldots, d_N), \\ &= \mathrm{diag}(g_1, g_2, \ldots, g_{N-M}, 0, \ldots, 0), \\ \Gamma &= \mathrm{diag}(\Gamma_1, \Gamma_2, \ldots, \Gamma_N), \\ &= \mathrm{diag}(1, 1, \ldots, 1, \pm\sqrt{1 + P_{N-M+1}}, \ldots, \pm\sqrt{1 + P_N}), \\ E &= \mathrm{diag}(\varepsilon_1, \varepsilon_2, \ldots, \varepsilon_N). \end{aligned} \tag{B.1}$$

We note also that $E = \Lambda$ at $x_0 = 0$ by Eq. (5.8). Recall that E arises in the ansatz construction from an auxiliary type-1 problem, so E is nondegenerate without loss of generality (see Appendix A).

With Eq. (B.1) in mind, we also rewrite Eqs. (5.5-5.7), the defining equations for the ansatz antisymmetric matrix S_M and for ansatz T, which are true at any x_0

$$\begin{aligned} &T = W_V + [V, S_M], \quad [V, W_V] = 0, \\ &T \frac{1}{2}(\Gamma + \mathbb{1}) \left|\gamma\right\rangle = 0, \end{aligned} \tag{B.2}$$

where S_M follows from

$$\Omega_E + [E, S_M] = \frac{\Gamma \left|\gamma\right\rangle\left\langle\gamma\right| + \left|\gamma\right\rangle\left\langle\gamma\right| \Gamma}{2}, \quad [E, \Omega_E] = 0. \tag{B.3}$$

We now prove that ansatz type-M $H(u) = T + uV$ constructed with Eq. (B.1) are in fact type-1 matrices. Consider a type-1 integrable matrix $\bar{H}(u) = \bar{T} + u\bar{V}$ family constructed through the methods of Sect. 2, with the substitution $\left|\gamma\right\rangle \to \frac{1}{2}(\Gamma + \mathbb{1})\left|\gamma\right\rangle \equiv \left|\bar{\gamma}\right\rangle$. This particular type-1 family is unrelated to the *auxiliary* type-1 family appearing in the ansatz construction. In the following, bars $\bar{X}$ will indicate quantities X that involve the type-1 integrable matrix family. We have

$$\begin{aligned}
&\bar{V} = \mathrm{diag}(\bar{d}_1, \bar{d}_2, \dots, \bar{d}_N) \\
&\left|\bar{\gamma}\right\rangle\left\langle\bar{\gamma}\right| = \bar{W}_E + [E, \bar{S}], \quad [E, \bar{W}_E] = 0, \\
&\bar{T} = \bar{W}_{\bar{V}} + [\bar{V}, \bar{S}], \quad [\bar{V}, \bar{W}_{\bar{V}}] = 0, \\
&\bar{T}\left|\bar{\gamma}\right\rangle = 0,
\end{aligned} \tag{B.4}$$

where E is the same as in Eq. (B.3), and therefore $[E, \bar{V}] = 0$. In particular, the reduced Hamiltonian $\bar{\Lambda}(u)$ (see Eq. (2.6)) of this type-1 family is

$$\bar{\Lambda}(u) = \left|\bar{\gamma}\right\rangle\left\langle\bar{\gamma}\right| + uE. \tag{B.5}$$

Recall that by construction,

$$[\bar{\Lambda}(u), \bar{H}(u)] = 0, \quad \forall. \tag{B.6}$$

Therefore, it suffices to show $[\bar{\Lambda}(u), H(u)] = 0$, $\forall u$, which combined with the non-degeneracy of $\bar{\Lambda}(u)$ implies $[\bar{H}(u), H(u)] = 0$, $\forall u$.

To this end, consider the commutator $[\bar{\Lambda}(u), H(u)]$

$$\begin{aligned} &[\bar{\Lambda}(u), H(u)] = \\ &= [|\bar{\gamma}\rangle\langle\bar{\gamma}|\,, T] + u\left([E, T] + [|\bar{\gamma}\rangle\langle\bar{\gamma}|\,, V]\right) + u^2[E, V]. \end{aligned} \tag{B.7}$$

The first term in Eq. (B.7) vanishes by Eq. (B.2), and the third term in Eq. (B.7) vanishes by construction. We then have

$$[\bar{\Lambda}(u), H(u)] = u\left([E, T] + [|\bar{\gamma}\rangle\langle\bar{\gamma}|\,, V]\right). \tag{B.8}$$

Eq. (B.8) is true for all x_0, but in order for its r.h.s. to vanish, we must have (see Eqs. (2.1-2.2))

$$\begin{aligned} T = \Omega_V + [V, s], &\quad [V, \Omega_V] = 0, \\ |\bar{\gamma}\rangle\langle\bar{\gamma}| = \bar{\Omega}_E + [E, s], &\quad [E, \Omega_E] = 0, \end{aligned} \tag{B.9}$$

where s is an antisymmetric matrix. Eq. (B.9) is not true for general x_0, but we can show it is true at $x_0 = 0$. From Eq. (B.2) and Eq. (B.4) we actually have

$$\begin{aligned} T = W_V + [V, S_M], &\quad [V, W_V] = 0, \\ |\bar{\gamma}\rangle\langle\bar{\gamma}| = \bar{W}_E + [E, \bar{S}], &\quad [E, \bar{W}_E] = 0. \end{aligned} \tag{B.10}$$

We now show that at $x_0 = 0$, $[V, S_M] = [V, \bar{S}]$, so that $s = \bar{S}$ in Eq. (B.9). This last step will complete the proof that $[H(u), \bar{H}(u)] = 0$. Consider the matrix elements $S_{M,ij}$ and $\bar{S}_{ij}$

in the eigenbasis of V, which obtain from Eq. (B.3) and Eq. (B.4)

$$\begin{aligned} S_{M,ij} &= \frac{\gamma_i(\Gamma_i+1)\gamma_j(\Gamma_j+1)}{4}\frac{1}{\varepsilon_i-\varepsilon_j} \\ &- \frac{\gamma_i(\Gamma_i-1)\gamma_j(\Gamma_j-1))}{4}\frac{1}{\varepsilon_i-\varepsilon_j}, \\ \bar{S}_{ij} &= \frac{\gamma_i(\Gamma_i+1)\gamma_j(\Gamma_j+1)}{4}\frac{1}{\varepsilon_i-\varepsilon_j}, \end{aligned} \tag{B.11}$$

but at $x_0 = 0$, Eq. (B.1) is true and therefore many $\Gamma_i = 1$. More precisely, we find

$$\begin{aligned} &S_{M,ij} = \bar{S}_{ij}, \quad \text{if } i \leqslant N-M, \text{ OR } j \leqslant N-M, \\ &S_{M,ij} \neq \bar{S}_{ij}, \quad \text{otherwise.} \end{aligned} \tag{B.12}$$

Now using Eq. (B.1) again, we see that $d_i - d_j = 0$ if $S_{M,ij} \neq \bar{S}_{ij}$, where d_i is the i-th diagonal entry of the diagonal matrix V. Therefore $[V, S_M] = [V, \bar{S}]$ at $x_0 = 0$, which implies Eq. (B.9) holds with $s = \bar{S}$, and therefore $[\bar{\Lambda}(u), H(u)] = 0$, $\forall u$. It follows that $[\bar{H}(u), H(u)] = 0$, $\forall u$ and $H(u)$ is type-1 at $x_0 = 0$.

Bibliography

[1] F. J. Dyson, Statistical Theory of the Energy Levels of Complex Systems. I, J. Math. Phys. **3**, 140 (1962).

[2] M. L. Mehta, *Random Matrices.* (Academic Press, San Diego, 1991).

[3] P. J. Forrester, *Log-Gases and Random Matrices.* (Princeton University Press, Princeton, 2010).

[4] O. Bohigas, M. J. Giannoni, C Schmit, Characterization of Chaotic Quantum Spectra and Universality of Level Fluctuation Laws, Phys. Rev. Lett. **52**, 1 (1984).

[5] C. W. J. Beenakker, Rev. Mod. Phys. **69**, 731 (1998).

[6] T. Guhr, A. Müller-Groeling, and H.A. Weidenmüller, Random-matrix theories in quantum physics: common concepts, Phys. Rep. **299**, 189 (1998).

[7] D. Poilblanc, T. Ziman, J. Bellissard, F. Mila, G. Montambaux, Poisson vs. GOE Statistics in Integrable and Non-Integrable Quantum Hamiltonians, Europhys. Lett. **22**, 537 (1993).

[8] D. A. Rabson, B. N. Narozhny, and A. J. Millis, Crossover from Poisson to Wigner-Dyson level statistics in spin chains with integrability breaking, Phys. Rev. B**69**, 054403 (2004).

[9] M. V. Berry and M. Tabor, Level clustering in the regular spectrum, Proc. R. Soc. Lond. A **356**, 375 (1977).

[10] A. Relaño, J. Dukelsky, J.M.G. Gómez, and J. Retamosa, Stringent numerical test of the Poisson distribution for finite quantum integrable Hamiltonians, Phys. Rev. E **70**, 026208 (2004).

[11] H. -J. Stöckmann and J. Stein, "Quantum" chaos in billiards studied by microwave absorption, Phys. Rev. Lett. **64**, 2215 (1990).

[12] C. Ellegaard, T. Guhr, K. Lindemann, H. Q. Lorensen, J. Nygard, and M. Oxborrow, Spectral Statistics of Acoustic Resonances in Aluminum Blocks, Phys. Rev. Lett. **75**, 1546 (1995).

[13] R. Püttner, B. Grémaud, D. Delande, M. Domke, M. Martins, A. S. Schlachter, G. Kaindl, Statistical Properties of Inter-Series Mixing in Helium: From Integrability to Chaos, Phys. Rev. Lett. **86**, 3747 (2001).

[14] E. P. Wigner, Characteristic Vectors of Bordered Matrices With Infinite Dimensions, The Annals of Math. **62**, 548 (1955).

[15] G. Casati, L. Molinari, and F.M. Izrailev, Scaling properties of band random matrices, Phys. Rev. Lett. **64**, 1851 (1990).

[16] M. Moshe, H. Neuberger, and B. Shapiro. Generalized Ensemble of Random Matrices, Phys. Rev. Lett. **73**, 1497 (1994).

[17] E. A. Yuzbashyan, B. L. Altshuler and B. S. Shastry, The origin of degeneracies and crossings in the 1d Hubbard model, J. of Phys. A **35**, 7525 (2002).

[18] B. S. Shastry, A class of parameter-dependent commuting matrices, J. of Phys. A **38**, L431 (2005).

[19] H. K. Owusu, K. Wagh, and E. A. Yuzbashyan, The link between integrability, level crossings and exact solution in quantum models, J. of Phys. A **42**, 035206 (2009).

[20] H. K. Owusu and E. A. Yuzbashyan, Classification of parameter-dependent quantum integrable models, their parameterization, exact solution and other properties, J. of Phys. A **44**, 395302 (2011).

[21] E. A. Yuzbashyan and B. S. Shastry, Quantum Integrability in Systems with Finite Number of Levels, J. Stat. Phys. **150**, 704 (2013).

[22] H. Lieb and F. Y. Wu, The one-dimensional Hubbard model: a reminiscence, Physica A **321**, 1 (2003).

[23] B. Sutherland: *Beautiful Models: 70 years of exactly solved quantum many-body problems'*, (World Scientific, Singapore, 2004).

[24] F. H. L. Essler, H. Frahm, F. Göhmann, A. Klümper, and V. Korepin, *The One-Dimensional Hubbard Model.* (Cambridge University Press, New York, 2005).

[25] C .N. Yang and C. P. Yang, One-Dimensional Chain of Anisotropic Spin-Spin Interactions. I. Proof of Bethe's Hypothesis for Ground State in a Finite System, Phys. Rev. **150**, 321 (1966). One-Dimensional Chain of Anisotropic Spin-Spin Interactions. II. Properties of the Ground-State Energy Per Lattice Site for an Infinite System, Ibid., **150**, 327 (1966).

[26] C. N. Yang and C. P. Yang, One-Dimensional Chain of Anisotropic Spin-Spin Interactions. III. Applications, Phys. Rev. **151**, 258 (1966).

[27] M. Takahashi, *Thermodynamics of One-Dimensional Solvable Models*,(Cambridge University Press, New York, 1999).

[28] Y. Wang, W-L. Yang, J. Cao, and K. Shi, *Off-Diagonal Bethe Ansatz for Exactly Solvable Models.* (Spring-Verlag, Berlin Heidelberg, 2015).

[29] M. Gaudin, *The Bethe Wavefunction.* (Cambridge University Press, New York, 2014).

[30] E. K. Sklyanin, Separation of variables in the Gaudin model, J. Sov. Math. **47**, 2473 (1989).

[31] M. C. Cambiaggio, A. M. F. Rivas, and M. Saraceno, Integrability of the pairing hamiltonian, Nucl. Phys. A **624**, 157 (1997).

[32] J. Dukelsky, S. Pittel, and G. Sierra, Colloquium: Exactly solvable Richardson-Gaudin models for many-body quantum systems, Rev. Mod. Phys. **76**, 643 (2004).

[33] M. P. Grabowski, P. Mathieu, Structure of the Conservation Laws in Quantum Integrable Spin Chains with Short Range Interactions, Ann. Phys. **243**, 299 (1995).

[34] J. Sirker, R.G. Pereira, and I. Affleck, Conservation laws, integrability, and transport in one-dimensional quantum systems, Phys. Rev. B **83**, 035115 (2011).

[35] H. Grosse, The symmetry of the Hubbard model, Lett. Math. Phys. **18**, 151 (1989).

[36] B. S. Shastry, Infinite Conservation Laws in the One-Dimensional Hubbard Model, Phys. Rev. Lett. **56**, 1529 (1986). Ibid., **56**, 2453 (1986).

[37] Excluding multiples of the identity matrix. Equivalently, one can take $H(u)$ and $H^i(u)$ to be traceless and later add $(c_1 + c_2 u)\mathbb{1}$ to the family.

[38] A u-independent symmetry means $H^i(u)$ are simultaneously block-diagonal thus reducing the problem to that for smaller matrices.

[39] R. Modak, S. Mukerjee, E. A. Yuzbashyan, B. S. Shastry, Integrals of motion for one-dimensional Anderson localized systems, N. J. Phys. **18**, 033010 (2016).

[40] J. A. Scaramazza, B. S. Shastry and E. A. Yuzbashyan, Integrable matrix theory: Level statistics, Phys. Rev. E **94**, 032106 (2016).

[41] $N \times N$ Hermitian quaternion-real matrices in general have N distinct real scalar quaternion eigenvalues. Such matrices can also be represented as $2N \times 2N$ complex Hermitian

matrices with N distinct real eigenvalues that each appear twice in the spectrum. We clarify that by considering non-degenerate quaternion E, we forbid degeneracies in the N quaternion eigenvalues.

[42] Matrices of this form, i.e. rank-one perturbations to Hermitian matrices have been previously studied in the context of simple perturbations about non-interacting or mean-field systems, see Refs. [43, 44] and references therein.

[43] I. L. Aleiner and K. A. Matveev. Shifts of Random Energy Levels by a Local Perturbation, Phys. Rev. Lett. **80**, 814 (1998).

[44] E. Bogomolny, P. Leboeuf, and C. Schmit, Spectral Statistics of Chaotic Systems with a Pointlike Scatterer, Phys. Rev. Lett. **85**, 2486 (2000).

[45] E. T. Jaynes, Information Theory and Statistical Mechanics, Phys. Rev. **106**, 620 (1957).

[46] We impose $\Gamma_i \neq -1$, for if some $\Gamma_i = -1$, it can be shown that additional constraints arise between ordinarily independent ansatz parameters.

[47] For unrestricted P_i the matrix $H(u)$ is generally complex symmetric. However, commutation relations $[H^a(u), H^b(u)] = 0$ still hold in this case. In fact, all parameters in our integrable matrix constructions can be unrestricted complex numbers, which result in complex symmetric integrable $H(u)$.

[48] A. Altland and M. R. Zirnbauer, Nonstandard symmetry classes in mesoscopic normal-superconducting hybrid structures, Phys. Rev. B **55**, 1142 (1997).

[49] S. Ryu, A. Schnyder, A. Furusaki, A. Ludwig, Topological insulators and superconductors: tenfold way and dimensional hierarchy, New J. Phys. **12**, 065010 (2010).

[50] M. Rigol, V. Dunjko, V. Yurovsky, and M. Olshanii, Relaxation in a Completely Integrable Many-Body Quantum System: An Ab Initio Study of the Dynamics of the

Highly Excited States of 1D Lattice Hard-Core Bosons, Phys. Rev. Lett. **98**, 050405 (2007).

[51] A. Polkovnikov, K. Sengupta, A. Silva, and M. Vengalattore, Colloquium: Nonequilibrium dynamics of closed interacting quantum systems, Rev. Mod. Phys. **83**, 863 (2011).

[52] E. A. Yuzbashyan, Generalized microcanonical and Gibbs ensembles in classical and quantum integrable dynamics, Ann. Phys. **367**, 288 (2016).

[53] A. Peres, Stability of quantum motion in chaotic and regular systems, Phys. Rev. A **30**, 1610 (1984).

[54] T. Gorin, T. Prosen, and T. H. Seligman, A random matrix formulation of fidelity decay, New. J. Phys. **6**, 20 (2004).

[55] T. Gorin, T. Prosen, T. H. Seligman, and M. Žnidarič, Dynamics of Loschmidt echoes and fidelity decay, Phys. Rep. **435**, 33 (2006).

[56] C. Chamon, A. Hamma, and E. R. Mucciolo, Emergent Irreversibility and Entanglement Spectrum Statistics, Phys. Rev. Lett. **112**, 240501 (2014).

Chapter 5

Integrable matrix theory: Level statistics

1 Introduction

It is generally believed that the energy levels of integrable systems [1] follow a Poisson distribution [2, 3, 4, 5, 6, 7, 8]. For example, the probability that a normalized spacing between adjacent levels lies between s and $s + ds$ is expected to be $P(s)ds = e^{-s}ds$. In contrast, chaotic systems exhibit Wigner-Dyson statistics, with level repulsion $P(s) \propto s^2$ or s at small s. Moreover, level statistics are often used as a litmus test for quantum integrability even though there are integrable models that fail this test, e.g. the reduced BCS model [5] (which is a particular linear combination of commuting Gaudin Hamiltonians). In this work, we quantify when and why Poisson statistics occur in quantum integrable models, while also characterizing exceptional (non-Poisson) behavior.

Poisson statistics have been numerically verified on a case-by-case basis for some quantum integrable systems, including the Hubbard [2] and Heisenberg [2, 3] models. On the other hand, general or analytic results on the spectra of quantum integrable models are lacking, in part due to the absence of a generally accepted unambiguous notion of quantum integrability, [9, 10] and in part because existing results usually apply to isolated models instead of members of statistical ensembles like random matrices [11]. Notably, Berry and Tabor showed [4] that level statistics in semiclassical integrable models are always Poissonian as long as the energy $E(n_1, n_2, \dots)$ is not a linear function of the quantum numbers $n_1, n_2, \dots$, i.e., the system cannot be represented as a collection of decoupled harmonic oscillators. As integrability is destroyed by perturbing the Hamiltonian, the statistics are expected to cross over from Poisson to Wigner-Dyson at perturbation strengths as small as the inverse system size [3].

Random matrix theory (RMT) [11, 12] captures level repulsion and other universal features of eigenvalue statistics in generic (non-integrable) Hamiltonians (see, e.g., Fig. 1.1). We recently proposed an integrable matrix theory [13] (IMT) to describe eigenvalue statistics of integrable models. This theory is based on a rigorous notion of quantum integrability and provides ensembles of integrable matrix Hamiltonians with any given number of integrals of motion (see below). It is similar to RMT in that both are ensemble theories equipped with rotationally invariant probability density functions. An important difference is that random matrices do not represent realistic many-body models, while integrable ones correspond to actual integrable Hamiltonians. We therefore have access not only to typical features, but also to exceptional cases and are in a position to make definitive statements about the statistics of quantum integrable models. Here, we study the nearest-neighbor level spacing distributions of the IMT ensembles.

The approach of Refs. [10, 13, 16, 17, 14, 15, 18] to quantum integrability operates with $N \times N$ Hermitian matrices linear in a real parameter x. A matrix $H(x) = xT + V$ is called *integrable* [16, 17, 19] if it has a commuting partner $\widetilde{H}(x) = x\widetilde{T} + \widetilde{V}$ other than a linear combination of itself and the identity matrix and if $H(x)$ and $\widetilde{H}(x)$ have no common x-independent symmetry, i.e., no $\Omega \neq c\mathbf{1}$ such that $[\Omega, H(x)] = [\Omega, \widetilde{H}(x)] = 0$. Fixing the parameter-dependence makes the existence of commuting partners a nontrivial condition, so that only a subset of measure zero among all Hermitian matrices of the form $xT + V$ are integrable [17].

Further, integrable matrices fall into different classes (types) according to the number of independent integrals of motion. We say that $H(x)$ is a type-M integrable matrix if there are precisely $n = N - M > 1$ linearly independent $N \times N$ Hermitian matrices [20]

$H^i(x) = xT^i + V^i$ with no common x-independent symmetry such that

$$\big[H(x), H^i(x)\big] = 0, \quad [H^i(x), H^j(x)] = 0, \tag{1.1}$$

for all x and $i, j = 1, \ldots, n$. A type-M family of integrable matrices (*integrable family*) is an n-dimensional vector space [20], where $H^i(x)$ provide a basis. The general member of the family is

$$H(x) = \sum_{i=1}^{n} d_i H^i(x), \tag{1.2}$$

where d_i are real numbers. The maximum possible value of n is $n = N - 1$, corresponding to type-1 or maximally commuting Hamiltonians.

Examples of well-known many-body Hamiltonians that fit into this definition of integrability are the Gaudin, 1D Hubbard and XXZ models, where x corresponds to the external magnetic field, Hubbard U and the anisotropy, respectively. Note, however, that these models have various x-independent symmetries, such as the z component of the total spin, total momentum, etc. Taken at a given number of spins or sites, they break down into sectors (matrix blocks) characterized by certain parameter-independent symmetry quantum numbers. Such blocks are integrable matrices according to our definition. For instance, the 1D Hubbard model on six sites with three spin up and three spin down electrons is a direct sum of integrable matrices of various types [17]. Sectors of Gaudin magnets, where the z-component of the total spin differs by one from its maximum or minimum value (one spin flip), or, equivalently, the one Cooper pair sector of the BCS model are type-1 [16], while other sectors are integrable matrices of higher types.

Prior work [16, 17, 15, 18, 10] constructed all type-1, 2, 3 integrable matrices and a certain subclass of arbitrary type-M, determined exact eigenvalues and eigenfunctions of these matrices, investigated the number of level crossings as a function of size and type, and showed that type-1 integrable families satisfy the Yang-Baxter equation. This work is a continuation of Ref. [13] where we formulated a rotationally invariant parametrization of

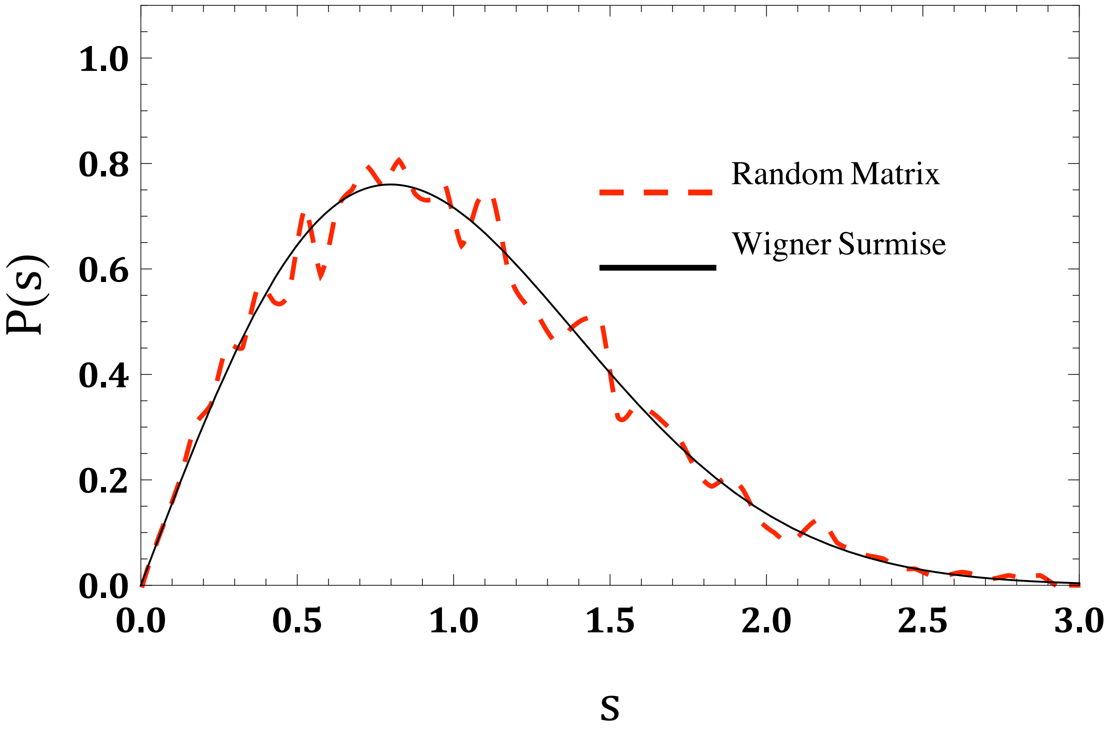

Figure 1.1: The level spacing distribution of a 4000 × 4000 random real symmetric matrix with entries chosen as independent random numbers from a normal distribution of mean 0 and off-diagonal variance 1/2 (diagonal variance of 1). Such a matrix belongs to the Gaussian orthogonal ensemble (GOE) of real symmetric matrices, studied in random matrix theory (RMT). The main feature of the spacing distribution here is its vanishing for small spacings, also known as level repulsion. The smooth curve is the Wigner surmise $P(s) = \frac{\pi}{2} s e^{-\frac{\pi}{4}s^2}$. See the integrable matrix case in Fig. 1.2.

integrable matrices and derived an appropriate probability density function (PDF) for the parameters, i.e., for ensembles of integrable matrices of any given type. The derivation is similar to that in the RMT and is based on either maximizing the entropy of the PDF or, equivalently, postulating statistical independence of independent parameters and rotational invariance of the PDF. Here, we use the results of Ref. [13] to generate and study numerically and analytically level spacing distributions in ensembles of integrable matrices of various types as well as in individual matrices.

Our main results are as follows. For a generic choice of parameters, the level statistics of integrable matrices $H(x)$ are Poissonian in the limit of the Hilbert space size $N \to \infty$

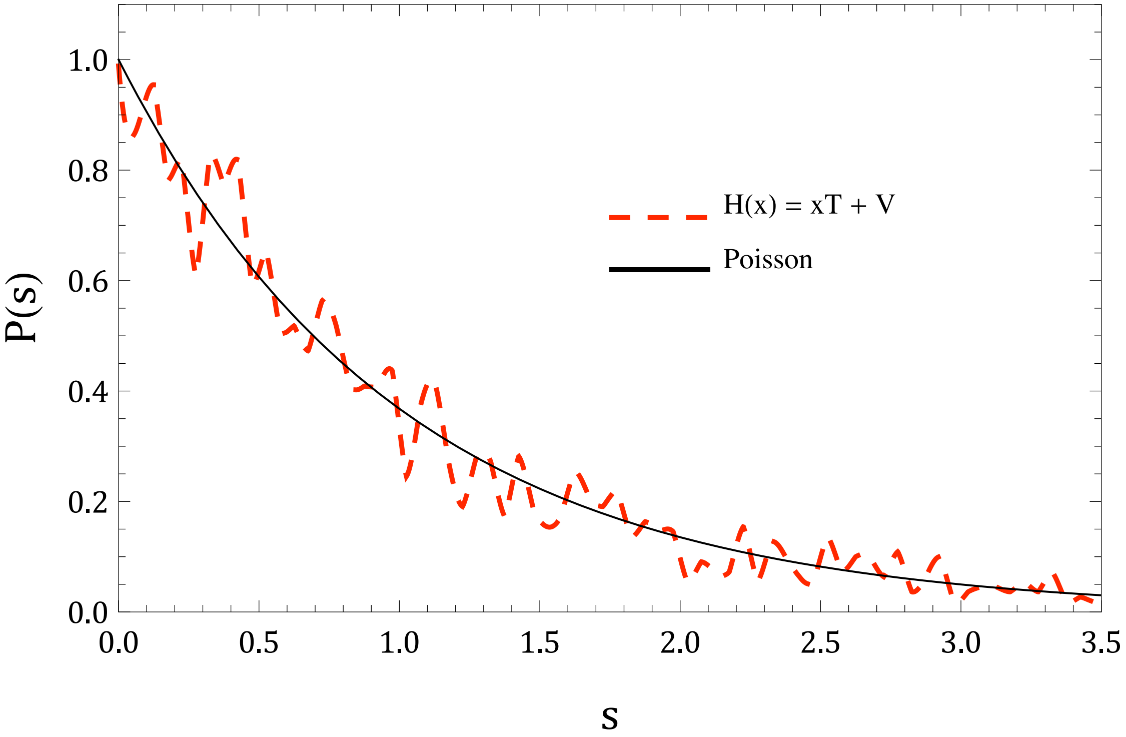

Figure 1.2: The level spacing distribution for a 4000 × 4000 real symmetric integrable matrix $H(x) = xT + V$ at $x = 1$. This particular matrix is a sum of 200 linearly independent matrices that commute for all values of the real parameter x. Note that the spacing distribution is maximized at $s = 0$, a feature known as level clustering. The smooth curve is a Poisson distribution, which is theorized to be typical of integrable matrices. Compare to the generic real symmetric matrix case in Fig. 1.1.

if the number of conservation laws n scales at least as $\log N$, see Fig. 1.2 for an example. Exceptions to Poisson statistics fall into two categories. First, it is always possible to construct an integrable matrix that has *any* desired level spacing distribution at a given isolated value, $x = x_0$, of the coupling (or external field) parameter. For a typical type-1 matrix there is always a single value of x where the statistics are Wigner-Dyson. The distribution quickly crosses back over, however, to Poisson at deviations from x_0 of size $\delta x \sim N^{-0.5}$, with the crossover centered at $\delta x \sim N^{-1}$. Second, one obtains non-Poissonian distributions by introducing correlations among the ordinarily independent parameters characterizing an integrable matrix $H(x)$; the reduced BCS model falls into this category. The statistics again revert to Poisson at $\mathcal{O}(N^{-0.5})$ deviations from such correlations. We also show numerically that as $N \to \infty$, integrable matrix ensembles satisfy two distinct definitions of ergodicity with respect to the nearest-neighbor spacing distribution $P(s)$. Not only are the statistics of a single matrix representative of the entire ensemble, but the statistics of the j-th bulk spacing across the ensemble are independent of j.

In Sect. 2, we present numerical results on the level statistics of type-1 matrices, defined to be integrable matrices $H(x)$ with the maximum number $n_{\max} = N-1$ of linearly independent commuting partners. Section 3 contains numerical results for integrable matrices with $n \leqslant n_{\max}$. We present our analytical justification of numerical results using perturbation theory in Sect. 4. Finally, we give numerical results on ergodicity in Sect. 5.

2 Level statistics of type-1 integrable matrices

2.1 Type-1 families, primary parametrization

Although our definition of integrable matrices encompasses the general Hermitian case, we restrict our focus in this work to real symmetric matrices. We begin with type-1 integrable $N \times N$ families which contain $N-1$ nontrivial commuting partners in addition to the scaled identity $(c_1 x + c_2)\mathbf{1}$. Such matrices are the simplest to construct, for the parametrization of type-M integrable families increases in complexity with M. Results on these higher types are deferred to Sect. 3.

We first summarize the essential points of the basis-independent type-1 construction of Ref. [13] in order to arrive at the parametrization of Eq. (2.2) useful for numerical calculations. By considering linear combinations of the $N-1$ basis matrices, defined in Eq. (1.2), and the identity, one can prove that every type-1 family contains a particular integrable matrix $\Lambda(x)$ with rank-1 T-part

$$\Lambda(x) = x\,|\gamma\rangle\langle\gamma| + E, \tag{2.1}$$

i.e., $[H(x), \Lambda(x)] = 0$ for all x and any $H(x) = xT + V$ in the family. There is an additional restriction $[V, E] = 0$, which follows from $\mathcal{O}(x^0)$ term in the commutator. It can be shown that the matrices E and V and the vector $|\gamma\rangle$ completely determine a given type-1 matrix $H(x) = xT + V$ modulo an additive constant proportional to the scaled identity.

If we consider any type-1 $H(x)$ in the shared eigenbasis of E and V, we find that the matrix elements of $H(x)$ can be parametrized in terms of the N eigenvalues ε_i of E, the N eigenvalues d_i of V, and the N vector components γ_i of $|\gamma\rangle$. Statistical arguments borrowed from RMT in Ref. [13] identify the ε_i and d_i as two independent sets of eigenvalues drawn from the Gaussian orthogonal ensemble. The γ_i are drawn from a $\delta(1 - |\gamma|^2)$ distribution. With these parameters, *any* $N \times N$ type-1 integrable matrix $H(x) = xT + V$ can be constructed in the following way:

$$\begin{aligned} [H(x)]_{ij} &= x\gamma_i\gamma_j \frac{d_i - d_j}{\varepsilon_i - \varepsilon_j}, \quad i \neq j, \\ [H(x)]_{jj} &= d_j - x\sum_{k\neq j} \gamma_k^2 \frac{d_j - d_k}{\varepsilon_j - \varepsilon_k}. \end{aligned} \tag{2.2}$$

We call Eq. (2.2) the "primary" parametrization, which is given specifically in the basis where V is diagonal and can be transformed into any other basis by an orthogonal transformation. Note that the quantities d_j act as coefficients of linear combination of *basis* *matrices* $H^i(x)$ defined by setting $d_j = \delta_{ij}$ in Eq. (2.2). Explicitly, nonzero matrix elements of $H^i(x)$ are

$$\begin{aligned}
&[H^i(x)]_{ij} = [H^i(x)]_{ji} = x\frac{\gamma_i\gamma_j}{\varepsilon_i - \varepsilon_j}, \quad j \neq i, \\
&[H^i(x)]_{jj} = -x\frac{\gamma_i^2}{\varepsilon_i - \varepsilon_j}, \quad j \neq i, \\
&[H^i(x)]_{ii} = 1 - x\sum_{k\neq i}\frac{\gamma_k^2}{\varepsilon_i - \varepsilon_k}.
\end{aligned} \tag{2.3}$$

and

$$H(x) = \sum_{i=1}^{N} d_i H^i(x). \tag{2.4}$$

From Eq. (2.4) we see that the ε_i and γ_i uniquely identify a type-1 commuting family whereas the choice of d_i produces a given member of the family.

To describe the spectrum of $H(x)$, we introduce an additional N parameters $\lambda_j = \lambda_j(x)$ determined by the following equation [16]:

$$\frac{1}{x} = \sum_{k=1}^{N}\frac{\gamma_k^2}{\lambda_j - \varepsilon_k}. \tag{2.5}$$

One can graphically verify that for any non-degenerate choice of ε_k there are N real solutions λ_j to Eq.(2.5) that interlace the ε_k. The N eigenvectors $v(x)$ and eigenvalues $\eta(x)$ of $H(x)$ are labeled by λ_j and take the form

$$[v_{\lambda_j}(x)]_k = \frac{\gamma_k}{\lambda_j - \varepsilon_k}, \quad \eta_{\lambda_j}(x) = x\sum_{i=1}^{N}\frac{d_i\gamma_i^2}{\lambda_j - \varepsilon_i}. \tag{2.6}$$

The components of the (unnormalized) eigenvectors $v_{\lambda_j}(x)$ are independent of the choice of d_i in Eq. (2.4), and are thus common to any member of the family defined by ε_k and γ_k.

2.2 Universality of Poisson statistics

Equipped with parametrizations of integrable matrix ensembles based on the number of commuting partners in a family, we can quantitatively outline both the origin and the robustness of Poisson statistics in these ensembles. We first explore the latter with numerical tests of the statistics of integrable matrices in Sects. 2.3 - 3.3. For clarity of exposition, the numerical results of Sects. 2.3, 2.4 and 2.5 are demonstrated strictly for type-1 matrices. In Sect. 3, we show that the same results apply generally to a construction of higher type integrable matrix families that by definition contain fewer than the maximum number of conservation laws. We present analytical considerations of numerical results in Sect. 4.

We emphasize that regardless of the choice of parameters we find Poisson level statistics in the overwhelming majority of cases, even near isolated points in parameter space with non-Poissonian statistics. For example, the least biased choice for d_i in Sect. 2.1 enforces GOE statistics at $x = 0$ since $H(0) = V$; by effecting a shift $x \to x + x_0$, the equivalent invariant statement is that each type-1 matrix has a parameter value x_0 such that $H(x_0)$ has Wigner-Dyson statistics. Another exception to Poisson statistics is when d_i and ε_i are correlated so that $d_i = f(\varepsilon_i)$, a smooth function at least over almost the entire range of ε_i. Nonetheless, as soon as we deviate from x_0 or $f(\varepsilon_i)$, the results of Sects. 2.3 and 2.4 show that statistics quickly revert to Poisson at deviations scaling as $\delta \sim N^{-0.5}$ in the limit $N \to \infty$.

Generally, we find that random linear superpositions of basis matrices within a given integrable family are crucial for obtaining Poisson level statistics. Basis matrices themselves, defined in Eq. (2.4) for the primary type-1 construction and in Eq. (3.5) for more general integrable matrices, show non-Poissonian statistics with strong level repulsion. Such repulsion washes away, however, for $H(x)$ that are random linear combinations of sufficiently many basis matrices. We see this behavior in Sect. 2.5 for all type-1 matrices, i.e., independent of the number m of basis matrices (conservation laws) in linear combination as long as $m > \mathcal{O}(\log N)$.

We fit all spacing distributions $P(s)$ to the Brody function [21] $P(s, \omega)$, where ω is the Brody parameter

$$P(s, \omega) = a(\omega) s^{\omega} e^{-b(\omega) s^{\omega+1}}. \tag{2.7}$$

The distribution in Eq. (2.7) has unit mean and norm with appropriate choices of constants

$a(\omega)$ and $b(\omega)$. It interpolates between a Poisson distribution $P(s) = e^{-s}$ at $\omega = 0$ and the Wigner surmise $P(s) = \frac{\pi}{2} s e^{-\frac{\pi}{4}s^2}$ at $\omega = 1$, and hence is a convenient fitting function. The Brody parameter ω can take all values $\omega > -1$, which means it also can detect enhanced level clustering or repulsion.

Note, however, that the Wigner surmise is not the exact nearest neighbor spacing distribution of GOE matrices. One may therefore expect our numerics to produce an $\omega \neq 1$ for GOE matrices. Fig. 2.2, where $\omega \approx .956$, shows that this is indeed the case. The exact distribution $P(s)$ can be found in Ref. [11] and was originally derived by Gaudin in terms of a Fredholm determinant [22]. Using Ref. [23] and a few lines of Mathematica code, we find that the same fitting procedure used for numerically generated matrices produces $\omega \approx 0.957$. Note that it is important to exclude $P(0) = 0$ in the fitting procedure for numerically generated finite-sized matrices.

2.3 Crossover in coupling parameter x

Here, we show that even if the statistics are non-Poissonian at a given coupling value $x = x_0$ (we set $x_0 = 0$), level clustering is restored at small deviations from x_0. For any N, the matrices T and V each have eigenvalues that mostly lie on an $\mathcal{O}(1)$ interval centered about zero. We consider the primary type-1 construction encountered in Eq. (2.2) and explore the level statistics of large matrices. In Fig. 2.1, we see qualitatively how the statistics change with x when $N = 4000$. We find Poisson statistics at $x \sim 1$ until a crossover to level repulsion begins near $x = N^{-0.5}$ and ends near $x = N^{-1.5}$.

To verify that the crossover scaling inferred from Fig. 2.1 is correct for all $N \gg 1$, in Fig. 2.2 we plot how the Brody parameter ω (see Eq. (2.7)) evolves with x for various choices of N. It turns out that $\omega(x, N)$ can be fit to a relatively simple function, for any $N \gg 1$

$$\omega(x, N) = \alpha - \beta \tanh\left(\frac{\log_N x - X_0}{Z}\right). \tag{2.8}$$

The numbers (α, β, X_0, Z) are fit parameters and take the values $(0.482, 0.474, -1.04, 0.157)$

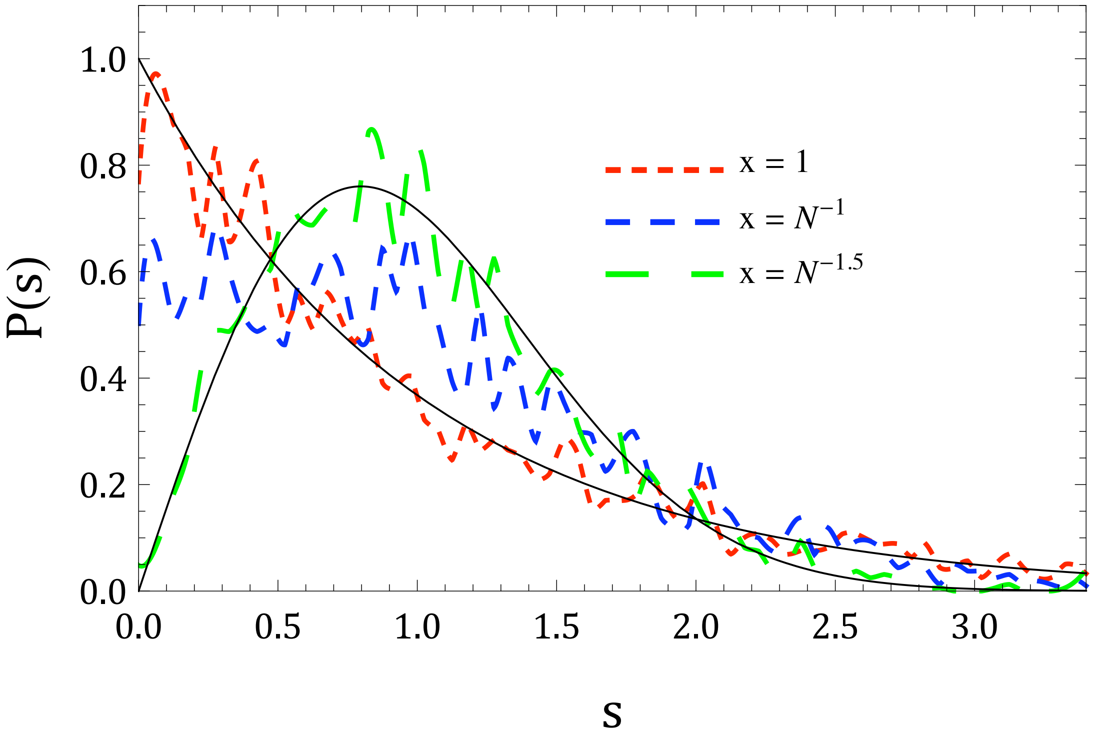

Figure 2.1: Crossover in coupling x of the level statistics of type-1 integrable $N \times N$ matrices $H(x) = xT + V$, $N = 4000$. See Sect. 2.1 for their parametrization. V is a random matrix so that $H(x = 0)$ has level repulsion. Each distribution contains the levels statistics of a single matrix $H(x)$ at a given value of x. Note that some level repulsion has set in by $x = N^{-1}$. Each numerical distribution is fit to the Brody function $P(s, \omega)$ from Eq. (2.7); for couplings $x = \left(1, N^{-1}, N^{-1.5}\right)$ the fits give $\omega = (0.01, 0.30, 0.94)$, respectively. The solid lines are reference plots of a Poisson distribution $P(s) = e^{-s}$ and the Wigner Surmise $P(s) = \frac{\pi}{2} s e^{-\frac{\pi}{4} s^2}$. See Fig. 2.2 for more on this crossover.

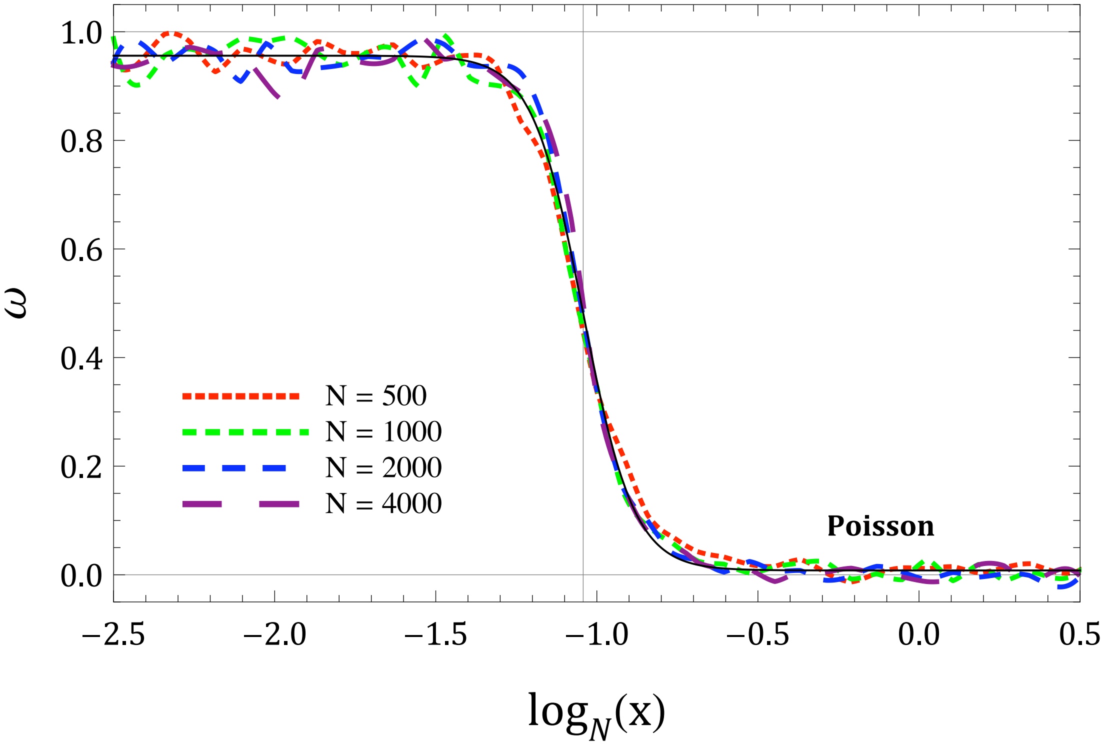

Figure 2.2: Crossover in level statistics with variation of coupling parameter x in type-1 integrable $N \times N$ matrices $H(x) = xT + V$, quantified by the Brody parameter $\omega(x, N)$ from Eq. (2.7). The two important limits are $\omega = 0$ for Poisson statistics and $\omega = 1$ for random matrix (Wigner-Dyson) statistics. Each plotted value $\omega(x, N)$ is computed for the combined level spacing distribution of several matrices from the ensemble. We extract the crossover scale by fitting $\omega(x, N)$ to Eq. (2.8) (solid curve) to all curves simultaneously, where most notably $X_0 \sim -1$ for all N investigated, indicating that crossovers to Poisson statistics are centered at that value for integrable matrices $H(x)$ when $H(x = 0)$ has level repulsion. The middle of the crossover is indicated by a vertical line.

in Fig. 2.2. Most important is that for any $N \gg 1$ we find $X_0 \sim -1$, which solidifies our claim that the crossover occurs between $x \sim N^{-1.5}$ and $x \sim N^{-0.5}$. Analytical arguments explaining this scaling are given in Sect. 4.

2.4 Correlations between matrix parameters

In the eigenbasis of V, our parametrization of integrable $N \times N$ matrices is given in terms of about $3N$ independent parameters (up to a change of basis). Through an explicit construction of the probability density function of integrable matrices obtained through basis-independent considerations, Ref. [13] shows that for a typical integrable matrix, d_i and ε_i

are indeed uncorrelated. We see in this section that if correlations are introduced between ε_i and d_i, the statistics become non-Poissonian. Small perturbations about these correlations, however, bring the statistics immediately back to Poisson. In this section, $x = 1$ for all matrices considered.

Continuing with type-1 matrices in the primary parametrization, Eq. (2.2), we recall that the eigenvalues η_{λ_j} of such a matrix $H(x) = xT + V$ are given by Eq. (2.6),where the $\lambda_j = \lambda_j(x)$ are obtained from Eq. (2.5). As we saw in Sect. 2.3, a typical choice of parameters will produce Poisson statistics, but this changes if we let d_i be some smooth function of ε_i. The simplest case is shown in Fig. 2.3 for which $d_i = \varepsilon_i$. As discussed in Refs. [13, 17], $H(x)$ for this choice of parameters describes a sector of the reduced BCS model and, independently, a short range impurity in a weakly chaotic metallic quantum dot studied in Refs. [24, 25].

The level repulsion for this case can be understood by a simple manipulation of Eq. (2.6) when $d_i = \varepsilon_i$:

$$\begin{aligned}\eta_{\lambda_j} &= x\sum_{i=1}^{N}\frac{\varepsilon_i\gamma_i^2 + \lambda_j\gamma_i^2 - \lambda_j\gamma_i^2}{\lambda_j - \varepsilon_i} \\ &= -x\sum_{i=1}^{N}\gamma_i^2 + \lambda_j,\end{aligned} \tag{2.9}$$

where we used Eq. (2.5). Then when $d_i = \varepsilon_i$ the eigenvalues of $H(x)$ are just the λ_j up to an additive constant. For the case when ε_i are random matrix eigenvalues, Ref. [24] derives the joint probability density of the set $\{\varepsilon_i, \lambda_j\}$ and Ref. [25] demonstrates that the λ_j are subject to the same level repulsion as the ε_i. Note also that Eq. (2.5) implies λ_j lie between consecutive ε_i and therefore the eigenvalues in Eq. (2.9) can have no crossings at any finite x. Numerically, we have found that λ_j exhibit level repulsion for *any* choice of ε_i (see Fig. 2.4). Fig. 2.3 also shows the level repulsion induced when $d_i = \sum_{k=1}^{4} A_k h_k(\varepsilon_i)$, where $h_k(\varepsilon_i)$ is the k-th order Hermite polynomial and A_k are independent random numbers drawn from a normal distribution. In this case, the level repulsion is mitigated relative to the case of

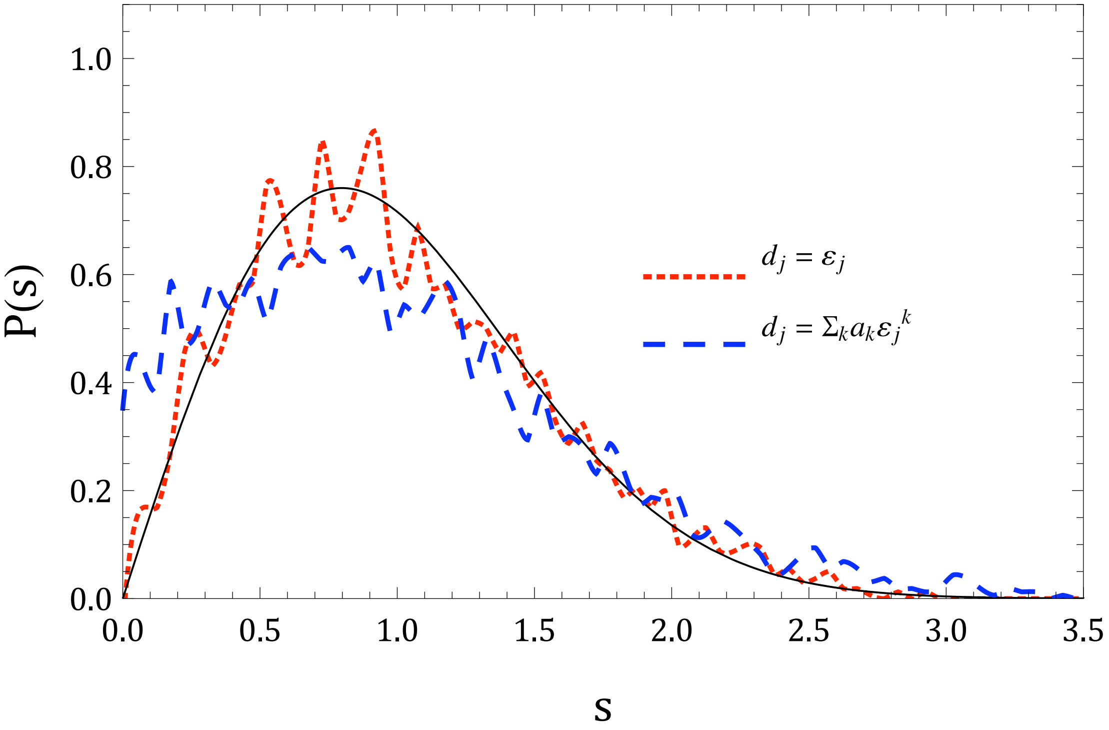

Figure 2.3: Level statistics of two $N \times N$ type-1 integrable matrices $H(x) = xT + V$, $x = 1$ and $N = 4000$, when correlations are introduced between d_j and ε_j (see Eqs. (2.2, 2.6), and then Eq. (2.9) for an example). Note that in contrast to Fig. 2.1, these integrable matrices exhibit level repulsion even for $x = 1$. Each of the two curves is generated from a single matrix. One numerical curve corresponds to the case when $d_i = \varepsilon_i$ and the other is when $d_i = \sum_{k=1}^{4} A_k h_k(\varepsilon_i)$, where $h_k(z)$ is the k-th order Hermite polynomial and $(A_1, A_2, A_3, A_4) = (2.3, 2.16, -1.46, 0.51)$, chosen randomly. Note that the polynomial dependence weakens the level repulsion as compared to the linear case. If higher order polynomials are included, the level repulsion eventually gives way to Poisson statistics. The solid curve is the Wigner surmise $P(s) = \frac{\pi}{2} s e^{-\frac{\pi}{4} s^2}$. See Fig. 2.5 for more on this behavior.

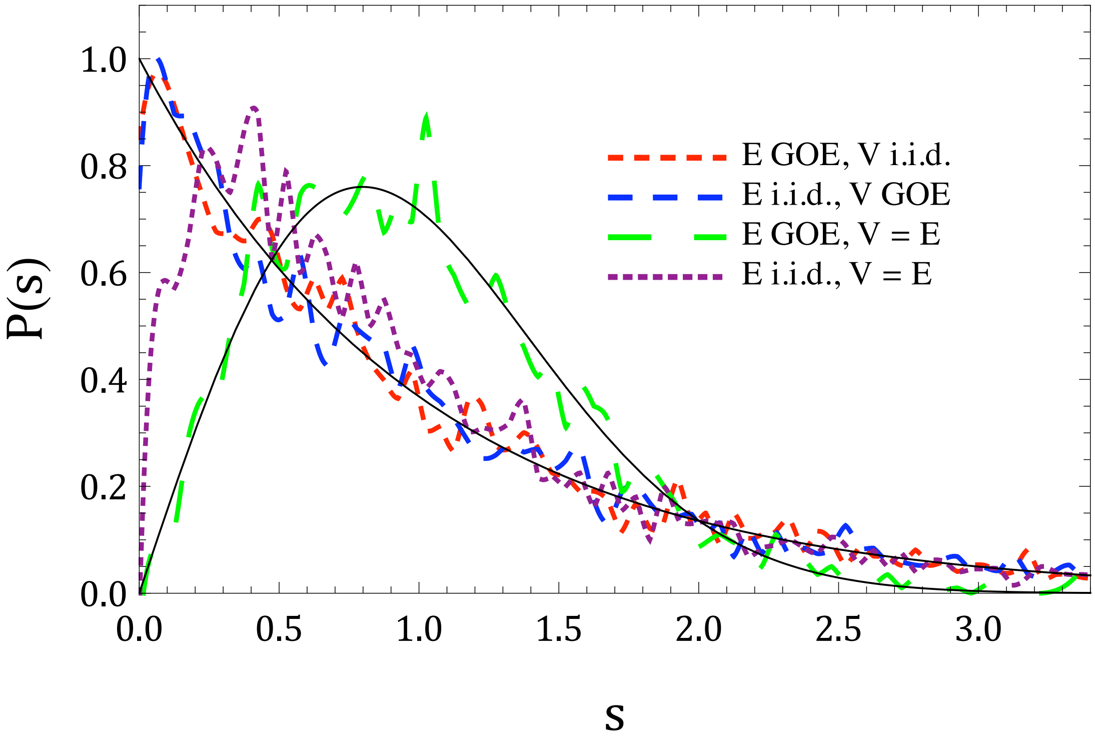

Figure 2.4: Illustrating that conclusions drawn about correlations between d_i (eigenvalues of V) and ε_i (eigenvalues of E) are independent of the particular choice of ε_i. Pictured are four numerically generated nearest-neighbor spacing distributions $P(s)$ for 5000×5000 type-1 matrices, $x = 1$, when the d_i and ε_i are either from a random matrix (GOE) or are independently and identically distributed numbers (i.i.d.) from a normal distribution. Each curve represents the level statistics of a single matrix chosen from the type-1 ensemble. Level repulsion survives in the two cases where d_i and ε_i are correlated ($V = E$), even though the overall shape of $P(s)$ depends on whether E's eigenvalues are GOE or i.i.d. numbers. The solid curves are the usual Poisson distribution $P(s) = e^{-s}$ and the Wigner surmise $P(s) = \frac{\pi}{2} s e^{-\frac{\pi}{4}s^2}$. We do not include plots for different choices of γ_i, which do not affect the general character of the results.

linear correlation. Sums to higher orders of $h_k(\varepsilon_i)$ (or any higher order polynomial) will eventually bring the statistics back to Poisson.

We now investigate the stability of induced level repulsion in $H(x)$ when correlations between d_i and ε_i are broken. In Fig. 2.5, we let $d_i = \varepsilon_i(1 + \delta D_i)$ where D_i is an $\mathcal{O}(1)$ random number from a normal distribution and δ is a number controlling the size of the perturbation. The crossover to Poisson statistics as δ increases is very similar to that in Fig. 2.2, which shows the crossover with x. In fact, we can fit the Brody parameter $\omega(\delta, N)$ to

$$\omega(\delta, N) = \alpha - \beta \tanh\left(\frac{\log_N \delta - X_0}{Z}\right). \tag{2.10}$$

Note that Eq. (2.10) is just Eq. (2.8) with the substitution $x \to \delta$. We find that the crossover occurs over the range $N^{-1.5} \lesssim \delta \lesssim N^{-0.5}$, indicating that any perturbation to correlations will immediately destroy level repulsion as $N \to \infty$. In particular, Fig. 2.5 gives $(\alpha, \beta, X_0, Z) = (0.479, 0.474, -1.03, 0.169)$ for linear correlations. This scaling is not restricted to the case $d_i = \varepsilon_i$, as seen in Fig. 2.6 where we again consider $d_i = \sum_{k=1}^{4} A_k h_k(\varepsilon_i)$ and find a similar crossover with $(\alpha, \beta, X_0, Z) = (0.237, 0.233, -0.914, 0.206)$.

2.5 Basis matrices: how many conservation laws?

Here we demonstrate that in order to obtain Poisson statistics, the number m of linearly independent conservation laws contained in an $N \times N$ integrable type-1 matrix can be much less than N. Consider a combination of m basis matrices $H^i(x)$ defined in Sect. 2.1

$$H(x) = \sum_{i=1}^{m} d_i H^i(x), \quad m \leqslant N - 1. \tag{2.11}$$

From the sum in Eq. (2.11), we can determine the number m needed to obtain Poisson statistics. Individual basis matrices $H^i(x)$ will exhibit level repulsion, and it is only when an integrable matrix is formed from an *uncorrelated* (w.r.t. ε_i, see Sect. 2.4) linear combination of sufficiently many of them will we observe Poisson statistics. Level repulsion in this

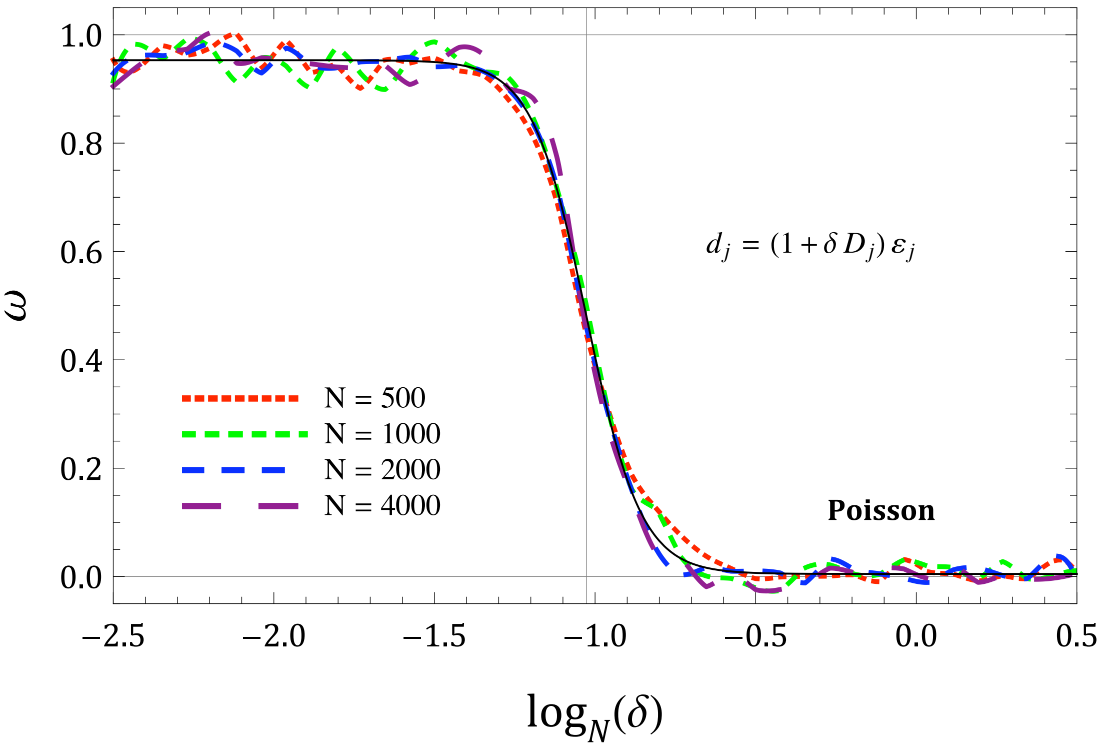

Figure 2.5: Variation in the Brody parameter $\omega(\delta, N)$ when $d_i = \varepsilon_i(1 + \delta D_i)$ in the level statistics of $N \times N$ type-1 integrable matrices $H(x)$ for various N, $x = 1$. The number δ is a parameter controlling the size of the perturbation from correlation, and D_i is an $\mathcal{O}(1)$ random number from a normal distribution. Note that the crossover in δ is very similar to that in x shown in Fig. 2.2. The numerical curves are fit to the function $\omega(\delta, N)$ given in Eq. (2.10) (solid curve), with a crossover centered at $X_0 \sim -1$, indicating that crossovers to Poisson statistics are centered at that value. Each plotted value $\omega(\delta, N)$ is computed for the combined level spacing distribution of several matrices from the ensemble. A vertical line indicates the center of the crossover on the plot. For a similar plot for nonlinear functions $d_i(\varepsilon_i)$ see Fig. 2.6.

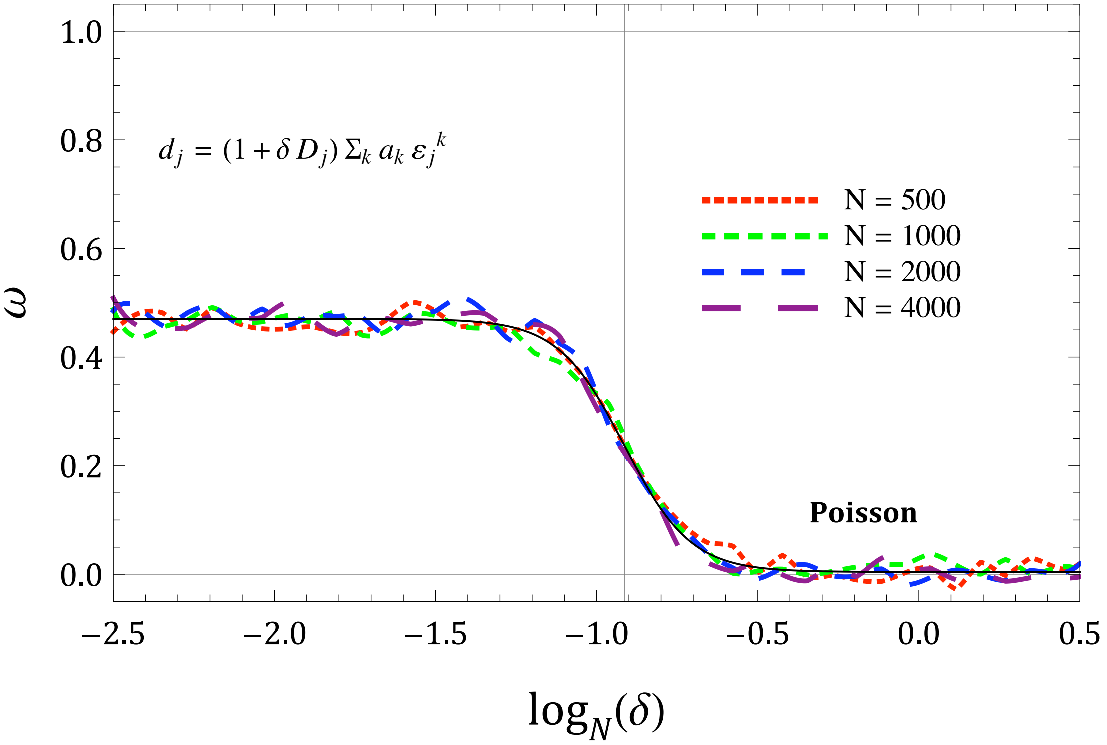

Figure 2.6: Variation in the Brody parameter $\omega(\delta, N)$ when $d_i = \sum_{k=1}^{4} A_k h_k(\varepsilon_i)(1 + \delta D_i)$ in the level statistics of $N \times N$ type-1 integrable matrices $H(x = 1)$ for various N. Here δ quantifies the deviation from the point $\delta = 0$ where the parameters d_i and ε_i defining the matrices are correlated, D_i and A_k are $\mathcal{O}(1)$ random numbers from a normal distribution, $h_k(z)$ is the k-th order Hermite polynomial. Each $\omega(\delta, N)$ is computed for the combined level spacing distribution of several matrices from the ensemble. The crossover in δ is very similar to that in x in Fig. 2.2 and in δ for linear correlations in Fig. 2.5. Because the correlations are nonlinear, the level repulsion is diminished in comparison to previous cases. Despite this, the crossover still demonstrates the same scaling – fitting the data to $\omega(\delta, N)$ given in Eq. (2.10) (solid curve), with a crossover centered at $X_0 \sim -1$ (vertical line), shows that $\delta \propto N^{-0.5}$ is enough for statistics to revert to Poisson.

case can be qualitatively understood by reasoning that a basis matrix only "contains" one nontrivial conservation law, itself. More concretely, we see from Eq. (2.6) that the eigenvalues of $H^i(x)$ are $x\gamma_i^2(\lambda_j - \varepsilon_i)^{-1}$, i.e., they are simple, mostly smooth functions of λ_j, which exhibit level repulsion.

Fig. 2.7 quantifies how many basis matrices m (i.e., conservation laws) are needed for Poisson statistics as a function of N, the matrix size. We find numerically that the plots of the Brody parameter ω (see Eq. (2.7)) vs. the number m of basis matrices in linear combination can be fit to a simple function

$$\omega(m, N) = a \exp\left[-\frac{b}{\log N}\, m\right], \tag{2.12}$$

where a and b are real constants. The fact that for different values of N we find that $b \sim 1$ supports the notion that we need only about $\log N$ conservation laws in order to induce Poisson statistics. We make this claim with caution because we only have data for $500 \leqslant N \leqslant 4000$, a range over which $\log N$ does not vary significantly. More precisely, Fig. 2.7 shows that having $m = \mathcal{O}(1)$ conservation laws is insufficient for inducing Poisson statistics, and that a useful upper bound on the lowest m necessary for Poisson statistics is $m_{\text{min}} < \mathcal{O}(N^{\alpha})$ where $0 < \alpha < 0.20$. We obtain the factor of 0.20 by rewriting Eq. (2.12) assuming the decay constant has power law dependence on N instead of logarithmic dependence

$$\omega(m, N) = a \exp\left[-\frac{c}{N^{\alpha}}\, m\right]. \tag{2.13}$$

Numerically we found that the parameter b in Eq. (2.12) satisifies $1.07 \leqslant b \leqslant 1.21$ when $500 \leqslant N \leqslant 4000$. By matching exponents between Eq. (2.13) and Eq. (2.12) for $(b_1, N_1) = (1.21, 500)$ and $(b_2, N_2) = (1.07, 4000)$, we find a maximum exponent $\alpha = 0.198$.

The basis matrices $H^i(x)$ contained in any integrable $H(x)$ are linearly independent conservation laws. The observed dependence of $P(s)$ on the number m of basis matrices in linear combination is reminiscent of the early work of Rosenzweig and Porter [26] (RP)

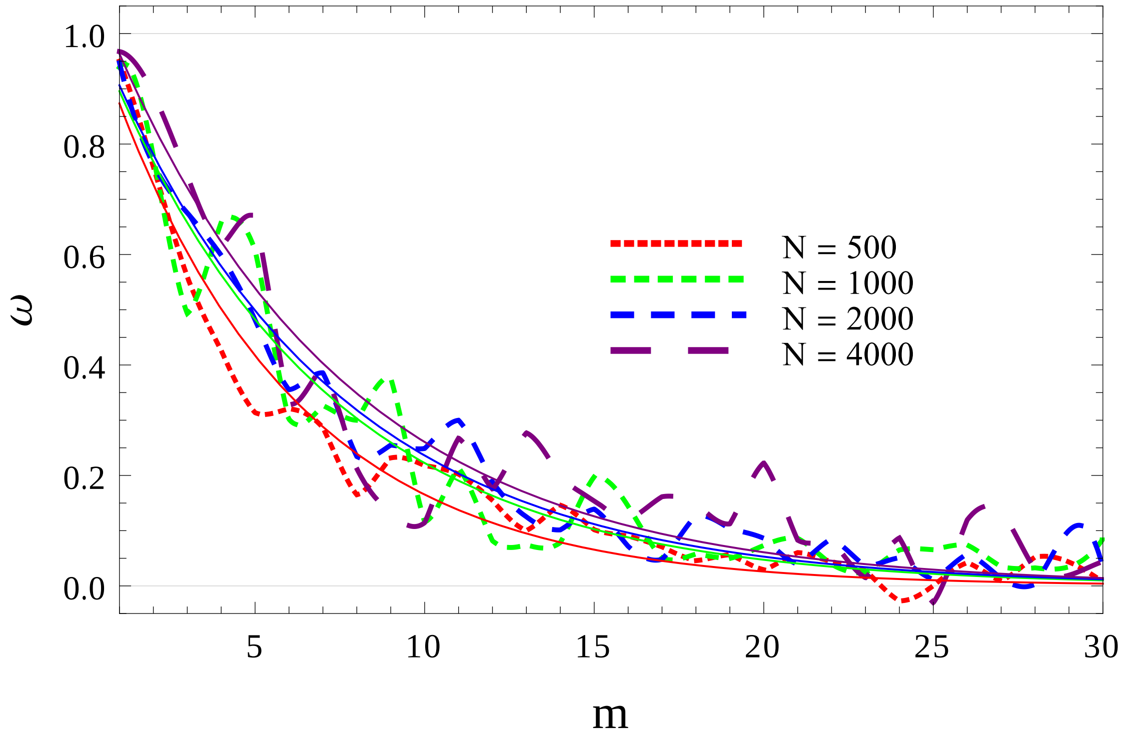

Figure 2.7: The Brody parameter $\omega(m, N)$ (see Eq. (2.7)) vs. number m of type-1 basis matrices $H^i(x)$ in linear combination $H(x) = \sum_{i=1}^m d_i H^i(x)$ for various N, $x = 1$. The fits presume exponential decay and are expressed in terms of two parameters (a, b) from Eq. (2.12). For $N = (500, 1000, 2000, 4000)$ we find the decay constant $b = (1.15, 1.07, 1.14, 1.21)$, indicating that we only need $m_{\text{min}} \approx \log N$ conservation laws for Poisson statistics to emerge. Figs. 3.2 and 3.3 show similar plots for higher types. Each plotted $\omega(m, N)$ is computed for the combined level spacing distribution of several matrices from the ensemble.

on the nearest neighbor spacing distribution of superpositions of independent spectra. Although the spectra of basis matrices $H^i(x)$ are not strictly independent and are added together instead of superposed ("superposed" here means "combined into a single list"), we see the same qualitative behavior as described by RP: a single basis matrix has level repulsion, but a sufficiently large number combined have Poisson statistics. In the case of m independent, superposed spectra with vanishing $P(0)$ that contribute equally to the mean level density, the value $P_m(0)$ of the superposed spectrum is given by the RP result

$$P_m(0) = 1 - \frac{1}{m}. \tag{2.14}$$

We see in Fig. (2.8) that $P_m(0)$ for m basis matrices in linearly combination differs from the RP result for small m, as expected, but asymptotically approaches Eq. (2.14) for large m and large N. Thus it seems reasonable to conceptually understand the emergence of Poisson level statistics in integrable matrices $H(x)$ as arising from the existence of conservation laws, whose spectra are statistically independent for large m and N.

Integrable matrix spectra are similar in structure to those of semiclassically integrable models studied by Berry and Tabor [4]. Such spectra are also sums (or simple functions) of rigid spectra, and they have Poisson nearest-neighbor level statistics in the semiclassical limit.

Berry's work [27] on semiclassical models shows that longer range spectral statistics of integrable and chaotic models deviate from the predictions of the Poisson ensemble [28] and Gaussian random matrix theory, respectively. Similar behavior occurs in purely quantum systems [29]. An example of such a long range statistic is $\Sigma^2(L)$, the spectral variance of the average number of eigenvalues contained in an interval of length L. For independent random numbers with unit mean spacing in an infinitely large spectrum, $\Sigma^2(L) = L$. For a given Hamiltonian, $\Sigma^2(L)$ will eventually saturate [30] at some $L_{\max}$, which depends on the system's classical periodic orbits and the energy scale.

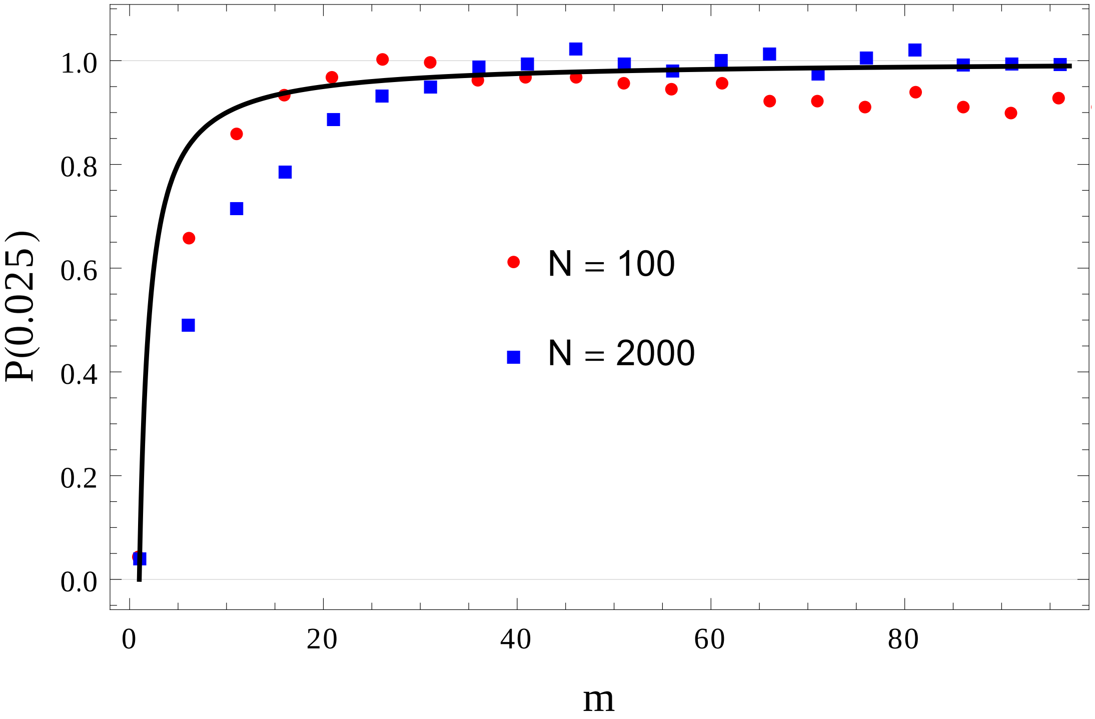

Figure 2.8: Plot of numerically generated $P_m(0.025)$ for *linear combinations* of m type-1 basis matrices, Eq. (2.11), for $N = 100$ and $N = 2000$ at $x = 1$. The solid curve gives the Rosenzweig-Porter prediction of $P_m(0) = 1 - 1/m$ for *superpositions* of m independent random matrix spectra. Physically, the RP curve represents $P_m(0)$ for the combined spectra of m blocks of different (parameter-independent) quantum numbers of a Hamiltonian. We note that although different mechanisms are involved in the RP and integrable matrix approach to Poisson statistics, the behavior of $P(0)$ is similar. This gives heuristic justification to why the existence of parameter-dependent conservation laws in $H(x)$ implies Poisson statistics. The sub-Poisson behavior for $N = 100$ is a finite-size effect.

We find no evidence of saturation of $\Sigma^2(L)$ in type-1 matrices on the ensemble average. Because we work with finite-size spectra, we compare numerically generated $\Sigma^2(L)$ to the corresponding Poisson ensemble averaged result for lists of R independent numbers with unit mean spacing and periodic boundary conditions

$$\overline{\Sigma}^2(R, L) = L\left(1 - \frac{L}{R}\right). \tag{2.15}$$

The overline indicates an average over the Poisson ensemble. Because numerical unfolding (see Appendix A) introduces spurious effects in long range spectral observables, we instead average over small regions containing $R = 2\sqrt{N}$ eigenvalues in the centers of $N \times N$ matrices where the level density is approximately constant. As seen in Fig. 2.9, the spectral variance of type-1 matrices satisfies Eq. (2.15), even at relatively small N.

While there is no saturation on the ensemble average, $\Sigma^2(R, L)$ in the Poisson ensemble has large fluctuations for $L \sim R/2$. Figs. 2.10 and 2.11 show how individual members of the Poisson ensemble and individual type-1 matrices can both exhibit saturation to values of $\Sigma^2(R, L)$ much smaller than Eq. (2.15) and have a spectral variance greatly exceeding Eq. (2.15). Type-M matrices, whose construction is detailed in the next section, exhibit similar behavior in $\Sigma^2(R, L)$ for small M, but we have not quantified how precisely $\Sigma^2(R, L)$ changes with increasing M.

Recent work by Prakash and Pandey [31] shows that a two particle non-interacting embedded matrix ensemble [32] exhibits saturation of $\Sigma^2(L)$ on the ensemble average. Embedded matrix ensembles model the structure of many body systems by constructing eigenenergies out of random k-body interactions between m particles, $k < m$. Ref. [31] contains an extended discussion of saturation and helpful references. We do not pursue spectral variance further in this work.

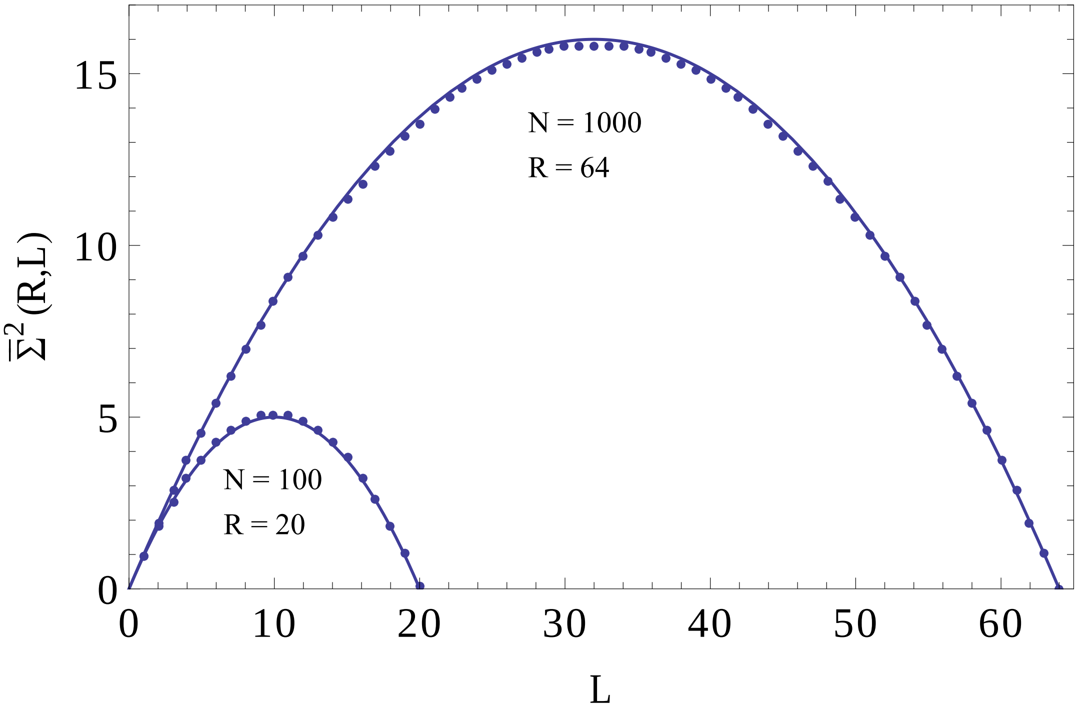

Figure 2.9: Ensemble averaged number variance $\overline{\Sigma}^2(R,L)$ in $N \times N$ type-1 matrices $H(x) = xT + V$ at $x = 1$ for $N = 100$ and $N = 1000$. In order to achieve a constant mean level spacing normalized to unity, we selected the middle $R = 2\sqrt{N}$ eigenvalues from each matrix and used periodic boundary conditions on the list of eigenvalues. The results are in excellent agreement with the Poisson ensemble predictions (solid curves), given by Eq. (2.15). There is no saturation on the ensemble average. We averaged over 10^4 matrices for $N = 100$ and 500 matrices for $N = 1000$.

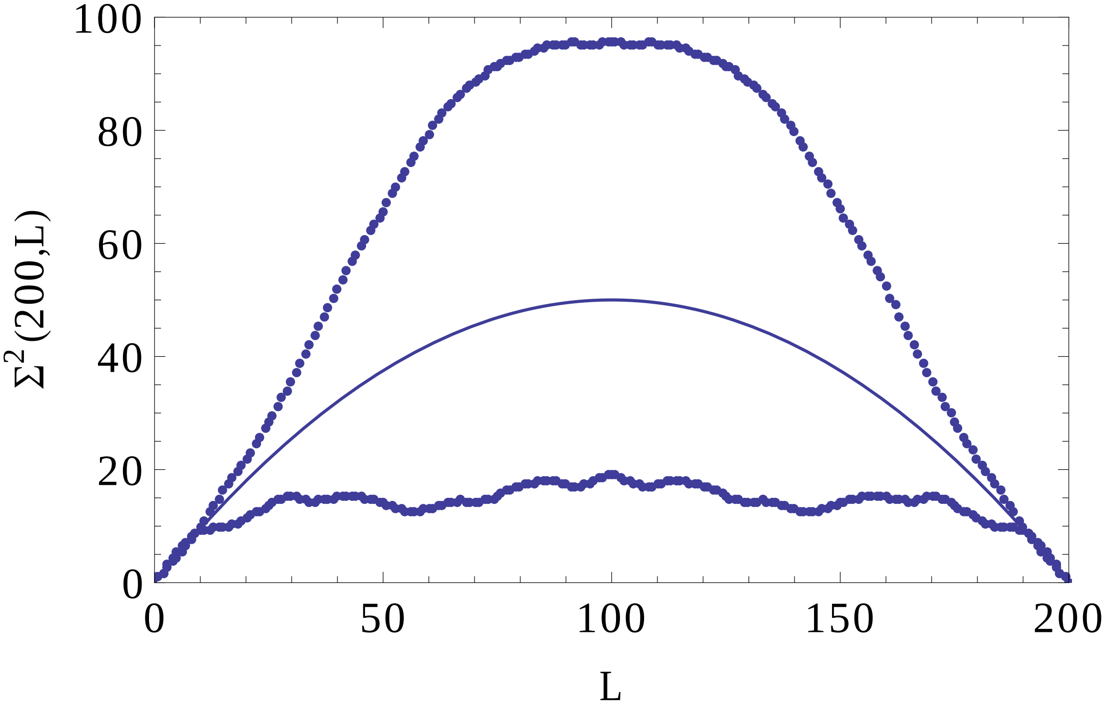

Figure 2.10: Deviations from the Poisson ensemble average Eq. (2.15) (solid curve) of number variance $\overline{\Sigma}^2(200, L)$ from of two members of the Poisson ensemble. Shown are the number variances of two different lists of 200 independent numbers from a flat distribution in order to illustrate the large fluctuations of long-range spectral observables in the Poisson ensemble. See Fig. 2.11 for similar behavior in type-1 spectra.

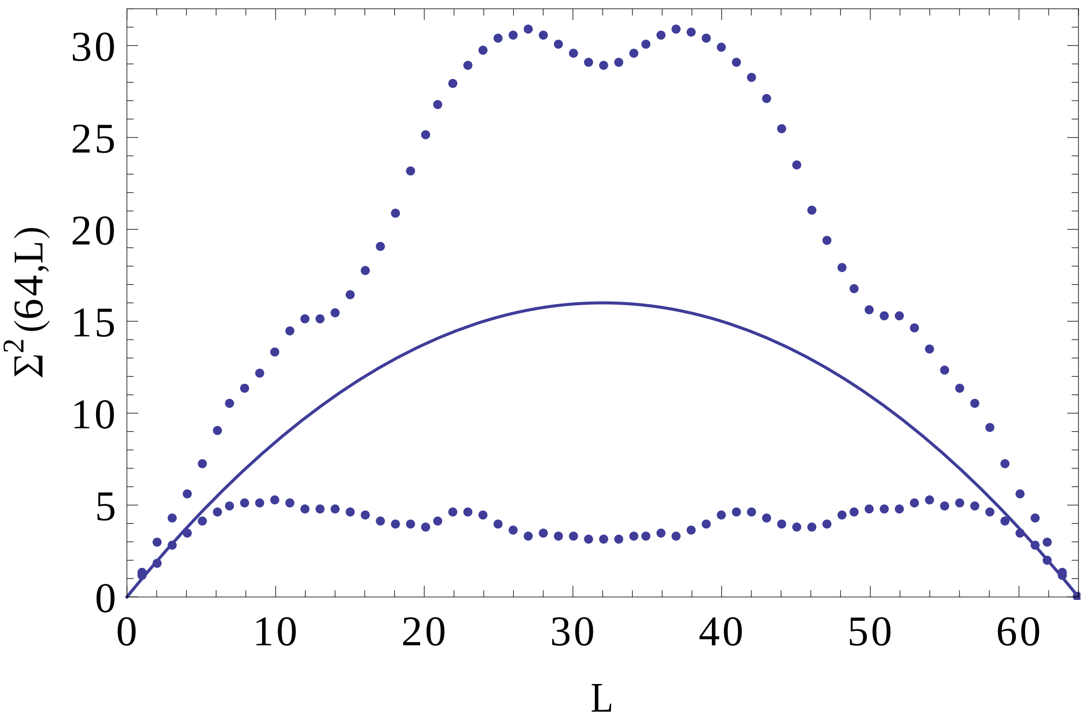

Figure 2.11: Deviations from the Poisson ensemble average Eq. (2.15) (solid curve) of number variance $\overline{\Sigma}^2(64, L)$ from of two members of the $N = 1000$ type-1 ensemble. Shown are the number variances of two matrices used in the ensemble average of Fig. 2.9. The saturation observed in the more rigid of the two spectra is reminiscent of that seen in members of the Poisson ensemble, see Fig. 2.10.

3 Statistics of integrable matrices of higher types

3.1 Ansatz type-M families

We do not yet have a method for directly generalizing the type-1 primary parametrization from Sect. 2.1 to higher type matrices that by definition have fewer commuting partners. Instead, we present another parametrization that produces a subset of integrable families of any type $M \geqslant 1$. The construction is in terms of $3N+1$ real parameters so that in choosing values for them one obtains a matrix $H(x) = xT + V$ with a desired number n of nontrivial commuting partners ($n = N - M$) and no parameter-independent symmetries. As in the type-1 primary parametrization, the parameters can be traced back to eigenvalues of two commuting constant random matrices and a random vector.

Here we present the results; more details can be found in Ref. [17] while the rotationally invariant construction is given in Ref. [13]. Again in the diagonal basis of V, the most general member of an ansatz type-M commuting family is

$$\begin{aligned} [H(x)]_{ij} &= x\gamma_i\gamma_j\left(\frac{d_i-d_j}{\varepsilon_i-\varepsilon_j}\right)\frac{\Gamma_i+\Gamma_j}{2}, \quad i \neq j, \\ [H(x)]_{ii} &= \\ &= d_i - x\sum_{j\neq i}\gamma_j^2\left(\frac{d_i-d_j}{\varepsilon_i-\varepsilon_j}\right)\frac{1}{2}\frac{(\Gamma_i+\Gamma_j)(\Gamma_j+1)}{\Gamma_i+1}, \end{aligned} \tag{3.1}$$

where

$$\begin{aligned} \langle i|i\rangle &\equiv \sum_{j=1}^{N}\frac{\gamma_j^2}{(\lambda_i-\varepsilon_j)^2}, \\ d_i &= \frac{1}{x_0}\sum_{j=1}^{N-M}\frac{g_j}{\langle j|j\rangle}\frac{1}{\lambda_j-\varepsilon_i}, \\ \Gamma_i &= \pm\sqrt{1+\frac{1}{x_0}\sum_{j=N-M+1}^{N}\frac{P_j}{\langle j|j\rangle}\frac{1}{\lambda_j-\varepsilon_i}}. \end{aligned} \tag{3.2}$$

This parametrization gives all type-1, 2, and 3 integrable matrices and only a subset of such for higher types. We call matrices obtained by this construction *ansatz type-M* as opposed to all type-M, these two notions being equivalent for $M = 1, 2, 3$.

Basis-independent considerations from Ref. [13] identify λ_i as eigenvalues of a matrix Λ selected from the GOE and γ_i as selected from a $\delta(1 - |\gamma|^2)$ distribution, as was the case for the primary parametrization of type-1 matrices in Sect. 2.1. One may alternatively select the ε_i as eigenvalues of a GOE matrix E and from them derive the λ_i. We find that this choice has no effect on the statistics. Unique to the ansatz parametrization are the $(N - M)$ parameters g_i and M parameters P_i. Ref. [13] identifies these parameters as eigenvalues selected from an $N \times N$ GOE matrix G [33] satisfying $[G, \Lambda] = 0$. The sign of Γ_i can be chosen arbitrarily for each i and each set of sign choices corresponds to a different commuting family. The λ_i by construction are solutions of the following equation with arbitrary (but fixed) real $x_0 \neq 0$:

$$\begin{aligned} f(\lambda_i) &\equiv \sum_{j=1}^{N} \frac{\gamma_j^2}{\lambda_i - \varepsilon_j} - \frac{1}{x_0} = 0, \\ F(\varepsilon_i) &\equiv \sum_{j=1}^{N} \frac{1}{\langle j|j\rangle} \frac{1}{\lambda_j - \varepsilon_i} - x_0 = 0. \end{aligned} \tag{3.3}$$

The second line of Eq. (3.3) follows from the first by writing both the partial fraction decomposition and factorized form of $F(z) = 1/f(z)$ and matching residues. Eqs. (3.2) and (3.3) mean that ansatz type-M matrices are written in terms of an auxiliary primary type-1 problem with parameter x_0 and (unnormalized) eigenstates $|i\rangle$, see Eq. (2.5) and Ref. [13]. Note the important distinction between x and x_0 – namely that x is free but x_0 is fixed for a given family of commuting matrices.

Due to the square root in the expression for Γ_i, Eq. (3.2), a given set of P_i will typically result in a complex set of Γ_i. The matrix $H(x)$ will subsequently be complex symmetric, rather than real, although it will still satisfy all requirements of integrability. Because in this work we study the eigenvalues of real symmetric integrable matrices, we elect to reparametrize Γ_i in a way that guarantees they be real without awkwardly scaling each set of P_i

$$\Gamma_i = \pm\sqrt{\frac{\prod_{j=1}^{N}(\phi_j - \varepsilon_i)}{\prod_{k=1}^{N}(\lambda_k - \varepsilon_i)}}, \tag{3.4}$$

where the M ϕ_j are real parameters such that (upon ordering ε_j and λ_j for argument's sake) $\varepsilon_j < \phi_j < \lambda_j$ if $x_0 > 0$ and $\lambda_j < \phi_j < \varepsilon_j$ if $x_0 < 0$. The resulting Γ_i are real-valued. As there is no existing basis-independent interpretation for ϕ_j, we simply choose them from a uniform distribution on their allowed intervals. We find that the choice of ϕ_i or P_i to generate the Γ_j has a numerically undetectable effect on the eigenvalue statistics.

Varying parameters g_j produces different matrices within the same commuting family, while varying the remaining parameters $\gamma_i, \lambda_i, \phi_i, x_0$ generates sets of matrices from different families. A natural way to choose a basis for the ansatz type-M commuting family is to define the $n = N - M$ nontrivial $H^k(x)$ such that $g_j = \delta_{kj}$ in Eq. (3.2) for $1 \leqslant j \leqslant N - M$. In other words,

$$\begin{gathered} H^k(x) = xT^k + V^k \text{ is given by Eq. (3.1) with} \\ d_i \to d_i^k = \frac{1}{x_0}\frac{1}{\langle k|k\rangle}\frac{1}{\lambda_k - \varepsilon_i}. \end{gathered} \tag{3.5}$$

for $k = 1, \ldots, N - M$. In particular,

$$V^k = \text{Diag}(d_1^k, d_2^k, \ldots, d_N^k) \tag{3.6}$$

A general member of the commuting family is

$$H(x) = \sum_{k=1}^{N-M} g_k H^k(x). \tag{3.7}$$

up to a multiple of the identity trivial to the study of level spacing statistics.

Ansatz type-M families have an exact solution in terms of a single equation similar to Eq. (2.5) given in Ref. [17], which has slight differences in notation as compared to here.

To study level statistics of ansatz matrices, we numerically diagonalize them rather than use the computationally cumbersome exact solution.

A fundamental difference between ansatz type-M matrices and the primary type-1 parametrization is that the eigenvalues of the matrix V in the former are heavily constrained by Eq. (3.2), while in the latter they are free parameters. In particular, as explained in Ref. [13] the primary type-1 V is selected from the GOE, while the ansatz V is a certain primary type-1 matrix evaluated at $x = -x_0$, i.e.,

$$V(x_0) = -x_0 T_{H_1} + H_1, \tag{3.8}$$

where H_1 has $N - M$ arbitrary eigenvalues g_i and M eigenvalues equal to zero. By the results of Sect. 2, ansatz $V = V(x_0)$ will typically have Poisson statistics. The resolution to this apparent disconnect between the two parametrizations is that for $|x_0| \ll 1$, $V(x_0)$ will have the eigenvalue statistics of H_1. We argue in Ref. [13] that the $N - M$ g_i are a subset of eigenvalues of an $N \times N$ matrix from the GOE, so that for M not too large and $x_0 \ll 1$ we obtain Wigner-Dyson statistics in ansatz V.

We then forgo studying crossovers in the coupling x of level statistics of ansatz type-M matrices $H(x) = xT + V$ because ansatz V have Poisson statistics for typical parameter choices. Instead, we focus on the behavior of the statistics with respect to parameter correlations, the number M and the number of basis matrices. In all numerical work on ansatz matrices we set $x_0 = 1$, as this is a typical coupling value for the auxiliary type-1 problem.

3.2 Correlations in ansatz parameters

Building on the results of Sect. 2.4, here we explore effects of parameter correlations on the statistics in general type-M ansatz matrices. Introducing correlations between d_i and ε_i in this case is more complicated than in Sect. 2.4 because the d_i here are not all independent. Fortunately, Eq. (3.2) admits a simple way to produce such correlations. As an example, consider the case when $g_j = \lambda_j$

$$\begin{aligned} d_i &= \frac{1}{x_0} \sum_{j=1}^{N-M} \frac{\lambda_j - \varepsilon_i + \varepsilon_i}{\langle j|j\rangle} \frac{1}{\lambda_j - \varepsilon_i} \\ &= \frac{1}{x_0} \varepsilon_i \left(\sum_{j=1}^{N-M} \frac{1}{\langle j|j\rangle} \frac{1}{\lambda_j - \varepsilon_i} \right) + (\text{const}) \\ &= \varepsilon_i \left(1 - \frac{1}{x_0} \sum_{j=1}^{M} \frac{1}{\langle j|j\rangle} \frac{1}{\lambda_j - \varepsilon_i} \right) + (\text{const}), \end{aligned} \tag{3.9}$$

where the second part of Eq. (3.3) was used. The sums in the third line of Eq. (3.9) introduce a randomizing factor that has a weak effect for small M but that destroys the correlation between d_i and ε_i at intermediate values of M. Fig. 3.1 shows the now familiar level statistics crossover in δ for ansatz matrices of different size and type with $g_k = \lambda_k(1+\delta G_k)$, where G_k is an $\mathcal{O}(1)$ random number chosen from a normal distribution and δ a parameter controlling the size of the perturbation. Just as in Sect. 2.4, the crossover to Poisson statistics is centered about $\delta \sim N^{-1}$. More generally, we can induce level repulsion in ansatz type-M matrices if $M \ll N$ when $g_k = f(\lambda_k)$, a smooth function of λ_k.

3.3 Basis matrices: ansatz higher types

We now generalize the type-1 results of Sect. 2.5 to apply to all ansatz type-M matrices. Recall that a general ansatz type-M matrix $H(x) = xT + V$ can be written as a linear combination of basis matrices $H^k(x)$ for which $g_i = \delta_{ik}$ (see Eq. (3.7)).

We see again in Figs. 3.2 and 3.3 that Poisson statistics emerge for relatively small linear combinations of basis matrices. Denoting m as the number of conservation laws contained in a linear combination, i.e.,

$$H(x) = \sum_{i=1}^{m} g_k H^k(x), \quad m \leqslant N - M, \tag{3.10}$$

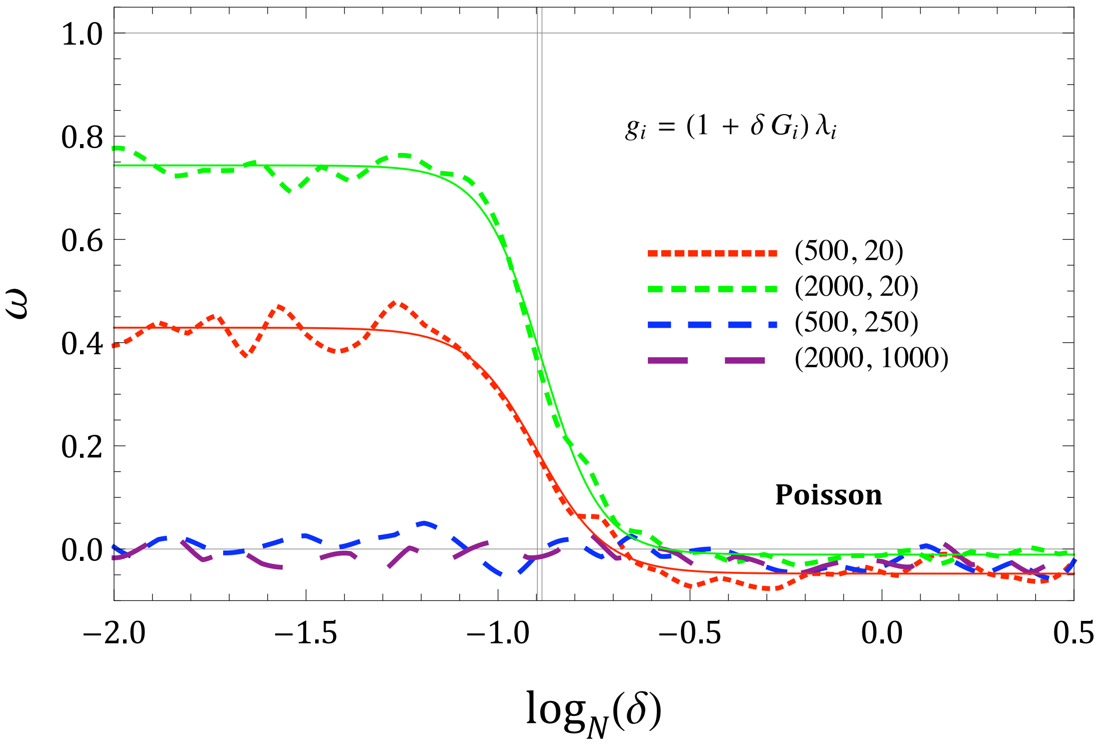

Figure 3.1: Variation in the Brody parameter $\omega(\delta, N)$ when $g_i = \lambda_i(1 + \delta G_i)$ in the level statistics of $N \times N$ ansatz type-M integrable matrices $H(x = 1)$, Eq. (3.1), for various N and M. Ordered pairs in the legend indicate size and type (N, M) of the matrices, δ controls the strength of the perturbation from the point $\delta = 0$ where the parameters g_i and λ_i defining these integrable matrices are correlated, and G_i is an $\mathcal{O}(1)$ random number from a normal distribution. The crossover in δ for small M is similar to the primary type-1 crossovers in δ and x seen in Figs. 2.2,2.5 and 2.6. For larger M, correlations cannot be introduced by this method, see Eq. (3.9). Despite type-M matrices having fewer than the maximum number of conservation laws, the crossover still demonstrates the scaling given in Eq. (2.10) (solid curves) with a crossover centered around $X_0 \sim -1$ (vertical line). As before, deviations from correlation of size $\delta \propto N^{-0.5}$ are enough for the statistics to become Poisson. Each plotted value $\omega(\delta, N)$ is computed for the combined level spacing distribution of several matrices from the ensemble. For the case of correlations in ansatz matrices, we choose all $\Gamma_k > 0$ in order to avoid pathological statistics in $H(x)$.

we investigate the Brody parameter $\omega(m, N)$ from Eq. (2.12). In Fig. 3.2, $N = 500$, $\omega(m, N)$ decays to zero as a function of m in nearly the same way for $M = 470$ as for $M = 20$. It is only for very large M, such as $M = 497$, that level clustering is forbidden, and this only because we can use a maximum of 3 nontrivial basis matrices. Similar behavior emerges for $N = 2000$ in Fig. 3.3. For all N and M tested we find $b \sim 1$ (with precise values given in the captions). Therefore, we can estimate a similar bound as in Sect. 2.5 for the minimum number of conservation laws needed for Poisson level statistics, namely $m_{\min} < \mathcal{O}(N^\alpha)$ where $0 < \alpha < 0.25$, obtained from the $M = N/2$ cases. Since m cannot exceed the total number of conservation laws $n = N - M$ for type-M matrices, this provides a lower bound $n_{\min} = m_{\min} < \mathcal{O}(N^\alpha)$ consistent with $m_{\min} \approx \log N$.

4 Analytical results: perturbation theory

Some of the numerical observations found in Sects. 2 and 3 can be understood using perturbation theory in the parameter x. We restrict our analysis to the primary type-1 parametrization because our arguments for this case are much more transparent than for the ansatz construction. The analysis for ansatz matrices is similar.

The eigenvalues $\eta_m(x)$ of $H(x)$ to first order in x are given by the second equation in Eq. (2.2), where we set constant $|\gamma_j|^2 = N^{-1}$ for clarity and to achieve proper scaling for large N

$$\eta_m(x) \approx d_m - \frac{x}{N} \sum_{j \neq m} \left(\frac{d_m - d_j}{\varepsilon_m - \varepsilon_j} \right). \tag{4.1}$$

The first term comes from V, which has a Wigner-Dyson $P(s)$, and the second term from T, which is determined by the integrability condition and whose level statistics we do not control. Let us estimate the x at which the two terms in Eq. (4.1) become comparable. Note that d_k and ε_k both lie on $\mathcal{O}(1)$ intervals so that T and V scale in the same way for large N. Suppose ε_k are ordered as $\varepsilon_1 < \varepsilon_2 < \cdots < \varepsilon_N$. When d_k and ε_k are uncorrelated $d_m - d_j$ is $\mathcal{O}(1)$ when j is close to m, i.e., when $(\varepsilon_m - \varepsilon_j) = \mathcal{O}(N^{-1})$. The second term in

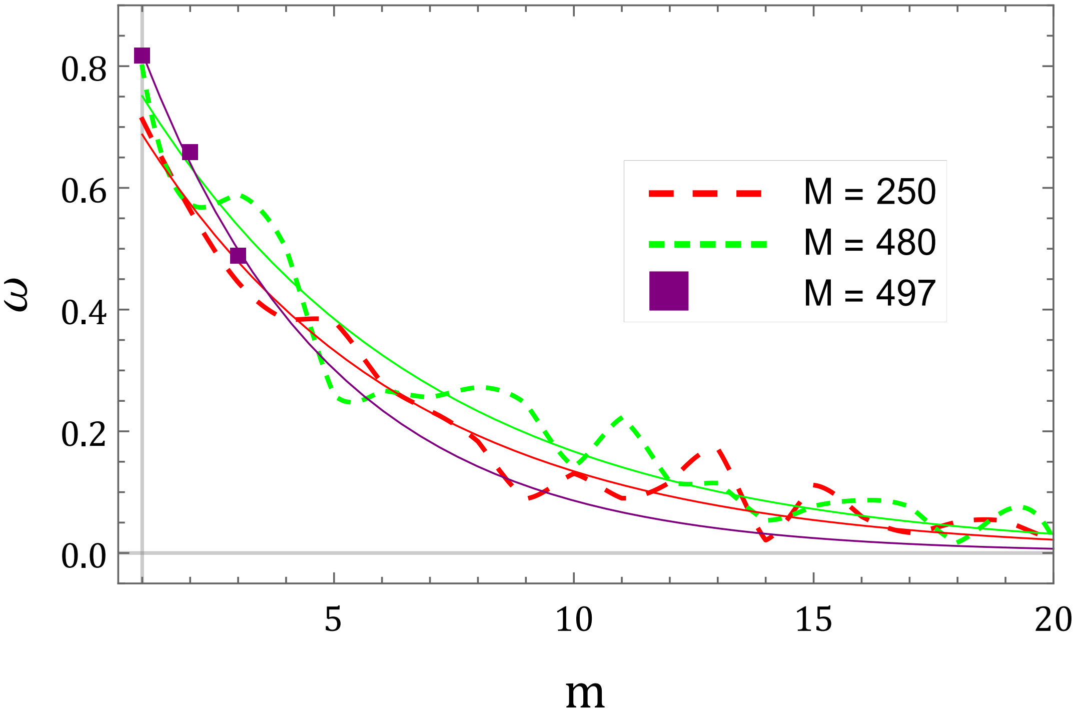

Figure 3.2: Graph of the Brody parameter $\omega(m,N)$ given by Eq. (2.7) vs. number m of ansatz type-M basis matrices $H^k(x)$, see Eq. (3.5), contained in linear combination $H(x) = \sum_{k=1}^{m} g_k H^k(x)$ for $N = 500$, $x = 1$. The fits presume exponential decay and are expressed in terms of two parameters (a, b) from Eq. (2.12). For $M = (250, 480)$ we find the decay constant $b = (1.13, 1.04)$, indicating that we only need $m_{\text{min}} \approx \log N$ conservation laws for Poisson statistics to emerge, independent of type. We do not observe Poisson statistics for $M = 497$ because the maximum number of nontrivial basis matrices is 3 in this case, and we see that we need at least ~ 15 conservation laws for Poisson statistics to start emerging for $N = 500$. See Fig. 3.3 for a similar plot for $N = 2000$ and Fig. 2.7 for the same concept in type-1 matrices. Each plotted value $\omega(m,N)$ is computed for the combined level spacing distribution of several matrices from the ensemble.

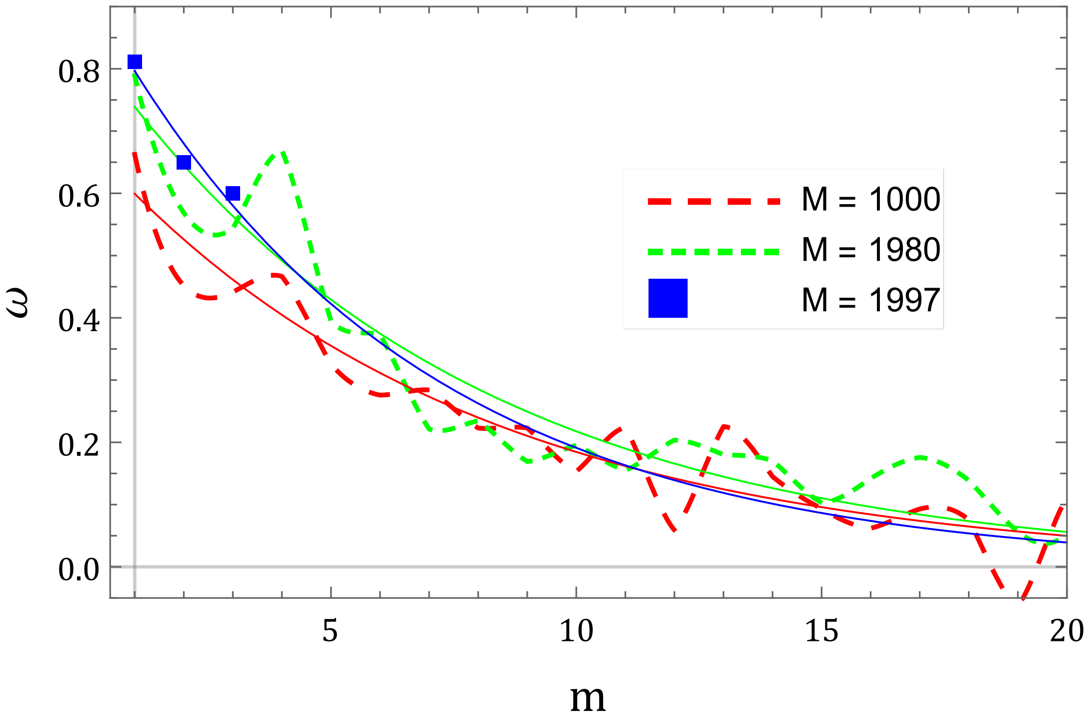

Figure 3.3: Brody parameter $\omega(m, N)$ (see Eq. (2.7)) vs. number m of ansatz type-M basis matrices $H^k(x)$, see Eq. (3.5), contained in linear combination $H(x) = \sum_{k=1}^{m} g_k H^k(x)$ for $N = 2000$, $x = 1$. The fits presume exponential decay and are expressed in terms of two parameters (a, b) from Eq. (2.12). For $M = (1000, 1980)$ we find the decay constant $b = (0.99, 1.03)$, indicating that we only need $m_{\min} \approx \log N$ conservation laws for Poisson statistics to emerge, independent of type. We do not observe Poisson statistics for $M = 1997$ because the maximum number of nontrivial basis matrices is 3 in this case, and we see that we need at least $\sim$ 20 conservation laws for Poisson statistics to start emerging for $N = 2000$. See Fig. 3.2 for a similar plot for $N = 500$ and Fig. 2.7 for the same concept in type-1 matrices. Each plotted value $\omega(m, N)$ is computed for the combined level spacing distribution of several matrices from the ensemble.

Eq. (4.1) is then $xc_m \ln N$, where $c_m = \mathcal{O}(1)$ is a random number only weakly correlated with d_m. We performed simple numerical tests that confirm this scaling argument.

If we now order d_m, c_m in general will not be ordered, i.e., if $d_{m+1} > d_m$ is the closest level to d_m and therefore $(d_{m+1} - d_m) = \mathcal{O}(N^{-1})$, the corresponding difference $(c_{m+1} - c_m) = \mathcal{O}(1)$. The contributions to level-spacings from the two terms in Eq. (4.1) become comparable for $x = x_c \approx 1/(N \ln N)$. It makes sense that the second term introduces a trend towards a Poisson distribution because it is a (nonlinear) superposition of ε_k and d_k – eigenvalues of two uncorrelated random matrices. Thus, we expect a crossover from Wigner-Dyson to Poisson statistics near $x = x_c$. In our numerics we observe a crossover over the range $N^{-1.5} \lesssim x \lesssim N^{-0.5}$ centered about $x_c \sim N^{-1}$ likely because we do not reach large enough N to detect the log component of the crossover.

This argument breaks down when $d_k = f(\varepsilon_k)$, since in this case $(d_m - d_j) = \mathcal{O}(N^{-1})$ when $(\varepsilon_m - \varepsilon_j) = \mathcal{O}(N^{-1})$. The two terms in Eq. (4.1) become comparable only at $x = \mathcal{O}(1)$; moreover, the second term no longer trends towards Poisson statistics. Relaxing the correlation between d_k and ε_k with $d_k = f(\varepsilon_k)(1 + \delta D_k)$, $D_k = \mathcal{O}(1)$, and going through the same argument, one expects a crossover to Poisson statistics at $\delta = \mathcal{O}(1/N \ln N)$ when $x = \mathcal{O}(1)$.

The level repulsion observed in basis matrices is a consequence of the level repulsion implicit in the parameters λ_i, independent of the choice of ε_i, see the text below Eq. (2.9) and Fig. 2.4. Indeed, basis matrices $H^i(x)$ in the primary type-1 parametrization, Eq. (2.2), have eigenvalues $\eta^i_j(x) = x\gamma_i^2(\lambda_j - \varepsilon_i)^{-1}$, which is a smooth function of λ_j except near ε_i. The $\eta^i_j(x)$ therefore inherit the level repulsion of the λ_j. Analogous reasoning applies to ansatz basis matrices.

5 Ergodicity in integrable matrix ensembles

The discussion and figures in this section make frequent reference to the "primary" construction of type-1 integrable matrices and the "ansatz" construction of type-M integrable matrices. These parametrizations are introduced in Sect. 2.1 and Sect. 3.1, respectively. Ensemble averages are taken with respect to the probability distributions for integrable matrices introduced in Ref. [13].

One of the goals of this work is to determine the extent to which ensembles of integrable matrices are "ergodic." Intuitively, an ensemble is called ergodic if a single randomly selected member has properties that are typical of the entire ensemble. Bohigas and Gianonni [34] expound the subject in generality for random matrices, and here we focus numerically on the meaning of ergodicity with regards to the nearest-neighbor level spacing distribution of integrable matrices. Rigorous results on ergodicty for Gaussian ensembles and the Poisson ensemble were derived by Pandey [35].

We distinguish between three separate ways of generating nearest-neighbor eigenvalue spacing distributions for $N \times N$ integrable matrix ensembles. We call $P_{i,N,R}(s)$ the level spacing distribution, normalized to unity, of the i-th member of the ensemble obtained from a spectral region R containing many eigenvalues (infinitely many as $N \to \infty$). The normalized distribution of spacings in R from all matrices in the ensemble is called $\mathcal{P}_{N,R}(s)$. A third way to characterize spacing statistics is through the normalized distribution of the j-th eigenvalue spacing of all matrices in the ensemble, which we call $p_{N,j}(s)$. Both the regions R and the numbers j are stipulated to be far from the edges of the spectrum. In general, $P_{i,N,R}(s)$, $\mathcal{P}_{N,R}(s)$ and $p_{N,j}(s)$ are distinct distributions. Conceptually, $\mathcal{P}_{N,R}(s)$ and $p_{N,j}(s)$ are ensemble properties while $P_{i,N,R}(s)$ characterizes the spectrum of an individual matrix. In the following definitions, we assume that the spacing distributions converge to a well-defined limit as $N \to \infty$, unlike known pathological examples such as the semiclassical spacing distribution of a harmonic chain [4]. This assumption is supported numerically.

We now describe a precise notion [35] of ergodicity that characterizes the limiting behavior of $P_{i,N,R}(s)$, $\mathcal{P}_{N,R}(s)$ and $p_{N,j}(s)$ as $N \to \infty$. First, we must determine whether

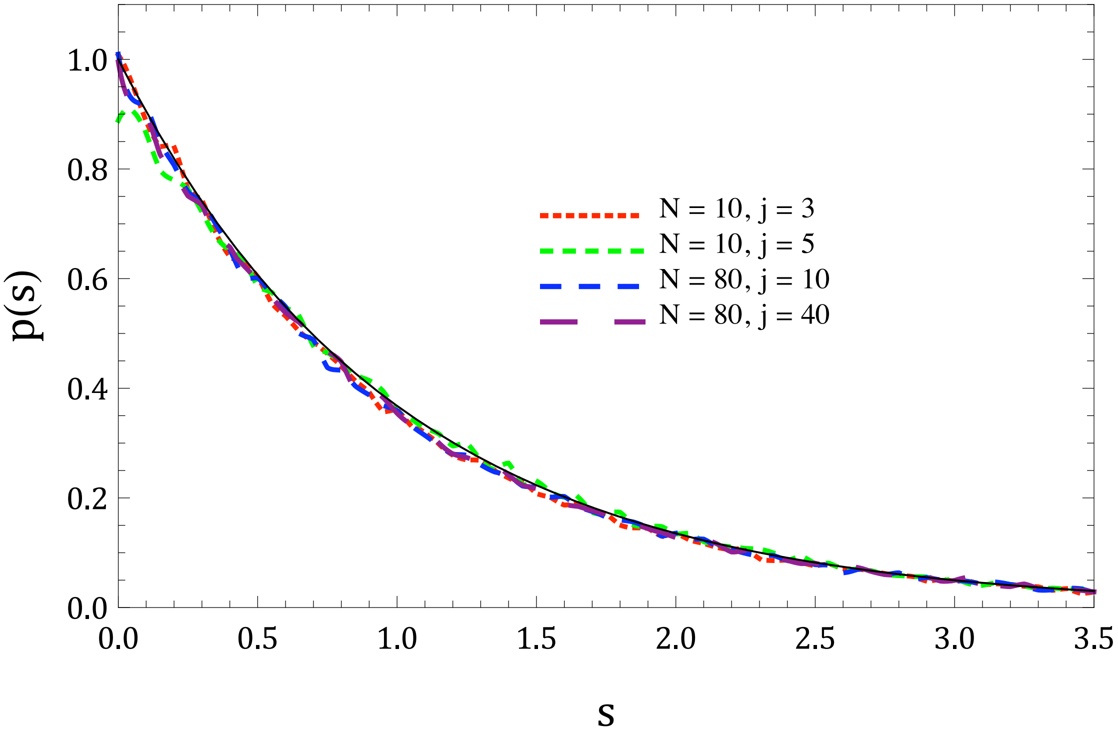

Figure 5.1: Demonstrating the stationary property Eq. (5.1) in type-1 $N \times N$ matrices $H(x)$, $x = 1$ in the primary parametrization. The four numerical curves show the statistics $p_{N,j}(s)$ for $(N, j) = (10, 3)$, $(10, 5)$, $(80, 10)$ and $(80, 40)$, each containing 10^5 eigenvalue spacings. The statistics are nearly independent of j for $N = 10$, and for $N = 80$ there is no perceptible difference between $j = 10$ and $j = 40$. The solid line is a Poisson distribution $p(s) = e^{-s}$. Stationarity is shown to hold also for type-M ansatz matrices in Fig. 5.2.

$p_{N,j}(s)$ is asymptotically stationary, i.e., independent of j

$$\lim_{N\to\infty} p_{N,j}(s) = p(s). \tag{5.1}$$

In the case of type-1 matrices in the primary parametrization, we see in Fig. 5.1 that the graphs of two different $p_{10,j}(s)$ closely resemble those of two different $p_{80,j}(s)$, the latter of which are clearly Poisson. The same is true for ansatz matrices of any type, but the convergence to a Poisson distribution does not become apparent until $N = 300$ as in Fig. 5.2. We conclude that Eq. (5.1) is true for integrable matrices.

We now turn to the notion of spectral averaging, i.e., the function $P_{i,N,R}(s)$. If Eq. (5.1)

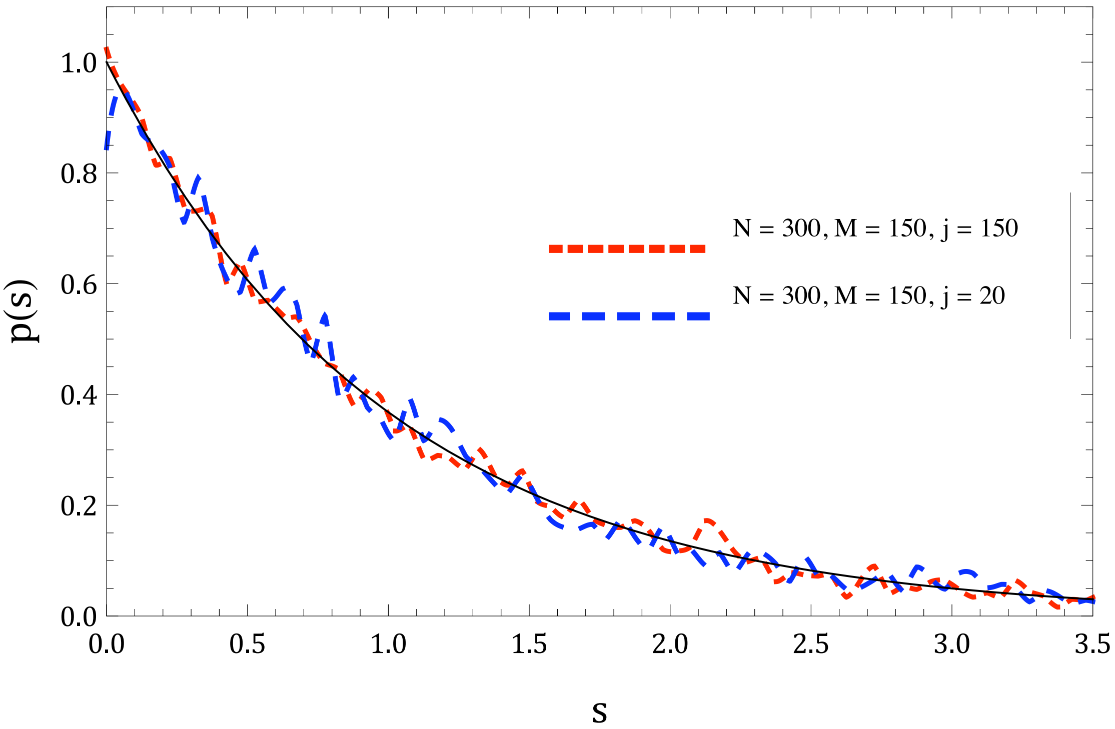

Figure 5.2: Demonstrating the stationarity property Eq. (5.1) in ansatz type-150 $N \times N$ matrices $H(x)$, $x = 1$ and $N = 300$. The two numerical curves show the statistics $p_{N,j}(s)$ for $(N, j) = (300, 150)$ and $(300, 20)$, each containing $\sim 10^4$ eigenvalue spacings. The statistics are nearly independent of j, although higher N would be needed in order for the differences to disappear. The solid line is a Poisson distribution $p(s) = e^{-s}$.

holds, the ensemble averaged $P_{i,N,R}(s)$, called $\mathcal{P}_{N,R}(s)$, satisfies

$$\lim_{N\to\infty} \mathcal{P}_{N,R}(s) = p(s), \tag{5.2}$$

independent of the region R. In practice, we numerically unfold the spectrum (see Appendix A) in order to take into account any effects a non-stationary mean level spacing can have on $P_{i,N,R}(s)$, which characterizes fluctuations about the mean level spacing. In this work, we say integrable matrices are spectrally stationary if

$$\lim_{N\to\infty} P_{i,N,R}(s) = P_i(s), \tag{5.3}$$

and ergodic with respect to nearest neighbor level statistics if

$$P_i(s) = p(s). \tag{5.4}$$

Two points are to be made about Eq. (5.3) and Eq. (5.4). First, Eq. (5.3) is similar in spirit to, but not implied by, Eq. (5.1). Figs. 5.3-5.6 show for various integrable matrices, basis matrices included, that the level statistics from a single large matrix, $P_{i,N,R}(s)$, do not depend on the spectral region R used.

Second, the limiting distribution is independent of the index i, which means that a single matrix's spacing distribution is typical of the ensemble. In rigorous work on Gaussian ensembles [35], this is proved by showing the ensemble averaged variance of $P_{i,N,R}(s)$ vanishes as $N \to \infty$. In this work, we compare numerically generated graphs of spectral spacing distributions to ensemble averaged ones for large N. By comparing Figs. 5.7, 5.8 to Figs. 5.3, 5.4, we see that for large N, $P_{i,N,R}(s) \to p(s)$.

The properties of stationarity and ergodicity are useful if they set in quickly for small N, because smaller matrices are more accessible both analytically and computationally. A classic example in Gaussian random matrix theory is the Wigner surmise, derived from 2×2

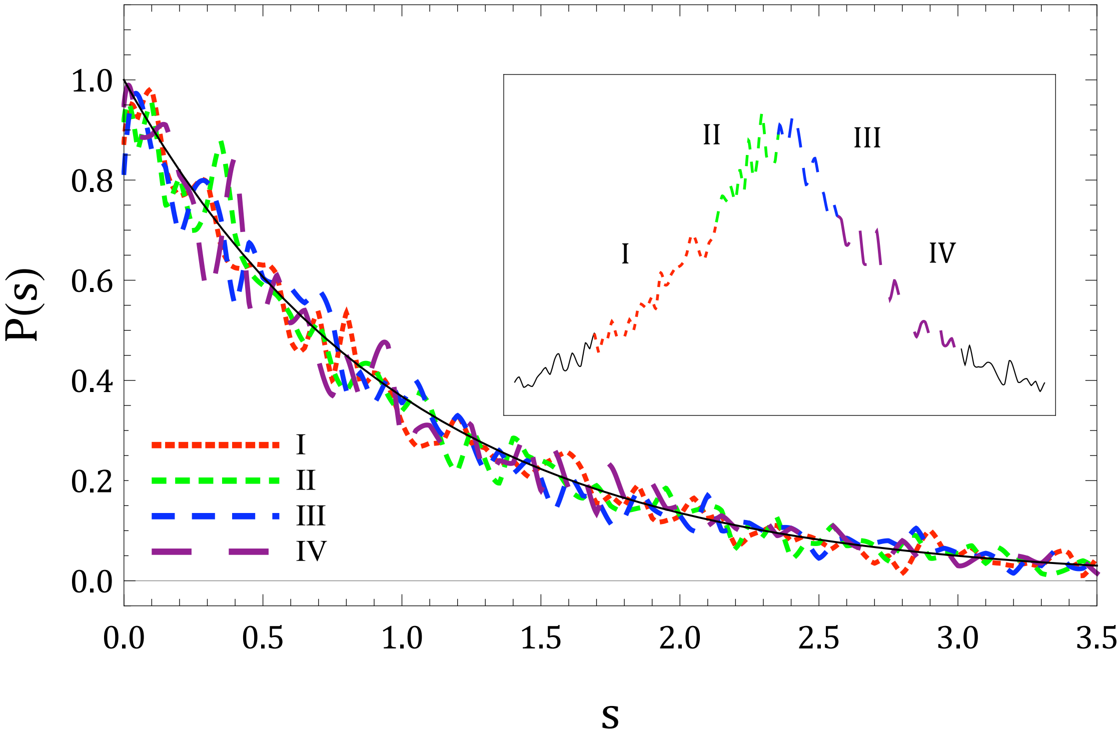

Figure 5.3: Demonstrating spectral stationarity Eq. (5.3) in type-1 matrices. Shown are the level statistics $P_{i,N,R}(s)$ of a single (i-th member of the ensemble) type-1 integrable matrix $H(x)$, $x = 1$ and $N = 20000$, for different regions R of its spectrum containing 4000 eigenvalues each. The inset shows the density of states of this matrix and indicates which numerical curve corresponds to which region R. The distributions $P_{i,N,R}(s)$ shown are independent of R, indicating that type-1 matrix spectra are stationary with respect to nearest neighbor level statistics. Noting that these distributions are Poisson, $P_{i,N,R}(s) \approx e^{-s}$ (solid curve) and comparing to Fig. 5.7 which gives $\mathcal{P}_{N',R}(s) \approx e^{-s}$ for $N' = 2000$, we see that ergodicity, Eq. (5.4), is satisfied for type-1 integrable matrices.

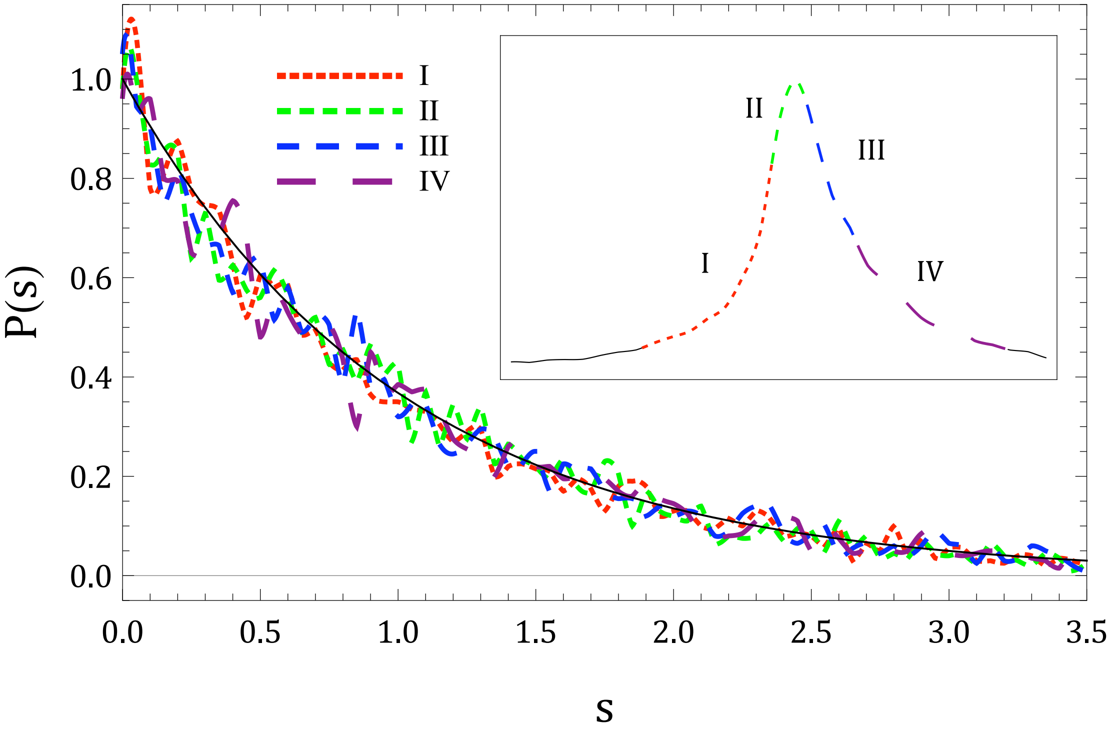

Figure 5.4: Level statistics $P_{i,N,R}(s)$ of a single integrable matrix $H(x)$, $x = 1$, $N = 20000$ and $M = 10000$, for different regions R of its spectrum (the subscript i indicates $H(x)$ is the i-th matrix in the ensemble) containing 4000 eigenvalues each. Inset: the density of states of $H(x)$ showing the correspondence between the distributions and regions R. The distributions $P_{i,N,R}(s)$ are independent of R, indicating that type-M matrix spectra are stationary with respect to nearest neighbor level statistics, i.e., Eq. (5.3) holds. Noting that these distributions are Poisson, $P_{i,N,R}(s) \approx e^{-s}$ (solid curve) and comparing to Fig. 5.8 which gives $\mathcal{P}_{N',R}(s) \approx e^{-s}$ for $N' = 2000$ $M' = 1000$, we verify the ergodic property, Eq. (5.4).

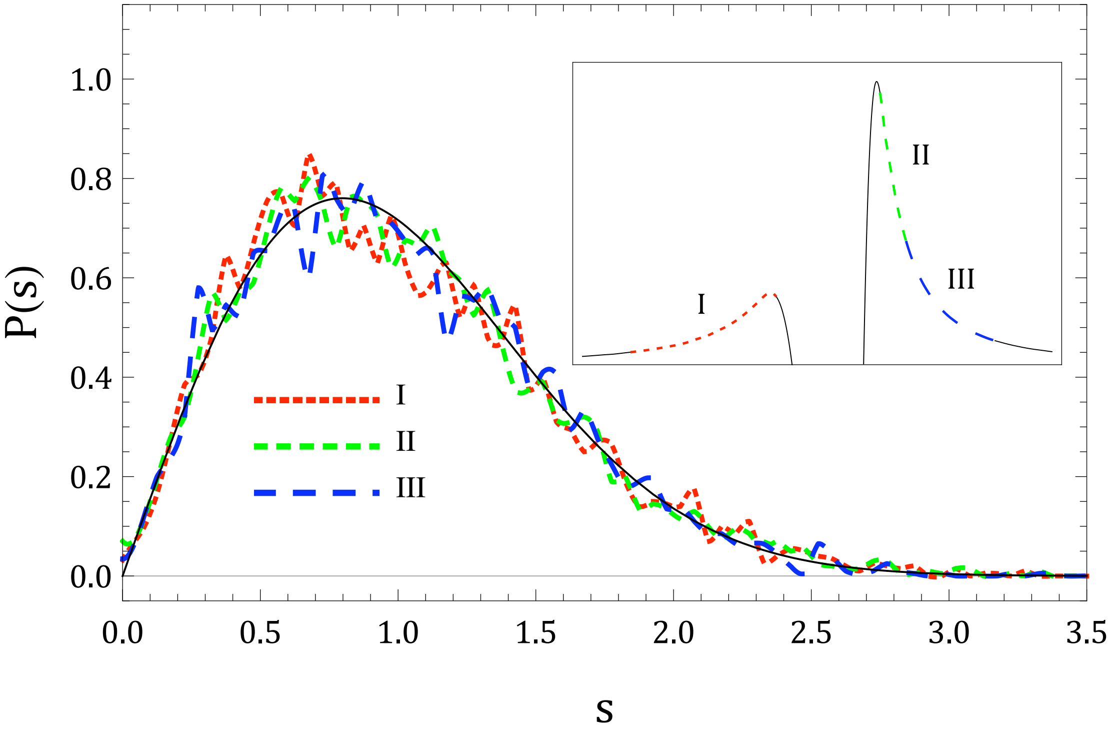

Figure 5.5: Demonstrating spectral stationarity, Eq. (5.3), in level statistics of primary type-1 basis matrices (defined in Sect. 2.1). Shown are the level statistics $P_{i,N,R}(s)$ of a single type-1 integrable basis matrix, $x = 1$ and $N = 20000$, for different regions R of its spectrum (the subscript i indicates $H(x)$ is the i-th matrix in the ensemble). Each spectral region R contains 4000 eigenvalues. The inset shows the density of states of this matrix and indicates which numerical curve corresponds to which region R. The distributions $P_{i,N,R}(s)$ shown are independent of R, indicating that type-1 basis matrix spectra are stationary with respect to level statistics. Even though there is a band gap, the level statistics on either side of the gap are the same. The solid curve is the Wigner surmise $P(s) = \frac{\pi}{2} s e^{-\frac{\pi}{4}s^2}$.

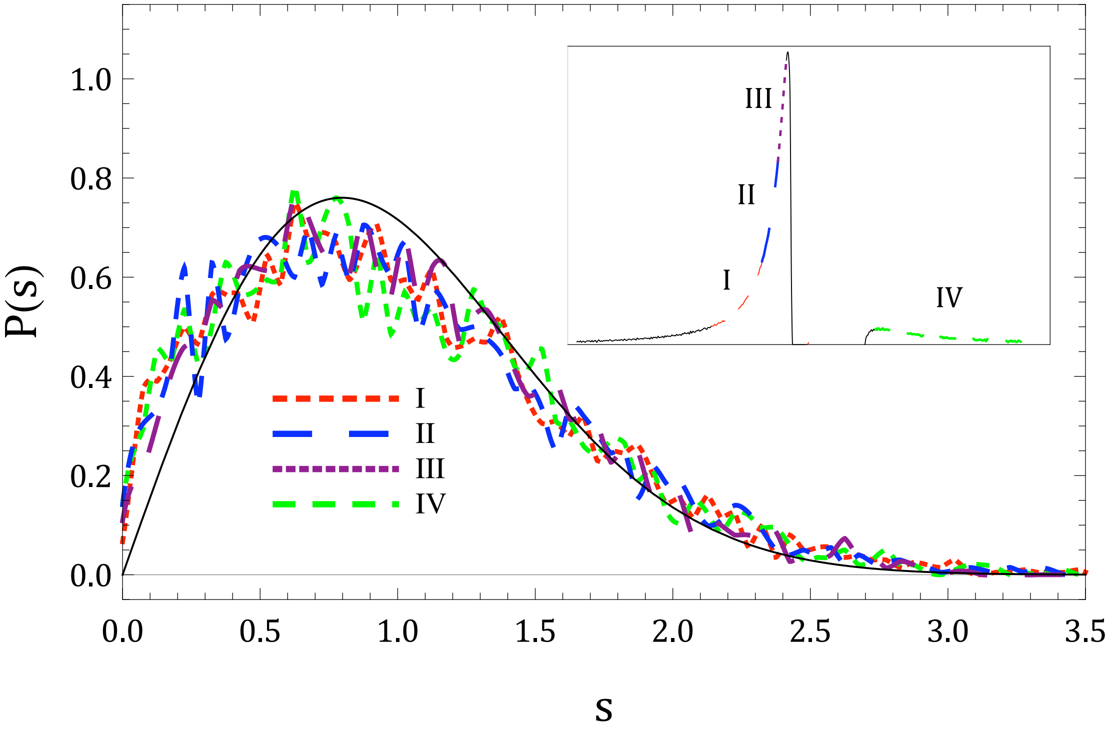

Figure 5.6: Demonstrating spectral stationarity, Eq. (5.3) in level statistics of ansatz basis matrices (defined in Sect. 3.1). Shown are the level statistics $P_{i,N,R}(s)$ of a single type-10000 integrable ansatz basis matrix, $x = 1$ and $N = 20000$, for different regions R of its spectrum (the subscript i indicates $H(x)$ is the i-th matrix in the ensemble). The inset shows the density of states of this matrix and indicates which numerical curve corresponds to which region R. The distributions $P_{i,N,R}(s)$ shown are independent of R, indicating that type-M basis matrix spectra are stationary with respect to level statistics. Even though there is a band gap, the level statistics on either side of the gap are the same. The solid curve is the Wigner surmise $P(s) = \frac{\pi}{2} s e^{-\frac{\pi}{4} s^2}$. Regions I - III use 4000 eigenvalues apiece, while region IV uses only 3000 and gets to within 1% of the spectrums edge.

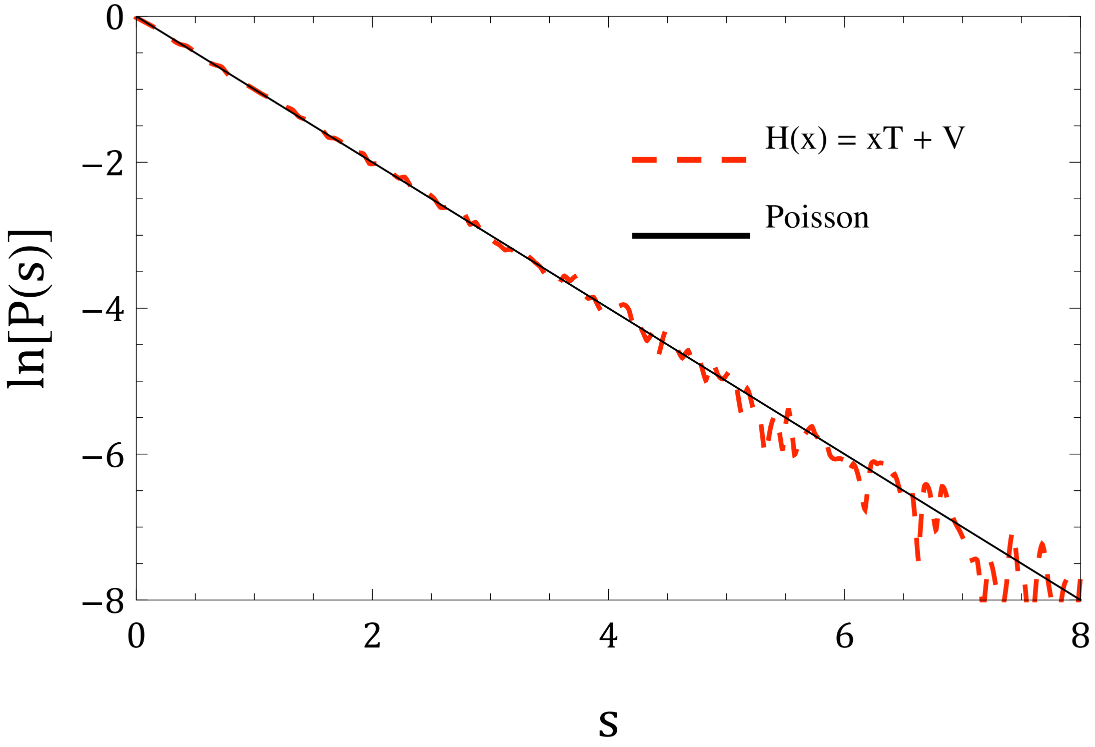

Figure 5.7: Demonstrating ergodicity Eq. (5.4) in type-1 matrices (continuing from Fig. 5.3). A plot of $\ln \mathcal{P}_{N,R}(s)$, $N = 2000$ for 100 type-1 matrices in the primary parametrization. We do not specify the spectral region R because Fig. 5.3 shows that the statistics are independent of R. The solid line is $f(s) = -s$, indicating that $\mathcal{P}_{N,R}(s)$ is indeed Poisson for $N = 2000$ type-1 matrices.

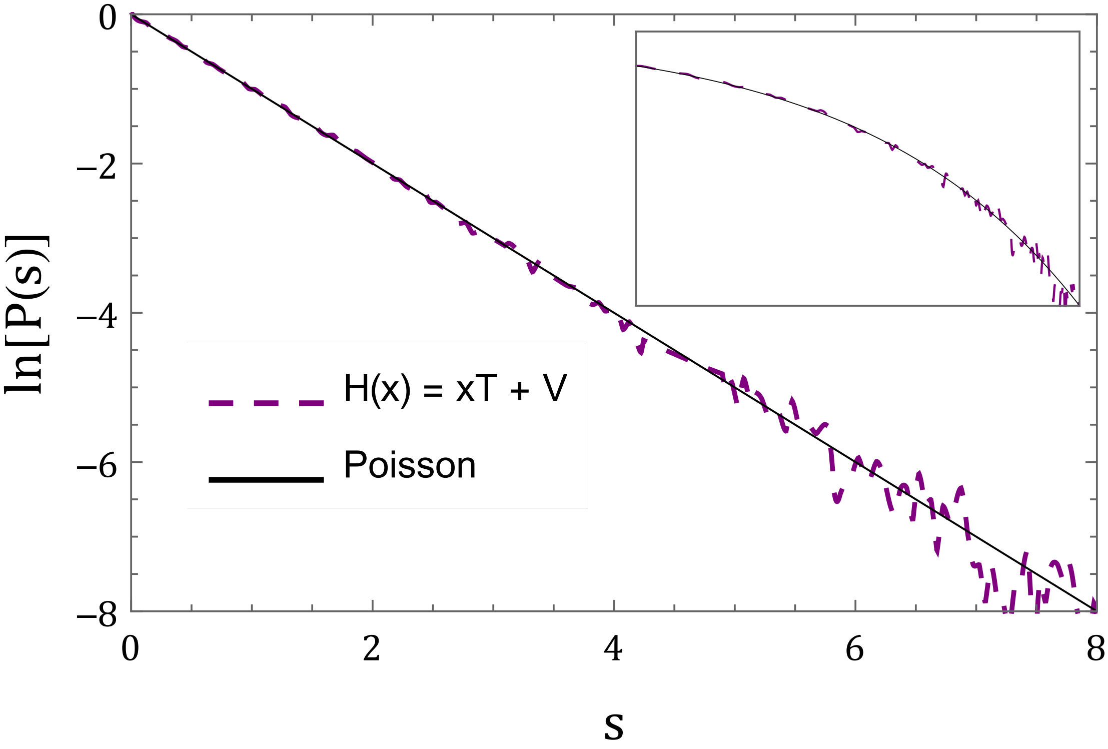

Figure 5.8: Demonstrating ergodicity Eq. (5.4) in type-M ansatz matrices (continuing from Fig. 5.4). A plot of $\ln \mathcal{P}_{N,R}(s)$, $N = 2000$ for 100 type $M = 1000$ matrices in the ansatz parametrization. We do not specify the spectral region R because Fig. 5.4 shows that the statistics are independent of R. The solid line is $f(s) = -s$, indicating that $\mathcal{P}_{N,R}(s)$ is indeed Poisson for $N = 2000$ type-1000 matrices. Inset: Log-log plot of the same data.

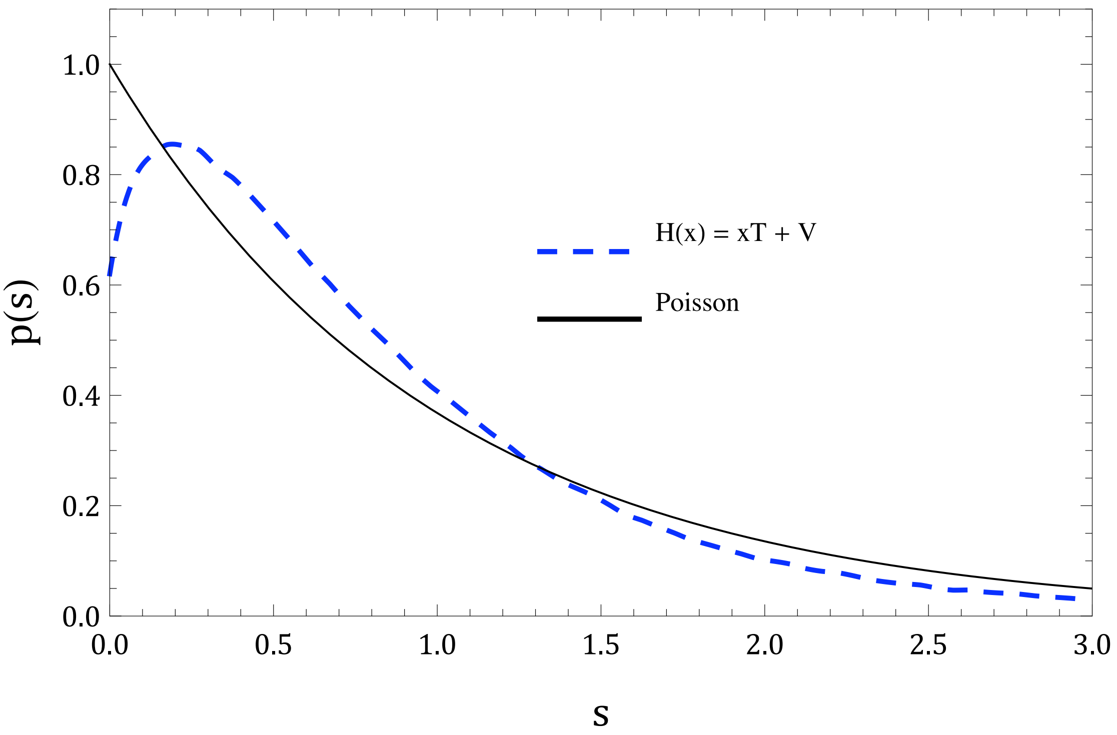

Figure 5.9: Plot of the statistics $p_{3,2}(s)$, the second spacing of 10^6 type-1 integrable matrices $H(x)$ of size $N = 3$ with $x = 1$. The distribution is not Poisson (solid line) and actually has a power law tail (see Fig. 5.10 for more on the tail). In order to observe the limit $p(s)$ of type-1 integrable matrices, defined in Eq. (5.1), we need to go to larger N as in Fig. 5.1.

matrices (see Fig. 1.1), which is extremely useful for characterizing $p(s)$ in the GOE.

We have seen that the nearest neighbor level statistics of integrable matrices $H(x)$ are generally stationary and ergodic, but the property does not set in for small N as quickly as it does for Gaussian random matrices. As an example, Figs. 5.9, 5.10 show $p_{3,2}(s)$, the distribution of the second eigenvalue spacing for $N = 3$, $M = 1$. This distribution differs markedly from a Poisson distribution, especially in the small s and large s regions. For small s there is slight level repulsion and for large s Fig. 5.10 shows that the decay of $p_{3,2}(s)$ is a power law. Numerical data generated in Sects. 2 and 3 used both $P_{i,N,R}(s)$ and $\mathcal{P}_{N,R}(s)$ to represent level statistics of integrable matrices. The results of this section show that for large N, it is valid to treat these two distinct distributions as equal.

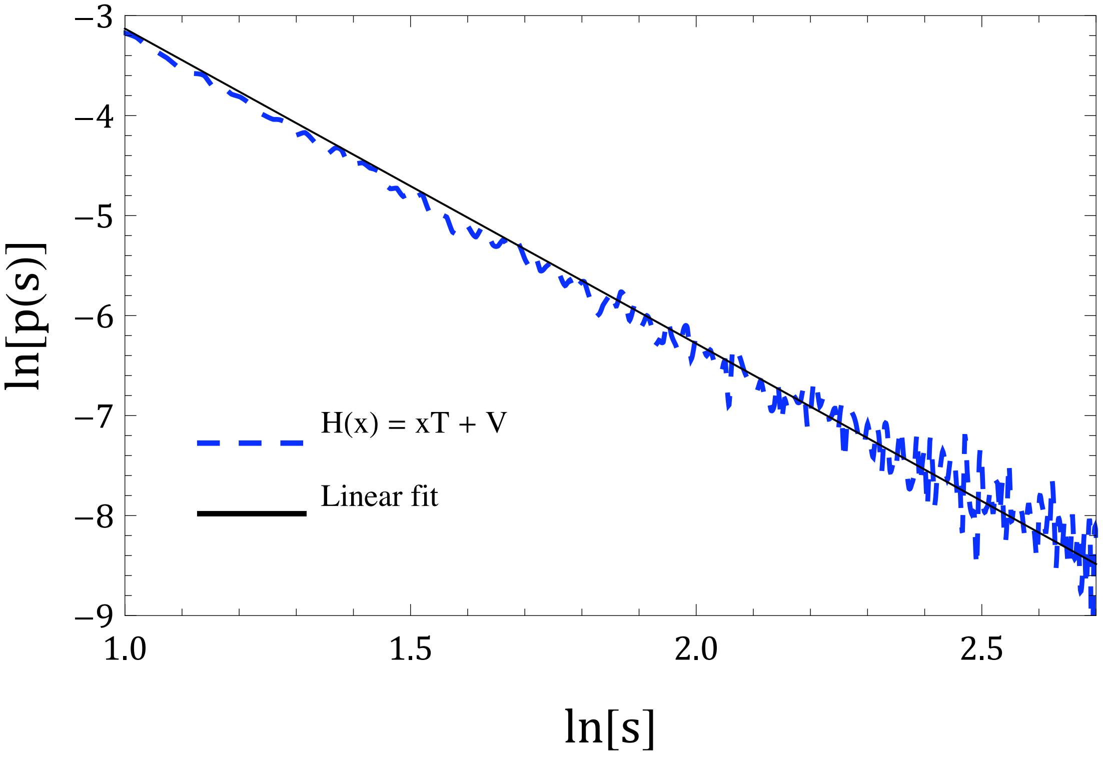

Figure 5.10: Log-log plot of the tail of the distribution $p_{3,2}(s)$ shown in Fig. 5.9, the statistics of the second spacing of 10^6 primary type-1 integrable matrices $H(x)$ of size $N = 3$ with $x = 1$. The linear fit $f(z) = -3.15z + 0.02$ shows that this portion of the tail of the distribution $p_{3,2}(s)$ follows a power law $s^{-\alpha}$ with exponent $\alpha \approx 3.15$. Because the distribution $p_{N,j}(s)$ transitions to Poisson for large N, as evidenced by Fig. 5.1 for type-1 primary matrices and Fig. 5.2 for type-M ansatz matrices, we conclude that exponential behavior in the far tail of $p_{N,j}(s)$ likely emerges only in the limit $N \to \infty$.

6 Conclusion

Just as ensemble averages in ordinary RMT are used to predict the average behavior of generic quantum systems, there now exists an analogous ensemble theory- integrable matrix theory - which we have used to firmly establish the source of Poisson statistics and exceptions in quantum integrable models.

The goal of this work was to demonstrate two properties of ensembles of type-M integrable $N \times N$ matrices linear in a coupling parameter $H(x) = xT + V$ as $N \to \infty$:

1) The nearest neighbor spacing distribution $P(s)$ is Poisson, $P(s) = e^{-s}$, for generic choices of parameters for almost all M. There are cases of level repulsion, but they correspond to sets of measure zero in parameter space.

2) Integrable matrix ensembles are both stationary and ergodic with respect to nearest neighbor level statistics as defined in Sect. 5. It remains to show whether this ergodicity extends to longer range spectral statistics, such as the number variance $\Sigma^2(L)$.

We find that integrable $N \times N$ matrices $H(x)$ have Poisson statistics as long as the number of conservation laws exceeds $n_{\min} \approx \log N$ (or at most $n_{\min} < N^{0.25}$). Basis-independent considerations require (for type-1) GOE statistics at a fixed x_0, but we find that Poisson statistics return at deviations $\delta x \sim N^{-0.5}$. Correlations between otherwise independent parameters also induce level repulsion, but Poisson statistics again return at $\mathcal{O}(N^{-0.5})$ deviations from such correlations. In both cases the crossover occurs roughly over the range $N^{-1.5} \lesssim \delta \lesssim N^{-0.5}$.

Some parameter choices produce matrices that correspond to sectors of certain known quantum integrable models, although general parameter choices do not map to known models. Most important is that, in addition to the linearity in x condition, the ensembles of matrices studied in this work are only constrained by symmetry requirements just like the Gaussian random matrix ensembles. The only difference here is that in the integrable case there are many more symmetries, and they are parameter dependent. We therefore expect our results to apply generally to quantum integrable models with coupling parameters.

Although we justified the numerical results to a certain degree using perturbation theory, an analytic justification for Poisson statistics for integrable matrices is still lacking. Given the relatively simple construction of integrable matrices through basis-independent relations (i.e., matrix equations) involving familiar RMT quantities such as GOE matrices and random vectors [13], we surmise that an analytic demonstration of our numerical results might be feasible – especially in the type-1 case, see, e.g., the discussion below Eq. (2.9) and Refs. [25, 24].

It is interesting to note that many-body localized [36] (MBL) systems are also expected to display Poisson level statistics [37, 38], and there exist random matrix ensembles which model localization and its statistical signatures [39, 40]. Such ensembles are basis dependent, which is natural because localization is a basis-dependent property. The commutation requirements of integrable systems, however, are basis independent, and therefore so is the accompanying integrable matrix theory. A priori, many-body localization and integrability are two independent concepts [41]. Despite this fact, integrable matrices do exhibit a parameter-dependent localization property [43] in which almost all eigenstates of the matrix $H(x) = xT + V$ are localized in the basis of V for all values of x. The stability of this property when a random matrix perturbation is added to $H(x)$, including the possibility of a multifractal phase accompanying the localized and delocalized regimes [40], is the subject of future study.

Acknowledgments: This work was supported in part by the David and Lucille Packard Foundation and by the National Science Foundation under Grant No. NSF PHY11-25915. E. A. Y. also thanks the University of California at Santa Cruz and Kavli Institute for Theoretical Physics, where a significant part of this research was conducted, for hospitality. The work at UCSC was supported by the U.S. Department of Energy (DOE), Office of Science, Basic Energy Sciences (BES) under Award # FG02-06ER46319. We acknowledge Daniel Hansen's contribution at an early stage of this work, especially to the unfolding technique in Appendix A. We also thank Joel Lebowitz for helpful discussions. Finally, we thank the PRE referees for suggestions and questions that led to a considerably improved draft of this work.

Appendix A

Unfolding spectra

The eigenvalue spacing distributions $P(s)$, $\mathcal{P}(s)$ and $p(s)$ (see Sect. 5 for definitions) considered in the level statistics data in this work characterize the fluctuations of spacings about their local means. Unfortunately, a non-constant density of states renders the actual spacings inadequate for measuring these fluctuations. Unfolding the spectrum of a matrix refers to the replacement of the actual eigenvalues η_j with a new set of numbers with unit mean spacing, but that preserve the character of local fluctuations.

We employ a simple method that essentially approximates the inverse density of states (i.e., mean level spacing) of a given matrix through linear interpolations. First, we write the eigenvalues η_j in increasing order, and express the j-th eigenvalue η_j in terms of the actual spacings S_k

$$\eta_j = \eta_1 + \sum_{k=0}^{j-1} S_k. \tag{A.1}$$

No unfolding has taken place as of yet, i.e., this is an exact expression. Now we postulate that we can write the kth spacing S_k as the product of a smoothly varying local mean spacing s_k and an $\mathcal{O}(1)$ fluctuating number $\rho_k = 1 + \delta_k$

$$\begin{aligned} \eta_j &= \eta_1 + \sum_{k=0}^{j-1} s_k(1+\delta_k) \\ &= \eta_1 + \sum_{k=0}^{j-1} s_k\rho_k. \end{aligned} \tag{A.2}$$

Note that the ρ_k have the form of fluctuating numbers with unit mean; they will therefore serve as our unfolded spacings. By their definition we can write them as

$$\rho_k = \frac{\eta_{k+1} - \eta_k}{s_k}. \tag{A.3}$$

Therefore, if we calculate the smoothly varying mean level spacings s_k from the given data, we can easily find the unfolded spacings. The ambiguity in our particular unfolding procedure lies in the calculation of s_k because its definition involves choosing how many spacings over which to average, a quantity we call $2r$

$$s_k = \frac{\eta_{k+r} - \eta_{k-r}}{2r}. \tag{A.4}$$

It is important to realize that s_k is just the inverse of the density of states. The parameter r is arbitrary except that it must satisfy two conditions:

1) r must be large enough to contain many eigenvalues, which is necessary in order for s_k to be a smooth function of k.

2) r cannot be too large or else s_k will actually smooth over features in the true inverse density of states.

In practice we have chosen r to be the floor function of the square root of the maximum number of eigenvalue spacings ν taken from each matrix. To avoid edge effects we have selected $\nu = 0.8N$. Then $r = \lfloor\sqrt{0.8N}\rfloor$. Here are some typical values of r used in this paper

$$\begin{aligned} N &= 500, \quad r = 22, \\ N &= 1000, \quad r = 31, \\ N &= 2000, \quad r = 44. \end{aligned} \tag{A.5}$$

Such a choice of r grows with N but also is small compared with N. In other words, we satisfy the requirement $1 \ll r \ll N$ as $N \to \infty$.

For even the best choices of r, our unfolding method can still fail if the inverse density of states varies too quickly or has singularities. Such a situation arises for example in small linear combinations of basis matrices (defined in Eq. (2.4) and Eq. (3.7)) for any type. Consider, for example, the insets of Figs. 5.5 and 5.6 that show the densities of state of integrable basis matrices. The large portions of the spectra where the density of states $D(\eta)$ drops to zero is typical of small linear combinations of basis matrices. This behavior is generic for basis matrices of all types, and it can be understood by first considering the expression for the eigenvalues of a type-1 basis matrix (in the primary parametrization) where $d_k = \delta_{k,q}$

$$\eta_j = \frac{\gamma_q^2}{\lambda_j - \varepsilon_q}. \tag{A.6}$$

As both the λ_j and ε_j have finite support, η_j in this case will only approach within a finite distance of zero.

An analogous argument exists for basis matrices in the ansatz parametrization for any type. For linear combinations of a small number of basis matrices, such gaps may overlap, but a mean level spacing s_k will still be ill-defined in many parts of the spectrum. As the number of basis matrices in the linear combination increases, the gaps smooth out until s_k is well-defined everywhere.

Given such gaps in spectra, no choice of r will give the consistent level statistics. This can be seen numerically by varying r and observing that $P(s)$ is strongly dependent on r. We must then avoid regions of the spectrum where $1/D(\eta)$ is poorly behaved.

The difficulty in this task is to automate it so that we can unfold many matrices in succession without having to examine each one by hand. Our solution is to notice that if there are a small number of spacings in the spectrum that are many times the local mean spacing, the standard deviation of the set of actual spacings will be large. If the standard deviation (normalized by the mean) of the actual spacings is near unity, we can be sure that there are no huge jumps such as the ones in Figs. 5.5 and 5.6.

With these considerations, here is our unfolding algorithm:

(1) Calculate $SD = \dfrac{\text{Standard Deviation}}{\text{Mean}}$ of the middle $(80\% + 2r)$ of the spectrum's actual spacings. If $SD < 1.2$, unfold this region of the spectrum with $r = \lfloor\sqrt{0.8N}\rfloor$ and continue to next matrix. If not, continue to step (2).

(2) Shift the region of the spectrum in question to the right by 10 eigenvalues.

(3) If $\eta_{\max} > \eta_{0.9N}$, use 10 fewer spacings AND restart $\eta_{\min} = \eta_{0.1N}$

(4) Calculate SD. If $SD > 1.2$, repeat back to step (2). If $SD < 1.2$ unfold this region of the spectrum with $r = \lfloor\sqrt{0.8N}\rfloor$ and continue to next matrix.

This procedure allows for fewer than $0.8N$ of the spacings to be used, but we are guaranteed to only investigate regions of the spectrum where the mean level spacing accurately represents the size of a typical spacing. Once a sufficiently large number of basis matrices are used in linear combination, the entire middle 80% of the spectrum behaves smoothly and the procedure given above terminates at step (1) for each matrix. The choice of a maximum SD of 1.2 is somewhat arbitrary, and in some parts of this work we used 1.5 in order to increase computation speed (i.e., keep more eigenvalue spacings per matrix). Apart from slight differences in distributions, our results are unaffected by this arbitrariness.

The unfolding procedure used in this paper assumes that the level statistics are the same in all regions of the spectrum, excluding the edges. Although in principle a Hermitian matrix can have different spectral statistics in different parts of its spectrum, we numerically showed in Sect. 5 that the statistics are the same in all parts of the spectrum of integrable matrices $H(u)$, i.e., they are translationally invariant.

Bibliography

[1] In this Introduction, by quantum integrable systems, models, or Hamiltonians we mean exactly solvable many-body models also colloquially called integrable. On the other hand, an ‘integrable matrix’ is a precise concept defined in the 4-th and 5-th paragraphs.

[2] D. Poilblanc, T. Ziman, J. Bellissard, F. Mila, G. Montambaux, Poisson vs. GOE Statistics in Integrable and Non-Integrable Quantum Hamiltonians, Europhys. Lett. **22**, 537 (1993).

[3] D. A. Rabson, B. N. Narozhny, and A. J. Millis, Crossover from Poisson to Wigner-Dyson level statistics in spin chains with integrability breaking, Phys. Rev. B **69**, 054403 (2004).

[4] M. V. Berry and M. Tabor, Level clustering in the regular spectrum, Proc. R. Soc. Lond. A **356**, 375 (1977).

[5] A. Relaño, J. Dukelsky, J.M.G. Gómez, and J. Retamosa, Stringent numerical test of the Poisson distribution for finite quantum integrable Hamiltonians, Phys. Rev. E **70**, 026208 (2004).

[6] H.-J. Stöckmann and J. Stein, “Quantum” chaos in billiards studied by microwave absorption, Phys. Rev. Lett. **64**, 2215 (1990).

[7] C. Ellegaard, T. Guhr, K. Lindemann, H. Q. Lorensen, J. Nygård, and M. Oxborrow, Spectral Statistics of Acoustic Resonances in Aluminum Blocks, Phys. Rev. Lett. **75**, 1546 (1995).

[8] R. Püttner, B. Grémaud, D. Delande, M. Domke, M. Martins, A. S. Schlachter, G.

Kaindl, Statistical Properties of Inter-Series Mixing in Helium: From Integrability to Chaos, Phys. Rev. Lett. **86**, 3747 (2000).

[9] J.-S. Caux, J. Mossel, J. Stat. Mech. Remarks on the notion of quantum integrability, J. of Stat. Mech. **2011**, 02023 (2011).

[10] E. A. Yuzbashyan and B. S. Shastry, Quantum Integrability in Systems with Finite Number of Levels, J. Stat. Phys. **150**, 704 (2013).

[11] M. L. Mehta, *Random Matrices.* (Academic Press, San Diego, 1991).

[12] T. Guhr, A. Müller-Groeling, and H.A. Weidenmüller, Random-matrix theories in quantum physics: common concepts, Phys. Rep. **299**, 189 (1998).

[13] E. A. Yuzbashyan, B. S. Shastry, and J. A. Scaramazza, Rotationally invariant ensembles of integrable matrices, Phys. Rev. E **93**, 052114 (2016).

[14] E. A. Yuzbashyan, B. L. Altshuler and B. S. Shastry, The origin of degeneracies and crossings in the 1d Hubbard mode, J. of Phys. A **35**, 7525 (2002).

[15] B. S. Shastry, A class of parameter-dependent commuting matrices, J. Phys. A **38**, L431 (2005).

[16] H. K. Owusu, K. Wagh, and E. A. Yuzbashyan, Journal of Physics A: Mathematical and Theoretical The link between integrability, level crossings and exact solution in quantum models, J. of Phys. A **42**, 035206 (2009).

[17] H. K. Owusu and E. A. Yuzbashyan, Classification of parameter-dependent quantum integrable models, their parameterization, exact solution and other properties, J. of Phys. A **44**, 395302 (2011).

[18] B. S. Shastry, Parameter-dependent commuting matrices, Plücker relations and related quantum glass models, J. Phys. A **44**, 052001 (2011).

[19] One can equivalently attach the parameter to the V-part, i.e., write $H(u) = T + uV$ as in some of the previous work, or introduce two parameters, $H(x, u) = xT + uV$, see Ref. [13] for more detail.

[20] Two matrices are considered equal if they differ by a multiple of the identity $(c_1 x + c_2)\mathbf{1}$, which is not included in $H^i(x)$. For example, linear independence means that $\sum_i a_i H^i(x) = (c_1 x + c_2)\mathbf{1}$ iff $a_i = 0$.

[21] T. A. Brody, A statistical measure for the repulsion of energy levels, Lett. N. Cimento **7**, 482 (1973).

[22] M. Gaudin, Sur la loi limite de l'espacement des valeurs propres d'une matrice aléatoire, Nuc. Phys. **25**, 447 (1961).

[23] F. Bornemann, On the numerical evaluation of Fredholm determinants, Math. Comp. **79**, 871 (2010).

[24] I. L. Aleiner and K. A. Matveev, Shifts of Random Energy Levels by a Local Perturbation, Phys. Rev. Lett. **80**, 814 (1998).

[25] E. Bogomolny, P. Leboeuf, and C. Schmit, Spectral Statistics of Chaotic Systems with a Pointlike Scatterer, Phys. Rev. Lett. **85**, 2486 (2000).

[26] N. Rosenzweig and C. E. Porter, "Repulsion of Energy Levels" in Complex Atomic Spectra, Phys. Rev. **120**, 1698 (1960).

[27] M. V. Berry, Semiclassical theory of spectral rigidity, Proc. R. Soc. Lond. A **400**, 229 (1985).

[28] Any ensemble composed of lists of independent random numbers is referred to as the "Poisson" ensemble.

[29] T. H. Seligman, J. J. M. Verbaarschot, and M. R. Zirnbauer, Spectral fluctuation

properties of Hamiltonian systems: the transition region between order and chaos, J. Phys. A **18**, 2751 (1985).

[30] Berry works with the spectral ridigity, which is a statistic closely related to the number variance.

[31] R. Prakash and A. Pandey, Phys. Rev. E **93**, 052225 (2016).

[32] T. A. Brody, J. Flores, J. B. French, P. A. Mello, A. Pandey, and S. S. M. Wong, Random-matrix physics: spectrum and strength fluctuations, Rev. Mod. Phys. **53**, 385 (1981).

[33] In this work, the g_j indeed are eigenvalues from an $N \times N$ GOE matrix, but are selected as a set of $N - M$ consecutive eigenvalues instead of $N - M$ randomly chosen ones. This choice does not affect the level statistics.

[34] O. Bohigas and M. J. Giannoni, Level density fluctuations and random matrix theory, Ann. Phys. **89**, 393 (1975).

[35] A. Pandey, Statistical properties of many-particle spectra: III. Ergodic behavior in random-matrix ensembles Ann. Phys. **119**, 170 (1979).

[36] D. M. Basko, I. L. Aleiner, and B. L. Altshuler, Metal–insulator transition in a weakly interacting many-electron system with localized single-particle states, Ann. Phys. **321**, 1126 (2006).

[37] V. Oganesyan and D. Huse, Localization of interacting fermions at high temperature, Phys. Rev. B **75**, 155111 (2007).

[38] A. Pal and D. Huse, Many-body localization phase transition, Phys. Rev. B **82**, 174411 (2010).

[39] P. Shukla, Random matrices with correlated elements: A model for disorder with interactions, Phys. Rev. E **71**, 026226 (2005).

[40] V. E. Kravtsov, I. M. Khaymovich, E. Cuevas, and M. Amini, A random matrix model with localization and ergodic transitions, N. J. Phys. **17**, 122002 (2015).

[41] MBL seems to be a broader class. Even though certain integrals of motion have been identified in MBL systems (see Ref. [42] for example), they have not been shown to be exactly solvable or integrable as defined in this paper.

[42] M. Serbyn, Z. Papić, and D. A. Abanin, Local Conservation Laws and the Structure of the Many-Body Localized States, Phys. Rev. Lett. **111**, 127201 (2013).

[43] R. Modak, S. Mukerjee, E. A. Yuzbashyan, and B. S. Shastry, Integrals of motion for one-dimensional Anderson localized systems, N. J. Phys. **18**, 033010 (2016).

Chapter 6

A note on Lee-Yang Zeros in the negative half-plane

1 Introduction

The zeros of the grand canonical partition function (GPF) $\Xi(z, \Lambda)$, of equilibrium systems in a region Λ at fugacity z, continue to be of interest [1] sixty years after their importance for identifying phase transitions was described by Lee and Yang [2], [3]. It turns out that in some simple models, the L-Y zeros are confined to the negative half z-plane, or even the negative real z-axis [4]- [10]. For example, Heilmann [11] showed that antiferromagnetic Ising models with pair interactions on line graphs (including, e.g., complete graphs) have L-Y zeros confined to the negative z-axis, which is a kind of antiferromagnetic analog to the circle theorem. For more recent work along this direction see [12] and references therein.

Another recent study of an antiferromagnetic Ising-Heisenberg model on a diamond chain found that the nature of the distribution of L-Y zeros corresponds to distinct quantum ground states [13]. In the model considered, one ferrimagnetic phase corresponds to the L-Y zeros confined to the negative z-axis, while another ferrimagnetic phase corresponds to the L-Y zeros being both on the negative axis and on the unit circle. It was also shown recently that when the zeros of the GPF all lie in the left half of the complex z-plane, the system satisfies a local central limit theorem [14], [15].

In this note we obtain some new results for the thermodynamic properties of systems with L-Y zeros confined to the negative half z-plane. We also discuss the relation between the location of the zeros and the sign of the virial coefficients of such systems. Along the way, we obtain an exact expression for the limiting behavior of the GPF for all systems with hard cores in the limit $z \to \infty$, Λ finite.

2 General properties of L-Y zeros

For systems with superstable [16] Hamiltonians, which includes all systems with hard cores and interactions decaying fast enough, as well as ideal fermions, $\Xi(z, \Lambda)$, $\Lambda \subset \mathbb{R}^d$ (or $\Lambda \subset \mathbb{Z}^d$), can be written as a product over its roots, $z_\alpha \equiv -1/\eta_\alpha$ [16]

$$\Xi(z, \Lambda) = \prod_{\alpha=1}^{N_m} (1 + \eta_\alpha z)\,, \quad 1 \leqslant N_m \leqslant \infty, \tag{2.1}$$

where $N_m = N_m(\Lambda)$ is the maximum number of particles that can be contained in Λ. We shall restrict ourselves here to systems with $N_m(\Lambda) < \infty$ and write $N_m = \rho_m |\Lambda|$, where $|\Lambda|$ is the volume of Λ (or the number of lattice sites), without explicitly indicating the dependence of ρ_m on Λ. The roots of $\Xi(z, \Lambda)$ are either negative or come in complex conjugate pairs and depend on Λ, the inverse temperature β, and the interactions - dependencies which we will not write out explicitly[1].

The pressure $p(z, \Lambda)$ is given by

$$\begin{aligned} p(z, \Lambda) &= \frac{\ln [\Xi(z, \Lambda)]}{|\Lambda|} = \frac{1}{|\Lambda|} \sum_{\alpha=1}^{N_m} \ln (1 + \eta_\alpha z) \\ &= \rho_m \Big\langle \ln(1 + \eta z) \Big\rangle. \end{aligned} \tag{2.2}$$

The angular brackets indicate an average over the η_α: $\langle f(z, \eta) \rangle \equiv \frac{1}{N_m} \sum_{\alpha=1}^{N_m} f(z, \eta_\alpha)$. Expanding Eq. (2.2) in powers of z, we obtain the Mayer fugacity expansion [17]

$$p(z, \Lambda) = \sum_{j=1}^{\infty} b_j(\Lambda) z^j, \tag{2.3}$$

---

[1] The zeros will also depend for finite systems on the boundary conditions. This dependence disappears in the thermodynamic limit as can be seen by taking limits in Eq. (2.4) as is done in Eq. (2.5).

where the $b_j(\Lambda)$ are given by

$$b_j(\Lambda) = \frac{(-1)^{j+1}}{j}\rho_m m_j(\Lambda), \tag{2.4}$$

with $m_j(\Lambda) \equiv \langle \eta^j \rangle$, the j-th moment of the η_α's.

Restricting our attention to regular [16] pair potentials $\phi(r)$, where r is the particle separation, the $b_j(\Lambda)$ are given by the Mayer cluster integrals [18]. For example, the second cluster integral $b_2(\Lambda)$ is given by

$$\begin{aligned} b_2(\Lambda) &= \frac{1}{2|\Lambda|}\int_\Lambda d\,\mathbf{r_2}\int_\Lambda (e^{-\beta\phi(r_{12})}-1)d\,\mathbf{r_1}, \\ \lim_{\Lambda\to\mathbb{R}^d} b_2(\Lambda) &= \frac{1}{2}\int_{\mathbb{R}^d}(e^{-\beta\phi(r)}-1)d\,\mathbf{r}. \end{aligned} \tag{2.5}$$

For lattice systems, the integral is replaced by a sum.

The average density in the grand canonical ensemble is given by

$$\begin{aligned} \rho(z,\Lambda) &= z\frac{dp(z,\Lambda)}{dz} = \rho_m\left\langle \frac{\eta\, z}{1+\eta\, z}\right\rangle \\ &= \sum_{j=1}^{\infty} j\, b_j(\Lambda) z^j. \end{aligned} \tag{2.6}$$

The virial expansion is then obtained by eliminating z between Eq. (2.3) and Eq. (2.6) and writing

$$p(\rho,\Lambda) \equiv p(z(\rho,\Lambda),\Lambda) = \sum_{j=1}^{\infty} B_j(\Lambda)\rho^j. \tag{2.7}$$

The relation between the $B_j(\Lambda)$ and $b_i(\Lambda)$, $i \leqslant j$ was derived in [19], but we will not make use of that here. We also do not consider the direct derivation of the virial expansion from the canonical partition function given in [20]. The latter differs from Eq. (2.7) by terms which vanish in the thermodynamic limit $\Lambda \to \mathbb{R}^d(\mathbb{Z}^d)$. The rate of approach to equality between the different ensembles may depend on z (see below).

The $|\eta_\alpha|$'s all lie in the range

$$|z_m(\Lambda)|^{-1} \leqslant |\eta_\alpha(\Lambda)| \leqslant |z_0(\Lambda)|^{-1}, \tag{2.8}$$

where $z_0(\Lambda)$ ($z_m(\Lambda)$) are the zeros of $\Xi(z,\Lambda)$ with the smallest (largest) absolute value. Note that $|z_0(\Lambda)| = R(\Lambda)$, the radius of convergence of the fugacity series Eq. (2.3). There is a simple lower bound to $R(\Lambda)$ uniform in $|\Lambda|$ [17], [21], [22] (for positive potentials it is $R(\Lambda) \geqslant \frac{1}{2e|b_2(\Lambda)|}$). Thus the $|\eta_\alpha(\Lambda)|$ remain bounded above when $|\Lambda| \to \infty$, but can approach zero in this limit. This fact and Eq. (2.4) ensures that there exists a limiting distribution for the η_α's in the thermodynamic limit, i.e. $\langle f(z)\rangle \to \int f(z,\eta)\nu(\eta)d\eta$.

The radius of convergence R of the power series in z, obtained by interchanging the sum in Eq. (2.3) and the limit $\Lambda \to \mathbb{R}^d$ satisfies $R \geqslant \lim_{\Lambda\to\mathbb{R}^d} R(\Lambda)$ [17] with equality when $\phi(r) \geqslant 0$. There is also a lower bound for the radius of convergence $\mathcal{R}(\Lambda)$ of the virial expansion [23], satisfying $\mathcal{R}(\Lambda) \leqslant \mathcal{R}$, where $\mathcal{R}$ is the radius of convergence of the series Eq. (2.7) when $B_j(\Lambda)$ is replaced with $B_j = \lim_{\Lambda\to\mathbb{R}^d} B_j(\Lambda)$.

3 Results for L-Y zeros in the negative half plane

It follows from Eq. (2.4) that if the zeros all lie on the negative z-axis, the $b_j(\Lambda)$ alternate in sign. This alternation of signs also holds if $\phi(r) \geqslant 0$ [24] although $\phi(r) \geqslant 0$ is not a necessary condition for the zeros to be on the negative z-axis [6]. If $\phi(r)$ is negative over any finite range, however, then there exists a β^* sufficiently large (i.e. a sufficiently low temperature) such that the alternation in sign does not hold. Therefore the L-Y zeros can only stay on the negative real z-axis for all temperatures if $\phi(r) \geqslant 0$.

Let $\eta_\alpha = x_\alpha + i\,y_\alpha$. Combining complex conjugate pairs in Eq. (2.6) leads to

$$\rho(z,\Lambda) = \rho_m\left(1 - \left\langle n(z)\right\rangle\right), \tag{3.1}$$

where the dependence of $n_\alpha(z)$ on η_α is given by

$$n_\alpha(z) \equiv \frac{1 + x_\alpha z}{(1 + x_\alpha z)^2 + y_\alpha^2 z^2}. \tag{3.2}$$

The fluctuation in particle number is given by differentiating Eq. (3.1)

$$z\frac{d\rho(z,\Lambda)}{dz} = \frac{1}{|\Lambda|}\left(\overline{N^2}(z,\Lambda) - \overline{N}^2(z,\Lambda)\right), \tag{3.3}$$

where an overbar $\bar{\cdot}$ indicates the ensemble average over the grand canonical measure. We now write Eq. (3.3) in terms of averages over η_α

$$z\frac{d\rho(z,\Lambda)}{dz} = \rho(z,\Lambda)\left(1 - \frac{\rho(z,\Lambda)}{\rho_m}\right) - \Big(V(z,\Lambda) - W(z,\Lambda)\Big), \tag{3.4}$$

where $V(z,\Lambda)$ and $W(z,\Lambda)$ are variances

$$\begin{aligned} V(z,\Lambda) &= \rho_m\left\langle \big(n(z) - \langle n(z)\rangle\big)^2 \right\rangle \geqslant 0, \\ W(z,\Lambda) &= \rho_m\left\langle m^2(z) \right\rangle \geqslant 0, \\ m_\alpha(z) &\equiv \frac{y_\alpha z}{(1 + x_\alpha z)^2 + y_\alpha^2 z^2}. \end{aligned} \tag{3.5}$$

where $\langle m(z)\rangle = 0$ by symmetry of the L-Y zeros about the negative z-axis[2].

When the L-Y zeros are in the negative half plane, i.e. $x_\alpha \geqslant 0$, it is helpful to rewrite Eq. (3.4) in the form

$$\begin{aligned} z\frac{d\rho(z,\Lambda)}{dz} &= 2\rho(z,\Lambda)\left(1 - \frac{\rho(z,\Lambda)}{\rho_m}\right) - 2V(z,\Lambda) - A(z,\Lambda), \\ A(z,\Lambda) &= \rho_m\left\langle \frac{x\,z}{(1 + x\,z)^2 + y^2 z^2} \right\rangle \geqslant 0 \quad \text{if} \quad x_\alpha \geqslant 0. \end{aligned} \tag{3.6}$$

It follows from Eq. (3.6) that when the L-Y zeros are restricted to the negative half z-plane, there is a lower bound on the inverse compressibility

---

[2] Note that the quantity $V(z,\Lambda) - W(z,\Lambda)$ in Eq. (3.4) is a measure of the difference in variance of the L-Y zeros along the real and imaginary directions.

$$\frac{dp(\rho,\Lambda)}{d\rho} \equiv \frac{\rho(z,\Lambda)}{z\frac{d\rho(z,\Lambda)}{dz}} \geqslant \frac{1}{2}\frac{1}{(1-\rho/\rho_m)}, \quad x_\alpha \geqslant 0. \tag{3.7}$$

When the zeros all lie on the negative z-axis, $y_\alpha = 0$, $x_\alpha = \eta_\alpha \geqslant 0$, and $W(z,\Lambda)$ in Eq. (3.4) vanishes. We therefore obtain

$$\frac{dp(\rho,\Lambda)}{d\rho} \geqslant \frac{1}{1-\rho/\rho_m}, \quad \eta_\alpha \geqslant 0. \tag{3.8}$$

Furthermore, differentiating $\rho(z,\Lambda)$ with respect to z when $\eta_\alpha \geqslant 0$ we find

$$\frac{d^k\rho(z,\Lambda)}{dz^k} = (-1)^{k+1}\rho_m\left\langle\frac{\eta^k}{(1+\eta\, z)^{k+1}}\right\rangle, \quad k \geqslant 1,\ \eta_\alpha \geqslant 0, \tag{3.9}$$

which alternates in sign with k.

The inequality Eq. (3.8) becomes an equality for the ideal lattice gas, when the only interaction is the hard core exclusion preventing the occupancy of any lattice site by more than one particle. In that case $\rho_m = 1$, $\Xi(z,\Lambda) = (1+z)^{|\Lambda|}$, and all the L-Y zeroes are located at $z = -1$, i.e. $\eta_\alpha = 1$ for all α. Therefore $V(z,\Lambda) = 0$ and $p(\rho,\Lambda) = -\ln(1-\rho)$.

While Eqs. (3.7-3.9) remain valid in the thermodynamic limit, where $p(\rho)$ is the same for all ensembles, including the grand canonical and canonical ensembles, the same is not true of the limiting equality

$$\lim_{z\to\infty}\left(1-\frac{\rho(z,\Lambda)}{\rho_m(\Lambda)}\right)\frac{dp(z,\Lambda)/dz}{d\rho(z,\Lambda)/dz} = 1, \quad N_m(\Lambda) < \infty. \tag{3.10}$$

Eq. (3.10) follows from the fact that for finite $N_m(\Lambda)$, the $|\eta_\alpha|$'s are bounded away from zero, and is valid independent of the location of the L-Y zeros. Note, however, that Eq. (3.10) may fail if the thermodyamic limit is taken before $z \to \infty$ or when one uses the canonical ensemble definition of the pressure. Such is the case for the lattice systems with extended hard cores discussed in Sect. 4.1.

Another (more interesting) way of writing Eq. (3.10), using Eq. (3.3), is

$$\lim_{z\to\infty}\left\{\frac{N_m(\Lambda)-\overline{N}(z,\Lambda)}{\overline{N^2}(z,\Lambda)-\overline{N}^2(z,\Lambda)}\right\}\frac{\overline{N}(z,\Lambda)}{N_m(\Lambda)}=1,\quad N_m(\Lambda)<\infty, \tag{3.11}$$

where both the numerator and the denominator vanish as $z\to\infty$. Eq. (3.11) also can be obtained by keeping only the terms proportional to z^{N_m-1} and z^{N_m} in the GPF when $z\to\infty$ at fixed Λ.

4 The virial expansion

The thermodynamic properties of a gas are determined at small densities by the virial expansion (VE) of the pressure $p(\rho,\Lambda)$ in powers of the density ρ given in Eq. (2.7). The low order terms in the expansion can be readily computed for classical systems with pair interactions $\phi(r)$ [18]. This can be done analytically or numerically in terms of the irreducible Mayer cluster integrals [25]. In practice one only computes $B_j=\lim_{\Lambda\to\mathbb{R}^d(\mathbb{Z}^d)}B_j(\Lambda)$.

For the system of hard spheres (HS) in $\mathbb{R}^d$, which is the paradigm model for representing the effective strong repulsion between atoms at short distances, the B_j are known in $d=3$ for $j\leqslant 12$ [26], with high accuracy for $j\leqslant 11$ (Boltzmann had computed the first four). In $d=2$, the B_j are known for $j\leqslant 10$ [27]. In $d=1$, $p=\frac{\rho}{1-\rho a}$, where $a=\rho_m^{-1}$ is the diameter of the hard rods, so that $B_j=a^{j-1}$, for all j. Remarkably, all known B_j for $d=1,2,3$ are positive, which has led to the speculation that in fact all B_j in $d=2,3$ are positive. It is known, however, that this is false in $d=5$, so that it is now generally expected that there will be negative B_j in $d=3$, but perhaps not in $d=2$.

The physical interest in the positivity of the B_j lies in the fact that one would like to extrapolate from the low density regime, well described by the first few terms in the virial expansion, to obtain information about $p(\rho)=\lim_{\Lambda\to\mathbb{R}^d}p(\rho,\Lambda)$ at higher densities, including possibly about the fluid-solid transition in $d=3$. Based on numerical simulations

(Monte Carlo or Molecular Dynamics), one expects this transition to occur at a density of $\rho_f \approx .49/v$ where $v = \pi/6\, a^3$ is the actual volume occupied by a sphere with diameter a. The extrapolations of the pressure to higher densities take many forms and are in very good agreement with the machine results for $\rho \lesssim \rho_f$ [28]- [31]; in particular, see Ref. [31] and references there for highly accurate results. Some even give very high accuracy results for the metastable extension between ρ_f and the random close-packing density $\rho_r \approx .64/v$, a region which may also contain a transition from metastable fluid to glass [32, 33, 34].

In many of these (approximate) extrapolations, the radius of convergence $\mathcal{R}$ of the virial expansion is determined by a singularity at some positive value of the density $\tilde{\rho} = \mathcal{R}$, with $\tilde{\rho} > \rho_f$ in $d = 3$ [29]- [31]. This will certainly hold when all B_j, or all but a finite number of them, are positive, but need not be the case otherwise. In fact, for hard hexagons on a triangular lattice $\mathcal{R}$ is determined by a singularity of $p(\rho)$ at ρ', with ρ' complex [35] and smaller in modulus than the disorder-order transition ρ_d [36], $|\rho'| < \rho_d$. If this were true also for hard spheres in $d \geqslant 2$ it would limit the utility of extrapolating the virial expansion beyond the rarified-gas phase.

Here we consider the relation between the signs of the B_j and the location of the Lee-Yang zeros in the complex z-plane. All the previously known examples of almost all positive (i.e. a finite number of negative) B_j were for systems for which all the L-Y zeros lie on the negative z-axis. This behavior fits in with the conjecture by Federbush, et al., that all the B_j for the monomer-dimer system on regular lattices are positive [37], since there the L-Y zeros are indeed on the negative z-axis [9]. Systems with strictly negative L-Y zeros do not have any phase transition, but this does not rule out the possibility that a system with a phase transition has almost all $B_j \geqslant 0$.

In fact, we do not find a direct connection between the negativity of the L-Y zeros and the possibility of almost all positive virial coefficients, and indeed we find models that have only the former property, only the latter, or both. This negative result leaves open the positivity of almost all positive virial coefficients for hard spheres in $d = 2$ or $d = 3$ ($\mathcal{R}$

could even be larger than the close packing density). There does seem, however, to be some connection between the proximity of L-Y zeros to the negative axis and the positivity of virial coefficients (see examples below) for which we have no complete explanation at the present time. For example, in terms of the moments $m_j = \langle \eta^j \rangle$ introduced in Eq. (2.4), the first few B_j are

$$\begin{aligned} B_1 &= 1 = \rho_m m_1, \\ B_2 &= \frac{\rho_m}{2} m_2, \\ B_3 &= \rho_m^2 m_2^2 - \frac{2}{3} \rho_m m_3. \end{aligned} \tag{4.1}$$

It follows that $B_2 > 0$ iff $\langle x^2 \rangle > \langle y^2 \rangle$, where the x_α and y_α are defined in Sect. 3 as the real and imaginary parts of the negative inverse L-Y zeros η_α, respectively.

4.1 Hard core lattice gases in 1D

(i) Consider a 1D lattice of N sites separated by unit distance (the lattice length is $L = N$) with the pair potential $u(x_{ij})$, $(x_{ij} = |i - j|)$

$$\begin{aligned} u(x_{ij}) &= 0 \text{ if } x_{ij} \geqslant q, \\ u(x_{ij}) &= \infty \text{ if } x_{ij} < q. \end{aligned} \tag{4.2}$$

The integer q, $q \geqslant 1$, is called the “exclusion factor” ($q = 1$ is the ideal lattice gas and $q = 2$ is isomorphic to the 1D monomer-dimer problem). Using the canonical ensemble, it was shown in Ref. [3] that for $L \to \infty$

$$\begin{aligned} p(\rho) &= \ln\left(1 + \frac{\rho}{1 - \rho/\rho_m}\right) \\ &= -\ln(1 - \rho/\rho_m) + \ln(1 - \rho/\rho_m + \rho), \end{aligned} \tag{4.3}$$

where $\rho_m = 1/q$. Note that $\lim_{\rho \to \rho_m} (1 - \rho/\rho_m) \frac{dp(\rho)}{d\rho} = 1/\rho_m \neq 1$ for $q > 1$, which gives an example of Eq. (3.10) failing when the thermodynamic limit is taken before letting $z \to \infty$.

Expanding Eq. (4.3) we see that

$$B_j = \frac{1-(1-\rho_m)^j}{\rho_m^j\, j} > 0,\ \forall j, \tag{4.4}$$

which agrees with the finite-L grand canonical virial coefficients from Eq. (2.7) only in the thermodynamic limit. If we introduce the lattice constant δ and take the continuum limit $q\,\delta \to a$ as $q \to \infty$, the problem reduces to that of hard rods of length a on a line with pressure

$$p(\rho) = \frac{\rho}{1-\rho/\rho_m}. \tag{4.5}$$

where $\rho_m = 1/a$. The L-Y zeros of the lattice model are on the negative real axis [7], as are those of the continuum model [5]. Note however the change in the nature of the singularity as $\rho \to \rho_m$, with the divergence in the continuum case much stronger than in the lattice.

One can also derive the distribution of the L-Y zeros when $L \to \infty$ for the q-exclusion models. The equation of state, Eq. (4.3), gives $z(p)$

$$z(p) = (e^p - 1)e^{p(q-1)}, \tag{4.6}$$

Upon using the Lagrange inversion formula to obtain the moments defined in Eq. (2.4), $m_j = \langle \eta^j \rangle$, we find

$$m_j^{[q]} = \lim_{\Lambda\to\infty} m_j^{[q]}(\Lambda) = \binom{j\,q}{j}, \quad j \geqslant 0. \tag{4.7}$$

For $q = 1$, the $m_j^{[1]} = 1$ are moments of a delta function $\delta(\eta - 1)$, which corresponds to the ideal lattice gas. The authors of Ref. [38] consider a more general set of binomial sequences $m_j^{[t,r]} = \binom{tj+r}{j}$. They find that the $m_j^{[t,r]}$ are moments of a probability density function $h_{t,r}(\eta)$ with support on a domain $\mathcal{D}_t \subseteq [0, t^t(t-1)^{1-t}$. Here we have $t = q \in \mathbb{N}$, $r = 0$, and

$h_{q,0}(\eta)$ can be written in terms of the Meijer G-function [38]. This permits, for some q, to express the limiting density of the η_α's in terms of elementary functions. For example, for $q = 2$

$$h_{2,0}(\eta) = \frac{1}{\pi\sqrt{\eta(4-\eta)}}, \quad \eta \in (0,4), \tag{4.8}$$

as also derived in [7]. The density $h_{3,0}(\eta)$ also has a simple expression in terms of elementary functions for $\eta \in (0, 27/4)$, which also diverges at the endpoints. The support of these divergences imply that the L-Y zeros of these two models reach infinity in the thermodynamic limit and that there is an accumulation of zeros near the smallest magnitude L-Y zero z_0.

(ii) The next model we consider is a lattice consisting of two rows in which particles exclude their nearest neighbor sites: two horizontal and one vertical. Using open boundary conditions $\Xi_{2N}(z)$ can be obtained using a transfer matrix M

$$\begin{aligned} \Xi_{2N}(z) &= \mathbf{u} \cdot M^{N-1} \cdot \mathbf{v}_2^T, \\ \mathbf{u} &= (1,1,1), \quad \mathbf{v}_2 = (1,z,z), \\ M &= \begin{pmatrix} 1 & 1 & 1 \\ z & 0 & z \\ z & z & 0 \end{pmatrix}. \end{aligned} \tag{4.9}$$

The fugacity z, as a function of pressure p in the $N \to \infty$ limit, is given by

$$z(p) = e^{2p} \tanh p. \tag{4.10}$$

To locate the L-Y zeros of this model in the thermodynamic limit, we first diagonalize the matrix M and expand $\Xi_{2N}(z)$ in terms of the eigenvalues. A necessary condition for $\Xi_{2N}(z)$ to vanish as $N \to \infty$ is $|\lambda_+(z)| = |\lambda_-(z)|$, where $\lambda_\pm(z) = \frac{1}{2}\left(\pm\sqrt{z^2+6z+1} + z + 1\right)$. The only z that satisfy this relation are real and negative. Therefore, as $N \to \infty$, the L-Y zeros lie on the negative z-axis.

To locate the singularities in the ρ plane, we get $p(\rho)$ from Eq. (4.10)

$$p(\rho) = -\rho_m \ln \left(1 - \frac{\rho}{\rho_m}\right) + \rho_m \ln \left(\frac{\rho}{\rho_m} + \sqrt{1 - 2\frac{\rho}{\rho_m} + 2\left(\frac{\rho}{\rho_m}\right)^2}\right). \tag{4.11}$$

where $\rho_m = 1/2$. The nearest singularities of $p(\rho)$ occur at the square-root singularity in Eq. (4.11), i.e. at $\rho_\pm = \frac{1}{4}(1 \pm i)$. Thus there are an infinite number of negative virial coefficients. Though we limited our analysis to the 2-row case, [8] studies the location of the L-Y zeros of a nearest neighbor exclusion model wound on a cylinder of circumference k and infinite height. It is found that for $k > 2$, the L-Y zeros move off the negative real axis.

(iii) The 2-row monomer-dimer system is considered in Appendix A. We prove that it has almost all $B_j \geqslant 0$. This is not as strong as what Federbush, et al conjecture, but it goes in that direction [37].

4.2 Square well interactions

In all examples so far, systems with positive virial coefficients also have all L-Y zeros on the negative z-axis. Next we give an example where almost all (possibly all) virial coefficients are positive, but the L-Y zeros are off axis. Consider the 1D lattice gas with a nearest neighbor pair potential ε. This system is isomorphic to the 1D Ising model with nearest neighbor interactions. The equation of state in the thermodynamic limit is (see [10], for example)

$$\begin{aligned} p(\rho) &= -\ln[1-\rho] + \ln\left[1 - \frac{1 - 2\alpha\rho - \sqrt{1 - 4\alpha(1-\rho)\rho}}{2(1-\alpha)}\right] \\ \alpha &= 1 - e^{-\varepsilon}. \end{aligned} \tag{4.12}$$

For $\alpha \geqslant 0$, the system is ferromagnetic and the L-Y zeros lie on a circle in the complex plane by the well-known L-Y circle theorem [3]. When $\alpha < 0$ the system is antiferromagnetic and the L-Y zeros are on the negative real axis with a known distribution [10].

The virial coefficients B_j, however, are almost all positive over a range of both positive and negative potentials. The power series of the first logarithm in Eq. (4.12) has all positive coefficients and a radius of convergence of $\mathcal{R}_1 = \rho_m = 1$. If the series expansion of the second logarithm in Eq. (4.12) has a radius of convergence $\mathcal{R}_2 > \mathcal{R}_1$, then it follows that its coefficients will eventually be smaller in magnitude than those of the first logarithm, and only a finite number of virial coefficients can be negative.

All singularities in the second logarithm occur when the square root in Eq. (4.12) vanishes. One finds

$$\begin{aligned} \mathcal{R}_2 &= \mathcal{R}_2(\alpha), \\ &= \inf_{\pm} \left| \frac{1}{2} \left(1 \pm \sqrt{1 - \frac{1}{\alpha}} \right) \right| . \end{aligned} \tag{4.13}$$

Note that for all $\alpha < 1$, $\mathcal{R}_2$ occurs at a complex value of ρ. For $|\alpha| \ll 1$, $\mathcal{R}_2 > \mathcal{R}_1$ and the virial coefficients are almost all positive. As we increase the magnitude of α, $\mathcal{R}_2$ decreases until it falls below $\mathcal{R}_1$, at which point there are an infinite number of negative virial coefficients. Only when $\alpha = 1$, the hard core limit, does $\mathcal{R}_2$ occur at a positive value of ρ. Defining α^* by $\mathcal{R}_2(\alpha^*) = \mathcal{R}_1$, we find

$$\begin{aligned} \alpha^* &= -\frac{1}{8}, \quad \alpha < 0, \\ \alpha^* &= \frac{1}{4}, \quad \alpha > 0. \end{aligned} \tag{4.14}$$

Eq. (4.14) shows that there is a range of positive and negative interactions over which all but a finite number of virial coefficients are positive, i.e.

$$-\ln \frac{9}{8} < \varepsilon < \ln \frac{4}{3}. \tag{4.15}$$

With numerical expansions of the equation of state Eq. (4.12), we find that within the range of Eq. (4.15) (including the endpoints), there are in fact no negative virial coefficients up to $\mathcal{O}(\rho^{2000})$.

Acknowledgements: We thank Eric Carlen, David Huse and Eduardo Waisman for helpful comments. We are particularly thankful to Gene Speer for great help with all aspects of this work. This work was supported by NSF grant DMR 1104500 and AFOSR Grant #FA9550-16-1-0037.

Appendix A

Virial coefficients for the 2-row monomer-dimer problem

Heilmann and Lieb [9] proved that monomer-dimer (MD) systems have all L-Y zeros on the negative real axis of the dimer fugacity z. It is conjectured in [37] that the virial coefficients are always positive for MD systems on regular lattices. We prove here that this is indeed the case for the 2-row infinite square lattice (more precisely, we prove that only a finite number of coefficients can be negative).

We use a standard transfer matrix formalism to obtain the grand partition function on a $2 \times N$ lattice with open boundary conditions. Any configuration of the system has one of five right-end states, corresponding to either no dimers, a single vertical dimer, a single horizontal dimer in the first or second row, or two horizontal dimers occupying both lattice sites on the far right-end of the lattice. Let $\mathbf{v}_N$ be the vector whose j-th component is the GPF for configurations on a $2 \times N$ lattice restricted to having the j-th right-end state. The total GPF $\Xi_N(z)$ is then

$$\begin{aligned} \Xi_N(z) &= \mathbf{u} \cdot \mathbf{v}_N^T \\ &= \mathbf{u} \cdot M^{N-1} \cdot \mathbf{v}_1^T, \end{aligned} \tag{A.1}$$

where

$$\begin{aligned} \mathbf{v}_1 &= (1, z, 0, 0, 0)\,, \\ \mathbf{u} &= (1, 1, 1, 1, 1)\,, \end{aligned} \tag{A.2}$$

and the transfer matrix M is

$$M = \begin{pmatrix} 1 & 1 & 1 & 1 & 1 \\ z & z & z & z & z \\ z & 0 & 0 & z & 0 \\ z & 0 & z & 0 & 0 \\ z^2 & 0 & 0 & 0 & 0 \end{pmatrix}. \tag{A.3}$$

For $z > 0$, one can verify that M^2 has strictly positive entries, which implies by the Perron-Frobenious theorem that there is a unique, real, largest modulus eigenvalue of M for $z > 0$. Let $\lambda_m(z)$ be the largest eigenvalue of M for $z \geqslant 0$, then

$$\begin{aligned} p(z) &= \lim_{N\to\infty} \frac{1}{2N} \ln \Xi_N(z), \\ &= \frac{1}{2} \ln \lambda_m(z), \quad z \geqslant 0. \end{aligned} \tag{A.4}$$

The characteristic polynomial $P(z,\lambda)$ of M satisfies the equation

$$P(z,\lambda) = -\lambda(\lambda + z)(\lambda^3 - (1+2z)\lambda^2 - z\lambda + z^3) = 0, \tag{A.5}$$

which implies that $\lambda_m(z)$ is the largest solution of

$$\lambda^3 - (1+2z)\lambda^2 - z\lambda + z^3 = 0. \tag{A.6}$$

To analyze the series $p(\rho) = \sum_{j=1}^{\infty} B_j \rho^j$, where ρ is the dimer density, we make a helpful change of variables to $t(z) \equiv \frac{z}{\lambda_m(z)}$. Using Eq. (A.6), we find

$$\begin{aligned} &\text{for } t \in [0, \phi^{-1}) : \\ &z(t) = \frac{t(1+t)}{(1-t)(\phi^{-1}-t)(\phi+t)}, \\ &p(t) = \rho_m \ln\left(\frac{1+t}{(1-t)(\phi^{-1}-t)(\phi+t)}\right), \\ &\rho(t) = \rho_m \left(1 - \frac{(1-t^2)(\phi^{-1}-t)(\phi+t)}{P_4(t)}\right), \\ &P_4(t) \equiv 1 + 2t - 2t^2 - 2t^3 - t^4. \end{aligned} \tag{A.7}$$

where ϕ is the golden mean, $\phi = (1+\sqrt{5})/2 \approx 1.6108$, and $\rho_m = 1/2$ is the maximum density.

Let $t_{1,2}$ be the two real roots of the polynomial $P_4(t)$, where $t_1 \approx -.394$ and $t_2 \approx .784$. On $\mathbb{T} = (t_1, t_2)$, $\rho(t)$ is a strictly increasing function, with $\rho(t) \to -\infty$ as $t \to t_1$ and

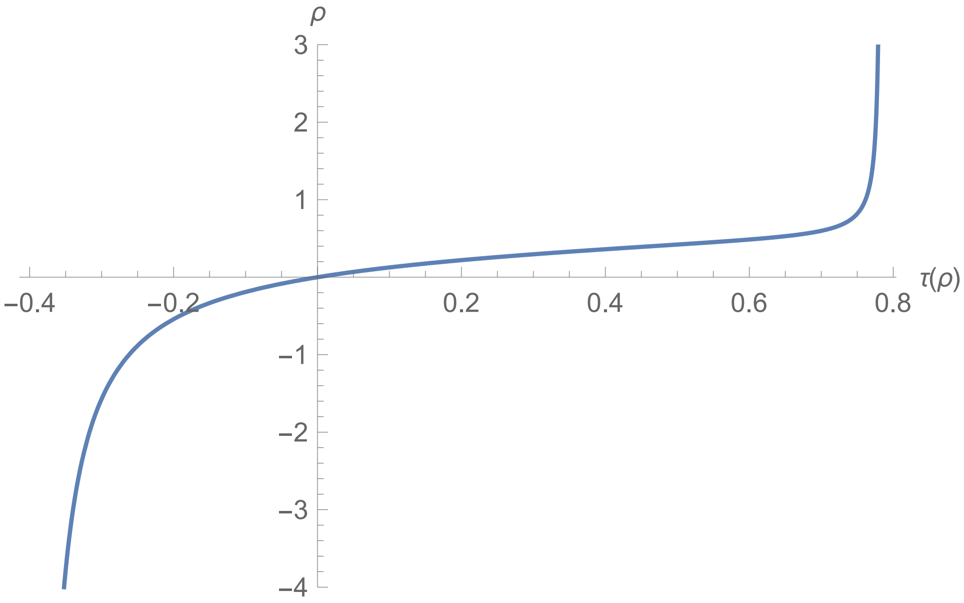

Figure A.1: The function $\tau(\rho)$ plotted on the horizontal axis. Note that $\tau(\rho)$ is a bijection from $\mathbb{R}$ to $\mathbb{T} \approx (-.394, .784)$.

$\rho(t) \to \infty$ as $t \to t_2$, so that we may define $\tau(\rho)$ to be the particular inverse function of $\rho(t)$ which takes values in $\mathbb{T}$. $\tau(\rho)$ is then a bijection from $\mathbb{R}$ to $\mathbb{T}$ (see Fig. A.1), with $\tau(\rho(t)) = t$ for $t \in \mathbb{T}$. This definition of $\tau(\rho)$ allows us to define $p(\rho)$ on $\rho \in (-\infty, \rho_m)$

$$\begin{aligned} p(\rho) &= -\rho_m \ln\left(1 - \rho/\rho_m\right) + \rho_m \ln\left(\frac{(1+\tau(\rho))^2}{P_4(\tau(\rho))}\right), \\ &= -\rho_m \ln\left(1 - \rho/\rho_m\right) + f(\rho), \quad \rho \in (-\infty, \rho_m)\,. \end{aligned} \tag{A.8}$$

We now analytically continue $p(\rho)$ from the domain $\rho \in (-\infty, \rho_m)$ into the complex plane in order to determine the location of its finite-ρ singularities. In particular, the first logarithm in Eq. (A.8) is singular only at ρ_m or $|\rho| \to \infty$. This term has all positive expansion coefficients about $\rho = 0$ and a radius of convergence of $\mathcal{R}_1 = \rho_m$. We will show that $f(\rho)$ is analytic inside a disk of radius $\mathcal{R}_2 > \mathcal{R}_1$. This implies that asymptotically the coefficients in the expansion of $f(\rho)$ are smaller in magnitude than those coming from the first term, and therefore there are at most a finite number of negative virial coefficients.

The singularities of the second logarithm in Eq. (A.8) occur either where $\tau(\rho)$ is singular or where $f(\rho)$ diverges. To discuss both of these possibilities it is convenient to define a single-valued “physical” branch of $\tau(\rho)$ in an appropriately cut complex ρ plane. We begin with $\tau(\rho)$ defined on the entire real axis (see Fig. A.1) and real analytic there. All possible singularities (branch points) t^* of $\tau(\rho)$ may be found by solving $\frac{d\rho(t)}{dt}\big|_{t^*}= 0$; using Mathematica to get numerical values, we find six solutions of this equation, with corresponding branch points in the ρ plane given by $0.313 \pm 0.536\,i$, $0.497 \pm 0.121\,i$, 0.438, and 1.039. We now introduce four cuts in the ρ plane, one beginning at each of the complex branch points and extending radially to ∞. The physical branch of $\tau(\rho)$ is defined in this plane by analytic continuation from the real axis, and is single valued. Note that we do not need to consider the two real branch points since this physical branch is known to be analytic on the real axis; these branch points lie on other sheets of $\tau(\rho)$.

The singularities we must consider in determining $\mathcal{R}_2$, the radius of convergence of the power series for $f(\rho)$ in powers of ρ, are thus the four complex branch points defined above and the points where $f(\rho)$ diverges. For the latter, we note that $f(\rho)$ diverges if $\tau(\rho) = -1$. Using Eq. (A.7), however, we see that $\tau(\rho) = -1$ implies that $\rho = \rho_m$, and we know that on the physical branch, $\tau(\rho_m) = \phi^{-1} \neq -1$; thus this singularity cannot occur on the physical branch. The only other way that $f(\rho)$ diverges is if $P_4(\tau(\rho)) = 0$. Here we again use Eq. (A.7) and we see that $|\rho(t)| = \infty$ if $P_4(t) = 0$; these singularities occur at ∞ in the ρ plane and cannot affect the value of $\mathcal{R}_2$.

Since each of the complex branch points of $\tau(\rho)$ has absolute value greater than ρ_m, we conclude that $\mathcal{R}_2 > \mathcal{R}_1$. It follows that for $j \to \infty$, the B_j are dominated by those obtained from the first logarithm in Eq. (A.8). Hence, there are at most a finite number of negative virial coefficients in the virial expansion.

The solution of the finite *periodic* 2-row lattice (not detailed here) yields the first $N-1$ infinite lattice virial coefficients exactly (see [39] for example). Numerically we checked the first 200 virial coefficients are positive, and we believe that the proven finite number of negative coefficients is indeed zero.

Bibliography

[1] I. Bena, M. Droz, and A. Lipowski, Statistical mechanics of equilibrium and nonequilibrium phase transitions: the Yang-Lee formalism, Int. J. Mod. Phys. B **19**, 4269 (2005).

[2] C.N. Yang and T .D. Lee, Statistical theory of equations of state and phase transitions. I. Theory of condensation, Phys. Rev. **87**, 404 (1952).

[3] T. D. Lee and C.N. Yang, Statistical theory of equations of state and phase transitions. II. Lattice gas and Ising model, Phys. Rev. **87**, 410 (1952).

[4] E. H. Hauge and P. C. Hemmer, On the Yang-Lee distribution of roots, Physica **29**, 1338 (1963).

[5] J. S. N. Elvey and O. Penrose, The Yang-Lee distribution of zeros for a classical one-dimensional fluid, J. Phys. A **1** 661 (1968).

[6] T. Niemeyer and A. Weijland, The Yang-Lee distribution of zeros of the grand partition function of the Takahashi gas, Physica **50**, 457 (1970).

[7] E. Hiis Hauge and P. C. Hemmer, J. O. Aasen, Distribution of zeros of the grand partition function, J. Math. Phys. **7** 35 (1966).

[8] T. S. Nilson and P.C. Hemmer, Zeros of the grand partition function of a hard-core lattice gas, J. Chem. Phys. **46**, 2640 (1967).

[9] O. J. Heilmann and E.H. Lieb, Theory of monomer-dimer systems, Commun. Math. Phys. **25** 190 (1972).

[10] S. Katsura and M. Ohminami, Distribution of zeros of the partition function for the one dimensional Ising models, J. Phys. A **5**, 95 (1972).

[11] O. J. Heilmann, Location of the zeros of the grand partition function of certain classes of lattice gases, Stud. App. Math. **50**, 385 (1971).

[12] J. L. Lebowitz, D. Ruelle, and E. R. Speer, Location of the Lee-Yang zeros and absence of phase transitions in some Ising spin systems, J. Math. Phys. **53**, 095211 (2012).

[13] N. S. Ananikian, V. V. Hovhannisyan, R. Kenna, Partition function zeros of the antiferrogmagnetic spin-1/2 Ising-Heisenberg model on a diamond chain, Physica A **396**, 51 (2014).

[14] P. J. Forrester and J.L. Lebowitz, Local central limit theorem for determinantal point processes, J. Stat. Phys. **157**, 60 (2014).

[15] J. L. Lebowitz, B. Pittel, D. Ruelle, and E. R. Speer, Central limit theorems, Lee-Yang zeros, and graph-counting polynomials, arXiv:1408.4153.

[16] D. Ruelle. *Statistical Mechanics: Rigorous Results.* (W.A. Benjamin, Inc. New York, Amsterdam, 1969). Eq. (3.2.27) and Exercise 3E.

[17] O. Penrose, Convergence of fugacity expansions for fluids and lattice gases, J. Math. Phys. **4**, 1312 (1963).

[18] G. Stell, Cluster expansions for classical systems in equilibrium, in *The Equilibrium Theory of Classical Fluids.* (Eds. H. L. Frisch and J. L. Lebowitz, W.A. Benjamin, New York, 1969).

[19] J. Mayer, Contribution to statistical mechanics, J. Chem. Phys. **10**, 67 (1942).

[20] E. Pulvirenti and D. Tsagkarogiannis, Cluster expansion in the canonical ensemble, Commun. Math. Phys. **316**, 289 (2012).

[21] J. Groeneveld, Two theorems on classical many-particle systems, Phys. Letters **3**, 50 (1962).

[22] D. Ruelle, Correlation functions of classical gases, Ann. Phys. **25**, 109 (1963).

[23] J. L. Lebowitz and O. Penrose, Convergence of virial expansions J. Math. Phys. **5**, 841 (1964).

[24] E. Lieb, New method in the theory of imperfect gases and liquids, J. Math. Phys. **4**, 671 (1963).

[25] R. K. Pathria and P.D. Beale. *Statistical Mechanics, Third Edition.* (Elsevier, 2011).

[26] R. J. Wheatley, Calculation of high-order virial coefficients with applications to hard and soft spheres, Phys. Rev. Lett. **110**, 200601 (2013).

[27] N. Clisby and B. M. McCoy, Ninth and tenth order virial coefficients for hard spheres in D dimensions, J. Stat. Phys. **122**, 15 (2006).

[28] A. Mulero, C. Galán, and F. Cuadros, Equations of state for hard spheres. A review of accuracy and applications, Phys. Chem. Chem. Phys. **3**, 4991 (2001).

[29] M. Robles, M. López de Haro, A. Santo, Note: Equation of state and the freezing point in the hard-sphere model, J. Chem. Phys. **140**, 136101 (2014).

[30] R. Bonneville, A semi empirical compact equation of state for hard sphere fluids at any density, Fluid Phase Equil. **421**, 9 (2016).

[31] H. Hansen-Goos, Accurate prediction of hard-sphere virial coefficients B6 to B12 from a compressibility-based equation of state, J. Chem. Phys. **144**, 164506 (2016).

[32] R. Jadrich and K.S. Schweizer, Equilibrium theory of the hard sphere fluid and glasses in the metastable regime up to jamming. I. Thermodynamics, J. Chem. Phys. **139**, 054501 (2013).

[33] G. Parisi and F. Zamponi, The ideal glass transition of hard spheres, J. Chem. Phys. **123**, 144501 (2005).

[34] A. P. Gast and W.B. Russel, Simple ordering in complex fluids, Phys. Today **51**, 24 (1998).

[35] D. S. Gaunt and G. S. Joyce, Virial expansions for hard-core fluids, J. Phys. A **13**, L211 (1980).

[36] R. J. Baxter, Hard hexagons: exact solution, J. Phys. A **13**, L61 (1980).

[37] P. Butera, P. Federbush, and M. Pernici, Positivity of the virial coefficients in lattice dimer models and upper bounds on the number of matchings on graphs, Physica A **437**, 278 (2015).

[38] W. Młotkowski and K. Penson, Probability distributions with binomial moments, Infin. Dimens. Anal. Quantum. Probab. Relat. Top. **17**, 1450014 (2014).

[39] J. L. Lebowitz and J. K. Percus, Thermodynamic properties of small systems, Phys. Rev. **124**, 1673 (1961).